IEKP-KA/2013-27

Untersuchung neuartiger Sensorkonzepte und Entwicklung eines effektiven Modells der Strahlenschädigung für die Simulation hochbestrahlter Silizium-Teilchendetektoren

Robert Eber

Zur Erlangung des akademischen Grades eines
DOKTORS DER NATURWISSENSCHAFTEN
von der Fakultät für Physik des
Karlsruher Instituts für Technologie (KIT)

genehmigte

DISSERTATION

von

Dipl.-Phys. Robert Eber
aus Karlsruhe

Tag der mündlichen Prüfung: 29.11.2013

Referent: Prof. Dr. Thomas Müller, Institut für Experimentelle Kernphysik
Korreferent: Prof. Dr. Willem de Boer, Institut für Experimentelle Kernphysik

Robert Eber:
Investigations of new Sensor Designs and Development of an effective Radiation Damage Model for the Simulation of highly irradiated Silicon Particle Detectors
November 2013

ZUSAMMENFASSUNG

Siliziumsensoren werden in der Hochenergiephysik eingesetzt, um Sekundärteilchenspuren aus Kollision an Teilchenbeschleunigern zu rekonstruieren. Der heute größte Silizium-Spurdetektor ist Teil des Compact Muon Solenoid-Experiments (CMS) am Large Hadron Collider (LHC) am CERN. Der LHC erzeugt hauptsächlich Proton-Proton-Kollisionen mit 40 MHz bei einer maximalen Schwerpunktsenergie von 14 TeV und einer Luminosität von $10^{34}\ \mathrm{cm}^{-2}\mathrm{s}^{-1}$. Die aus den Kollisionen entstehenden geladenen Sekundärteilchen durchqueren die Siliziumsensoren und hinterlassen ein detektierbares Signal.

Die durchquerenden Teilchen verursachen auch Strahlenschäden in den Siliziumsensoren, welche zu einer Beeinträchtigung deren Funktionstüchtigkeit führen. Die nach der nominalen Betriebsdauer erwartete Fluenz von $2 \times 10^{14}\ n_{eq}\mathrm{cm}^{-2}$ führt zu einem erhöhten Leckstrom der Silizium-Halbleitersensoren sowie zu einer erhöhten Verarmungsspannung und einem verminderten Signal. Diese Veränderungen führen insgesamt zu einer geringeren Effizienz und Ortsauflösung des Spurdetektors.

Ein Ausbau des jetzigen Teilchenbeschleunigers LHC ist für das Jahr 2022 geplant. Die Luminosität soll dabei um einen Faktor fünf auf $5 \cdot 10^{34}\ \mathrm{cm}^{-2}\mathrm{s}^{-1}$ gesteigert werden. Der Beschleuniger befindet sich dann in der Hochluminositätsphase, HL-LHC. Dadurch wird die Anzahl der erzeugten Sekundärteilchen deutlich gesteigert und führt zu einer höheren Spurdichte und einer extremen Strahlenbelastung des CMS-Spurdetektors. Die jetzt eingebauten Sensoren, welche bis zu dieser Erneuerung des Beschleunigers bereits vorgeschädigt sein werden, sind diesem Strahlenumfeld für die geplante Dauer der Hochluminositätsphase nicht gewachsen. Der CMS-Spurdetektor muss daher mit strahlenharten Siliziumsensoren neu konstruiert werden. Eine groß-angelegte Kampagne zur Bestimmung des geeigneten Siliziummaterials für das Phase-II-Upgrade des CMS-Spurdetektors wurde angestoßen und ist in vollem Gange.

In dieser Kampagne wurden Testsensoren, -dioden und -strukturen auf unterschiedlichen Siliziumgrundmaterialien und Wafern unterschiedlicher Dotierung gefertigt. Die Sensoren und Dioden sind mit Hilfe der Probestation hinsichtlich ihrer Streifenparameter sowie ihres Leckstroms und ihrer Kapazität qualifiziert worden. Im Zuge dessen sind Simulationen dieser Strukturen durchgeführt worden, um die Eigenschaften und die Effizienz der Strukturen besser zu verstehen.

Im Laufe dieser Arbeit wurde, um die Strahlenschädigung von Dioden zu untersuchen, ein Picosekundenlaser-Messystem am Institut aufgebaut, welches in der Lage ist, die Signale kurzer Laserpulse in einer Diode zeitlich aufzulösen. Diese Art der Messung wird auch als Transient-Current-Technique (TCT) bezeichnet. Sie bietet die Möglichkeit, das elektrische Feld in Dioden zu rekonstruieren.

Ein Entwurf einer Siliziumdiode, welche sowohl für Messungen in der am IEKP errichteten Probestation als auch für Messungen mit dem neuen Picosekundenlasersystem geeignet ist und eine verbesserte Isolation der Schutzringe bietet, wird anhand von Simulationen und zwei verschiedenen Produktionen vorgestellt.

Ein neuartiges Sensorkonzept, das für das Phase-II-Upgrade entworfen worden ist und das den Pitchadapter, welcher nötig ist, um die Auslesestreifen des Streifensensors an die Elektronik anzuschließen, direkt auf dem Sensor integriert, ist erstmals auf den Wafern gefertigt worden. Dieser Sensor ist dann sowohl elektrisch als auch in einem Streifenauslesesystem getestet worden. Die Implementierung des Pitchadapters auf dem Sensor, welcher zu einer Materialersparnis im zukünftigen Spurdetektor führen kann, erfolgte dabei in der ersten oder in der zweiten Aluminiumlage. Simulationen konnten dazu beitragen, ein unerwünschtes Koppeln von Signalen zu Nachbarstreifen in der ersten Aluminiumlage zu erklären.

Um die Strahlenhärte der Sensoren zu testen, wurden die Sensoren und Dioden mit Protonen und Neutronen bestrahlt. Die Fluenz, zu welcher bestrahlt wurde, entspricht dabei der

erwarteten Fluenz von geladenen und neutralen Teilchen, die den Sensor im zukünftigen CMS-Spurdetektor am HL-LHC schädigen werden.

Die Daten aus den Messungen mit dem Picosekundenlasersystem zusammen mit den Erkenntnissen aus der elektrischen Qualifizierung fließen in die Entwicklung eines effektiven Defektmodells für die Strahlenschädigung dieser Dioden und Sensoren im HL-LHC-Bestrahlungsszenario ein. Das Defektmodell, welches sich hauptsächlich auf Strom-Spannungs-Kurven und Kapazität-Spannungs-Kurven sowie TCT-Messungen stützt, ist ein Substrat-Defekt-Modell für die kommerzielle T-CAD-Software Synopsys Sentaurus. Es kann die elektrischen Felder in Dioden, die zu den charakteristischen zwei Maxima (Doppelpeaks) in den TCT-Messungen führen, gut wiedergeben. Die Bestimmung der Parameter des Zwei-Defekt-Modells wird vorgestellt. Es ist das erste Modell, welches die Vorhersage des Leckstroms, der Verarmungsspannung, den zeitlichen Verlauf der driftenden Ladungsträger und die gesammelte Ladung nach Bestrahlung in einem Modell vereinigt und beschreiben kann.

Desweiteren ist das entwickelte Modell verwendet worden, um das Zusammenspiel von Strahlenschädigung im Siliziumsubstrat und auftretenden Oberflächenschäden in der Simulation zu untersuchen. Oberflächenschäden haben einen starken Einfluss auf die Leistungsfähigkeit der Streifensensoren im Hinblick auf die gesammelte Ladung und auf hohe elektrische Felder in der Nähe der Streifen, welche zu erhöhtem Rauschen, Ladungsvervielfachung oder einem frühzeitigen Durchbruch der Sensoren führen können. Die Ladungssammlung ist in guter Übereinstimmung mit Messdaten simuliert und die auftretenden elektrischen Felder in den Sensoren sind ausführlich analysiert worden.

Beginnend mit einer kurzen Einführung des CMS-Experiments am LHC am europäischen Kernforschungszentrum CERN wird in dieser Arbeit die Funktionsweise von Siliziumsensoren als Teilchendetektor dargestellt und die Auswirkungen von Strahlenschäden auf ihre Eigenschaften erläutert. Alle Messtechniken und die dazugehörigen verwendeten Messysteme sowie Bestrahlungseinrichtungen werden vorgestellt. Die Simulation ist ein bedeutender Bestandteil dieser Arbeit; das Simulationspaket und die verwendeten Parameter werden daher ausführlich diskutiert.

Zu den Messungen an unbestrahlten Sensoren und Dioden werden die zugehörigen Simulationen der gemessenen Strukturen präsentiert und analysiert. Der Entwurf einer Diode sowie ein neuartiges Sensorkonzept, das den Pitchadapter direkt auf dem Sensor integriert, um zusätzliches Material im Spurdetektor einzusparen, wird erörtert.

Mit den Daten der bestrahlten Sensoren und Dioden wird die Entwicklung des effektiven Zwei-Defekt-Modells für die Strahlenschädigung des Siliziumsubstrats diskutiert. Das effektive Zwei-Defekt-Modell wird eingesetzt, die Strahlenschädigung in Dioden und Sensoren vorherzusagen. Die Simulation kritischer elektrischer Felder im Siliziumsensor, welche nach hoher Bestrahlung auftreten können, ist eine wichtige Anwendung des Simulationsmodells und findet sich im letzten Abschnitt dieser Arbeit.

IEKP-KA/2013-27

Investigations of new Sensor Designs and Development of an effective Radiation Damage Model for the Simulation of highly irradiated Silicon Particle Detectors

Robert Eber

Zur Erlangung des akademischen Grades eines
DOKTORS DER NATURWISSENSCHAFTEN
von der Fakultät für Physik des
Karlsruher Institut für Technologie

genehmigte

DISSERTATION

von

Dipl.-Phys. Robert Eber
aus Karlsruhe

Tag der mündlichen Prüfung: 29.11.2013

Referent: Prof. Dr. Thomas Müller, Institut für Experimentelle Kernphysik
Korreferent: Prof. Dr. Willem de Boer, Institut für Experimentelle Kernphysik

Robert Eber:
Investigations of new Sensor Designs and Development of an effective Radiation Damage Model for the Simulation of highly irradiated Silicon Particle Detectors
November 2013

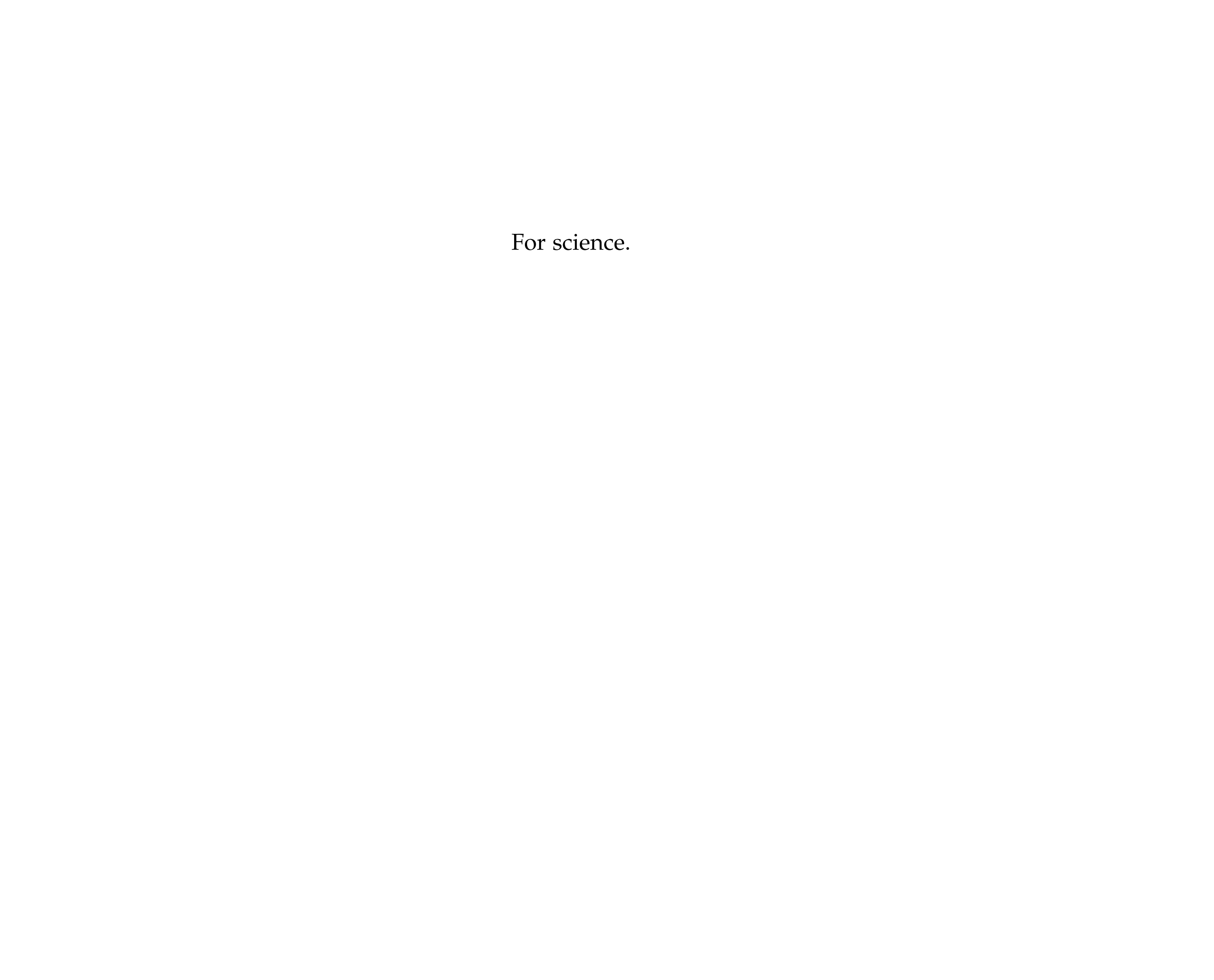

For science.

ABSTRACT

The Compact Muon Solenoid experiment (CMS) located at the Large Hadron Collider (LHC) at CERN makes use of silicon sensors in its tracker, currently the world's largest all-silicon tracker. The CMS Tracker detects secondary particles from the primary proton-proton collisions with a center-of-mass energy of up to 14 TeV and a luminosity of $10^{34}\,\mathrm{cm^{-2}s^{-1}}$. During its nominal lifetime, the sensors with an active area of $200\,\mathrm{m}^2$ suffer from radiation damage induced by these particles. The expected maximum fluence for the current tracker is $2 \times 10^{14}\,n_{eq}\mathrm{cm}^{-2}$, leading to an increase in leakage current and depletion voltage and a reduction of the signals in the silicon sensors. Other parameters are affected as well, decreasing the performance and resolution of the detector.

An upgrade of the LHC with a five-fold increase in luminosity to $5 \times 10^{14}\,\mathrm{cm^{-2}s^{-1}}$ is planned for about 2022 – the high luminosity (HL) LHC. To cope with the increase in luminosity, the CMS Tracker has to be upgraded with very radiation hard sensors. A campaign is in full progress to identify the future silicon material for the CMS Tracker Upgrade Phase II, including test sensors, diodes and other test structures fabricated on n-bulk and p-bulk.

The un-irradiated sensors and diodes are electrically characterized and simulated as well to understand the performance of these devices. A newly designed sensor with integrated pitch adapter on the sensor is analyzed with corresponding simulations in a version with a second metal layer on the sensor. Moreover, several diode layouts with different geometries for high voltage stability and proper CV measurements have been designed, simulated, fabricated and measured.

To test the available materials for radiation hardness, the different structures are irradiated in the HL-LHC-like scenario with protons and neutrons to the expected fluences.

In the course of this thesis, a picolaser setup has been built and advanced to analyze the performance of diodes after irradiation. Together with electrical tests done in the IEKP probe station, the data is used to develop an effective two-defect irradiation model, which can describe the measurement data and predict the performance of diodes irradiated to $10^{14}\,n_{eq}\mathrm{cm}^{-2}$ – $10^{15}\,n_{eq}\mathrm{cm}^{-2}$. The advantages and drawbacks of such a model are discussed in detail.

Furthermore, the model is used to simulate silicon strip sensor and analyze the interplay between the effective two-defect model, which is a bulk damage model, and surface damage in the sensors. With respect to the performance of the sensors, both quanities affect the performance of the sensor. Electric field, charge collection and charge multiplication are discussed considering measurements and simulation.

Beginning with a general introduction to the CMS experiment at the Large Hadron Collider, the thesis shortly introduces silicon as a particle detector and the effects of radiation on the silicon sensors. The description of the used measurement techniques, irradiation and measurement facilities follows. The simulation framework and all the parameters used in the simulation is described and discussed in more detail in chapter 7.

Having introduced the simulation basics, the un-irradiated devices, diodes and sensors, are studied in detail. A new diode design for correct CV measurements on p-bulk diodes with p-stop isolation is proposed in chapter 9; the functionality of the sensors with integrated pitch adapter is discussed in the consecutive chapter.

The main part of the thesis, developing a two-defect radiation model, its tuning and application is explained and discussed in the chapters 11 and 12 for diodes and sensors. The results from the different chapters are summarized.

CONTENTS

I INTRODUCTION AND BASICS 1

1 INTRODUCTION AND MOTIVATION 3

2 THE LARGE HADRON COLLIDER AND THE CMS EXPERIMENT 5

- 2.1 The Large Hadron Collider 5
- 2.2 The CMS Detector in a Nutshell 6
- 2.3 Upgrade 9
  - 2.3.1 Upgrade of the Large Hadron Collider 9
  - 2.3.2 Upgrade of CMS 9
- 2.4 The HPK-Campaign 12
  - 2.4.1 Materials and Structures 12
  - 2.4.2 Naming 12
  - 2.4.3 Impurity Contents 13
  - 2.4.4 Irradiation and Qualification Procedure 14

3 SILICON PARTICLE DETECTORS 15

- 3.1 Working Principle 15
- 3.2 Layout of Silicon Sensors 17
  - 3.2.1 Isolation Techniques 18
- 3.3 Properties of Silicon used as Particle Detector 19
  - 3.3.1 Silicon – A Special Semiconductor 19
  - 3.3.2 Silicon Band Structure 19
  - 3.3.3 Fermi Level 22
  - 3.3.4 Silicon Crystal Structure 22
  - 3.3.5 Doping 23
  - 3.3.6 Properties of the pn-Junction 23
  - 3.3.7 Silicon Growth Techniques 30

4 RADIATION DAMAGE IN SILICON 32

- 4.1 Bulk Defects 32
- 4.2 NIEL-Scaling 32
  - 4.2.1 The Hardness Factor 34
- 4.3 Impact of Defects 34
  - 4.3.1 Generation Current 36
  - 4.3.2 Change of effective Doping Concentration and Depletion Voltage 36
  - 4.3.3 "Type Inversion" 37
- 4.4 Annealing of Defects 38
  - 4.4.1 Current 38
  - 4.4.2 Effective Doping Concentration 39
- 4.5 Trapping 40
- 4.6 A Summary of important Defects 41
- 4.7 Surface Damage 41

II TECHNIQUES AND EQUIPMENT 43

5 MEASUREMENT TECHNIQUES 44

- 5.1 Electrical Measurements 44
  - 5.1.1 Current-Voltage (IV) 44
  - 5.1.2 Capacitance-Voltage (CV) 44
  - 5.1.3 Strip Measurements 46
  - 5.1.4 Flatband Voltage 47
- 5.2 Transient Current Technique (TCT) 49

5.2.1 Optical Absorption in Silicon . . . 49
5.2.2 Charge Carrier Transport . . . 50
5.2.3 Drift Signal . . . 51
5.2.4 Charge Collection Efficiency . . . 52
5.2.5 Trapping Time . . . 52
5.2.6 The Origin of the Double Peak in irradiated Sensors . . . 53
5.2.7 "Type Inversion" in TCT . . . 54
6 IRRADIATION AND QUALIFICATION 56
6.1 Irradiation Facilities . . . 56
6.1.1 Neutron Reactor in Ljubljana . . . 56
6.1.2 Karlsruhe Cyclotron . . . 56
6.2 Qualification Infrastructure . . . 57
6.2.1 Probe Station . . . 57
6.2.2 Strip Sensor Readout System (ALiBaVa) . . . 57
6.2.3 The Picolaser Setup . . . 59
6.2.4 Data Storage and Access . . . 61
7 SIMULATION FRAMEWORK 64
7.1 Synopsys Sentaurus TCAD . . . 64
7.1.1 The Workflow . . . 64
7.1.2 Modeling of Devices . . . 64
7.1.3 Models and Parameters used in the Simulation . . . 65
7.1.4 The Simulation Command File . . . 69
7.1.5 Analysis of the Results . . . 70
7.1.6 Simulation of Radiation Damage . . . 70
7.2 Comparison with Silvaco Atlas . . . 72
7.2.1 Bandgap . . . 73
7.2.2 Saturation Velocity . . . 74
7.2.3 Charge Carrier Mobility . . . 74
7.2.4 Impact Ionization . . . 75
7.2.5 Impact on the Simulation Results . . . 76
7.2.6 Summary of the Comparison . . . 77

III STUDIES 79
8 ANALYSIS AND SIMULATION OF DEVICES 80
8.1 Performance of un-irradiated Diodes . . . 80
8.1.1 Simulation of Diodes – Diode Layout . . . 80
8.1.2 Full Depletion Voltage and Doping Profile . . . 81
8.1.3 Leakage Current . . . 87
8.2 CV Measurements and the Guardring . . . 90
8.2.1 Active Area of Diodes . . . 90
8.2.2 Comparison of the Dimensions with the GDS file . . . 92
8.2.3 Direct calculations . . . 93
8.2.4 Comparison of the Curve Shapes . . . 93
8.2.5 Evaluation of the Depletion Voltage . . . 95
8.2.6 Summary of the CV Evaluation . . . 95
8.3 Signals in Diodes . . . 98
8.3.1 Implementation . . . 98
8.3.2 SPICE Models . . . 99
8.3.3 TCT . . . 99
8.3.4 Charge Collection Efficiency . . . 100
8.4 Simulation of Silicon Strip Sensors . . . 102
8.4.1 Layout of Strip Sensors . . . 102
8.4.2 Coupling Capacitance . . . 103

8.4.3 Interstrip Capacitance . . . 104
8.4.4 Spice Network . . . 105
8.4.5 Current in Strip Sensors . . . 105
8.4.6 Electric Field at the Strips . . . 106
8.4.7 Charge Collection Efficiency . . . 107
8.4.8 Edge-TCT . . . 110
9 ADVANCED DIODE DESIGN 113
9.1 Layouts . . . 113
9.1.1 Guard Rings . . . 113
9.1.2 Isolation . . . 114
9.2 Simulations . . . 115
9.2.1 Breakdown . . . 116
9.3 Layouts on the Wafer . . . 117
9.4 Measurements (ITE) . . . 118
9.4.1 Current . . . 118
9.4.2 Capacitance . . . 118
9.4.3 Resistance between Pad and Guard . . . 119
9.4.4 Conclusion on ITE Diodes . . . 120
9.5 Measurements (CNM) . . . 121
9.5.1 Breakdown . . . 122
9.5.2 Capacitance . . . 123
9.5.3 Resistance between Pad and Guard . . . 123
9.6 Conclusions . . . 125
10 SENSOR WITH INTEGRATED PITCH ADAPTER 126
10.1 Integration on first Metal Layer . . . 126
10.1.1 BPA: Coupling Capacitance . . . 126
10.1.2 BPA: Interstrip Capacitance . . . 127
10.1.3 BPA: Signals . . . 128
10.1.4 Simulation of BPA . . . 131
10.2 Integration on second Metal Layer . . . 134
10.2.1 DMPA: Interstrip capacitance . . . 134
10.2.2 DMPA: Signal Measurements . . . 135
10.2.3 Simulations . . . 136
10.2.4 Summary . . . 137

IV IRRADIATED SILICON SENSORS 141
11 TWO-DEFECT MODEL 142
11.1 Measurement Data . . . 142
11.1.1 Current . . . 142
11.1.2 Full Depletion Voltage . . . 143
11.2 Model Building . . . 144
11.2.1 Parametrisation of the Leakage Current . . . 145
11.2.2 Donor Removal . . . 147
11.2.3 Full Depletion Voltage . . . 147
11.2.4 Neutron Model . . . 149
11.2.5 Proton Model . . . 149
11.3 The Double Peak Transient Current Pulses . . . 151
11.4 Transient Current Pulses . . . 154
11.4.1 Measurement and Simulation Results . . . 154
11.4.2 Influence of Saturation Velocity . . . 157
11.4.3 Influence of Mobility . . . 158
11.5 Electric Fields . . . 160
11.5.1 FZ320N . . . 160

11.5.2 P-Bulk Diodes 160
11.6 Trapping 165
11.6.1 Experimental Results 165
11.6.2 Simulated Trapping Time 166
11.6.3 Discussion on Trapping Times 167
11.7 Charge Collection Efficiency 171
11.8 Temperature Dependence of the Proton Model 172
11.9 Annealing Time 172
11.10Summary and Discussion 174
12 IRRADIATED STRIP SENSORS 177
12.1 Electric Fields at the Strips 177
12.1.1 N-Bulk Sensors 177
12.1.2 P-Bulk Sensors 180
12.2 Signal Simulation in irradiated Strip Sensors 183
12.2.1 Transient Signals 183
12.2.2 Charge Collection Efficiency 184
12.3 Charge Multiplication in Silicon Strip Sensors 188
12.3.1 Dependence on Oxide Charge 188
12.3.2 Dependence on Strip Geometry 189
12.4 Conclusion 193

V SUMMARY 195
13 SUMMARY 196

VI APPENDIX 199
A SIMULATION FILES 200
A.1 The Device File 200
A.2 The Simulation Command File 201
A.2.1 Mobility Models 201
A.2.2 Recombination Models 202
A.2.3 Electrode 202
A.2.4 File 203
A.2.5 Physics 203
A.2.6 Device in a Small Signal Analysis 203
A.2.7 System 204
A.2.8 Plot 204
A.2.9 Math 204
A.2.10 Solve 205
A.2.11 Optics 206
A.2.12 Heavy Ion 207
A.2.13 Transient 208
B MEASUREMENT SPECIFICATIONS 209
B.1 Probe Station 209
B.2 TCT and CCE Measurements 210
C MEASUREMENT DEVICES 211
C.1 Probestation 211
C.2 ALiBaVa 211
C.3 Picolaser Setup 211
D THE IEKP DATABASE 212
D.1 Structure 212
D.2 Tables in Detail 212
D.2.1 info 212
D.2.2 alibava 215

D.2.3 Probestation 216
E ROOT FRAMEWORK FOR DATABASES 218

BIBLIOGRAPHY 221
List of Figures 231
List of Tables 235

Part I

INTRODUCTION AND BASICS

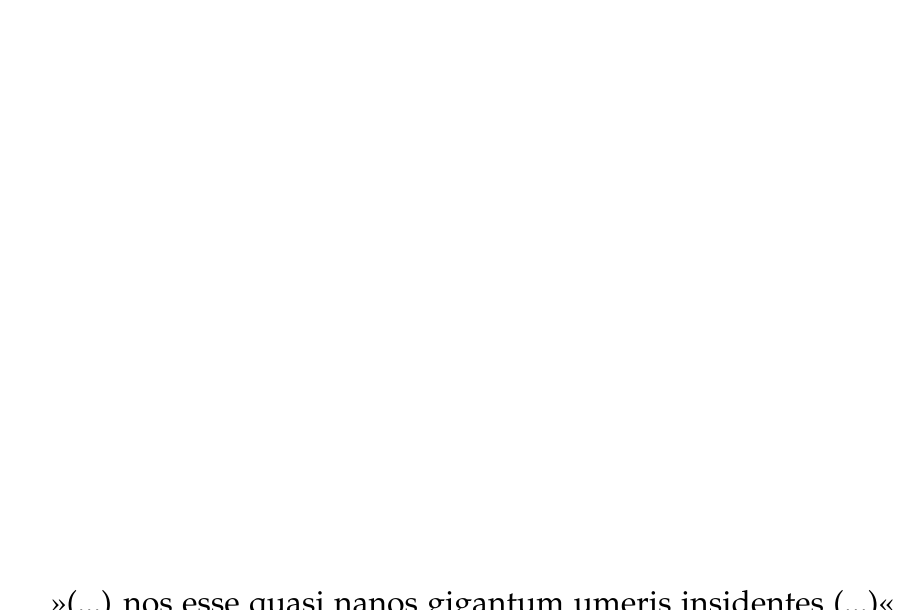

»(...) nos esse quasi nanos gigantum umeris insidentes (...)«

Bernhard von Chartres

1 INTRODUCTION AND MOTIVATION

The discovery of the Higgs Boson in 2012 at the two large experiments at CERN, ATLAS and CMS, completes the set of particles in the Standard Model of Particle Physics. The Higgs Mechanism, which gives masses to the particles, was postulated in the 1960's by Peter Higgs, François Englert and Robert Brout. The Nobel Prize in Physics was awarded to François Englert and Peter Higgs in 2013.

The success of the discovery of the Higgs Boson is based on the accelerator complex of the LHC and the particle detectors recording the information of the Higgs decay products. During their operation, the particle detectors suffer from radiation damage, which results from a huge number of crossing particles in the detector.

The CMS Experiment uses an all-silicon tracker with an area of $200\,\mathrm{m}^2$ for the track finding of charged particles. Next to the very inner silicon pixel detector, the silicon strip tracker covers a radius from 40 cm to 120 cm. At the end of its nominal lifetime, the detector suffers from a decreased performance and resolution due to the radiation damage.

After 2022, the LHC will be upgraded to the high luminosity LHC, which will result in a five-fold increase in luminosity. The increase in luminosity comes with the drawback of increased radiation damage in the particle detectors, which have to withstand the harsh radiation environment. A new tracker will be constructed for CMS for the high luminosity phase. Still, silicon is the most promising material for the CMS Tracker and a large campaign has been conducted to find the best silicon material for the CMS Phase II Tracker Upgrade. Many wafers with several different structures, among them a small version of the strip sensors, diodes and new structures, have been fabricated in several thicknesses and two different bulk dopings.

Key points in understanding the performance of silicon sensors, diodes and new structures are

- the performance of un-irradiated diodes and sensors,
- the investigation of thin materials,
- the functionality and performance of new structures,
- the improvement of existing structures,
- the influence of radiation damage on diodes and sensors.

To solve these points, not only measurements but also simulations have been used extensively. For advanced measurements of diodes, a new setup – the IEKP picolaser setup – has been developed and built. This enables the measurement of time-resolved pulses generated by a laser. For the simulations, a commercial T-CAD package has been used and adapted for the simulation of silicon sensors.

Diodes and sensors have been measured as produced by the manufacturer with the probestation at the IEKP to gain information about the quality of the un-irradiated structures. Accompanying simulations can reflect the measured performance. The basic structures of diodes and sensors are used later on for the simulation of radiation damage.

A new structure analyzed in this work has been designed to reduce the material budget in the tracker. It provides the pitch adapter for the connection to the readout electronic directly on the sensor. The sensor with integrated pitch adapter has been studied extensively in the strip

measurement setup. The signal coupling to the routing lines, which results in a signal loss in the pitch adapter region, is reduced in a version with a second metal layer. The simulation helps to understand these features.

A diode fabricated on p-bulk with a p-stop isolation has been designed and fabricated according to simulations to cure a feature in the CV measurement.

Of course, the radiation hardness of these materials is of particular importance for the future CMS Tracker.
Thus, sensors and diodes have been irradiated to particle fluences, which are expected at the end of the high luminosity phase of the LHC. To account for the mixture of different particles in the experiment, the structures have been irradiated with neutrons, protons and a mixture of both particles. Corresponding to different radii in the CMS Tracker, different fluences have been chosen in the range of $10^{14}\ n_{eq}cm^{-2}$ up to $15 \times 10^{14}\ n_{eq}cm^{-2}$.

The data obtained from diodes after irradiation by measurements in the IEKP probestation and the new-built picolaser setup is used to establish a simulation model for the radiation damage in silicon sensors. The goal of the radiation damage model is to reflect the measurements and predict the sensor performance in the expected fluence range of the HL-LHC or even beyond the fluences, to which the diodes and sensors are irradiated.

The radiation damage model is based on an effective two-trap model, which describes the defects in silicon as a donor and an acceptor with energy levels in the silicon bandgap. The model is well-tuned to reflect the measurements available for diodes, including not only current-voltage and capacitance-voltage characteristics but also charge collection measurements as well as measurements of transient signals.

The obtained radiation damage model is used to extract electric fields in the silicon bulk as well as trapping times, which are both very important regarding charge collection efficiency in irradiated silicon sensors.

Furthermore, the radiation damage model is used in combination with surface damage, additionally appearing in AC-coupled sensors, for the comparison of the performance of irradiated silicon strip sensors in the measurement and the simulation. Again, electric fields in the bulk but also at the surface have been extracted for the sensors, showing a superior configuration in p-bulk sensors.

The charge multiplication effect, occuring in very highly irradiated silicon strip sensors, can be predicted with the radiation damage model to some extent.

This thesis starts in chapter 2 with an introduction of the CMS Experiment at the LHC. The basics of silicon used as a particle detector are explained (chapter 3), followed by the description of radiation damage and its impact on silicon detectors in chapter 4.

The experimental techniques are introduced in chapter 5. The new-built picolaser setup is described in chapter 6, where also measurement stations and irradiation facilities are described, which have been used in this work. The simulation package and its parameters are introduced and discussed extensively in chapter 7.

The analysis of the un-irradiated diodes and sensors is presented in chapter 8. The sensor with integrated pitch adapter is analyzed and simulated in chapter 10 and the re-design of an advanced p-bulk diode in chapter 9.

The effective two-defect radiation model, its tuning and application are presented in chapter 11. Extracted electric fields and trapping times can be found in this chapter, too. The simulation of the performance of silicon strip sensors is shown in chapter 12. Here, electric fields, charge collection efficiency and charge multiplication are discussed.

2

The Large Hadron Collider and the CMS Experiment

The CMS Experiment [CMS], located at the world's largest collider experiment, the Large Hadron Collider (LHC), is a huge particle detector, aimed to detect new particles or even new physics. CMS is an acronym for Compact Muon Solenoid, which already describes the strong points of the detector. Its functionality and design layout will be characterized later on. The CMS Experiment, detecting the remaining particles coming from mainly proton-proton, but also lead-proton or lead-lead collisions in the center of the detector, has been incredibly successful so far. During the last few years the Standard Model of Particle Physics has been completely rediscovered. But the setup of such a large experiment would not have been worth such a huge effort, wouldn't the analyses have shown a sign of a new particle in 2011, which was proudly confirmed and announced in 2012 to be a "Higgs-like" particle, if not *the* Higgs boson [The13]. There is still much work to be done for the current analyses and a lot of data to be collected after the extended technical stop in 2013 and 2014, after which the LHC will be ramped up to its design energy of 14 TeV, allowing for even more statistics and a higher energy range to explore for the experiments located at the LHC.

Besides the CMS Experiment, ATLAS [ATL] is the other out of two big general purpose experiments at the LHC. With a slightly different design and a toroidal magnet in the outer part, ATLAS (A Toroidal Lhc ApparatuS) it is the largest particle detector ever constructed and aims also to detect and confirm the Higgs-Boson and search for new physics beyond the Standard Model.

Apart from the general purpose experiments, two smaller experiments take part in the particle research at the LHC: LHC-b [LHC] and ALICE [Ali]. The Large Hadron Collider beauty experiment is especially designed to measure the CP violation appearing mostly in forward decays. This is an essential quantity, partly responsible for the matter-antimatter asymmetry directly after the Big Bang. ALICE, A Large Ion Collider Experiment, on the other hand searches for a new phase of matter, the quark-gluon-plasma. Appearing at »extreme matter densities« in lead-lead collisions, its »existence (...) and its properties are key issues in QCD (Quantum Chromo Dynamics, editor's note) for the understanding of confinement (...)« [Ali].

2.1 The Large Hadron Collider

One important ingredient for the research is common to all experiments: the Large Hadron Collider, the world's largest particle accelerator. Originally designed to run at a center of mass energy of 14 TeV, it started running in 2010 with a center of mass energy of 7 TeV after an incident in 2009, that had to be reworked. In 2012, it was even running at $\sqrt{s} = 8\,\text{TeV}$; in 2013 and 2014 all connections will be remastered to reach its design energy in 2015.

Picture 2.1 shows a sketch of the LHC, located at the swiss-french border between the lake of Geneva and the Jura mountains.

At four points in the 27 km long circular tunnel the two proton beams running contrariwise collide and produce particle fragments detectable by the four mentioned LHC experiments. The general purpose detectors, CMS and ATLAS, are located at the main colliding spots. LHC-b and ALICE can handle and experience less luminosity at their points. Luminosity is an important quantity in accelerator physics, a measurement of brightness. Multiplied by the cross

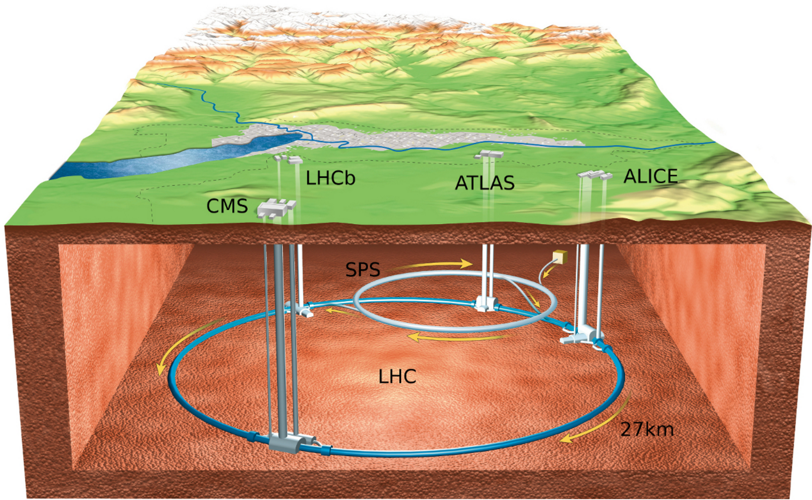

Figure 2.1: The LHC accelerator complex and the experiments located at CERN, the european center for nuclear research near Geneva [CER]. Picture by [Mou06].

section of a certain particle production mechanism, it is the rate of the particle's production. An introduction to important quantities like luminosity is given in [Y^+06].

Generating such large beam energies and intensities, the LHC needs a set of pre-accelerators. This staged accelerator complex currently consists of the LINAC[1], where the injection of hydrogen ions or other ionized atoms takes place, the PS Booster, the Proton Synchrotron (PS) and Super Proton Synchroton (SPS), in which the injection energy of the LHC, 450 GeV, is reached. Finally the LHC is fed with the accelerated protons clockwise and counterclockwise and ramped to its ultimate operating energy.

2.2 The CMS Detector in a Nutshell

A more detailed description is dedicated to the CMS detector and its tracker, which are of importance in this work. Picture 2.2 shows the CMS detector.

In the very center of the detector, collisions taking place in the beampipe running through the detector produce secondary particles at a rate of 20 MHz to 40 MHz. With the help of several sub-detectors, CMS is designed to resolve and record interesting events at such a high rate chosen by a trigger system. The whole detector, starting from the innermost subdetector except for the beam pipe, consists of a tracker, divided into pixel and strip detector; followed by an electromagnetic and hadronic calorimeter, which are within the superconducting solenoid magnet. Outside the magnet, several alternating layers of myon chambers and the iron return yoke follow. Alltogether this makes up for the name of the composite detector; being a very compact object, it can resolve the tracks and energy of myons very well with the help of a large solenoid magnetic field: the Compact Myon Solenoid detector. Detailed information can be found in [The08].

Starting from the outer parts, a description of the components is given:

MYON CHAMBERS: Three different techniques, namely drift tubes, cathode strip chambers and resistive plate chambers, detect myons, which are the only particles to cross the iron layers of the return yoke as well as the calorimeters. Still lying in a magnetic field, this provides a good lever arm for the reconstruction of myons.

SOLENOID MAGNET AND IRON RETURN YOKE: The solenoid magnet, surrounding the tracker and the calorimeters, provides a 3.8 T magnetic field in the inner part and an

1 Linear Accelerator

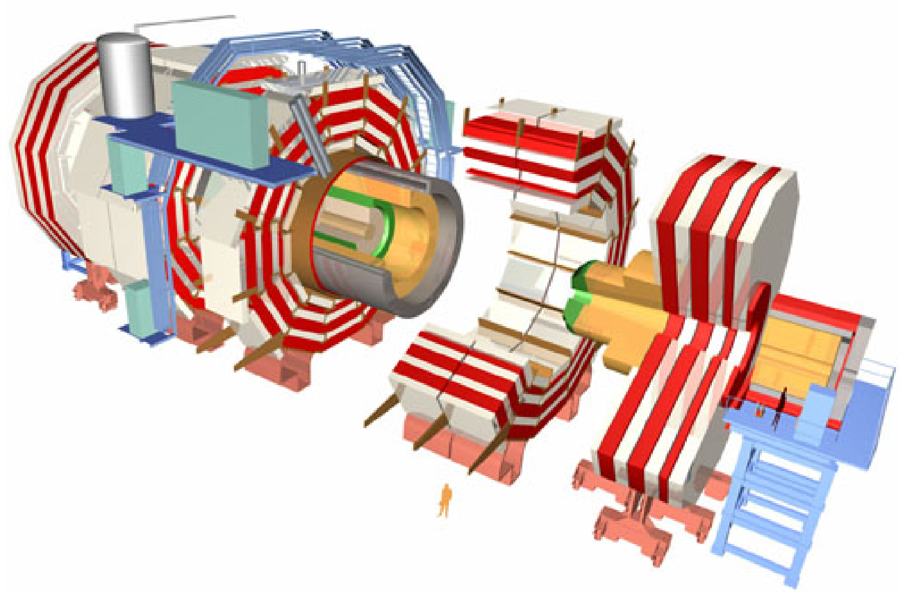

Figure 2.2: The CMS detector [CMS].
Consisting of 15 single sections, which can be pulled apart for maintenance, it weighs 12500 tons but is only 15 m wide and 21.6 m long.

almost 2 T strong magnetic field in the outer part, concentrated by the iron return yoke. The iron return yoke consists of several layers with openings for the myon chambers. To provide such a strong magnetic field, the magnet is superconducting and has to be cooled to only some Kelvin above absolute zero.

HADRONIC CALORIMENTER: The hadronic calorimeter is responsible for the energy measurement of hadrons, like protons or pions. Constructed as a sampling calorimeter, many alternating layers of brass and plastic scintillator lead to the energy loss of the hadrons measure their energy. Incoming hadrons are most likely absorbed in this calorimeter, no other particles than myons cross the subsequent magnet. Because the hadronic calorimeter is residing within the magnet, it is quite compact at the expense of energy resolution.

ELECTROMAGNETIC CALORIMETER: It is the task of the electromagnetic calorimeter, to measure the energy of only electromagnetic interacting particles, especially electrons, positrons and photons. Lead tungstate crytals serve as scintillator material. Crossing particles create electromagnetic showers and are likely to deposit their energy within the calorimeter. The resolution of the electromagnetic calorimeter is important for the decay of the higgs boson into two photons with high energy, which will be measured only by this calorimeter. The scintillating crystals allow for fast and precise energy measurement in the photo detectors, installed at each crystal.

TRACKER: Finding particles' tracks is tracker's most important task. Silicon sensors, divided into a pixel region near the interaction point and strip sensors following after the pixel sensors, provide track points. It is the world's largest silicon only tracker in a high energy physics experiment. Due to the bending of charged particles' tracks, the momentum of the particle can be reconstructed. Only charged particles generate a signal in the silicon sensors, which can be used for the reconstruction of tracks.

The innermost region, the pixel detector, has the highest resolution and can determine the tracks of secondary particles from short-lived particles. In total, 65 million pixels with a size of $100\,\mu m \times 150\,\mu m$ each in three layers and pixel end caps constitute the pixel region. In contrast to the strip sensor region, a recorded track point provides real 3d resolution.

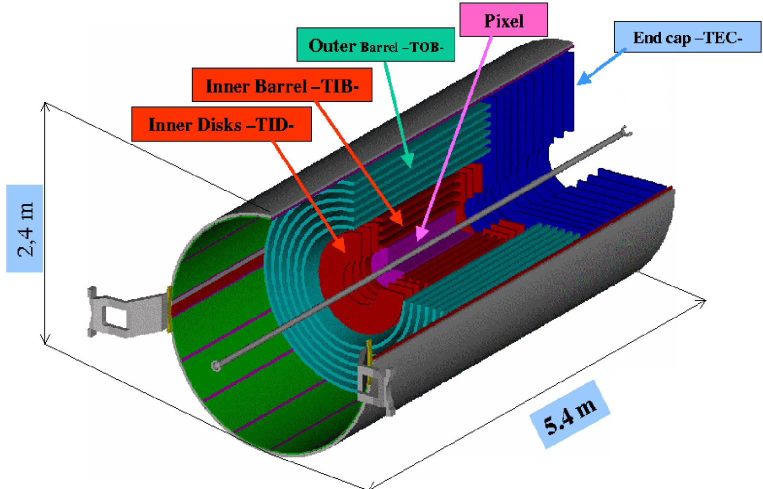

Figure 2.3: The CMS all-silicon tracker with its components: the pixel detector and several layers of silicon sensors with end caps [CMS].

Because of its proximity to the interaction point, the pixel detector has to be very radiation tolerant. Even in a distance of 8 cm from the interaction point, the particle rate is still $10^7\,\mathrm{cm}^{-2}\mathrm{s}^{-1}$. In order to maintain a good performance of the pixel detector, it will be replaced during the extended technical stop in 2016.

Further out, silicon strip sensors take over, up to a distance of 120 cm from the interaction point. Divided into tracker inner barrel (TIB), tracker outer barrel (TOB), tracker inner disc (TID) and tracker end cap (TEC), more than 15000 sensors are assembled. In total, 10 million channels are recorded by 80000 readout chips. Strip sensors can provide a quite good resolution perpendicular to their strips. By slightly rotating the strips in different layers, a reasonable 3d resolution is achieved. The IEKP took part in testing and qualifying sensors and assembling so called petals, consisting of several sensors, cooling pipes and a support frame, for one half of the tracker end caps. The strip sensors, due to their position further out in the tracker, are not so heavily damaged by crossing particles. After the nominal lifetime of the CMS detector (at $500\,\mathrm{fb}^{-1}$), a maximum fluence of $1.6 \times 10^{14}\,n_{eq}\mathrm{cm}^{-2}$ for the inner strip sensors is reached, dropping towards the outer strip sensors to a fluence of $0.5 \times 10^{14}\,n_{eq}\mathrm{cm}^{-2}$ [Gut].

The complete silicon tracker is cooled to prevent the annealing of radiation damage in silicon sensors or to prevent overheating of the readout chips. Irradiated silicon sensors have to be cooled, to prevent them from annealing and thermal runaway, as irradiated sensors have a higher leakage current and produce more thermal power. Originally, it was foreseen to operate the strip detector at $T = -10\,°\mathrm{C}$ and even lower for the pixel region [CMS98].

The silicon tracker with its components, having a length of 5.4 m and a diameter of 2.4 m, can be seen in figure 2.3.

The particle identification in CMS, for which each of the described components of the CMS detector is required, can be seen in figure 2.4. Charged particles, in contrast to neutral particles, generate signals in the tracker. Electrons, positrons and photons deposit their energy in the electromagnetic calorimeter, whereas hadrons penetrate to the hadronic calorimeter and are absorbed there. Myon chambers track the only particles, which are left after crossing the magnet coil and parts of the iron return yoke.

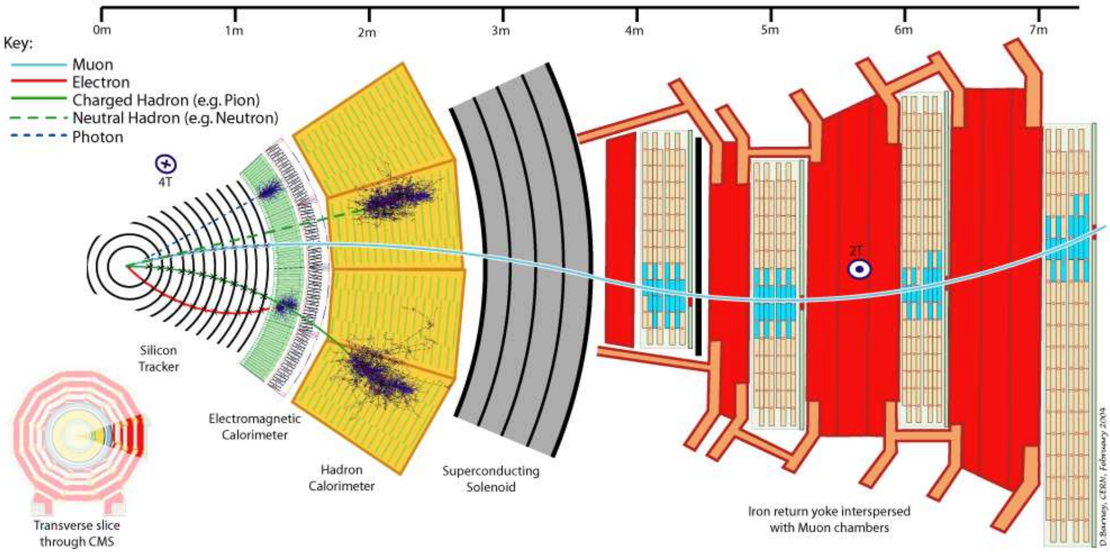

Figure 2.4: Cross section of the CMS detector. All sub-detectors, tracker, calorimeters and myon chambers in the magnetic field, contribute to the particle identification. Picture from [CMS].

2.3 Upgrade

The LHC and the attributed experiments are foreseen to run until the year 2022. After this nominal lifetime of the LHC and the experiments, new upgrade plans have already evolved, while the experiments have been taking data. With some modifications of the LHC and its accelerator complex, it can achieve even higher luminosities, its upgrade is therefore called High Luminosity Large Hadron Collider, HL-LHC. CMS is also preparing to upgrade several components. Because the pixel detector is already replaced during the LHC runtime, the preparations for the HL-LHC are called phase-II upgrade. In this phase, the tracker and the pixel detector are going to be replaced with new radiation hard sensors along with a new cooling concept and an additional track trigger.

A brief outline of the upgrade of the LHC and the CMS detector is depicted with emphasis on the CMS tracker.

2.3.1 Upgrade of the Large Hadron Collider

The high luminosity LHC shall raise the instantaneous luminosity of the LHC by at least a factor of five: from the design luminosity $L = 10^{34}\,\mathrm{cm}^{-2}\mathrm{s}^{-1}$ to $10^{35}\,\mathrm{cm}^{-2}\mathrm{s}^{-1}$. This can significantly increase the statistics for rare events at high energies. It will also enable exact measurements of the properties of the “higgs-like” boson [The12]. The physics motivation together with an upgrade scenario is outlined by Tricomi [Tri08]. The up-to-date plans for the upgrade are also briefly described on the website of the LHC [SLH].

2.3.2 Upgrade of CMS

The CMS detector has to be upgraded for the HL-LHC, the CMS tracker including pixel and strips has to be replaced. The sensors in this parts are damaged by the radiation and not performant and efficient enough any more. The CMS Tracker Upgrade is outlined in more detail by Hall [Hal08]. The replacement of the calorimeters is also under discussion.

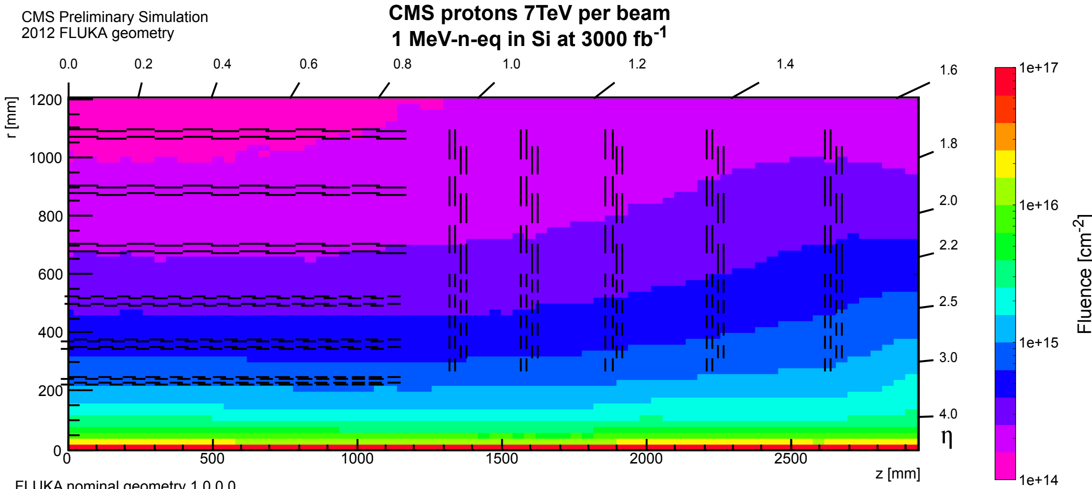

Figure 2.5: Total equivalent fluence at the CMS tracker at an integrated luminosity of 3000 fb^{-1}.
The graph shows the new CMS Tracker layout with 2S-modules and PS-modules on the fluence map simulated with the current CMS Tracker layout. [CMS13]

An increase of the instantaneous luminosity has a large impact on the requirements of the future silicon sensors and the overall performance of the tracker. Four important points are to be considered:

- An increase in fluence requires very radiation hard sensors.
- Thinner sensors reduce the material budget in the tracker and hence the radiation length.
- Due to the increased number of particles, a higher granularity reduces the occupancy for a better track finding.
- A trigger implemented in the tracker can help to identifiy events with high transverse momentum.

The pixel detector and the inner parts of the strip tracker have to cope with a significant increase in fluence. This is shown in figure 2.5.

For the strip tracker, this means that at a distance of 50 cm to the interaction point a total equivalent fluence of $F \approx 7 \times 10^{14}\, n_{eq} cm^{-2}$ is reached. In the outer parts of the strip tracker, even higher fluences than the maximal fluences for the strips at the LHC are reached. The search for radiation hard silicon material and the sensor layout studies have found themselves subject to studies in a dedicated campaign to find the future silicon sensors for the upgrade of the CMS tracker. Details on this campaign are summarized in chapter 2.4.

Together with the search for new material, also thinner materials are investigated. They do not only have the advantage of less material in the tracker and therefore a small radiation length, but also less trapping of the signal generated by traversing particles. Studies on the radiation hardness for the outer layers of the future tracker can already be found in the work of Hoffmann [Hof13] and Frech [Fre12].

Reducing the granularity can be achieved by smaller sensors or a new sensor layout with segmented strips. To keep the production as simple as possible, the sensors should be read out at the sensor edge. New ideas are being developed, like the FOSTER, a four-fold segmented sensor with edge readout [Str12] [Hof13]. The difference between the status quo and the estimated number of particles and tracks in the tracker is visualized in picture 2.6.

The readout of the new sensors has to be adapted, too, to the increased number of tracks. The huge increase in the number of tracks and channels leads a large number of data channels to be read out in the tracker. The data links and the computing for the offline trigger decision

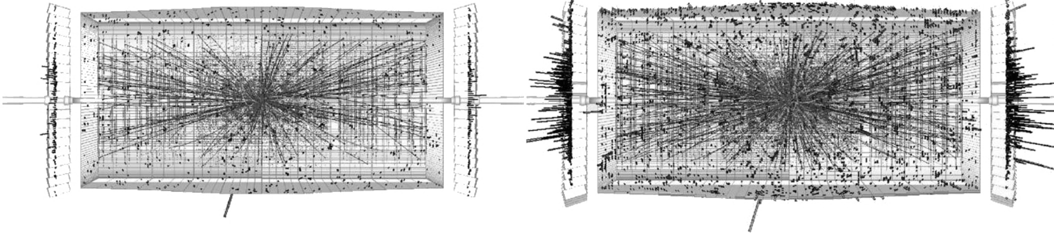

Figure 2.6: Comparison of the simulated number of tracks at the LHC and HL-LHC:
The number of tracks in the current tracker for one event is significantly lower than for an event at the HL-LHC at a ten-fold increase of the luminosity. Figure taken from [Die09].

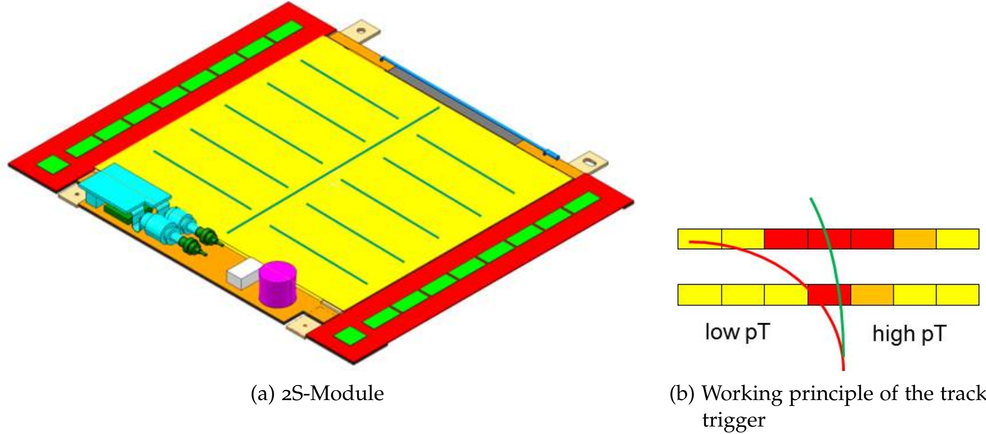

(a) 2S-Module

(b) Working principle of the track trigger

Figure 2.7: 2S-Module and the working principle of the track trigger: Two closely spaced sensor provide information about the stiffness of a charged particle's track. If the hit strips are within in a certain search window, the track is read out, otherwise it is rejected. Pictures taken from [H^+09] and modified.

cannot handle such a large amount of data. To cope with this huge increase of data, a track trigger is being developed on the basis of the "2S-Module" or the "PS-Module". A first version of this module is described by Hall [H^+09]. This module embodies the idea, that two closely spaced sensor provide an information about the stiffness of a track in the magnetic field. If the particle's momentum is high enough, it hits a strip on one sensor nearby a strip on the other sensor. Given a low momentum of the particle, the strip hit on one sensor is not any more in the search window for a stiff track on the other sensor. The data is rejected in the latter case but read out and stored in the former case. A 2S-Module and the working principle are sketched in figure 2.7.

The choice on the future sensor material are to be taken at the time, this thesis is written. The layout of the future tracker and the implementation of the track trigger are to be investigated with prototype sensors.

The campaign, to identify the future silicon material for the CMS Tracker Upgrade Phase II is described in the next section.

2.4 The HPK-Campaign

The campaign to identify the future technology baseline for the CMS Tracker Upgrade Phase II is described in detail by Hoffmann [Hof11]. As this work bases on structures, which have been placed on the designed wafers of this project, a brief overview is given here.

2.4.1 Materials and structures

There are three different silicon base materials, out of which the wafers are made:

- Float zone (FZ),
- Magnetic Czochralski (MCz) and
- Epitaxially grown silicon (Epi).

The fabrication process of these materials is outlined in section 3.3.7. They come in both n-bulk and p-bulk material. The bulk resistivities are in the order of $k\Omega cm$. For the FZ n-bulk wafers, the resistivity is $1.2 - 2.4\,k\Omega cm$, for the FZ p-bulk wafers $3 - 8\,k\Omega cm$. MCz wafers (n-bulk) have $> 0.5\,k\Omega cm$ and (p-bulk) $> 2\,k\Omega cm$. Expitaxial wafers are in the range of $0.5 - 2\,k\Omega cm$.

Different thicknesses are explored to investigate the performance of the devices after irradiation. 320 µm thick wafers are available to compare with the performance of sensors in the current CMS Tracker. FZ wafers with less active thickness (200 µm, 120 µm), but still physically 320 µm thick as well as 200 µm physically thin wafers for FZ and MCz have been chosen. Epitaxial wafers only come with an active thickness of 100 µm and 50 µm, some n-bulk wafers with a thickness of 75 µm. The epitaxial wafers are about 300 µm thick.

Processed by Hamamatsu Photonics K.K. (HPK), the wafers contain many structures for the investigation of different geometries and material features. The structures used in this work are explained here, a picture of them can be found in figure 2.8.

- Diode: in total, 16 diodes have been placed on the wafer; twelve large diodes (Diode or DiodeL) and four small diodes (DiodeS). Designed to study IV, CV and TCT they provide insight into the basic features of the material.
- Baby Standard Sensor (Bstd): a strip sensor with AC-coupled readout strips. This small sensor is similar to sensors used in the current CMS Tracker, the geometry has been modified. It's purpose is to study the signal behaviour with irradiation and annealing.
- Baby Pitch Adapter Sensor (BPA): a strip sensor like the Bstd, but with a pitch adapter included on the sensor. The routing scheme is analyzed.
- Test Structures (TS): designed to monitor the quality of the wafer processing. The Metal On Semiconductor (MOS) device provides information about oxide charges in the silicon dioxide layer after irradiation.

2.4.2 Naming

The naming of the structures has been chosen to be unique for each structure on each wafer. It includes the wafer material, the active thickness, the type of bulk doping, the wafer number, the structure's name and the structure's number on the wafer, separated by an underscore character.
MaterialThicknessBulkdoping_WaferNumber_Structure_StructureNumber
To name a few examples: FZ320N_07_DiodeL_1, MCz200P_10_BPA_1, Epi100Y_01_DiodeS_02.

The letter standing directly after the active thickness refers to the bulk doping. P and Y denote the different isolation methods implemented on the p-bulk wafer. Where P refers to

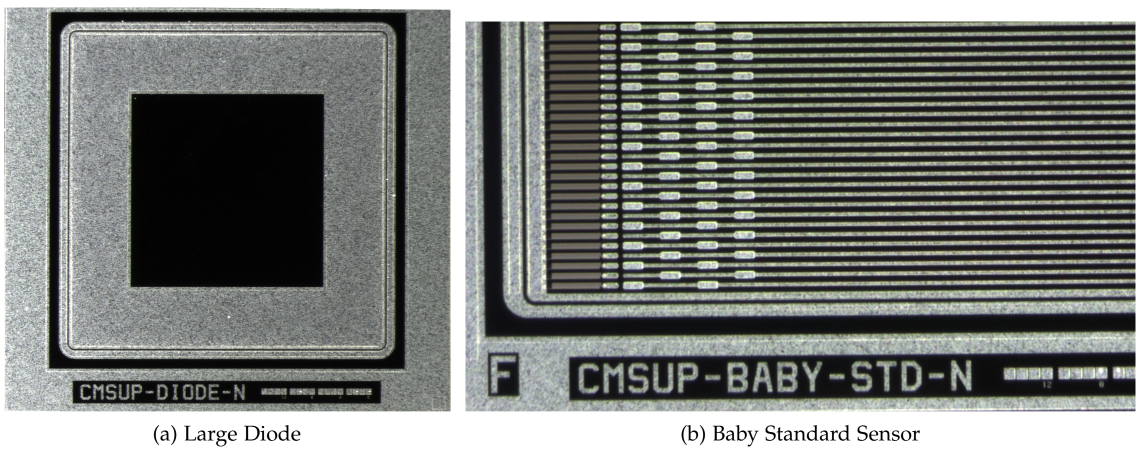

(a) Large Diode (b) Baby Standard Sensor

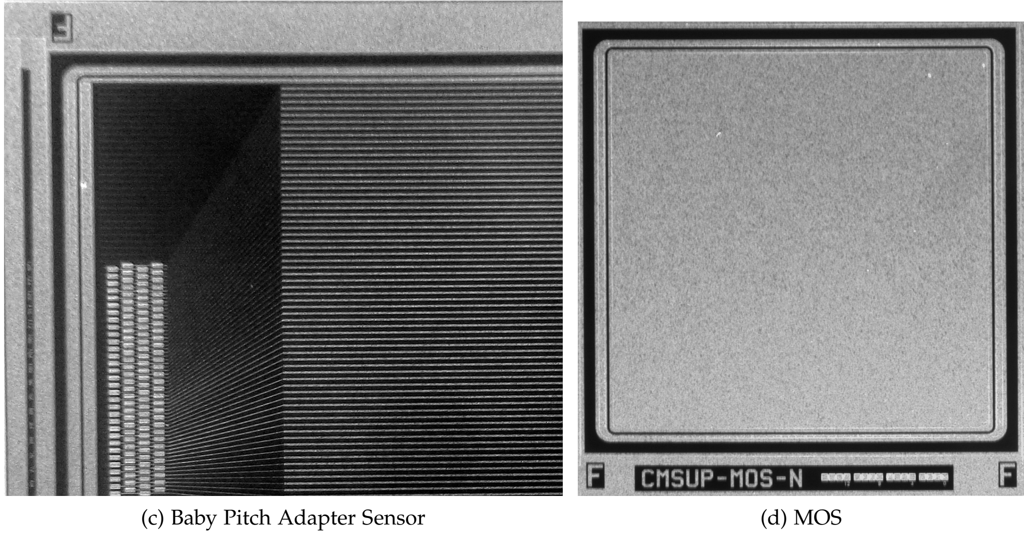

(c) Baby Pitch Adapter Sensor (d) MOS

Figure 2.8: Important structures on the HPK wafer:
(a) large diode with an opening window for the laser and one guard ring; (b) baby standard sensor with guard ring, bias ring, DC pads and two rows of staggered AC pads; (c) baby pitch adapter sensor, view on the fan-in region; (d) metal on semiconductor device.

the p-stop isolation method, Y stands for the use of a p-spray layer. The different methods are explained in section 3.2.1.

Real thin float zone material is named FTH (Float zone THinned) to distinguish it from its partner with only reduced active thickness.

2.4.3 IMPURITY CONTENTS

Impurity contents, expecially oxygen and carbon, can influence the radiation hardness of the material. Hence, the oxygen and carbon concentration in the fabricated wafers has been analyzed with secondary ion spectroscopy (SIMS, [ITM]) by ITE [ITE].

Magnetic Czochralski, as expected, shows a quite high concentration of oxygen. In contrast to the expected low concentration of oxygen in float zone material, it was found to be quite high, especially in wafers with less active thickness. This is found to be in relation with the thinning process. In FZ320 material, the concentration is $10^{16}\,\mathrm{cm}^{-3}$ or below, whereas FZ200 and FZ120 material show a significant increase in the oxygen concentration, which is comparable with the concentration of the magnetic Czochralski material. FTH material, which has been fabricated

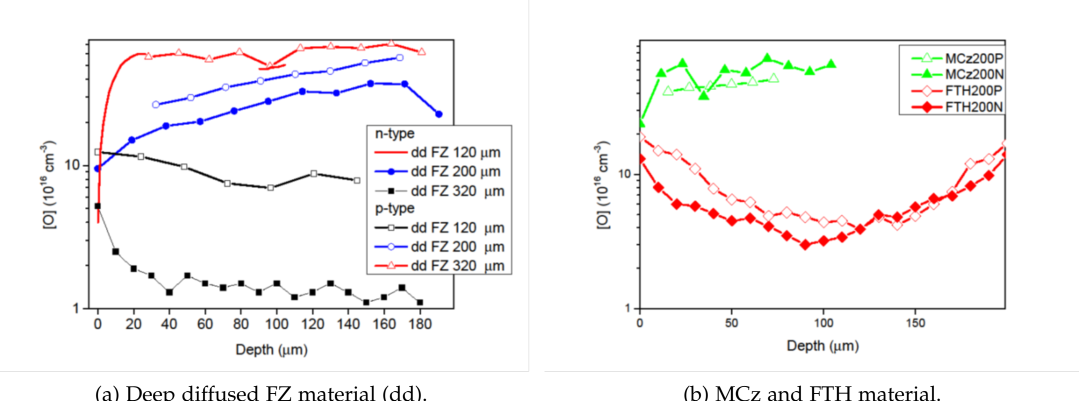

(a) Deep diffused FZ material (dd).

(b) MCz and FTH material.

Figure 2.9: Oxygen concentration in HPK material, measured with SIMS [ITM]. Figure from [Ste13].

differently from the FZ material, shows a lower concentration of oxygen. Figure 2.9 shows the measured oxygen concentration in the different materials of the HPK-campaign.

With regard to radiation hardness, FZ material may behave not so much different from MCz material due to the same amount of oxygen in the bulk.

2.4.4 IRRADIATION AND QUALIFICATION PROCEDURE

Before irradiating the diodes and sensors, all structures undergo an initial qualification procedure.

For diodes, this includes IV and CV measurements on all of them, on some diodes TCT and CCE measurements are performed as reference measurements. For sensors, in addition to IV and CV, strip measurements (see section 5.1.3 for details) are performed.

After the initial qualification, the structures are irradiated with either protons or neutrons. The irradiation facilities used are explained in section 6.1. Being shortly annealed for ten minutes at 60 °C to account for transportation, they are again qualified. This means IV and CV for diodes and sensors, TCT/CCE for diodes, strip ramps and signal measurements for sensors.

Because the sensors in the CMS Tracker experience a mixture of charged and neutral hadrons, they are irradiated with the missing particle type, neutrons or protons. Again, a short annealing for ten minutes at 60 °C followed by the qualification procedure takes place. Subsequently, diodes and sensors are characterized in an annealing study, including IV, CV and signal measurements.

The full measurement specification, as decided by the participating institutes, is found in the appendix B.

3

Silicon Particle Detectors

Silicon detectors are largely deployed in today's particle detectors like CMS. Designed as position sensitive detectors, they deliver information about charged particle's tracks and momenta after the reconstruction of the tracks. The use of silicon sensors was enabled by the semiconductor industry, which uses the same techniques for the fabrication of electronics.

As a basic feature, silicon sensors offer operation in a wide temperature range from cryogenic temperatures up to room temperature. Being a semiconductor however, a change in the temperature will affect the leakage current and therefore the noise in the sensors. Usually, the sensors are cooled to keep a low leakage current and in the case of irradiated sensors to avoid high noise and thermal runaway.

Sencondly, the signals generated by ionizing particles are quite fast (ca. 10 ns, depending on the thickness of the sensor) in thin silicon sensors. This enables the detectors to cope with a high bunch crossing rate of 40 MHz at the LHC.

As a great advantage, silicon sensors themselves are quite radiation tolerant. However, at the end of the lifetime of the current CMS Tracker, the sensors will be heavily irradiated. With different silicon bulk materials and engineering techniques it is possible to extend the application domain up to fluences reached at the high luminosity LHC.

This chapter describes the basic working principle of a silicon sensor as used in the CMS Tracker and the campaign to find radiation hard material for the application in the future CMS Tracker at the HL-LHC. Furthermore, for the investigation of this material, it is necessary to understand the fabrication of the material along with its properties pointed out in this chapter. Then a short summary of the features of the pn-junction is given, which are exploited for several measurement techniques described in chapter 5.

3.1 Working Principle

The functionality of a semiconductor used as a particle detector is based on the interaction of charged particles with matter. By crossing matter and interacting with shell electrons, charged particles loose part of their energy. The atoms of the crossed matter are mostly ionized hereby.

The mean energy loss in matter can be described by the Bethe-Bloch relation [Bet30][Blo33]: the energy loss per distance $-dE/dx$ can be calculated as

$$-\frac{dE}{dx} = \frac{4\pi}{m_e c^2}\frac{nz^2}{\beta^2}\left(\frac{e^2}{4\pi\epsilon_0}\right)^2\left[\ln\frac{2m_e c^2\beta^2}{I\cdot(1-\beta^2)} - \beta^2\right] \tag{3.1}$$

with $\beta = v/c$; c is the speed of light, v and $z \times e$ are the velocity and charge of the crossing particle; n is the electron density and I is the mean excitation potential of the atoms. The energy deposition within the material doesn't depend on the particle's mass but only on its energy [PRSZ06]. The typical value for the mean excitation potential is $I = 16\,eV \times Z^{0.9}$ with atomic numbers > 1, for silicon it is measured to be $I = 173.0\,eV$ [The].

A silicon sensor is basically a semiconductor with pn-junction, which is operated under reverse bias. Because the depletion zone created by the applied voltage can be extended throughout the whole sensor due to its high resistivity, the sensor is free of charge carriers in the depleted zone. When a charged particle traverses the sensor, electron-hole-pairs are created. Because of the applied electric field, the created electron-hole-pairs cannot recombine and drift

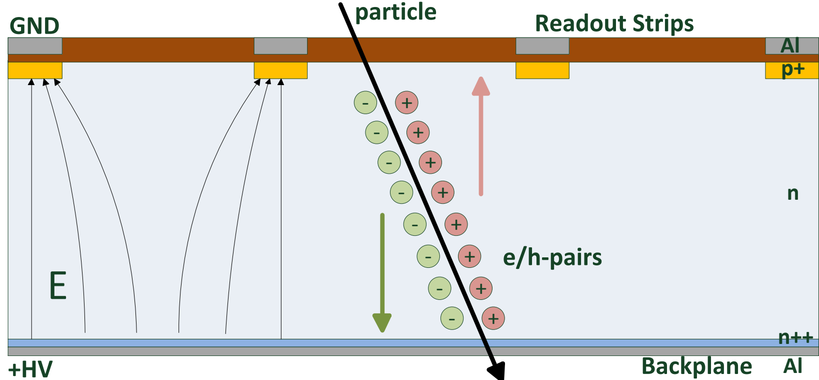

Figure 3.1: Working principle of a silicon detector: the pn-junction (here shown as strips) is biased reversely, the detector is depleted of free charge carriers. A traversing particle creates electron-hole-pairs, which are separated by the electric field and read out at the electrodes.

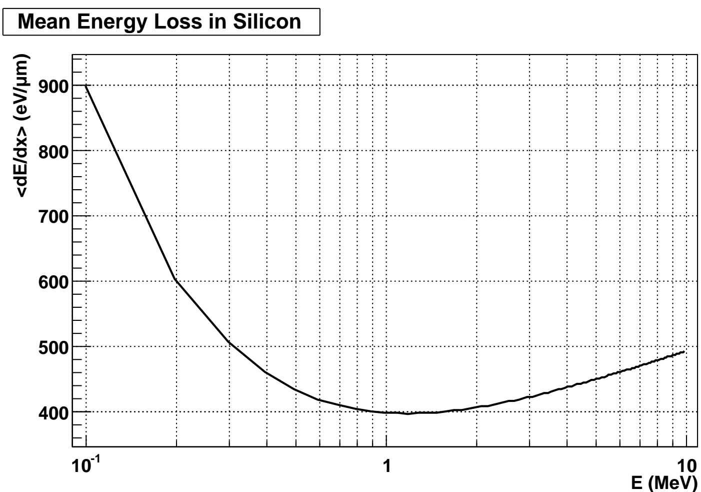

Figure 3.2: The mean energy loss of electrons in silicon. A particle at the minimum is called a minimum ionizing particle, MIP.

to the readout electrodes. Because there are almost no other charge carriers in the depleted zone, the drifting charges can be detected as a signal. The working principle of a silicon strip sensor, where there are structured pn-junctions, is illustrated in figure 3.1. The features of the pn-junction will be explained later in this chapter.

The created charge in the silicon sensor is proportional to the absorbed energy. Divided by the ionization energy, which is 3.6 eV for silicon, one gets the deposited charge. The energy loss in silicon is illustrated in figure 3.2. For low energy particles, the energy loss drops until a minimum at $p/m_0c \approx 4$. For electrons in silicon, this is at an energy about 1.5 MeV. As seen from figure 3.2, the minimal loss of energy is about 390 eV/µm, which results in 108 deposited electron-hole-pairs per micrometer.

However the deposited energy is a Landau distribution. The most probable signal is therefore 75 electron-hole-pairs per micrometer (see figure 3.3), resulting in a total collected charge of 22500 electrons or holes at each electrode for a 300 µm thick sensor [Har09].

Of all particles, the electron has the lowest energy loss in matter because of its low mass. Having an energy, which corresponds to the minimal energy loss according to equation 3.1, the particle is called minimum ionizing particle, MIP. If a silicon sensor can detect a signal from a MIP, it can possibly detect all larger signals from more strongly ionizing particles.

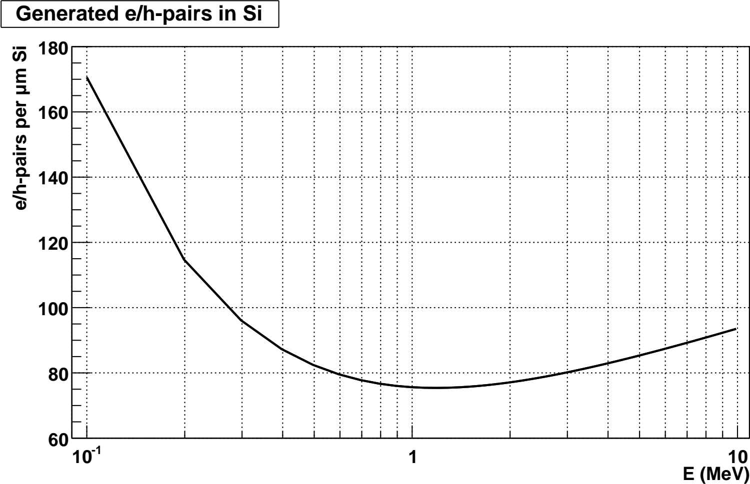

Figure 3.3: Generated electron-hole-pairs in silicon. Due to Landau fluctuations, the most probable created charge is lower than expected from the mean energy loss. A MIP creates about 75 electron-hole-pairs per micrometer.

A ^{90}Sr source is often used to generate MIP-like electrons from a β-decay. ^{90}Sr decays into ^{90}Y with a half life time of 28.78 years. This electron has quite a low energy and is absorbed by the enclosure of the source. Y^{90} then decays relatively fast ($t_{1/2} = 64\,h$) to ^{90}Zr, setting free an electron with an endpoint energy of 2.280 MeV and a mean energy of 933.6 keV [Bro97], which is very close to the mininum.

3.2 Layout of Silicon Sensors

Looking at the CMS Tracker, there are only two types of sensors, which are built in the detector: silicon pixel sensors and silicon strip sensors. For testing purposes, there are some more devices of interest in this work, whose structure is described here in detail. The devices are fabricated on one wafer, therefore the backside processing is the same for all devices and the processing differs only at the frontside. Usually, the backside doping is of the same type as the bulk doping and the pn-junction is formed at the contrary doped front implant. For silicon sensors, the doping concentration of the bulk is in the order of $N_{bulk} \approx 10^{12}\,cm^{-3}$, the highly doped regions at the backside and for the strips is in the order of $N \approx 10^{18}\,cm^{-3}$ to $10^{20}\,cm^{-3}$.

The devices discussed here are considered n-bulk devices with p-doped regions at the front side (n-type or p-in-n), however it is also possible to fabricate them with the pn-junction at the backside (n-type, n-in-n) or as p-bulk devices (p-type or n-in-p), where an additional isolation of the p-doped implants is necessary.

3.2.0.1 *Diode*

The diode is a very simple device one can think of in terms of a particle detector: a thin highly p-doped region with contact to an aluminum electrode at the front and a weakly n-doped bulk form a pn-junction, which can be extended throughout the whole bulk by applying reverse bias. At the backside, there is a highly n-doped region to limit the depletion region and to form a good contact to the aluminum layer. A cut through a diode is sketched in figure 3.4.

Being a simple device, it nevertheless provides all features needed to investigate the radiation hardness of the silicon base material.

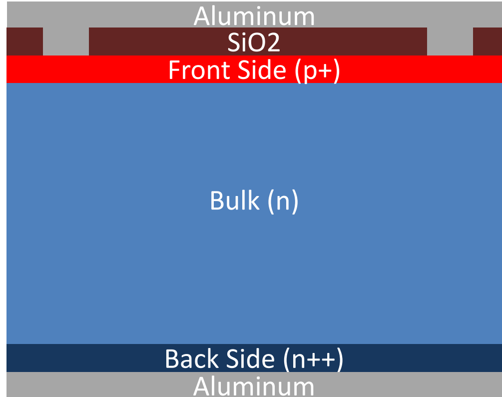

Figure 3.4: Cut through a diode. From top to bottom there is an aluminum layer, the highly doped p-region contacting the aluminum layer by a via through the silicon dioxide, the weakly doped n-bulk, the highly n-doped backside implant and another aluminum contact layer.

3.2.0.2 *MOS*

The metal-oxide-semiconductor (MOS) is used for the determination of the flatband voltage (see section 5.1.4). As the name of the device already indicates, it consists of an aluminum layer on the semiconductor bulk material, separated by an insulation oxide, here silicon dioxide. The back side is like the one for the diode. Figure 3.5 shows the cut through a MOS device.

3.2.0.3 *Silicon Strip Sensor*

The silicon strip sensor is the device, which is used in the CMS Tracker to detect particles and provide information about the position. Two space coordinates can be given by a single strip sensor: the position perpendicular to the strips can be measured very accurately since the strips usually have a pitch between 70 µm and 200 µm, the coordinate along the 1 cm up to 10 cm long strips is unknown.

The configuration of the strip sensor is far more complicated than a diode. The 3d schematic of a strip sensor is sketched in figure 3.6.

Each p^+-doped strip implant creates a pn-junction with the n-doped bulk. The strip implant can be contacted on the DC aluminum pad, which is directly connected to it for testing purposes. The aluminum strips running over the implants are separated from the latter by a silicon dioxide layer, which insulates the aluminum from the implant; the aluminum strip is AC coupled. The strips as a whole are surrounded by the bias ring, which consists of a p^+-implant and an aluminum strip running above, connected with each other by vias. The bias ring is connected to the DC pads and therefore to the strip implants by the bias resistor, a resistive polysilicon meander. To ensure high voltage operation, one (or more) additional guard rings surround the bias ring and level the potential to the high voltage area. For protection, the sensor surface is covered with a passivation layer consisting of silicon dioxide. At the borders of the sensor, a n^{++}-implant prevents high electric fields at the cut edges. The doping is the same as the doping on the backside of the sensor, which connects to the aluminum on the backside.

3.2.1 ISOLATION TECHNIQUES

Silicon sensors fabricated on a p-doped bulk suffer from a disadvantage compared to sensors made of n-bulk: because the silicon dioxide on the upper side of the detector is always charged slightly positive, electrons are attracted at the silicon-silicon dioxide surface and establish an

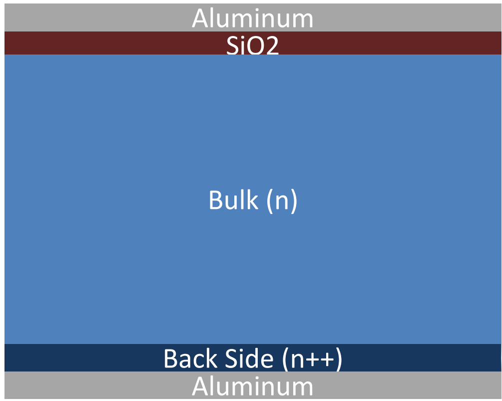

Figure 3.5: Cut throug a MOS device. There is an aluminum layer separated from the silicon bulk by insulating silicon dioxide. On the back side there is a highly doped region with the same dopants as the bulk material and an aluminum contact.

electron accumulation layer. The n-doped regions of a structured sensor are shorted hereby, the sensor's functionality is affected. To prevent the shortening of the n-doped regions in the p-type sensor, an additional isolation is required. There are in principal two different possibilities, which can also be combined.

The *p-spray* isolation is a homogeneous layer of highly p-doped silicon, which covers the just the surface of the whole structure up to a depth of 200 nm to 1.5 µm. Typical doping concentrations are in the range of $10^{15}\,\mathrm{cm}^{-3}$ to $10^{17}\,\mathrm{cm}^{-3}$. The doping concentration, which is higher than the bulk doping concentration, prevents the accumulation of free electrons.

In contrast to the former, the *p-stop* isolation is a structured isolation. A strip like implant with a higer doping concentration than the one of the p-spray with $10^{16}\,\mathrm{cm}^{-3}$ to $10^{18}\,\mathrm{cm}^{-3}$ and a depth of around 1 µm to 1.5 µm is placed between the n-doped structures. The implant cuts the electron accumulation layer and isolates the strips.

For the HPK sensors, two p-stops between two neighbouring strips are implemented, one p-stop surrounding each readout strip. This p-stop structure is called atoll, because each strip has its own isolating structure. Even the bias ring has its p-stop ring. This is illustrated in figure 3.7.

A single p-stop structure between the strips on the other hand is called p-stop common; the readout strips share one isolation structure.

3.3 Properties of Silicon used as Particle Detector

3.3.1 Silicon – a special semiconductor

Silicon is the most abundant element in the earth crust. It has the atomic number 14 and is element of the IV. main group in the periodic table. Due to its large abundance, mostly as silicon dioxide in sand, it is an inexhaustible source for semiconductor industries. No wonder it is the mostly and widely used semiconductor. This and many reasons already mentioned earlier make it perfect and affordable for large-scale experiments in high energy physics.

3.3.2 Silicon band structure

The interactions of the shell electrons of atoms in a solid body create bonds between the atoms, which keep the body together. After forming the bonds, the electrons cannot occupy each state

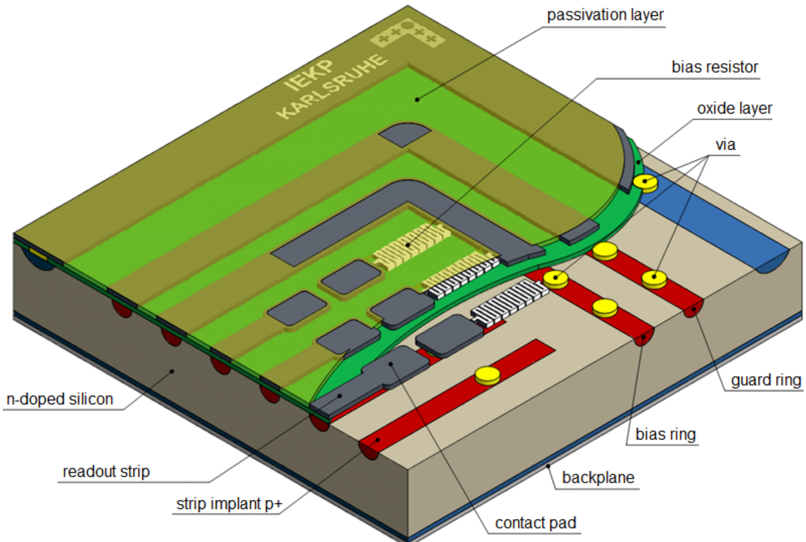

Figure 3.6: 3d schematic of a silicon strip sensor.
Each p-doped strip of the sensor forms its own pn-junction with n-doped bulk. The strips are DC coupled via the bias resistor to the bias ring, which is connected to ground in operation mode. The strips are AC coupled to the aluminum readout strips, insulated by a silicon dioxide layer. The bias ring is surrounded by the guard ring, which is usually left floating to shape the electric field to the border of the sensor. The bias ring and the guard ring are directly connected to the aluminum ring lying over them. The strips can be accessed on the AC pads (aluminum) or DC pads (p+ implant just beneath). The surface of the detector is usually covered with a passivation oxide. The very surrounding structure prevents high electric fields at the borders because it has the same doping as the n^{++} layer on the backside, which is fully covered with aluminum. The backside is set to reverse bias in operation mode. From [Har09].

in the crystal. They can be described as particles in a periodic potential. The allowed states for the electrons can be calculated by the Schrödinger equation

$$\left(-\frac{\hbar}{2m}\Delta + V(\vec{r})\right)\Psi(\vec{r}) = E\Psi(\vec{r}) \tag{3.2}$$

together with the periodicity of the potential (the lattice for solid crystals)

$$\Psi(\vec{r}) = \Psi(\vec{r}+\vec{a}). \tag{3.3}$$

The solutions are Bloch waves, which show a degeneration between the atoms in the crystal. The lattice constant for silicon is $a = 543102.032 \pm 0.033\,\text{fm}$ [WB90]. The description of the crystal lattice is usually given in the k-space, which is the reciprocal momentum space. The momentum of the electron in the crystal $\hbar\vec{k}$ is depending on the wave vector $\vec{k}$. The motion

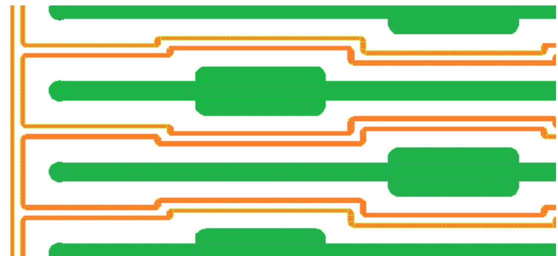

Figure 3.7: p-stop atoll isolation as it is implemented on the HPK sensors.
Each strip with staggered contact pads (shown in green) is surrounded by its own narrow p-stop shown in orange.

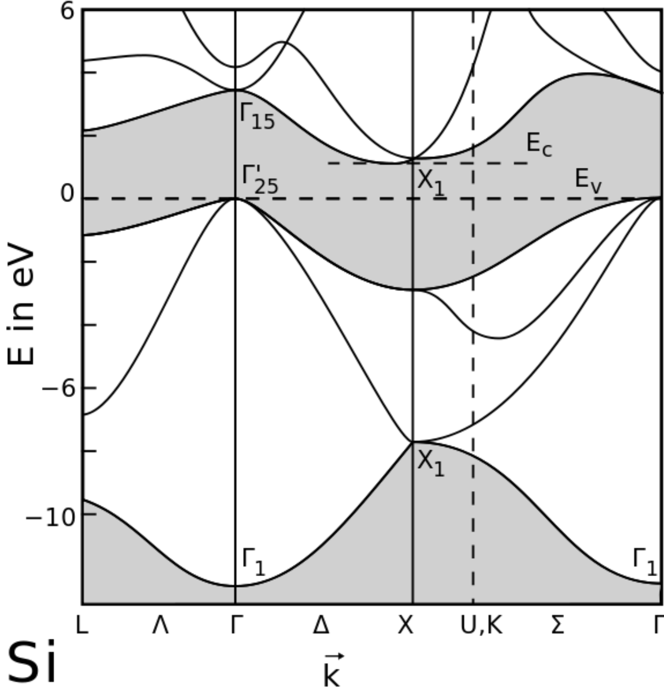

Figure 3.8: Reduced zone scheme of silicon. After [CC74].

of the electron is depending on this wave vector. The dispersion relation then expresses the electron's energy as a function of its momentum.

Transforming all neighbouring potentials into an elementary cell, which is sufficient to construct the whole periodic lattice, one gets the first Brillouin zone in the reciprocal momentum space, the analogue of the elementary cell in the position space, the Wigner-Seitz cell. The band structure can be illustrated very well in the reduced zone scheme in the k-space, as the Brillouin zone is a difficult 3d structure. Special symmetry points are pointed out in the reduced zone scheme shown in figure 3.8, e.g. the maximum of the valence band Γ, which is E=0 per definition, and the lowest point of the conduction band at X.

Between the maximum of the valence band and the minimum of the conduction band, a forbidden band gap is formed. Due to this band gap, silicon is characterized as a semiconductor. The distribution fo electrons at $T = 0\,K$ characterizes this property. The three cases are illustrated in figure 3.9.

`Metal`
The highest band available for the electrons is only partially filled with electrons. Electrons can move freely within this band, a metal is usually a good conductor.

`Isolator`
In an isolator, the fully occupied valence band is separated from the conduction band by a relatively large energy gap. Because the valence band and all lower bands are occupied, the electrons can't move and are hindered to pass to the conductance band because of the large bandgap.

`Semiconductor`
The band strucure in a semiconductor also shows a bandgap like the isolator. The valence band is fully occupied, the next higher band is empty. If the bandgap is not too large however, thermally excited electrons have a chance to ascend to the conductance band, when the temperature is high enough ($T > 0\,K$). In the conduction band, the electron can move and con-

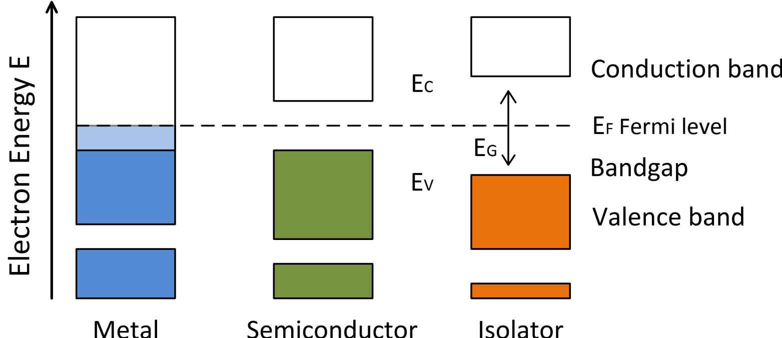

Figure 3.9: Classification of solids into metals (conductors), semiconductors and isolators. E_g is the bandgap, E_C and E_V are the edges of the conductance and the valence band respectively. States are occupied up to the fermi level E_F and shown with filled colours. Figure after [IL09] and modified.

tribute to a current; in the valence band, electrons can occupy the spot of the missing electron, so-called holes can move. The difference between insulators and semiconductors is not exactly defined. For most semiconductors the bandgap is less than 3 eV. The bandgap in silicon is $E_g = 1.1700$ eV for $T = 0$ K and $E_g = 1.1242$ eV for $T = 300$ K [Dan97].

But as seen from figure 3.8, the transition from the valence band to the conduction band with only an energy of 1.12 eV is not possible without changing the momentum $\vec{k}$. Hence an additional phonon is required to excite the electron from the valence band to conduction band. Silicon therefore is called an indirect semiconductor in contrast to a direct semiconductor, where there's no phonon required. Because phonons are considered lattice vibrations, the probability for the transition in an indirect semiconductor decreases with decreasing temperature.

3.3.3 FERMI LEVEL

The fermi level is the energy level, up to which all states are fully occupied at T=0 K. Above this energy, all states are empty. By increasing the temperature, some electrons can transit from the fully occupied valence band. The increase in entropy and temperature compensates for the higher energy of the electron states, staying in a minimum for the free energy [Wür09].

The electron distribution function, which satisfies the pauli principle and the demand for a mininum free energy, is the Fermi distribution

$$f(E) = \frac{1}{e^{[(E-E_F)/kT]} + 1} \tag{3.4}$$

with the fermi energy E_F. In silicon, the fermi level is lying in the middle between valence and conduction band. It can be shifted by doping.

3.3.4 SILICON CRYSTAL STRUCTURE

Silicon, being a member of the IV'th main group in the periodic table, has four valence electrons in the atomic shell. Thus four covalent bonds are formed, if silicon is arranged in periodic lattice. The neighbouring atoms share these four electrons to form energetically preferred states. The result is a tetrahedal structure, also called sp^3-hybridisation, with an angle between the bonds of the silicon atoms of 109.5°. The formed lattice is called diamond like. The structure in the face centered cubic (fcc) orientation can be seen in figure 3.10.

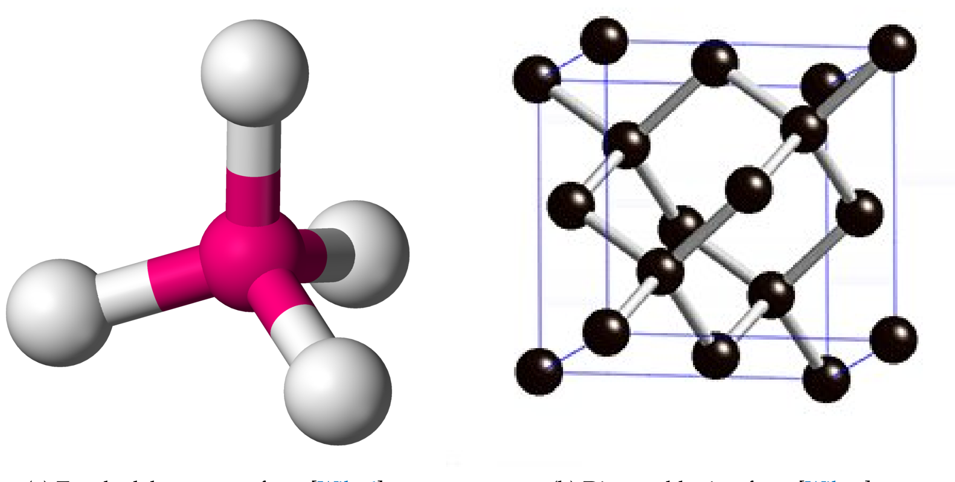

(a) Tetrahedal structure, from [Wik06].

(b) Diamond lattice, from [Wik05].

Figure 3.10: The tetrahedal structure of bond silicon atoms with four neighbours and the resulting diamond lattice in the face centered cubic orientation.

In the silicon lattice, displacements and disorders can appear, which lead to states influencing the properties of the silicon crystal. Also dopants can replace silicon atoms and lead to energy states in the silicon bandgap.

3.3.5 DOPING

The intentional introduction of impurities into silicon is called doping. The doped semiconductor is reffered to as extrinsic in contrast to an intrinsic semiconductor without doping. Doping changes the conductivity of the semiconductor. Silicon as a group IV semiconductor is usually doped with atoms from group III or V. Atoms from the III'rd group are missing one valence electron and provide an energy state in the silicon band gap just above the valence band. Used elements are boron or less often gallium or indium. The broken bond of these elements act as holes, which can accept electrons (Acceptor) and contribute to the current flow. The resulting semiconductor is called p-doped.

Phosphorus or arsenic from the V'th group provide an additional electron (Donor), which can contribute to the current flow. The energy level of these atoms in the silicon band gap is just below the conduction band. The semiconductor doped with these elements is called n-type.

3.3.6 PROPERTIES OF THE PN-JUNCTION

For silicon detectors, it is essential to detect the $\mathcal{O}(10^4)$ electrons induced by signal. To reduce the $\mathcal{O}(10^9)$ free charge carriers in an intrinsic silicon substrate, a reverse-biased pn-junction is used. Bringing together p-doped and n-doped silicon, an abrupt junction forms and a space charge region free of carriers is established.

This is shown in figure 3.11: before the contact is made, n-type and p-type silicon are electrically neutral. The fermi niveau for doped silicon is in between the conduction band and the donor level for n-type and between the valence band and the acceptor level for p-type silicon. In the p-doped section, an excess of holes is present while in the n-doped section, electrons are abound. In the moment of contact, electrons diffuse from the n-side to the p-side and holes

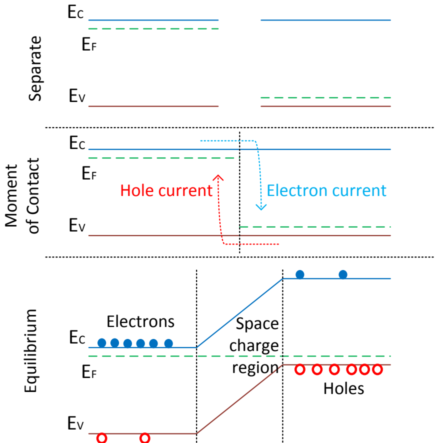

Figure 3.11: pn-junction at the moment of contact. Explanation is given in the text. Figure after [Har09].

vice versa. The pn-junction in the moment of contact is deduced from [Wür09]. From Fick's first law

$$J_{diff} = -eD \text{ grad } n \tag{3.5}$$

which does not depend on the concentration of the charge carriers n, one can derive a concentration dependent expression:

$$J_{diff} = -\frac{enD \text{ grad } n}{n} \tag{3.6}$$

Making use of

$$\text{grad } n/n = \text{ grad } \ln(n/N) \tag{3.7}$$

and introducing the chemical potential

$$\mu - \mu_0 = kT \ln \frac{n}{N} \tag{3.8}$$

where N is the effective density of states for the charge carrier, the diffusion current for electrons is

$$J_{diff,e} = \frac{enD}{kT} \text{ grad } \mu_e \tag{3.9}$$

and for holes

$$J_{diff,h} = \frac{enD}{kT} \text{ grad } \mu_h \tag{3.10}$$

The diffusion constant can be related to the mobility b of the charge carrier by the Einstein equation

$$\frac{b}{D} = \frac{e}{kT} \tag{3.11}$$

Because no external voltage is applied, the total current is still zero.

$$J = 0 \tag{3.12}$$

Because an electric field is building up due to the ionized dopants, there is also a field current

$$J_{field} = enbE = -enb \text{ grad } \phi \tag{3.13}$$

Combining the diffusion and the field current for electrons (e) or holes (h)

$$J_{e/h} = \pm n_{e/h} b_{e/h} \text{ grad } (\mu \mp e\phi) = \pm n_{e/h} b_{e/h} \text{ grad } \eta_{e/h} \tag{3.14}$$

so that for $J = 0$

$$J = n_e b_e \text{ grad } \eta_e - n_h b_h \text{ grad } \eta_h = 0 \tag{3.15}$$

The chemical environment does not change very much due to the small fraction of dopants in the n-type or p-type silicon. That means, that the chemical potential μ is the same in the p-doped and the n-doped region ($\mu_e^p = \mu_e^n$). Only a difference in the electrical potential occurs between the two regions. Using

$$\eta_e^p = \mu_e^p + kT \ln \frac{n_e^p}{N} - e\phi^p = \eta_e^n = \mu_e^n + kT \ln \frac{n_e^n}{N} - e\phi^n \tag{3.16}$$

the potential difference reads

$$\phi^n - \phi^p = kT/e \ln \frac{n_e^n}{n_e^p} = \frac{kT}{e} \ln \frac{N_D N_A}{n_i^2} \tag{3.17}$$

with $n_e^n = N_D$, the number of electrons from the donors in the n-doped region, and $n_e^p = n_i^2/N_A$.

The diffusion current of electrons from the n-doped silicon to the p-doped silicon and the hole current from the p-doped silicon to the n-doped silicon continues up to the point, where the electrical potential difference $\Delta\phi$ is established, so that both electrochemical potentials are zero ($\eta_e = 0, \eta_h = 0$).

In a region around the contact of the two differently doped regions a region stabilizes, which is free of charge carriers – the space charge region (SCR).

Following the description of [Sze85] and [Har09]: the potentials are shifted according to the electric field, the fermi level is constant over the two regions. The potential difference is the so-called built-in voltage, which appears when the two regions are brought in contact. It is dependent on the doping concentration of the two regions. Because both regions have been electrically neutral before contact, charge neutrality still holds and the charge carrier density in the depth of the space charge region must be equal in both regions.

$$N_A \times x_n = N_D \times x_p \tag{3.18}$$

with $N_{A/D}$ as the ionised acceptors and donors and $x_{n/h}$ the width of the space charge region. This means, if one side is heavier doped than the other, the space charge region will extend much further into the lowly doped region.

The complete description is depicted in figure 3.12 and given by the poisson equation describing the electrostatic potential $\phi(x)$

$$-\frac{\partial^2 \phi}{\partial x^2} = \frac{\rho(x)}{\epsilon\epsilon_0} = \frac{e}{\epsilon\epsilon_0}(N_D - N_A) \tag{3.19}$$

if complete ionization is assumed with N_A and N_D the concentration of ionised acceptors and donors. Integrating the poisson equation, linear electric fields in each region appear. The electric field strength $|E|$ reads

$$|E_n(x)| = \frac{eN_D}{\epsilon\epsilon_0}(x + x_n); \qquad |E_p(x)| = \frac{eN_A}{\epsilon\epsilon_0}(x - x_p) \tag{3.20}$$

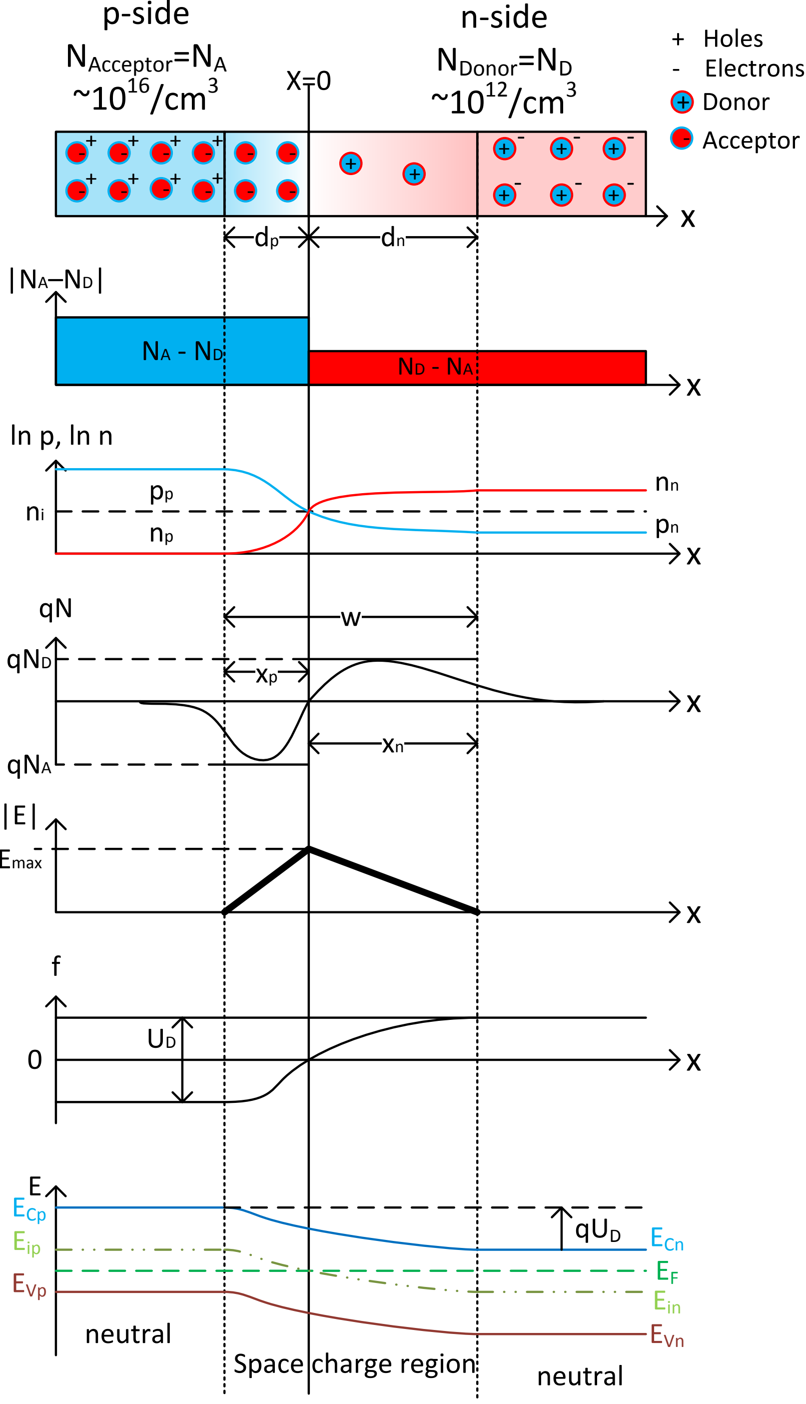

Figure 3.12: Forming of the space charge region without any external field:
In the picture from top to bottom, a simple charge configuration, the doping profile, the mobile charge density, the space charge density, the electric field, the electric potential and the band diagram across the pn-junction is given. Figure after [Har09].

The total width of the space charge region is (if x_p is located at the negative x-coordinate according to figure 3.12

$$w = x_p - x_n \tag{3.21}$$

Further integrating equation 3.20, the electric potential is obtained, leading to a parabolic distribution. Assuming a very abrupt junction, as usually used in for silicon particle detectors, it reads

$$\phi(x) = -\frac{1}{2}\frac{eN_{eff}}{\epsilon\epsilon_0}(x-w)^2 \quad \text{for} \quad 0 \leqslant x \leqslant w \quad \text{and} \quad w \leqslant d \tag{3.22}$$

In this equation, the depletion depth in the highly doped region is neglected. N_{eff} is describing the concentration of the ionised donors and acceptors in the lowly doped region, in which the depletion region is extending.

Applying an external voltage distorts the bands such, that the difference between the n-side and p-side (the built-in voltage without an external potential) is increased by the external voltage. For the situation at $x = 0$, the depleted width can be extracted extracted with the expression $\phi(x = 0) = -V_{bi} - V$:

$$w(V) = \sqrt{\frac{2\epsilon\epsilon_0}{e|N_{eff}|}(V + V_{bi})} \quad \text{for} \quad w \leqslant d \tag{3.23}$$

Reaching the rear contact, the junction has been fully depleted of free carriers at the full depletion voltage V_{dep}. Neglecting the built-in voltage, because it is small compared to the usually applied external reverse bias voltage, the full depletion voltage is fully determined by the device's effective doping concentration $|N_{eff}|$ and its depth d.

$$V_{dep} = \frac{e}{2\epsilon\epsilon_0}|N_{eff}|d^2 \tag{3.24}$$

Since silicon particle detectors are not operated under forward bias condition before irradiation – all of the signal would be lost because of recombination of the charge carriers – this case is not considered here.

3.3.6.1 *Current*

The current flow through a diode is given by the Shockley equation [Sze85].

$$J = J_0 \left[\exp\left(\frac{eV}{k_B T}\right)\right] = J_p + J_n \tag{3.25}$$

This ideal current-voltage characteristics is given by the diffusion current density of electrons and holes, J_n and J_p.

$$J_{n/p} = \frac{eD_{n/p} n/p_{p/n,0}}{L_{n/p}} \left[\exp\left(\frac{eV}{k_B T}\right) - 1\right] \tag{3.26}$$

In this equation, the diffusion length L for electrons or holes is defined as $L_{n/p} = \sqrt{D_{n/p}\tau_{n/p}}$ with the carrier lifetimes $\tau_{n/p}$ and the diffusivity $D_{n/p}$. The equilibrium density of electrons on the p-side or holes on the n-side is denoted by $n_{p,0}$ or $p_{n,0}$. The sum of electron and hole and diffusion current is the Shockley equation, where the saturation current density J_0 is depicted by

$$J_0 = \frac{eD_p n_i^2}{L_p N_D} + \frac{eD_n n_i^2}{L_n N_A} \tag{3.27}$$

The ideal current-voltage characteristics of a diode is plotted in figure 3.13.

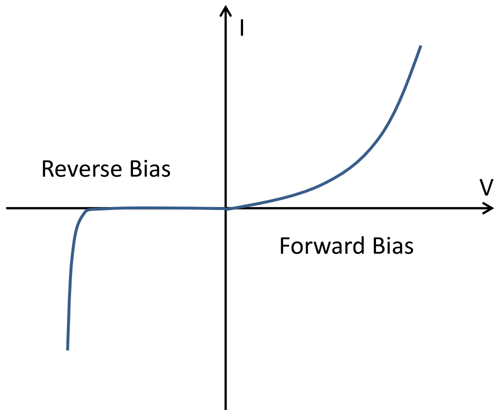

Figure 3.13: Current-voltage characteristics of an ideal diode.

While in forward bias mode, the current is increasing exponentially, in reverse bias the "leakage" current saturates, until the diode breaks down.

The leakage current of the diode in reverse bias mode can be described by two components: the diffusion current and the generation current, which appears in real-case diodes. The diffusion current is given by the Shockley equation. Thermally stimulated charge carriers arising from defects near the middle of the bandgap, which are either process induced or radiation induced, are described by the generation current density J_{gen}. Since the current is determined by the depleted space charge region, only defects there contribute and the current depends on the depleted width, which in turn is proportional to the applied bias voltage.

$$J_{gen} \propto w \propto V \qquad \text{for} \quad V \leqslant V_{dep} \tag{3.28}$$

After full depletion has been reached, the leakage current will saturate. Introducing a generation time, which is the inverse probability per unit time to generate an electron-hole pair by a defect, the generation current density can be expressed as

$$J_{gen} = \frac{e n_i w(V)}{\tau_{gen}} \tag{3.29}$$

with the voltage dependent depletion width $w(V)$ and the intrinsic charge carrier concentration n_i.

Around room temperature, the generation current density dominates the current-voltage characteristic; the saturation value depends only on τ_{gen}. At higher temperatures $J_{n/p}$ will dominate.

3.3.6.2 *Temperature Dependence of the Leakage Current*

The current in a diode is found to be proportional to the following formula [Chi11]:

$$I(T) \propto T^2 \exp\left(-\frac{1.21\,\text{eV}}{2k_B T}\right) \tag{3.30}$$

A current measured at temperature around room temperature, the current-voltage characteristic can be normalized to room temperature by

$$I(T_{20\,^\circ\text{C}}) = I(T) \times \left(\frac{293\,\text{K}}{T}\right)^2 \exp\left(-\frac{1.21\,\text{eV}}{2k_B}\left[\frac{1}{293\,\text{K}} - \frac{1}{T}\right]\right) \tag{3.31}$$

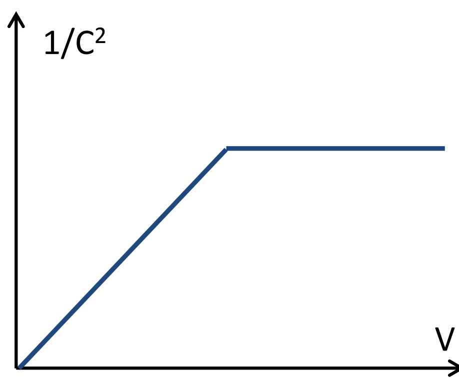

Figure 3.14: Ideal capacitance-voltage characteristics. $1/C^2$ is plotted versus voltage.
The inverse squared capacitance increases linearly with voltage and saturates after full depletion is reached.

3.3.6.3 *Capacitance*

The building up of the space charge region in a reverse biased pn-junction prevents most of the current flow. The pn-junction can be approximated as an insulator with a dielectric constant ϵ. Its capacitance can be calculated as

$$C(V) = \frac{dQ}{dV} = \frac{dQ}{dw}\frac{dw}{dV} \tag{3.32}$$

The fraction of space charge is given in terms of depleted width w $dQ = eN_{eff} \times Adw$, where A denotes the area of a diode. The depleted width on the other hand is dependent on the applied voltage. The expression for the total capacitance of the diode then reads

$$C(V) = \frac{\epsilon_0 \epsilon \times A}{w(V)} \quad \text{for} \quad w \leqslant d. \tag{3.33}$$

After reaching the full depletion voltage V_{dep}, the total depth d of the diode contributes to the capacitance:

$$C = \frac{\epsilon_0 \epsilon \times A}{d}. \tag{3.34}$$

This expression is purely geometrical and determines the geometrical end capacitance, a diode reaches. After the full depletion voltage, the depletion depth does not increase any further and thus the capacitance does not decrease any more but remains constant. This can be seen in figure 3.14.

If the doping profile of the pn-junction is not that abrupt, the capacitance can decrease even slightly further due to additional depleted width in the highly doped region.

The capacitance for a diode can be expressed as a function of the effective doping concentration, which determines the full depletion voltage:

$$C(V) = A\sqrt{\frac{\epsilon \epsilon_0 e |N_{eff}|}{2(V + V_{bi})}} \tag{3.35}$$

When the capacitance is plotted as $1/C^2$ versus the bias voltage, one can instantly read off the depletion voltage at the kink, see figure 3.14.

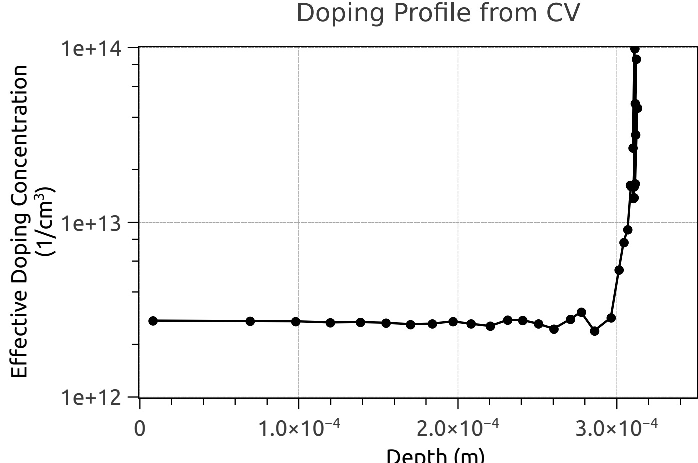

Figure 3.15: Doping profile of a FZ320N diode obtained from a CV measurement: *The effective doping concentration is about* $3 \times 10^{12}\,\mathrm{cm}^{-3}$ *with an active thickness of about* $305\,\mu\mathrm{m}$.

To gain a profile of the effective doping concentration in the bulk, one can calculate the derivative of $1/C^2$ versus the depleted depth of the device, see equation 3.23.

$$\frac{d(1/C^2)}{dV} = -\frac{2}{A^2 \epsilon_0 \epsilon e |N_{eff}|} \tag{3.36}$$

Figure 3.15 shows the doping profile of a $320\,\mu\mathrm{m}$ thick float zone n-bulk diode with an active thickness of about $305\,\mu\mathrm{m}$ obtained from a capacitance measurement.

3.3.7 SILICON GROWTH TECHNIQUES

Semiconductor silicon sensors require very pure, single-crystal silicon. As nature provides only silicon dioxide as sand, it has to be reduced and purified in a series of melting processes. During the melting process at 1500 °C - 2000 °C, carbon is introduced, which forms carbon monoxide with the oxygen from the SiO_2.

Many impurities present in the sand are filtered in a next step by a reaction with hydrochloric acid. The resulting $SiHCl_3$ is then being distilled.

In the last step, the `chemical vapor deposition` (CVD), the $SiHCl_3$ is vaporized and forms pure silicon growing for several days at 1000 °C.

$$SiHCl_3 + H_2 \rightarrow Si + 3HCl \tag{3.37}$$

After this step, specific impurities like phosphorus or boron can be introduced for doping.

The purification of the ingots, out of which the wafers are cut, is done with either the float zone or the magnetic Czochralski process. The epitaxial process is working slightly differently.

3.3.7.1 *Floatzone*

For the float zone process, a poly-crystalline silicon ingot is brought in contact with a single-crystal seed crystal. The silicon ingot is heated locally by an induction coil. The heated region is melting. While the heater is moving along the silicon ingot, the melt slowly solidifies again, forming nearly perfect monocrystalline silicon according to the seed crystal. Impurities tend to stay in the melted zone. By repeating this process, the purity of the silicon can be improved very much. The boarder region, containing most of the impurities, is cut off.

The whole process is taking place in an inert gas atmosphere. Due to this fact, the oxygen concentration is usually quite low in silicon produced with this procedure. The average concen-

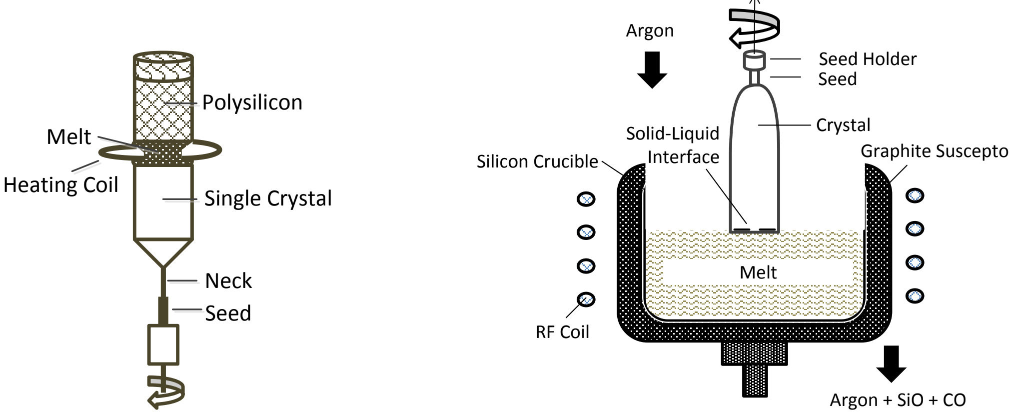

(a) Float zone process. Reproduced from [NN00] (b) Czochralski process. Reproduced from [Sze85].

Figure 3.16: Processing of mono-crystalline silicon:
(a) By an induction coil, the silicon rod is locally melted. It crystallizes in the order of the seed crystal.
(b) The seed crystal is rotatingly pulled out of the melt, forming a single-crystal silicon ingot. The melt is heated by an RF coil. In the magnetic Czochralski process, the melt is additionally in a magnetic field.

tration of oxygen or carbon, depending on the process details, is found to be below $10^{16}\,\mathrm{cm}^{-3}$. By adding oxygen to the gas atmosphere, it can thermically diffuse into the silicon.

Picture 3.16a sketches the working principle of the float zone process.

3.3.7.2 *Magnetic Czochralski*

In the Czochralski process, which was first applied and described by Czochralski [Cz017], a silicon melt is held just above the silicon melting temperature at 1420 °C. A rotating seed crystal is slowly pulled out of the melt. The silicon grows according to the seed crystal in the given mono-crystalline order. Dopants can be added to the silicon melt to design the desired resistivity of the ingot.

The whole process – shown in figure 3.16b – is taking place in an inert argon gas atmosphere. Oxygen is mostly flushed away by the argon gas, but a certain concentration is still present in the grown silicon ingot. The oxygen concentration can be influenced partly by adjusting the rotation speed. Also carbon is present in the silicon melt. The graphite susceptor is reacting with the silicon monoxide and forms carbon monoxide, which is partly absorbed in the silicon melt. Typical impurity concentrations of oxygen and carbon are $c_O \approx 5 \times 10^{17} - 10 \times 10^{17}\,\mathrm{cm}^{-3}$ and $c_C \approx 5 \times 10^{15} - 50 \times 10^{15}\,\mathrm{cm}^{-3}$.

The higher oxygen content can form more thermal double donor or shallow thermal donors, which can change the resistivity of the material and hence have a negative influence. On the other hand, dislocations in the silicon are less possible, because more oxygen makes the silicon more resistant against thermal stress. Silicon with more oxygen is furthermore found to be more radiation tolerant [L+01] and influences the charge carrier lifetime in a positive way [H+03].

However, the Czochralski process is not perfect. The crystal growth is disturbed by convection und flows in the silicon melt. Inhomogeneities of impurities and lattice defects are the effect. A strong horizontal or vertical magnetic field can countervail the turbulent flow. By applying the magnetic Czochralski process, the oxygen content in the crystal can be further reduced and the impurities are distributed more homogeneously throughout the silicon crystal.

4

RADIATION DAMAGE IN SILICON

Silicon used in semiconductor particle detectors experiences severe radiation damage by crossing particles. Defects are formed, which drastically change the detector's performance. Defects created by radiation can be divided into two different kinds of damage: bulk damage and surface damage. Bulk damage is mainly created by hadrons whereas surface damage is mostly created by photons.

This chapter will introduce the radiation damage arising in silicon particle detectors. The damage dealt by different particles can be scaled in order to compare the fluences of different particle types (NIEL scaling). The impact on the silicon particle detector and its macroscopic parameters will be explained. Since defects can move in the lattice, the change of the detector's properties is described in the annealing process. A summary of the most important defects with respect to a HL-LHC like particle composition is given.

Radiation damage in silicon microstrip detectors is more but only bulk damage created by hadrons. Because of their segmented surface, damage in the surface structures has to be considered, too. The total radiation damage is a complex interplay between the bulk and surface damage in the sensors.

The analysis and influence of defects on the silicon sensors is investigated by the RD50 group [RD5].

4.1 Bulk Defects

If particles traverse the silicon detector and interact with the silicon lattice knocking off a silicon atom, defects in the lattice are created. The first atom to hit is called primary knock on atom (PKA). It leaves behind a vacancy (V) in the lattice and can move through it as an interstitial (I) atom.

Only if the threshold energy of about 25 eV is exceeded, the silicon atom can be knocked off its place. If the PKA still has sufficient energy, it can create further defects along its path through the lattice or looses its energy through ionization. At low energies, the non-ionising interactions dominate. At the end of the PKA's track, clusters of disordered atoms form. These regions are called cluster defects.

While protons and pions can interact via Coulomb interactions and mostly do so, they generate point defect as well as cluster defect. Neutrons on the other can only hand scatter at the nuclei and nearly all the energy is transferred to the PKA. Defects created by neutrons are more likely cluster defects.

The different damage distributions are illustrated in figure 4.1. Low energy protons create a lot of point defects, high energy protons create less point defects but more cluster defects, neutrons solely create cluster defects. A simple demonstration of a vacancy and an interstitial atom is sketched in figure 4.2.

4.2 NIEL-Scaling

The energy, that a particle looses due to displacements of atoms in a material, is referred to as non-ionising energy loss. The particle actually creates damage to a crystal lattice. The NIEL-scaling hypothesis states, that the created damage scales linearly with the energy that has been

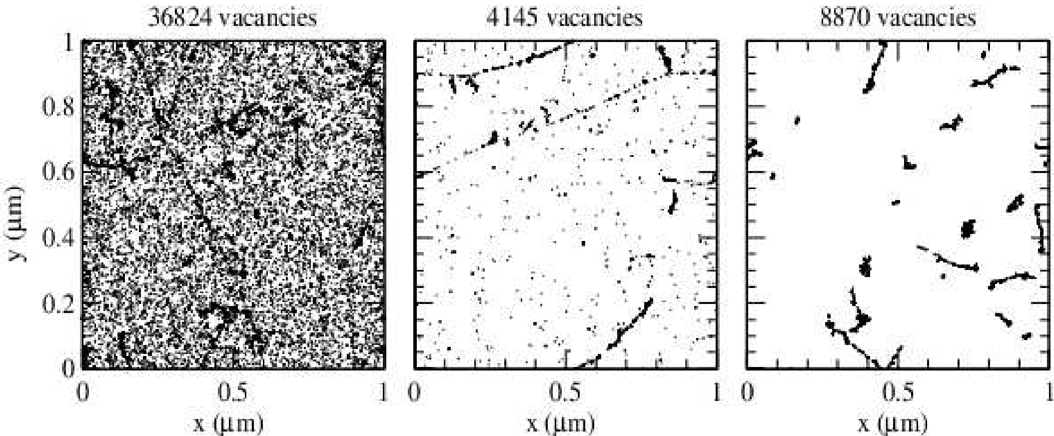

Figure 4.1: Simulation of vacancy generation and distribution in silicon projected over 1 µm in depth: *the irradiation with a fluence of* $10^{14}\,n_{eq}cm^{-2}$ *has been done with 10 MeV protons (left), 24 GeV protons (middle) and 1 MeV neutrons (right).* From [Huh02].

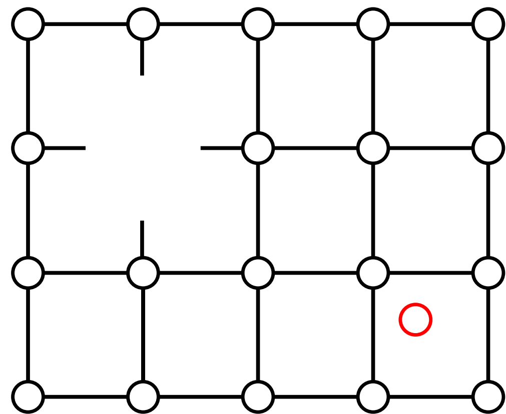

Figure 4.2: Crystal defects in silicon: *vacancy and interstitial atom.*

lost in the displacement of atoms. The primary knock-on atom, which owns most of the energy of the primary particle, creates further damage in the silicon lattice, dependent on the recoil energy E_R, but – most important – independent of the primary particle's type and interaction process.

The Lindhard partition function $P(E_R)$ analytically calculates the energy going into displacements rather than into ionisation. It can be used to calculate the non-ionising energy loss in silicon by different particles. The damage function or more explicitly the cross section for displacement damage reads [L+87]:

$$D(E) = \sum_{\nu} \sigma_{\nu}(E) \int_{E_d}^{E_R^{max}} f_{\nu}(E, E_R) P(E_R) dE_R \tag{4.1}$$

The possible reaction by a particle ν is described by the cross section σ_{ν}. The probability to create a PKA due to this reaction is $f_{\nu}(E, E_R)$ depending on the the particle's energy E and the recoil energy E_R. E_d is the lower limit for the production of a displacement (25 eV in the silicon lattice).

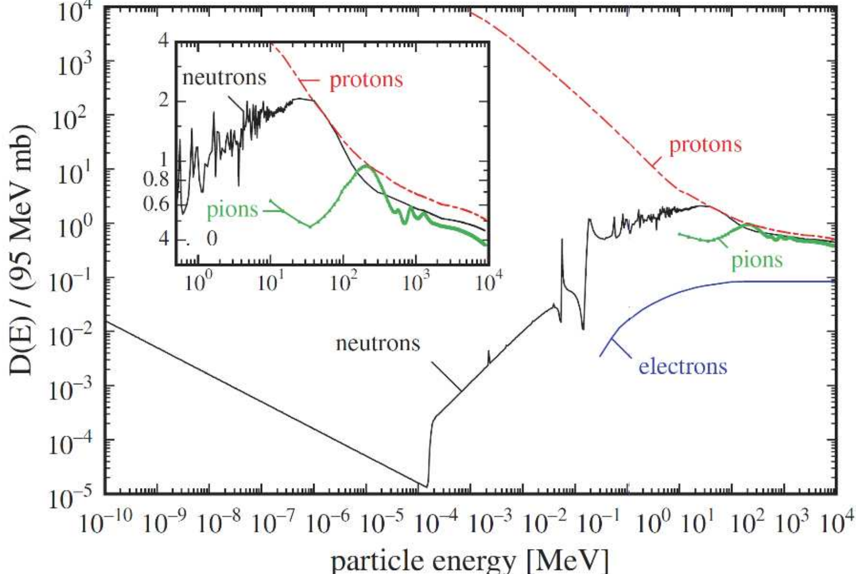

Figure 4.3: Displacement damage functions for neutrons, protons, pions and electrons normalized to 95 MeVmb. The functions show the damage, which is equivalent to 1 MeV neutrons. From [Lin03].

The damage done by different particles depending on their energy is illustrated in figure 4.3. The normalization procedure for the comparison of the damage done by different types of particles at different energies is described in the next section. High energy particles tend to create the same damage. The damage done by low energy protons increases in contrast to neutrons that inflict less damage at low energies.

A detailed description of the NIEL-scaling is given in [Mol99].

4.2.1 THE HARDNESS FACTOR

The scaling of the damage inflicted by a particle with a specified energy E can be scaled to the damage caused by a 1 MeV neutron. The scaling factor is called hardness factor κ:

$$\kappa = \frac{\int D(E)F(E)dE}{D(E_n = 1\,\text{MeV})\int F(E)dE} \tag{4.2}$$

where $D(E_n = 1\,\text{MeV}) = 95\,\text{MeV}\,\text{mb}$. The damage at a given fluence of one particle type can now be compared to the damage done by the corresponding fluence of 1 MeV neutrons. The fluence scaled to 1 MeV neutrons is called 1 MeV neutron equivalent fluence, F_{eq}.

$$F_{eq} = \kappa \times F = \kappa \times \int F(E)dE \tag{4.3}$$

All given fluences are usually corrected by the hardness factor. Table 4.1 lists the hardness factors for particles in this work.

4.3 IMPACT OF DEFECTS

Defects in the silicon lattice influence and change the behaviour of a silicon particle detector. The changes with impact on the sensor performance are explained in more detail in this section.

Table 4.1: Hardness factors of particles used in this work.

Particle	Energy	Hardness Factor	Reference
Protons	23 MeV	2	[Die03]
Neutrons	≈ 1 MeV	0.90 ± 0.03	[Zon98]

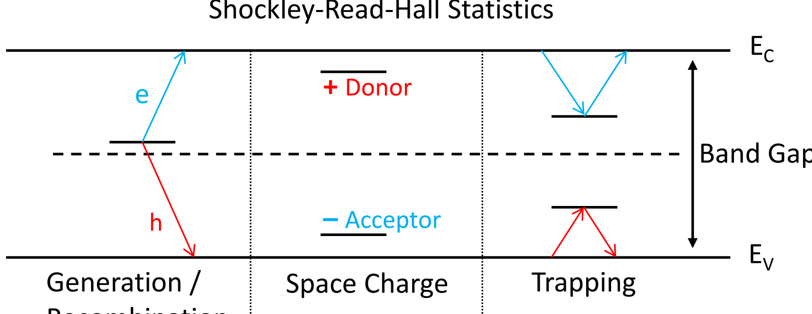

Figure 4.4: Impact of defects in silicon on the sensor properties:
Defects near the middle of the bandgap increase the current (left). Charge carriers can recombine and be generated easier. The doping concentration is affected by the space charge created by charged donors or acceptors (center). Charges can be trapped by defects for some time and do not contribute to the signal (right).

Created defects like vacancies and interstitial atoms can react further to form different defects or anneal out. If an interstitial atom for example finds a vacany again, the silicon lattice is restored.

$$V + I \rightarrow Si \tag{4.4}$$

But a vacancy can also react with other vacancies or impurities like carbon or oxygen in the silicon. The result can be a double vacancy, a vacancy-oxygen complex, a vacancy-phosphorus complex or many others.

$$V + V \rightarrow V_2 \qquad V + O \rightarrow VO \qquad V + P \rightarrow VP \tag{4.5}$$

Possible reactions of vacancies and interstitials with themselves and other impurities and their possibilities are listed in [Huh02]. The creation of the different defect complexes leads to different energy levels in the silicon band gap.

Depending on the defect properties, mainly three effects can be distinguished: defects leading to an increased leakage current; defects creating space charge and thus affecting the effective doping concentration; and defects, which act as charge traps. These effects are visualized in figure 4.4.

The impact of a defect is very much dependent on the energy level of the defect in the silicon bandgap. Levels near the middle of the bandgap mostly generate current. Donors or acceptors near one of the bands are are easily ionized and thus can generate space charge and contribute to the effective doping concentration. Defects with energy levels in between the middle of the bandgap and the valence or conduction band do both, but can also act as charge trapping centers. Electrons or holes can be trapped for some time and are released some time later. Charges from a signal may be trapped and lost for the readout.

In principle, the defect properties are related to the energy level in the bandgap. In reality however, bulk defects can be classified in two major categories: point defects and cluster de-

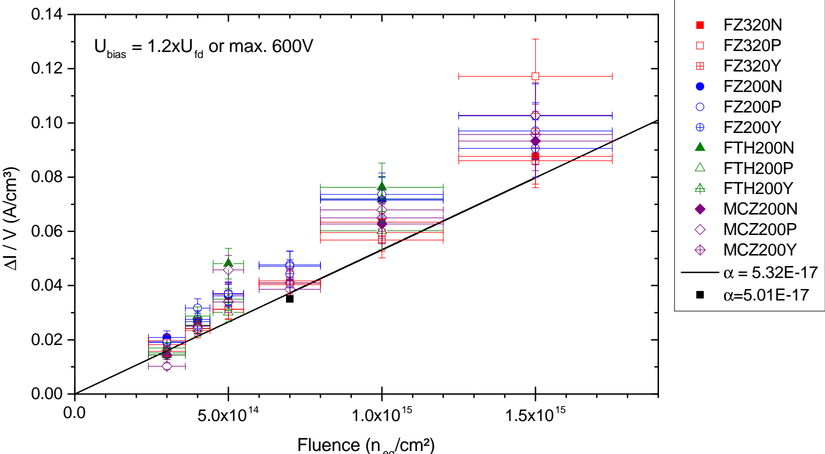

Figure 4.5: Volume generated current dependent on the equivalent fluence for HPK Bstd sensors. From [Fre12].

fects. The latter are complicated conglomeration of several defects, difficult to analyze and can contribute to several effects. The former are usually only very local defects like a vacancy, an interstitial atom or an impurity like the dopants (phosphorus, boron) or oxygen, carbon, gold, etc.

The generation of current and space charge as well as their annealing behaviour is explained in detail in the following sections. Trapping is outlined only shortly, it will be covered in a later chapter.

4.3.1 GENERATION CURRENT

The defects near the center of the bandgap mainly generate current. The current is taken at the depletion voltage ([Mol99]) or at 20% over depletion for the HPK Campaign. The increase in current ΔI is the current of the un-irradiated device subtracted from the current of the irradiated device. After irradiation with high fluences, the initial current is almost negligible ($\mathcal{O}(10^{-5}\,\mathrm{A/cm^3})$) compared to the current after irradiation ($\mathcal{O}(0.1\,\mathrm{A/cm^3})$) at $20\,^\circ\mathrm{C}$. The current is generated in the depleted bulk only, therefore the increase in current is scaled to the volume (Vol.) of the device. Figure 4.5 shows, that the volume scaled increased current is proportional to the equivalent fluence. The proportionality is expressed by α, the current related damage rate.

$$\frac{\Delta I}{\mathrm{Vol.}} \propto F_{eq} \Rightarrow \frac{\Delta I}{\mathrm{Vol.}} = \alpha \times F_{eq} \tag{4.6}$$

The current related damage rate is independent of the particles' type or energy, if the fluence is scaled with the hardness factor to the equivalent fluence. α has the same temperature dependence as the current, see section 3.3.6.2. All current measurements are performed with grounded guard ring for a defined volume. Measurements from sensors can exhibit slightly larger currents than the expected ones due to their segmented surface, a further increase in current due to lateral depletion and errors arising from the temperature scaling.

4.3.2 CHANGE OF EFFECTIVE DOPING CONCENTRATION AND DEPLETION VOLTAGE

Defects creating space charge change the effective doping concentration and hence electric fields and the depletion voltage of the device. Starting from the initial doping concentration

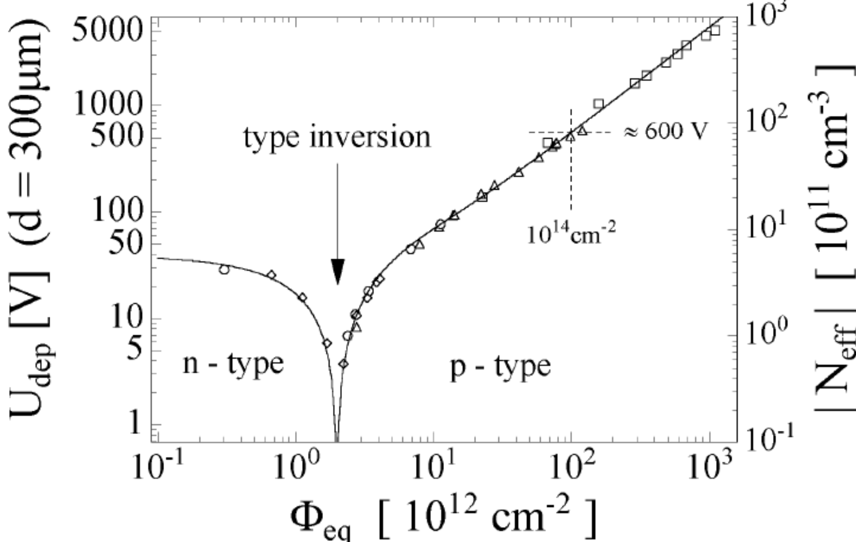

Figure 4.6: Type inversion in n-bulk silicon:
The effective bulk concentration decreases up to a certain fluence. After this fluence is reached, the bulk behaves more like p-type silicon and the effective doping increases again. From [Mol99].

by phosphorus or boron, the effective doping concentration is changed during the irradiation process. The initial doping concentration of high resistivity material is usually in the order of $N_{eff} \approx 10^{12}\,cm^{-3}$. During the irradation, donors and acceptors are created. Depending on the particle type and energy, the ratio between donors and acceptors can differ. Two options are possible for the behaviour of the diode. The example is given for a n-bulk FZ diode, for a p-bulk diode the behaviour is just vice versa.

- If more donors than acceptors are created, the positive space charge will increase and with it the depletion voltage.
- If more acceptors are created, negative space charge will build up, cancelling the positive space charge from the initial donor concentration. At some fluence, the effective space charge will be zero. With more irradiation, the negative space charge will increase further and the material behaves like p-bulk material. The device is called "type-inverted". The depletion voltage, proportional to the effective doping concentration, will decrease first and increase again.

4.3.3 "TYPE INVERSION"

The effect of the type inversion occuring mostly in n-bulk material is shown in figure 4.6. The depletion voltage (U_{dep}) starting at 40 V decreases continuously up to $2 \times 10^{12}\,n_{eq}cm^{-2}$. After the cancelling of the donors, the absolute effective space charge N_{eff} increases again. The increase of the effective space charge is quite linear over the fluence at higher fluences. Given the fact, that the power supplies in the current CMS Tracker only supply voltage up to 600 V, 300 μm thick devices could be depleted up to a fluence of $10^{14}\,n_{eq}cm^{-2}$ in the current case.

An additional effect, called donor removal, comes into play for irradiated n-bulk devices. The initial doping concentration is lowered, because a vacancy can combine with a phosphorus atom or a carbon atom to form a vacancy-phosphorus-complex (V-P) or a V-C complex [W+96]. The V-P complex, or E-center, is electrically neutral [WC64] and does not contribute to the doping concentration anymore. The "type-inversion" then occurs already at lower fluences. The effect of the donor removal is dependent on the creation of defects, thus the particle's type and energy.

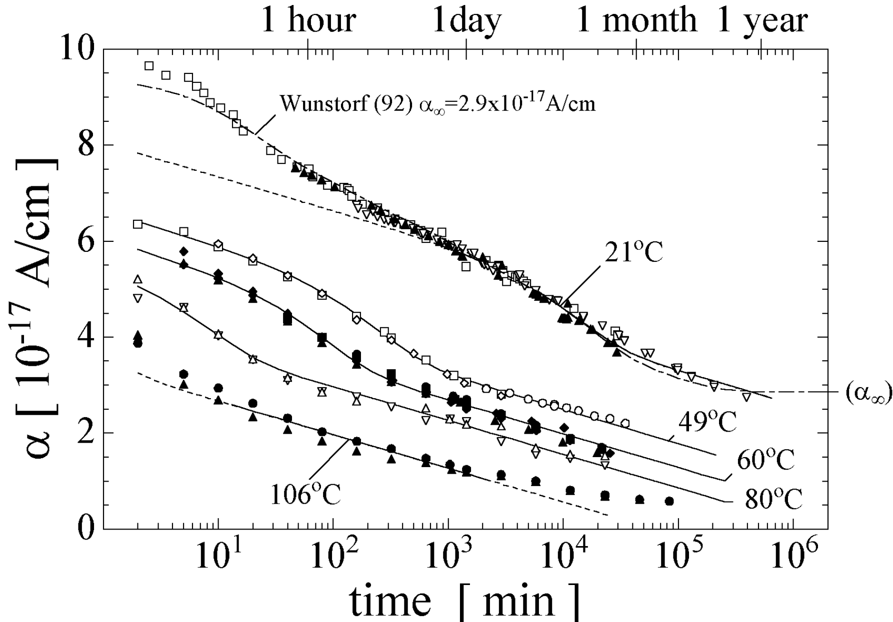

Figure 4.7: Annealing of the current related damage rate α as a function of different temperatures. From [Mol99].

4.4 Annealing of Defects

Defects are not stable in the silicon lattice. They can move through the lattice, repair created defects or merge with other defects.

The movement of defects in the silicon lattice is highly temperature dependent. At -20 °C, the defects are almost frozen, at +20 °C they moderately change the sensor performance and at +60 °C or +80 °C, the annealing processes happen quickly. The annealing affects the leakage current as well as the effective doping concentration. However, the two quanitities are affected on a different timescale.

The annealing is most important for silicon sensors during operation and especially in maintenance periods. During maintenance, the sensors experience warm periods and negative effects on the sensor's performance are to be avoided.

4.4.1 CURRENT

The current is observed to decrease with annealing time. The curves are described by a sum of exponentials.

$$\alpha(t) = \alpha_1 \times \exp\left(-\frac{t}{\tau_1}\right) + \alpha_0 - \beta \times \ln\left(\frac{t}{t_0}\right) \tag{4.7}$$

For higher temperatures, the process happens faster. Because the current can be expressed in terms of the current related damage rate and fluence, α is used to describe the current annealing. The time constant τ_1 models the disappearance of the defects, responsible for the leakage current. The fit for $\alpha(t)$ at different temperatures has been done by Moll [Mol99] and is shown in figure 4.7.

The fits at different temperatures and annealing times can be exploited to investigate the annealing behaviour at long times. The annealing can be accelerated by heating the device. α can be normalized to 20 °C.

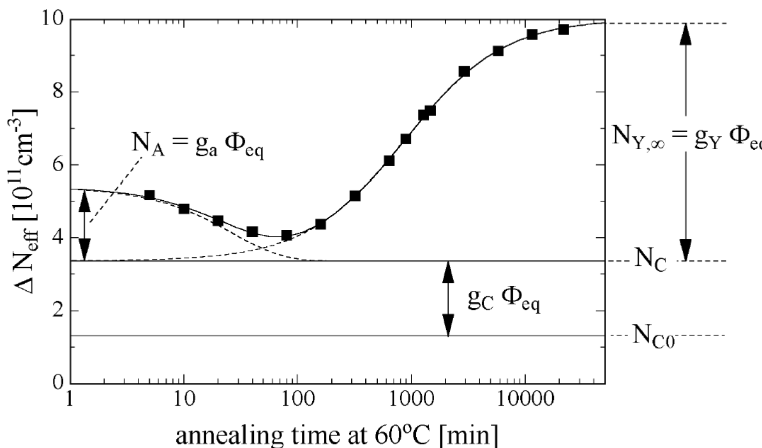

Figure 4.8: Annealing of the effective doping concentration:
the process can be described by a stable damage component, a short annealing component lowering the effective doping and a reverse annealing component increasing the effective doping. From [Mol99].

4.4.2 EFFECTIVE DOPING CONCENTRATION

The annealing of the effective doping concentration is described by the Hamburg-Model. Figure 4.8 shows an example of a diode annealed at 60 °C at several time steps. The effective doping concentration first decreases for the n-bulk diode, reaches a minimum and increases again.

The two parts are referred to as beneficial annealing (decrease of space charge, lower depletion voltage) and reverse annealing (increase of space charge, higher depletion voltage).

The annealing process of the effective doping concentration can be described by three terms: a constant damage term

$$N_C = N_{C0}(1 - \exp(-cF)) + g_C F \tag{4.8}$$

a beneficial annealing term

$$N_A(F,T,t) = g_A F \times \exp\left(\frac{t}{\tau_A(T)}\right) \tag{4.9}$$

and a reverse annealing term

$$N_Y(F,T,t) = N_{Y,\text{inf}}\left(1 - \frac{1}{1 + t/\tau_Y(T)}\right) \tag{4.10}$$

Alltogether, the change of the effective doping concentration is the sum of these contributions:

$$\Delta N_{eff}(F,T,t) = N_C + N_A(F,T,t) + N_Y(F,T,t) \tag{4.11}$$

where "ΔN_{eff} is the radiation induced change in the effective doping concentration with respect to its initial value before irradiation" [Mol99].

$$\Delta N_{eff}(F,T,t) = N_{eff,0} - N_{eff}(F,T,t) \tag{4.12}$$

For several materials, the constants have been determined. Depending on the material or irradiation type, they can vary. Table 4.2 lists the default paramters for FZ n-bulk material determined by Moll [Mol99].

The stable damage term in equation 4.8 is divided into two parts. The stable damage constant g_C increases linearly with the fluence. The second term takes care of the donor removal during the irradiation. The fraction of the removable donor concentration can be identified with N_{C0}, the fraction of the removed donors after a high fluence when $F > 1/c$, is $N_{C0}/N_{eff,0}$.

Table 4.2: Parameters of the Hamburg-Model, determined for FZ n-bulk. [Mol99]

Parameter	Weighted average
g_C	$(1.49 \pm 0.04) \times 10^{-2}\,\mathrm{cm}^{-2}$
$N_{C0} \times c$	$(7.5 \pm 0.6) \times 10^{-2}\,\mathrm{cm}^{-2}$
g_A	$(1.81 \pm 0.14) \times 10^{-2}\,\mathrm{cm}^{-1}$
$\tau_A (60\,^\circ\mathrm{C})$	$(24.1 \pm 2.3)\,\mathrm{min}$
g_Y	$(5.16 \pm 0.09) \times 10^{-2}\,\mathrm{cm}^{-1}$
$\tau_Y (60\,^\circ\mathrm{C})$	$(1060 \pm 110)\,\mathrm{min}$

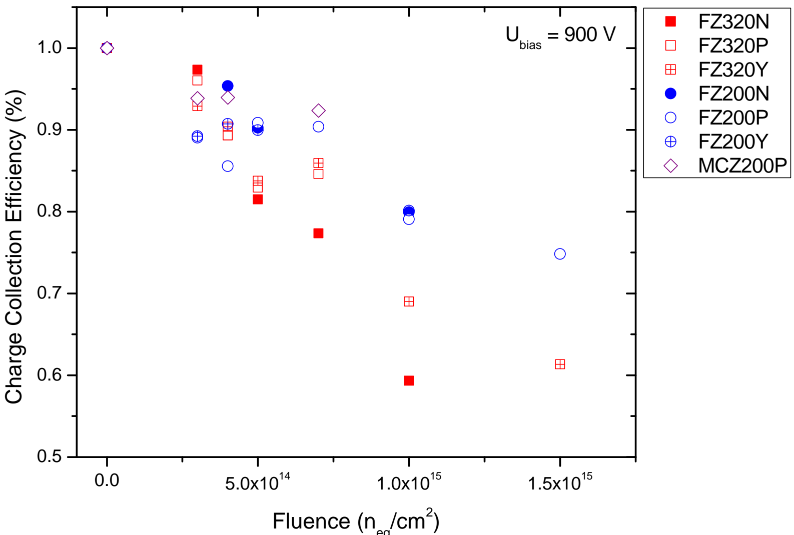

Figure 4.9: Loss in charge collection efficiency due to irradition for HPK Bstd sensors: *the charge collection efficiency drops at higher fluences. A significant part of the charge is lost due to trapping since most of the sensors are fully depleted at 900 V.* From [Fre12].

4.5 Trapping

Irradiated sensors lack signal, even at high voltages well above the depletion voltage, compared to un-irradiated sensors. This phenomenon is called trapping. Possibly responsible for this are defects in the center between the middle of the bandgap and the conduction or valence band. They reduce the most important parameter for the experiments at the LHC, the charge collection efficiency. It even becomes the dominating effect at highly irradiated sensors at the HL-LHC.

The defects trap the charges of the generated signal and keep them for a time, which is larger than the readout time of the chip. The signal is lost for the readout. So far, no defects directly responsible for trapping have been identified, although this has been possible for the defects responsible for the current and space charge [Jun11].

Figure 4.9 shows an example of trapping in irradiated sensors. Even at high voltages the sensor does not reach 100% charge collection efficiency any more. Thinner sensors gain in signal at the same fluence and voltage, because the charge carriers travel a smaller distance to the readout and the electric fields are higher.

Table 4.3: Important defects in silicon irradiated with hadrons.
The energy of the defect is given from the valence band with a positive sign (+) or from the conduction band with a negative sign (-). They either create positive or negative space charge (+/-SC) or generate current.

Defect	Type	Energy	$\sigma_e(cm^{-2})$	$\sigma_h(cm^{-2})$	Effect	Reference
$BD^{0/++}$	Donor	-0.26 eV	6×10^{-15}		+SC	[Jun11]
$V_2^{-/0}$	Acceptor	-0.422 eV	2.2×10^{-15}		Current	[Jun07]
E5	Acceptor	-0.46 eV	7.8×10^{-15}		Current	[Jun11]
E205a	Acceptor	-0.395 eV	1.7×10^{-15}		Current	[Jun11]
E(30K)	Donor	-0.1 eV	2.3×10^{-14}		+SC	[PLJF09]
H(116K)	Acceptor	+0.33 eV		4.0×10^{-14}	-SC	[PFL08]
H(140K)	Accpetor	+0.36 ev		2.5×10^{-15}	-SC	[PFL08]
H(151K)	Acceptor	+0.42 eV		2.3×10^{-14}	-SC	[PFL08]

4.6 A Summary of important Defects

Microscopic defects, which have been found and analyzed with impact on the sensor properties, are summarized in table 4.3. Defects listed here either create space charge, denoted by SC, or generate current due to their poximity to the middle of the bandgap. Experimentally, only one cross section of a defect can be measured with good accuracy, only this value is given here. The other cross section is usually lower. The sign convention for the energy level in the bandgap is the following: levels, which have been measured from the conduction band are denoted by a negative sign, levels from the valence band are given a positive sign. Table 4.3 lists only the defects, which are created by irradiation with hadrons, like in an LHC scenario. More on the microscopic properties of the defects can be found in [Jun11].

4.7 Surface Damage

The expression "surface damage" is usually used to summarize all the damage, which does not appear in the silicon bulk of the sensor. The "surface" of the silicon sensors usually exists of silicon dioxide, but there can be an additional layer of silicon nitride on top of it. The damage appears in the silicon dioxide or at the interface of the silicon dioxide to the silicon of the bulk. There are different damage types to distinguish (after [SN07]):

OXIDE TRAPPED CHARGE: If electron-hole pairs are created in the SiO_2, they can be captured by electron traps or hole traps in the silicon dioxide. They are then called "oxide trapped charges" and can be positive or negative, depending on the defect property. Radiation damage can create defects in the silicon dioxide, leading to additional defects, which can act as charge traps.

FIXED OXIDE CHARGE: Fixed oxide charges are deep level defects in the silicon dioxide, appearing in a thin layer of several nm from the $Si - SiO_2$ interface. In this transition region, the atoms are highly disordered. The deep defects trap holes and thus are positive. Figure 4.10 shows the increasing fixed oxide charge concentration as a function of the ionising dose. It takes about three years to anneal 50% of the fixed oxide charges at 20 °C [Zha13]. Regarding cooled sensors, the fixed oxide charges can be considered fixed.

INTERFACE TRAPS: At the silicon–silicon-dioxide interface, dangling bonds of the atoms create energy levels in the bandgap near its center. The interface traps near the middle of the bandgap contribute to the surface generation current.

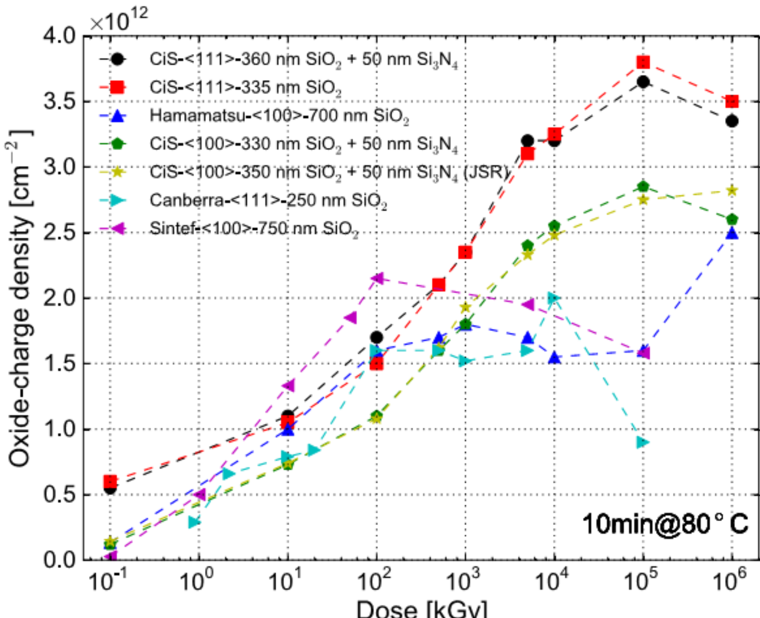

Figure 4.10: Fixed oxide charge concentration as a function of ionising dose for different materials. From [Zha13].

Surface damage is mostly created by ionizing radiation. Hence, the concentration of the mentioned defects increases with the ionising dose and influences the silicon sensor. Surface damage is very crucial for segmented silicon sensors, especially AC-coupled sensors, because their electrical properties are very prone to changes at the surface. This can lead to an increased current due to surface currents, an electron accumulation layer at the interface and an increase in full depletion voltage. Diodes on the other hand do not feature a segmented surface and are not so much affected by surface damage.

Part II

TECHNIQUES AND EQUIPMENT

5

MEASUREMENT TECHNIQUES

Several techniques are available to measure the characteristics of a silicon sensor, all of them deducted from and also used in semiconductor industries. The most simple is the measurement of the leakage current when high voltage is applied. To determine the full depletion voltage, a capacitance-voltage measurement is performed. These are the two basic electrical measurements, which are standard for all sensors. For strip sensors, additional electrical measurements characterizing the strip quality are available, in the following summarized as *strip measurements*. Further details of the sensor can be investigated by using the Transient Current Technique (TCT) mostly applied on diodes or edge Transient Current Technique (eTCT), useful for strip sensors. This section describes these techniques and their conventional application.

5.1 Electrical Measurements

All electrical measurements are performed using the probe stations described in section 6.2.1. Because of their simplicity and easy realizability, every sensor undergoes these measurements as a proof of functionality. The evolution of these parameters after irradiation then gives a first hint on the performance of irradiated sensors.

5.1.1 current-voltage (iv)

The measurement of a current-voltage curve is done by applying high voltage to the back plane of the sensor and connecting the pad (Diode) or bias ring (strip sensor) to ground via an ampere-meter. A good resolution of the ampere-meter is necessary due to the very low current generated in detector-grade silicon (few nA per cm^3 at -20 °C). Without connecting the guard ring of the sensor, the current of the whole sensor including surface currents is measured. This corresponds to the modus operandi in the detector.

If one wants to determine the current generated in a well defined volume, the guard ring has to be connected to ground too. The current of the guard ring is additionally measured by an ampere-meter. All currents coming from the outer parts of the detector including surface currents and edge effects is drawn by the guard ring. The area used for the calculation of the volume is constrained by the center between the guard ring and the pad (or bias ring). However, this operation mode affects the high voltage stability and can lead to an earlier breakdown of the sensor. An IV curve of an un-irradiated diode can be seen in figure 5.1. The current of the pad and the guard ring add up to the current when the guard ring is not connected. A breakdown occurs at higher voltages, if the guard ring is connected.

5.1.2 capacitance-voltage (cv)

The capacitance-voltage curve is recorded with an LCR-meter. The connection scheme is the same as for the IV measurement, the LCR meter is AC coupled to the circuit because of the high voltage. Intrinsically, the LCR-meter measures the impedance or admittance and one can record the real and the imaginary part corresponding to the capacitance and the conductance or resistance. Two measurement modes are available: the serial or parallel mode. Depending on the characteristic of the sensor, one or the other mode may be preferred.

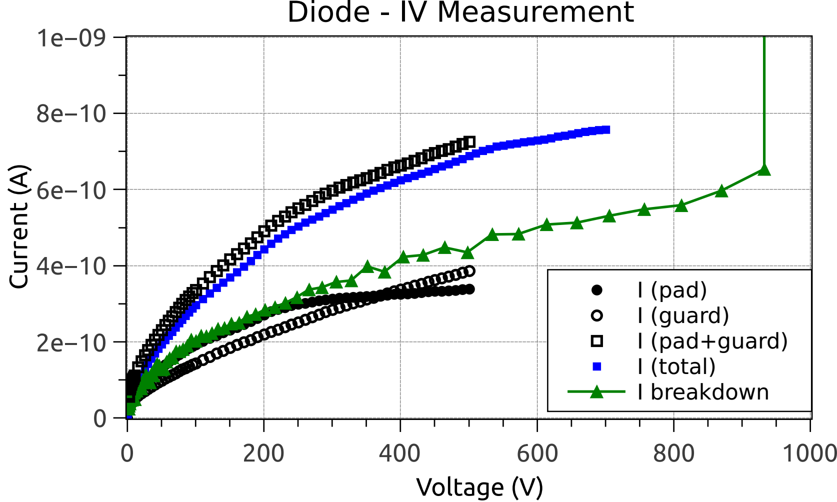

Figure 5.1: IV measurement of an un-irradiated diode:
The current of the pad and guard ring add up to the total current measured without the guard ring connected. At high voltages, a breakdown can occur.

In general, the sensor can be described as a capacitance with a resistor in parallel (leakage current) and in series (bulk resistance). For sensors, which are not irradiated, the bulk resistance can be neglected and the parallel mode applies. For irradiated sensors, the leakage current is higher and the bulk resistance becomes more important. Depending on the ratio of the two resistors, the serial mode is a better description.

The usual measurement procedure envisages the parallel mode. Both values, the capacitance and the conductance are stored. In this way, one can easily convert the parallel capacitance C_P into the serial capacitance C_S using the following relation:

$$Z^{-1} = Y \tag{5.1}$$

Z is the impedance measured by the LCR-meter in the serial mode and Y is the admittance, measured in the parallel mode.

$$Z = R + jX = R_S - j\frac{1}{\omega C_S} \tag{5.2}$$

$$Y = G + jB = \frac{1}{R_P} + j\omega C_P \tag{5.3}$$

j denotes the imaginary unit. $X = -\frac{1}{\omega C_S}$ is called the reactance, G the conductance and $B = \omega C_P$ the susceptance. $\omega = 2\pi f$ is the angular frequency of the low voltage, which is modulated upon the high voltage. Usually a frequency of 1 kHz and an alternating voltage of 1 V is applied.

There are some parameters, which can be calculated using the CV measurement.
First of all, the CV measurement is used to determine the full depletion voltage. Therefore $1/C^2$ is plotted versus the applied voltage. According to equation 3.35 the capacitance decreases with the square root of the voltage, a linear increase of $1/C^2$ is expected up to the full depletion voltage, where the curve saturates. By fitting two linear slopes to each of these sections, the full depletion voltage is obtained at the intersection point of the two lines (see figure 5.2).

Secondly, from the capacitance reached after full depletion, the total active thickness d of the sensor can be estimated, assuming that the sensor is approximately a plate capacitor, for which the volume $(A \times d)$ is well defined, that is, the guard ring is connected to ground:

$$d = \epsilon_0 \epsilon_r \frac{A}{C_{end}} \tag{5.4}$$

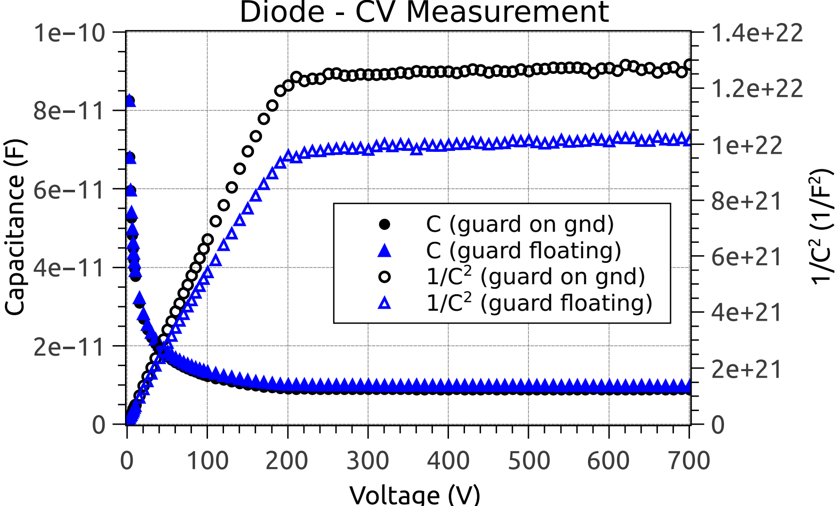

Figure 5.2: CV measurement of an un-irradiated diode:
With the guard ring connected to ground, a lower capacitance is measured. This does not affect the full depletion voltage.

If the guard ring is not connected to ground, the lateral depletion zone gets larger at higher voltages and a higher end capacitance is reached. In this case, the estimation results in a wrong thickness. This effect can be corrected, considering a larger volume for the calculation (see section 8.2).

Thirdly, from the full depletion voltage V_{dep} and the active thickness d , the effective doping concentration N_{eff} in the bulk of the sensor can be calculated using equation 3.35:

$$|N_{eff}| = 2\epsilon_0\epsilon_r \frac{V_{dep}}{e \cdot d^2} \tag{5.5}$$

Equations 5.4 and 5.5 only hold for un-irradiated sensors. For irradiated sensors, the CV measurement depends on the sensor's temperature and measurement frequency. These equations cannot be more than a rough estimate then. The change of the CV curve varying with temperature and frequency can be seen in figure 5.3 and depends on the properties of the defects induced by irradiation. Due to that, the full depletion voltage is also varying [CCS02]. Hence irradiated samples are measured at 455 Hz and -20 °C in addition.

A measurement technique using these dependencies to measure the activation energy and cross sections of defects was proposed by Borchi et al. [BBPS98]. However, this technique is not very accurate and other techniques like DLTS and TSC, usually used to determine defects in diodes after irradiation, are more reliable. The method could be used to determine effective defects at the measurement temperature.

5.1.3 STRIP MEASUREMENTS

Strip measurements summarize a set of six different measurements to determine the strip quality of a sensor after fabrication or irradiation:

1. single strip leakage current (I_{leak}),
2. current over dielectricum (over the silicon dioxide decoupling the DC strip from the aluminum readout strip, I_{diel} or "pinhole"),
3. bias resistance (R_{poly} or R_{bias}),
4. interstrip resistance (R_{int}),

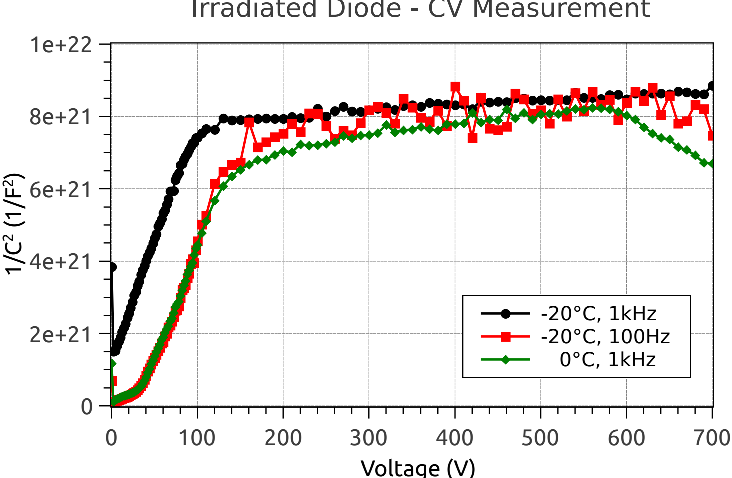

Figure 5.3: CV measurement of an irradiated diode:
Different values are obtained at different temperatures and frequencies.

5. interstrip capacitance (C_{int}) and
6. coupling capacitance (C_{AC} or CC).

The details of these measurements, connection schemes and typical values can be found in [Hof13], [Har09] and [Fur06].

The measurement of the interstrip resistance in particular can provide a good insight in the electrical isolation of the guard ring and the pad on diodes and is thus used to determine the isolation quality of p-spray or p-stop. Since this measurement is used in section 9, it will be shortly explained here:

The back plane of the diode is connected to high voltage, the pad is connected to ground and the current on the pad is measured. The guard ring is connected to a low voltage source. The low voltage is ramped from 0 V to 1 V in several steps. The additional current on the pad is then recorded and the resistance between pad and guard ring R_{PG} is calculated as the slope of the current versus the voltage on the guard ring.

$$R_{PG} = \frac{\Delta V_{guard}}{\Delta I_{pad}} \tag{5.6}$$

A typical measurement can be seen in figure 5.4; the isolation sets in when ramping up the high voltage and is usually very good above the depletion voltage (section 5.1.4). Below the depletion voltage, the resistance is an indication of the isolation quality of the isolation technique (section 3.2.1).

5.1.4 FLATBAND VOLTAGE

The flatband voltage is measured on a metal oxide semiconductor (MOS) structure. The high voltage is connected to back plane, the front of the MOS is connected to ground. A LCR-meter measures the capacitance of the MOS. On a p-type sensor, electrons are attracted to the positively charged oxide. When the high voltage is ramped up, the device depletes and at a certain voltage, the flatband voltage, the electron accumulation layer vanishes. This is seen in a change of the total capacitance. From the flatband voltage, one can conclude on the total oxide charge, or, because electrons can't enter the oxide, the surface oxide charge density, given in $1/cm^2$. If the sensor is very clean of defects, this density is very low ($< 10^{11}\,cm^{-2}$). After irradiation the oxide gets charged and typically the oxide charge saturates

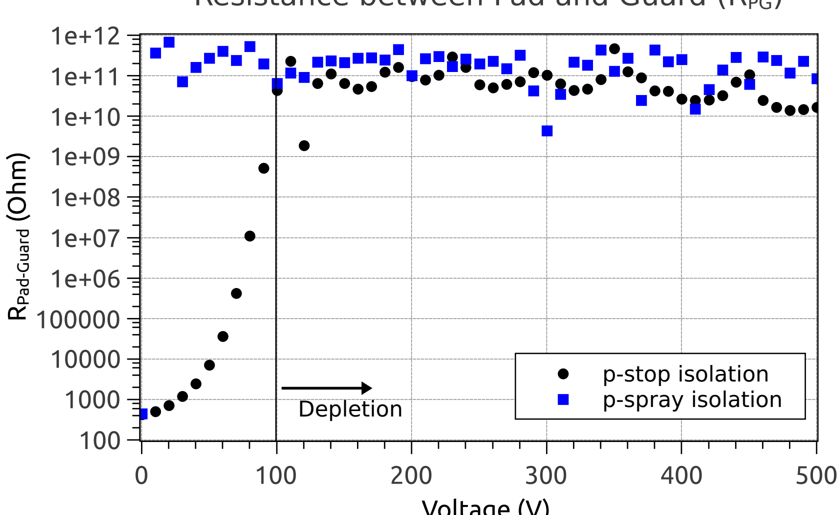

Figure 5.4: The resistance between pad and guard is plotted versus voltage:
The isolation for p-spray is very good and the maximum resistance is shown as an upper limit of the measurement. Because of the missing p-stop between pad and guard ring, the isolation for the p-stop diodes sets in only after depletion.

at about $2 \times 10^{12}\,\text{cm}^{-2}$ (just below 100 V), depending on the manufacturer of the oxide (see figure 4.10 in section 4.7). Figure 5.5 shows the measurement of a MOS structure before and after irradiation.

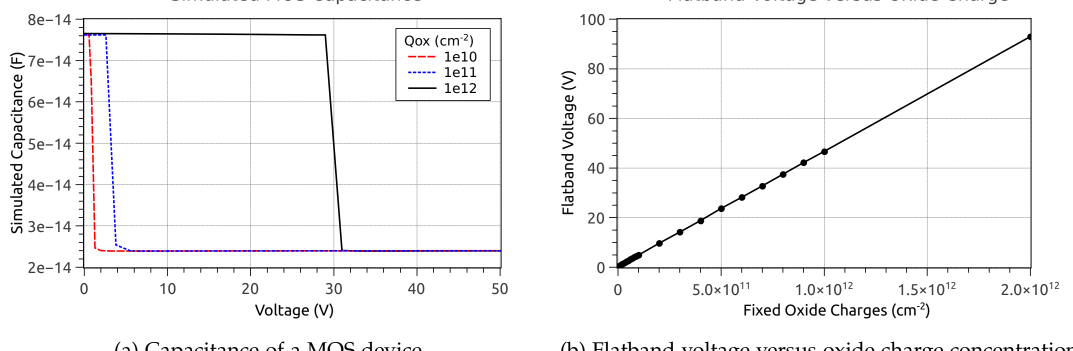

(a) Capacitance of a MOS device.

(b) Flatband voltage versus oxide charge concentration.

Figure 5.5: Determination of the flatband voltage on a MOS device:
The capacitance is constant up to the flatband voltage, has a steep transition to a lower capacitance and saturates again. The flatband voltage is proportional to the oxide charge concentration.

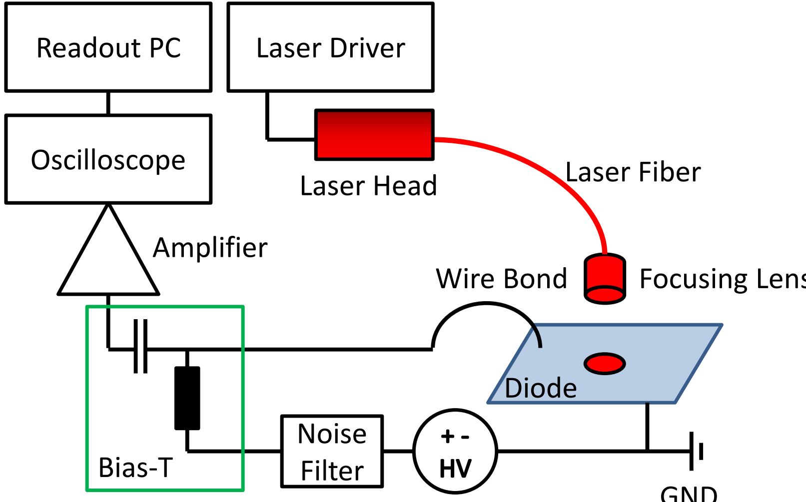

Figure 5.6: Sketch of the TCT setup:
A short light pulse generates a signal in the silicon sensor, which is then decoupled from the high voltage line by a bias-T, fed to an amplifier and recorded by a gigahertz oscilloscope.

5.2 Transient Current Technique (TCT)

The Transient Current Technique (TCT) has been used successfully for quite some time now to determine the properties of silicon sensors. As silicon sensors became more and more important as detectors in the field of high energy physics, the interest in their properties after irradiation grew. "Radiation hardness of silicon detectors - a challenge from high-energy physics", a paper from Linström et al. [LMF99], describes very well the challenges and mentions the TCT as a method correlating defect analysis and detector performance.

Especially after high fluences, the electric field in the bulk of the sensor plays a very important role: additional charge loss occurs in low field regions in the bulk besides the underdepletion of the device. This so called trapping of the charge carriers at defects in the bulk reduces the obtained signal. To investigate trapping probabilities of single charge carriers, holes or electrons, the dependence on the electric field and the charge collection efficiency (CCE), one can look at the time resolved transient current of induced signals.

The signal is generated by the optical absorption of a very short light pulse generated by a laser. The additional current in the device produced by the drifting charge carriers can be recorded by a fast oscilloscope after amplification. Depending on the setup, the signal has to be decoupled from the high voltage line by a bias-T. A sketch of the TCT setup as used at the IEKP can be seen in figure 5.6. This chapter describes the basic principles of the Transient Current Technique whereas the experimental implementation is found in chapter 6.2.3.

5.2.1 OPTICAL ABSORPTION IN SILICON

The signal for the TCT is generated by the absorption of a short laser pulse. Depending on the wavelength of the short laser pulse, the light is absorbed near the impact point (red light) or is partially transmitted through the silicon crystal (infrared light). Figure 5.7 shows the different absorption of light in silicon. In the case of the infrared light, the absorption coefficient is larger than the typical silicon thickness of about 300μm and hence a large amount of light is transmitted.

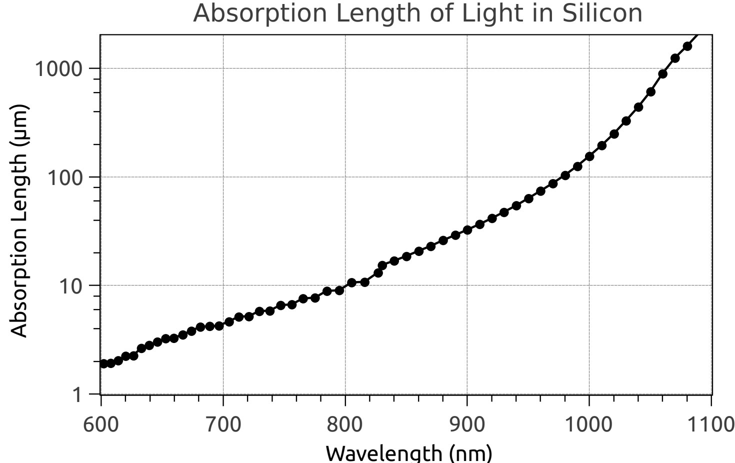

Figure 5.7: Absorption length of light with different wavelengths in silicon at 300 K. Values from [Syn12].

Table 5.1: Parameters of the drift velocity model for electrons and holes calculated after [JCOQ77].

Parameter	Electrons	Holes
$V_{sat}(ms^{-1})$	$1.09 \cdot 10^5$	$0.84 \cdot 10^5$
β	1.09	1.21
$\mu_0(m^2V^{-1}s^{-1})$	0.1605	0.0486

With a red laser, only one type of charge carrier drift throughout the whole bulk, the other type doesn't have a large contribution because the drift length to the surface is very short. In this way, the different drift velocities of holes and electrons and the different trapping probabilities of holes and electrons can be seen.

The infrared laser on the other hand penetrates the silicon crystal, generating electron-hole pairs along it's trajectory, which are separated by the electric field and drift to the corresponding electrode. This nearly reflects the situation of a charged particle traversing the sensor.

In picture 5.8 the signal generation of an infrared laser and a red laser is illustrated.

5.2.2 CHARGE CARRIER TRANSPORT

Canali et al. describe the charge transport in silicon [CMMO75]:

$$v_{drift} = \frac{\mu_0 E}{\left(1 + \left(\frac{\mu_0 E}{v_{sat}}\right)^{\beta}\right)^{1/\beta}} \tag{5.7}$$

If an external voltage is applied to the silicon semiconductor, the charge carriers drift along the field lines of the electric field. The drift velocity is different for electrons and holes and hence the parameters in the equation 5.7 differ. In table 5.1 the parameters for electrons and holes are listed. E is the electric field, v_{sat} describes the saturation velocity, the charge carriers can reach maximally, μ_0 is the zero-field mobility and β parameterizes the transition from the low field to the high field regime. A more general and temperature dependent parameterization of the model is given by Jacoboni et al. [JCOQ77].

Along with the drifting of the charge carriers, diffusion occurs. Because the charge carriers describe a local maximum in the depleted silicon bulk and because of the statistically different

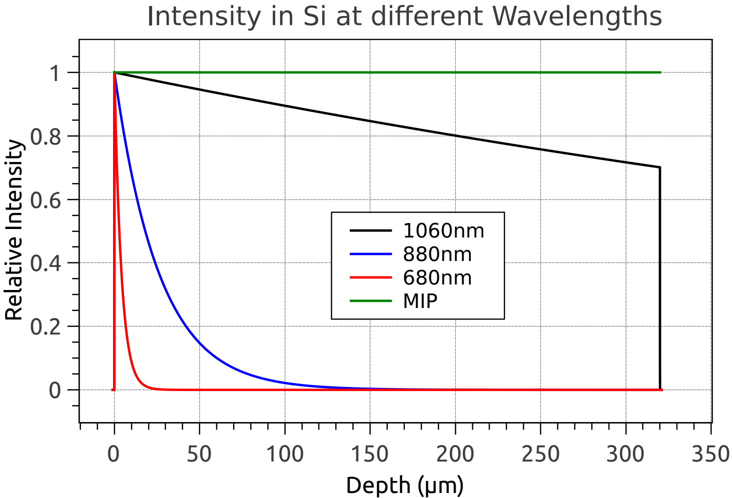

Figure 5.8: Absorption of red or infrared light in silicon compared to the charge generation by a particle: *Red light is absorbed near the surface of the impact, so only electrons or holes are drifting through the bulk. Infrared light generates charge carriers throughout the whole bulk, but looses intensity towards the backside. A minimum-ionising particle (MIP) creates a constant amount of charge throughout the bulk.*

momenta of the charge carriers, the charge cloud broadens. The flux $\vec{F}$ of the charge carriers is decribed by the diffusion equation

$$\vec{F} = -D\vec{\nabla}n \tag{5.8}$$

D is the diffusion constant. The Einstein equation relates the mobility μ with the diffusion constant

$$D = \frac{k_B T}{Q} \times \mu \tag{5.9}$$

where Q is the total charge, T the temperature and k_B the Boltzmann constant. The total current density is thus a sum of drift and diffusion:

$$\vec{J} = -Q\mu n\vec{E} - QD\vec{\nabla}n \tag{5.10}$$

5.2.3 DRIFT SIGNAL

The drifting charge in the silicon sensor is what can be recorded on the oscilloscope in the readout system. The current is described by

$$I(t) = Q\vec{E}_w(\vec{r}(t)) \times \vec{v}_{drift}(\vec{r}(t)) \tag{5.11}$$

The weighting field in a diode is simply $\vec{E}_w = -\frac{1}{d}$ [GM86]. With the solution of the equation of motion $\vec{r}(t)$, the equation above simplifies to

$$I(t) = -Q\frac{1}{d}v_{drift}(t) \tag{5.12}$$

In the unirradiated case, the electric field drops linearly from the pn-junction towards the back side of the device. If the diode is biased above full depletion, the electric field spans the whole bulk. The charge carriers follow the electric field and the drift velocity is proportional to the electric field at all times. If biased under depletion, the electric field drops linearly from the pn-junction, reaching zero at some point. The drift velocity of the charge carriers then just falls off exponentially.

5.2.4 CHARGE COLLECTION EFFICIENCY

When speaking of the TCT, the charge collection CC is defined as the integral of the current over time.

$$CC = \int I(t)dt \tag{5.13}$$

The charge collection efficiency is then the value of the charge collection of an irradiated device divided by the collected charge of an unirradiated device above full depletion voltage.

$$CCE = \frac{\int I(t)_{irr} dt}{\int I(t)_{unirrad, V>V_{fd}} dt} \tag{5.14}$$

Usually, the charge collection efficiency is determined using minimum ionising particles (MIP). As mentioned earlier, using an infrared laser is very similar to this situation. The laser has some advantages after all: no radioactive source is needed, the beam can be very well focused and the angle of incident can be controlled very precisely. Furthermore, the intensity can be raised to some 100 MIPs, allowing for a more precise measurement of CCE because of much better signal to noise ratio.

In the unirradiated case, the charge collection of a silicon sensor rises continuously up to the full depletion voltage, where the charge collection saturates. In the irradiated case, the charge collection is lower than in the unirradiated case, again rising up to the full depletion voltage. At the full depletion voltage, the irradiated sensor doesn't reach 100% of the unirradiated sensor, but the collected charge still increases with the applied voltage. This is due to the trapping of charge carriers, which is suppressed at higher electric fields.

5.2.5 TRAPPING TIME

Charge carriers moving in the silicon sensor have a chance to get trapped by defects for a certain time. If this time is longer than the usual readout time of the electronics, this charge is lost. The probability of a charge carrier being captured increases with the number of defects in the bulk. It is parameterized as

$$\frac{1}{\tau_{eff}} = \sum N_i (1 - P_i^{e,h}) \sigma_{i_{e,h}} v_{drift_{e,h}} \tag{5.15}$$

τ_{eff} is called the trapping time [KLF93] and reflects the mean free path of a charge carrier in an irradiated device. N_i is the concentration of the defects, which are responsible for capturing a charge carrier. P_i is the probability, that a trap is already occupied and σ_i is the cross section for the given defect.

The current in the sensor can be written as (according to equation 5.12)

$$I(t) = e \times N_{e,h}(t) \frac{1}{d} v_{drift_{e,h}} \tag{5.16}$$

with $Q = N_{e,h} \times e$, the number of drifting charge carriers with elementary charge e. The number of drifting charge carriers now decreases because of trapping. With an effective trapping time τ_{eff}, the number of drifting charge carriers at a certain time t can be written as

$$N_{e,h}(t) = N_{e,h}(0) \times e^{\frac{-t}{\tau_{eff_{e,h}}}} \tag{5.17}$$

Thus, the current in the sensor drops exponentially with time.

$$I(t) = I_0(t) \times e^{\frac{-t}{\tau_{eff_{e,h}}}} \tag{5.18}$$

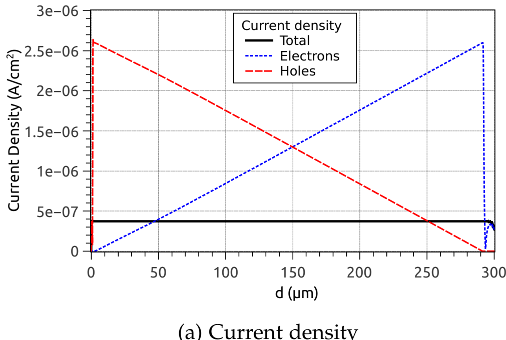

(a) Current density

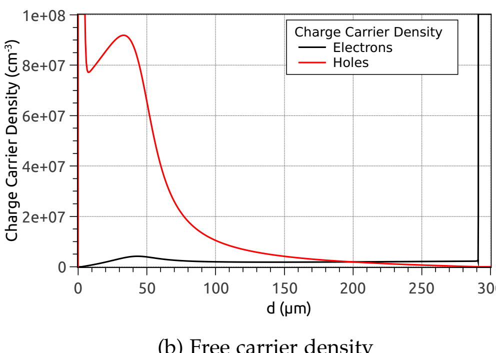

(b) Free carrier density

Figure 5.9: Current density (a) and free carrier density (b) in an irradiated n-bulk sensor (100 V): *the free carrier density is proportional to the amount of trapped charges in the defects.*

For sensors, which are not irradiated to very high fluences, the trapping was found to be proportional to the fluence.

$$\frac{1}{\tau} = \beta \times F \tag{5.19}$$

The proportionality is expressed by β, which is different for electrons and holes of course, but can also depend on the irradiation particle type.

The trapping becomes a more and more important parameter when looking at the signal of irradiated sensors.

5.2.6 THE ORIGIN OF THE DOUBLE PEAK IN IRRADIATED SENSORS

Several TCT measurements of irradiated diodes have revealed a double peak shape of the signal [EVL02][E+04][V+07][L+10b]. Assuming, that the drift velocity of the charge carriers is proportional to the electric field, which is true, if the drift velocity is below the saturation drift velocity, the electric field also has to show two peaks.

Following the explanation of Eremin [EVL02], in n-bulk sensors deep donors trap more positive charge carriers and thus create more positive space charge at the p^+-contact whereas deep acceptors create more negative space charge at the n^+-contact. The filling of the defects is very dependent on the total charge carrier density – the leakage current of the device – also enhanced by defects. The free carrier density distribution is proportional to the charge carriers trapped by the defects. This is illustrated in figure 5.9.

The electric field is resulting from the Poisson equation

$$\text{div } E = N_{eff} \times \frac{-e}{\epsilon_r \epsilon_0} \tag{5.20}$$

and will also show two peaks according to the distribution of the effective doping concentration N_{eff}. This is shown in figure 5.10.

The charge carriers, injected by a red laser from one or the other side, follow the doubly peaked electric field and hence show a doubly peaked signal.

From the depletion point of view, the sensor is sensitive below full depletion at both sides whereas the center of the bulk remains undepleted. At higher voltages, the depleted regions from both sides meet and the whole bulk gets active again. Depending on the defects' energy levels in the silicon bandgap and their occupation, one side dominates.

An example of a double peak signal can be seen in figure 5.11. At low voltages, two separate peaks are visible. They merge in the course of higher bias voltages and the space charge

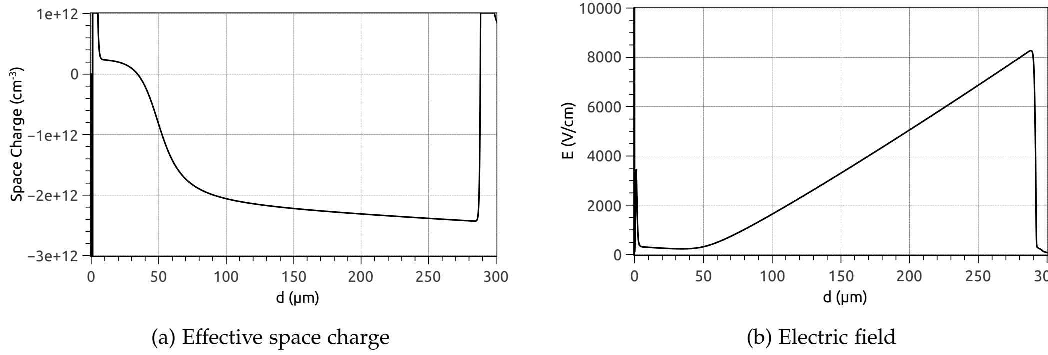

(a) Effective space charge

(b) Electric field

Figure 5.10: Effective space charge and electric field in an irradiated n-bulk sensor (100 V): *In a n-bulk sensor, positive space charge accumulates at the* p^+*-contact and negative space at the* n^+*-contact. The resulting electric field is high in regions with high space charge and low near the zero space charge region.*

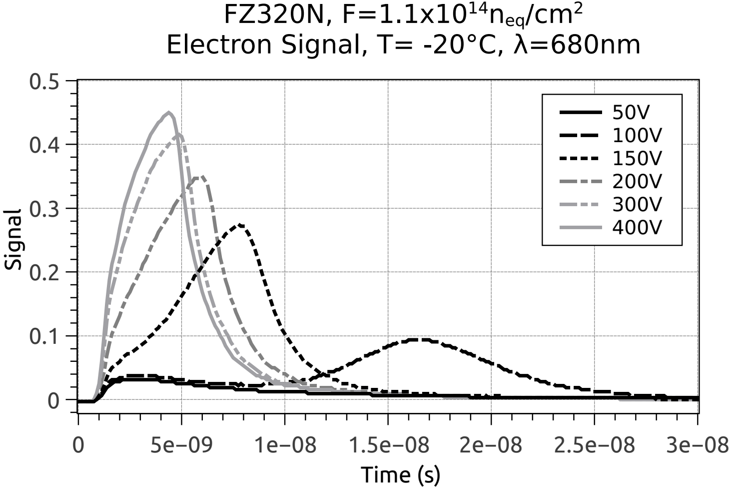

Figure 5.11: Double Peak signal in a TCT measurement: *electrons drift in a 320 μm thick n-bulk diode from the front* (p^+) *to the back* (n^+)*. The two separate peaks at low voltage merge at high voltage.*

created by the acceptors dominates. At some voltage, the two peaks merge and the electric field appears again more linear over the bulk.

The effect can be well modelled by only two traps, a donor and an acceptor, the energies of which are aligned in the silicon bandgap such, that they can well reproduce the double peak electric field. More on this is explained in the in chapter 11.

5.2.7 "TYPE INVERSION" IN TCT

The "type inversion" in sensors can be very well determined by TCT. If a bunch of sensors is irradiated to different fluences before and after type inversion happens, the inversion point can be very well reconstructed from CV measurements. The CV measurement of a single diode however fails to judge, if the diode is type-inverted or not. Here the Transient Current Technique can help. Before irradiation, the electric field is linearly decreasing over the bulk. Right after irradiation, the change of the slope of the electric field can be estimated from

Table 5.2: Classification of TCT pulse shapes according to the electric field in the sensor.

Pulse shape	n-bulk electrons, p-bulk holes		n-bulk holes, p-bulk electrons	
	Electric Field	Classification	Electric Field	Classification
		un-irradiated, irrad.		type-inv.
		type-inv.		un-irradiated, irrad.
		irrad.		type-inv.
		type-inv.		irrad.

the TCT. In principle, four cases can occur, taking into account the double peak electric field described in the section before.

Table 5.2 shows the different pulse shapes occuring in TCT measurements. Double peak electric field shapes only occur after irradiation. Depending on the charge carrier type and bulk doping, the pulse shows a single peak with an increasing or decreasing shoulder. These shapes can occur in irradiated devices, too.

If the pulse after irradiation shows the opposite slope compared to the pulse before irradiation, the electric is pulled towards the back side of the device and the device is called type-inverted.

6

IRRADIATION AND QUALIFICATION

6.1 Irradiation Facilities

Beginning with a short description of the irradiation facilities providing neutrons or protons, this chapter is dedicated to enlighten the techniques used to characterize irradiated silicon sensors.

6.1.1 NEUTRON REACTOR IN LJUBLJANA

Neutron irradiations have been performed at the TRIGA Mark II reactor [TRI] at the Jozef Stefan Institute in Ljubljana, Slovenia. It is a light-water reactor fuelled by solid elemts with a maximum power of 250 kW. Several tubes in the core can be easily accessed for irradiation purposes. For irradiations the reactor power can be changed to achieve fluxes ranging from $2 \times 10^{9}\, ncm^{-2}s^{-1}$ up to $2 \times 10^{12} ncm^{-2}s^{-1}$. At full power, a total equivalent fluence of $10^{16} n_{eq} cm^{-2}$ is reached within one hour. A hardness factor has been obtained [Zon98] for the normalization of the neutron spectrum reaching up to energies of 10 MeV, which is $\kappa = 0.90 \pm 0.03$. The accuracy of the neutron fluence is given as 10% [Kra01].

6.1.2 KARLSRUHE CYCLOTRON

Irradiations with protons are done by the IEKP at the compact cyclotron of ZAG[1], a private company situated at the Campus North of KIT. The cyclotron accelerates negative hydrogen ions on a spiral path in a magnetic field. Having reached their maximum energy, the electrons are stripped on a foil and the remaining protons circle in the opposite direction and leave the cyclotron through the beamline.

After a distance of 50 cm after the beamline, a box with an entrance window for the protons made of Kapton is mounted on a moving table. In the box the structures to be irradiated can be mounted on an aluminum frame. A stacking of up to three frames after each other is possible to extensivly use the beam on the one hand, but not to create too much damage in the structures on the other hand because of the energy loss of the protons in the previous frames. The box is cooled by nitrogen with a temperature of -30 °C, necessary to prevent the structures from annealing during the irradiation.

The proton beam coming from the beam line is widened and has a diameter of about 9 mm. However the beam cannot fully fill the irradiation frame with the dimensions 44 cm×17 cm. Hence the box with the mounted frames is moved continuously in the x-direction and gradually vertically perpendicular to the beam for a homogenous irradiation.

The cyclotron offers protons with an energy of 23 MeV and usually a beam current of about 1.5 µA. The fluence is geometrically calculated (given in [Die03]) and can be converted into an equivalent fluence using a hardness factor (see section 4.2) of $\kappa = 2$.

$$F_{n_{eq}} = n \times \frac{I_{beam}}{e \times v \times \Delta z} \times \kappa \tag{6.1}$$

1 Zyklotron AG, http://www.zyklotron-ag.de

n is the number of scans in the x-direction, I_{beam} the beam current, ν the velocity of the moving box and Δz the vertical stepwidth. To verify the estimated fluence, nickel foils are placed behind the structures. After the irradiation, the foils can be used for dosimetry. Nickel irradiated with protons (^{58}Ni) is transformed into (^{57}Ni), which decays with a half life period of about 36 h, radiating off a photon for detection. The uncertainty of the irradiation at the cyclotron is higher compared to the reactor neutron irradiation and estimated to be lower than 20%.

6.2 Qualification Infrastructure

6.2.1 Probe Station

The two probe stations at IEKP are self-build semi-automatic probe stations, providing measurement equipment and techniques also used in semiconductor industries. In 2008, the second probe station was refurbished: the equipment of the other probe station was cloned, a new isolation and shielding box was constructed [Erf09] and both stations were equipped with a cold chuck, enabling the measurements down to -20 °C, which is in the temperature range of the future application of the samples [Hof13].

Several devices, stored in racks next to each probe station, provide the basic features needed for the measurements like IV, CV and strip measurements described in chapter 5:

- high voltage up to 1000V,
- current measurement in the range of 1 pA up to 1 mA,
- an additional current measurement in one of the stations,
- capacitance measurements with frequencies between 20 Hz and 1 MHz
- an isobox, decoupling the high voltage from the LCR-meter,
- a low voltage supply up to 100 V,
- relais switching matrices to autmatically switch between measurement configurations,
- a 760 W power supply for the peltier elements cooling the chuck
- and a temperature measurement card, reading out four Pt-1000 attached to cold chuck.

A list of devices and specifications can be found in appendix C.

Silicon samples up to the size of a 6”-wafer can be placed on the chuck, fixated by small vacuum holes in the chuck. Up to five needles at the same time can be placed on the silicon sample with the help of a microscope and camera. The shielding box can be flooded with dry air to prevent condensation. A separation made of plexi glass with openings for the hands enables the handling of the needles even at low temperatures. The front door finally closes the station for a dark measurement. The full system can be seen in picture 6.1.

A software written in LabView runs all devices needed for the measurements, controls the temperature of the cold chuck and records the measurement data. Predefined sets of measurements according to the measurement sample are available. All measurement data is additionally stored in a database on the server at the IEKP.

6.2.2 Strip Sensor Readout System (ALiBaVa)

There are two strip sensor readout systems at the IEKP, making use of the ALiBaVa[2] system [MH10]. They are almost identical, except for a laser source and movable tables in the more complex system, which is described here.

2 **A Li**verpool **Ba**rcelona **Va**lencia readout system

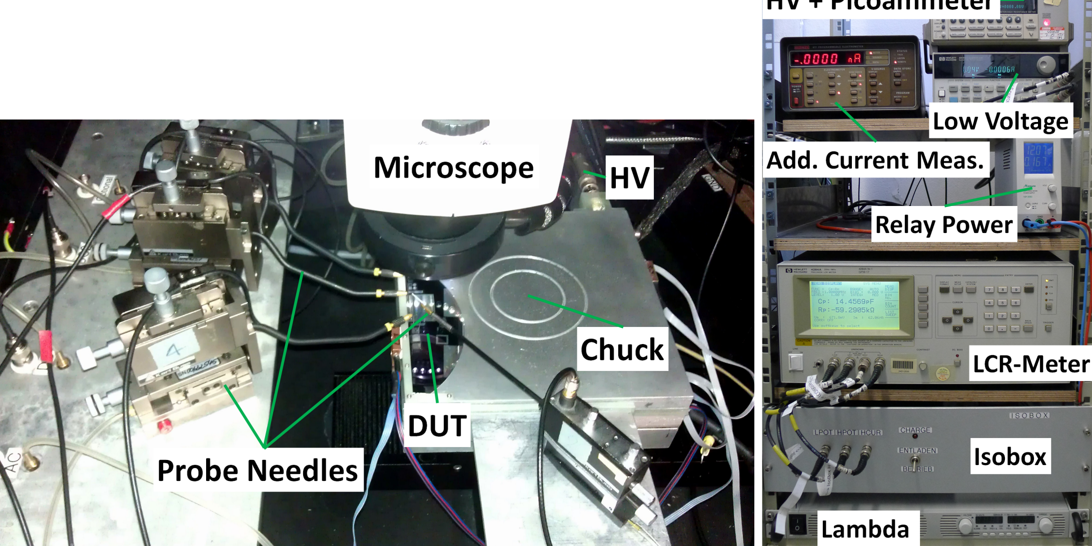

Figure 6.1: The probe station at IEKP:
Sensors and diodes can be measured on a cold chuck down to -20°C. Micrometer needles contact the structures on the surface. A microscope and camera can help placing the needles. The equipment for the diversity of possible measurements is placed in a rack next to the isolation box.

The station was first set up by Pfister [Pfi10] and recalibrated by Frech [Fre12]. Picture 6.2 shows the current setup: the ALiBaVa daughterboard, on which the sensor is hosted and bonded, is mounted on a cooling bridge. A X-Y-Z stage can be used to position the ^{90}Sr source or the laser optics over the sensor. If the source is used, the electrons can penetrate the thin circuit board, the sensor is fixed to, and move through a hole in the cooling bridge to be detected in the scintillator with attached photomultiplier.

The high voltage is provided by an ISEG power supply with a maximum current of 2 mA at 2000 V. The high voltage of the powersupply is filtered by a lowpass filter on the daughterboard. Separate connectors for high voltage and ground allow for IV and CV measurements directly in the system.

The daughterboard is connected to the ALiBaVa motherboard with a flat band cable. The trigger coming from the scintillator is processed on the motherboard and the signals from the beetle chips are read out and sent to the PC via USB.

The cooling bridge is able to cool down to -30 °C and heat up to 80 °C for annealing with two peltier elements. The peltiers are pre-cooled with water. The power is served by a `Lambda ZUP 20-10`. The temperature on the bridge and on the daughterboard directly is measured by Pt-1000, which are connected to the IEKP temperature board, which also controls the polarity of the applied voltage of the peltiers.

The whole system is placed in a box to ensure a dark and dry environment for the measurements.

The analysis is done offline with the help of the ALiBaVa anlysis framework. Usually, a 5σ cut on the signal to noise ratio for the seed strip and a 2 σ cut on the signal to noise ratio of the neighbouring strips is applied to find clusters. A Landau-Gaußfunction is fitted to the signal distribution and the most probable value in ADCs is used as the "signal". A calibration depending on chip temperature and beetle chip number can be used to convert the ADC values into an electron signal. The software now also provides a calibration run for this purpose.

The results are finally stored in the IEKP database.

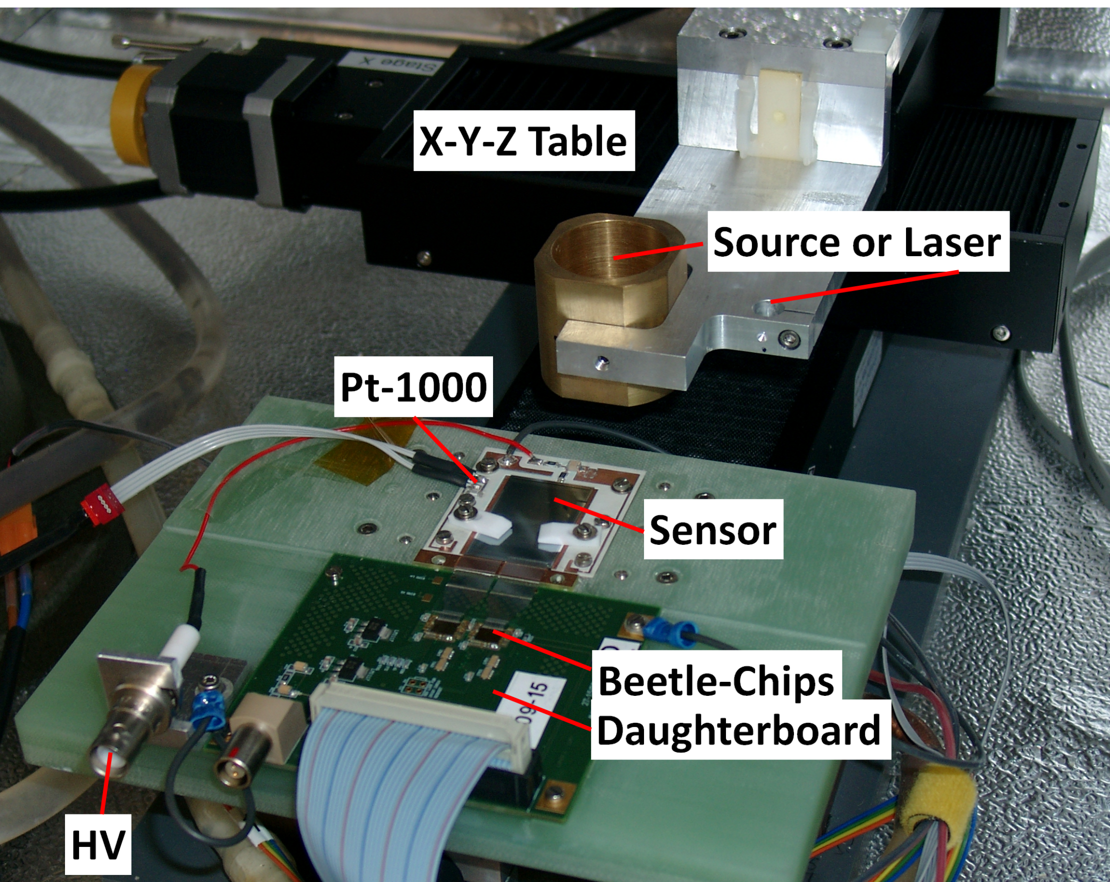

Figure 6.2: Strip sensor readout system:
The system makes use of the ALiBaVa hardware and software. Signals in strip sensors, generated by a source or a laser can be read out and analyzed. The sensor can be cooled and heated for annealing.

6.2.3 THE PICOLASER SETUP

The Transient Current Technique has been performed successfully at the IEKP for some time now. However, the necessity to perform measurements in an environment like in the experiment later made it inevitable to set up a new system. In the course of setting up the new system with new components and some new equipment, changes in the measurement software have been conducted.

6.2.3.1 *Components and Hardware*

Figure 6.3 shows the base component of the picolaser setup. The device under test is mounted on a cold chuck, which has been desigend especially for this setup. It consists of a copper ground plate, which is cooled by water. A peltier element can cool or heat the decoupled top copper plate down to -30 °C or up to +80 °C for measurements and annealing. The top copper plate provides several screw holes to fix a box with the device under test to the plate in order to achieve a good thermal contact. Pt-1000 elements attached to the lower and upper copper plate can measure the pre-cooling temperature and the actual temperature near the mounted device. The peltier element can take up to 12 V and about 5 A from a `TDK Lambda ZUP 20-10`, the resulting 60 W can heat and cool the device quite quickly and keep it stable at ±0.5 K. The polarity of the applied voltage can be switched by the temperature readout card, which at the same time reads out the Pt-1000. From the measured resistance, the temperature readout

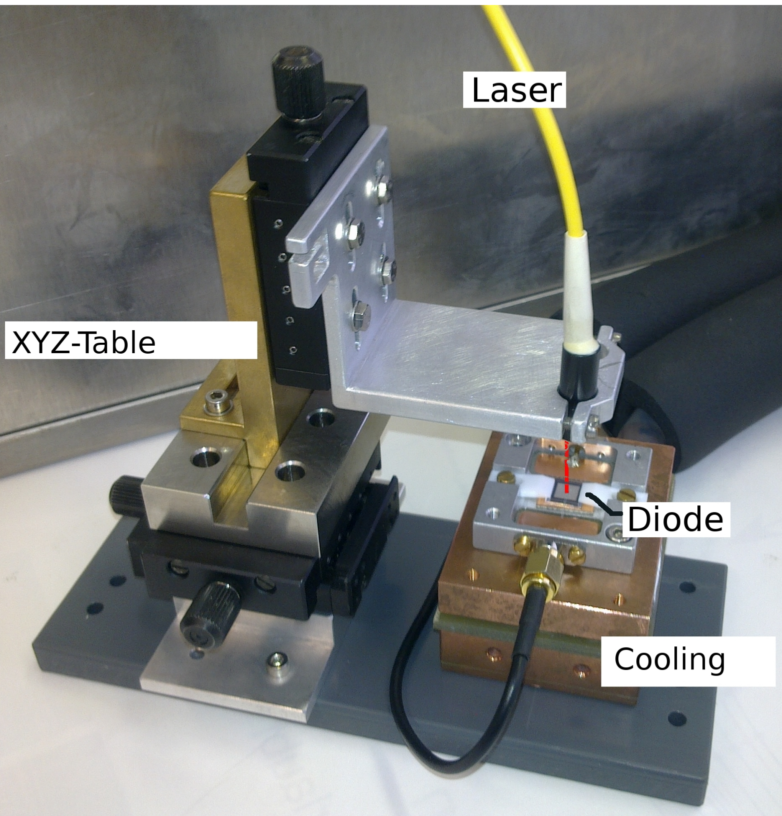

Figure 6.3: Cold chuck and laser mount at the Picolaser Setup:
The diode box is fixed to the cold chuck. The laser can be positioned over the device using the X-Y-Z stage. The peltier is pre-cooled by water.

board calculates the temperature and sends it to the readout PC. The pre-cooling temperature is usually set to -4 °C to ensure a wide temperature range operability.

Also visible in figure 6.3 is the laser mount. Two fiber heads with a focusing lens can be positioned over the device under test. The fibers can be switched quickly by sliding the laser mount to the right position and fixing it with screw. A X-Y-Z table can be used to fine-tune the position of the laser spot on the device. With the z-position, the focus of the laser can be adjusted. In a distance of 12 mm, the focusing lens has a minimum spot width of 10 µm. The two laser fibers are necessary, because there are three different laser wavelengths available for the setup: 679 nm, 880 nm and 1055 nm. The infrared laser and the 880 nm laser can share one fiber, whereas the red laser needs its own fiber because of the different absorption in the fibers.

The laser systems come from `Advanced Laser Diode Systems` and are named `PiLas (Pico-second Injection Laser)`. The fibers are connected to the laser head, at which the laser signal is generated. The laser driver is a separate box, at which the user can set all settings. In the application for the picolaser setup, the laser is self-triggered with a frequency, that can be set up between 1 Hz and 1 MHz. The output of the trigger is connected to the oscilloscope for synchronisation. At a tune of 65%, the FHWM of the gaussian-like shape in time is 33 ps with a jitter of only 3 ps [Adv04]. This very short pulse is the ideal prerequisite for TCT and CCE measurements. Because the short pulse is very intense, an attenuator is placed between the laser head and the fiber optics. Its attenuation is adjusted such, that the laser does not generate more charge per shot than 100 minimum-ionizing particles.

The box of the device under test can be seen in picture 6.4. It is designed for diodes and small sensors, larger boxes exist for larger sensors. The back side of the device is placed over a hole in the box, enabling laser measurements from the back side of the device. The box has two SMA connectors, which share the same ground. Bonding areas for each of the connector

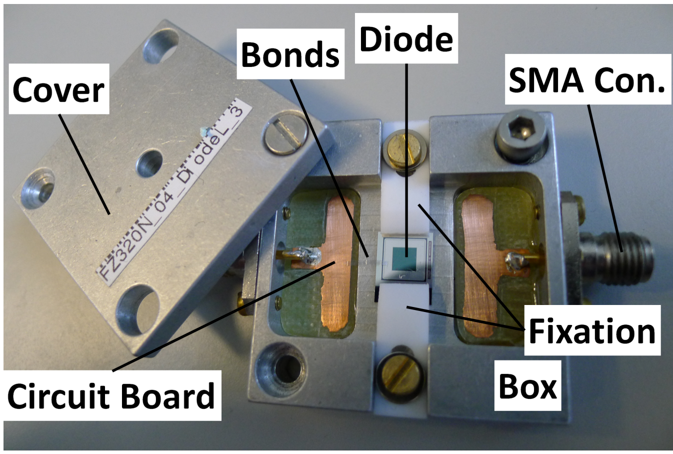

Figure 6.4: Diode handling and measurement box.
The diode is fixed by two clamps on the diode box. The electrical contact is made by bonding to the circuit board. The box can be attached to the cold chuck with two screws.

are available to bond the device, e.g. the diode's pad and its guard ring. The bonding area, a copper pcb, is optimized for a low stray capacitance. Two plastic clamps, which touch only the very outer part of the device, fix it in the box. A cover protects the whole box and allows turning it to the back side.

The high voltage for powering the device is provided by a Keithley 2410. It can provide a maximum current of 1 mA at 1100 V. The high voltage is fed through a Bias-T (`Picosecond PulseLabs 5531 HV`), which decouples the signal of the device from the high voltage. The signal line further connects to a 51 db `Miteq AM 1309` amplifier and ends at the `Tektronix TDS 5104B` oscilloscope, which records and visualizes the amplified signals. It has a resolution of 5 GS/s at a bandwidth of 1 GHz.

The oscilloscope, the Keithley 2410, the power supply for the peltier element and temperature card are connected to a PC for readout and controls.

The system including the cold chuck, the laser mount, the bias-T and the amplifier are placed in box, which shields the whole system against electronic noise. Its volume can be flushed with dry air to prevent condensation on the cold chuck and the device and ensures a dark environment during the measurement. The full picolaser setup can be seen in figure 6.5.

6.2.3.2 *Software*

The TCT DAQ software has already been used for measurements with the old TCT system [Ebe09] and has been revised to work with the new setup. It is written in LabView for easy visualisation and easy handling of the measurement devices. Minor changes have been implemented to use the Tektronix oscilloscope. Because of the peltier cooling, the software has been linked to the *Temperature Control* software of the IEKP.

6.2.4 DATA STORAGE AND ACCESS

6.2.4.1 *The IEKP Database*

The in-house database at the IEKP was already installed in 2008 [Ebe09] and stores measurement data from the measurement stations: the two probe stations, the two ALiBaVa stations and the Picolaser Setup. It is a MySQL database and has been optimized for the specific measurements done at the different setups.

For the probe stations, all IV, CV and strip measurements with the full data of the curves is stored. For the Picolaser Setup, also the full transient curves with the set of measurement

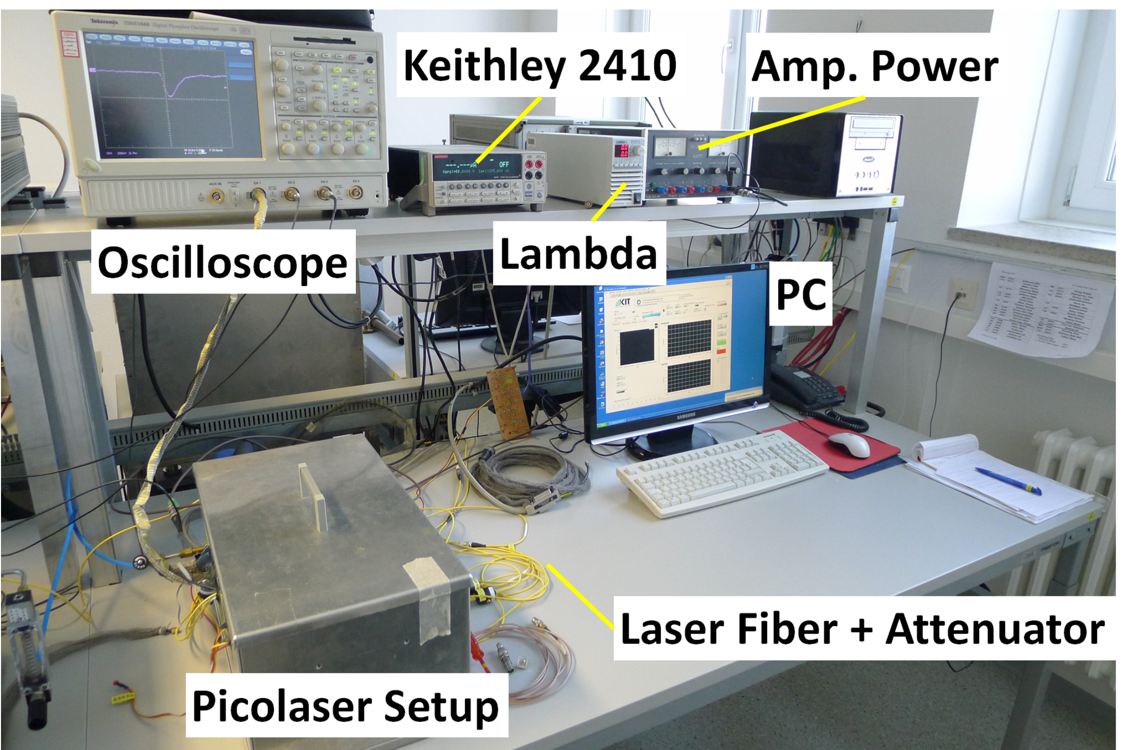

Figure 6.5: The Picolaser Setup with the different components at the IEKP.

parameters is saved. For the ALiBaVa system, only the measurement parameters and the analysis results are stored, as it would blow the database to save binary data with a size greater than 1 GB per run. The detailed structure of the database can be found in D.1.

6.2.4.2 *The CMS Upgrade Database*

Measurement data obtained in the scope of the HPK campaign has to be stored in a database accessible by all members of the campaign, too. Therefore, a framework, converting the data saved in the IEKP database to an XML format readable by the CMS upgrade database, has been developed. IV, CV and strip measurement data can be easily converted using the web interface of the IEKP database (see section 6.2.4.3) and selecting the corresponding measurements.

The CMS upgrade database is hosted at the university of Lyon [3].

6.2.4.3 *The Database Interfaces*

To provide an easy access to the database, a web interface for both databases has been developed during this work. In the course of growing tables and larger data volume during the campaign, phpMaker [TL] has been used to design the customized web interface. A personal (IEKP) or general login (CMS) is required to protect the database from unauthorized requests.

IEKP WEB INTERFACE [4]:
All tables available can be easily accessed and some parameters can be changed by authorized users. Joint tables combining measurements with irradiation and annealing data for a better visualization of the data can be found for probe station measurements and ALiBaVa measurements. In these views, the data can also be plotted (plot) using a self-written framework in root, exported to root-trees (along with plot), exported to text files

3 http://www.in2p3.fr
4 http://ikcms02.fzk.de/probe/phpMaker

(export) and to the CMS upgrade database format (XML). For the IEKP database, also an older version of the web interface is still available, providing some functionality for irradiations and structure handling not yet implemented in the new interface.

CMS UPGRADE DATABASE WEB INTERFACE [5]:
The web interface of the CMS upgrade database uses a direct connection to the database. Probe data like IV, CV and strip measurements can be quickly accessed, plotted and exported, also in combination with fluence and annealing time. In contrast to the web interface, the root framework, which is the same for the IEKP database, but has been extended to be able to handle this database, uses the so called "relay connection" to the CMS upgrade database. Additional information on irradiation, annealing, test centers taking part in the campaign and ongoing transfers can be read out.

BIGBROWSER [6]:
A tool provided by the university of Lyon to upload and access all data is the BigBrowser [Uni]. It is able to handle all actions provided by the database framework. Only to name some of the most important actions:

- registering sensors,
- viewing the inventory describing which sensor is stored at each institute,
- generating and viewing running transports of sensors between the institutes,
- viewing all table descriptions,
- uploading data,
- flagging data as *valid* or *notvalid*,
- marking destroyed sensors,
- generating and saving SQL queries.

The BigBrowser is therefore a good tool to administrate sensors and data from the institutes. However the web interface mentioned above provides more options for visualization and export of desired data.

6.2.4.4 *Root Framework for Databases*

During this work, quite some effort has been devoted to set up a framework, which provides easy access to the stored data. The framework is written in C++ with libraries mainly included from ROOT[7] [Roo]. First, the demands within in the community have been settled: exporting data to local files, visualize data and converting data between the local database and XML required by the CMS upgrade database.

The framework is held very modular, so that it can be easily expanded or changed, if one of the components is altered. To access data, queries are provided for both databases. The data can then be stored in a ROOT-Tree for local data handling. For the web interface, the data can be plotted with several options. The axes, heading, layout and legend are created automatically. Local data can be converted to XML, providing the measurements needed for an upload to the CMS upgrade database. Local experiments like the ALiBaVa stations and probe stations can use the framework to write their data to the database.

The framework is well structured into the different parts mentioned above. The details of the programming are not given here but can be read in appendix E.

5 http://ikcms02.fzk.de/probe/lyon2
6 https://lyonsvn.in2p3.fr/constructiondb/wiki/Download
7 http://root.cern.ch

7

SIMULATION FRAMEWORK

7.1 Synopsys Sentaurus TCAD

Sentaurus TCAD is a commercial simulation package offered by Synopsys [Syn]. It is designed to simulate semiconductor technology for various applications, not necessarily for silicon sensors in high energy physics. There are plenty of options available to design silicon devices and many models to simulate silicon sensors under operation conditions. This includes a basic analysis of the leakage current, an AC small signal analysis and a transient analysis for the time evolution of the signals. Changes in the parameters of certain models are made to describe silicon sensors; they are introduced during this work.

An overview of the basic commands to build and simulate a silicon sensor is given in the next sections. Because most papers do not describe the models used very well, some time is spent to state, which models have been used in the simulation in this work and how they work. In addition to that, the source code of a device design and a simulation command file is given. Furthermore, the implementation of radiation damage is described in detail. That is of importance in the chapters dealing with radiation damage later on.

7.1.1 The workflow

The use of the simulation package is quite easy. The bookkeeping tool to run simulations and handle the results is Sentaurus Workbench `swb`. Several tools can be run in a chain to generate the simulation device, simulate and analyze the result. The tools are named Sentaurus Device Editor `sde`, Sentaurus Device `sdevice` and `Inspect` or `svisual` accordingly. Input files are needed to set things up: a device file (section A.1), a parameter file (section 7.1.3.1), a simulation file (section 7.1.4) and an analysis file (section 7.1.5).

Parameters, which are not fixed in the files can be varied in the workbench directly. Variables enclosed by @, e.g. @temperature@, can be put in the files instead of the values. The values are then added dynamically during the operation of Sentaurus Workbench. This way, a large variation of parameters can be achieved. The different files needed are subject to explanation below.

7.1.2 Modeling of devices

In a first step, the silicon devices have to be modeled. In a second step before the simulation, a mesh is generated. The simulation will then solve the selected equations for each of these points on this grid.

In principle, there are two types of simulation devices, which can be generated: 2d or 3d models. 2d models have the decisive advantage, that they need much less mesh points and therefore the simulation needs acceptable computing time and memory. Usually all properties can be extended in the third dimension virtually by setting the corresponding parameter in the simulation command file. 3d models on the other hand model the reality but they need a huge amount of mesh points, comuting time and memory to be performed. If chosen carefully, symmetries can be exploited to accelerate the simulation of 2d and 3d devices.

The design of a device starts with simple geometries, e.g. the silicon, the aluminum electrodes and the silicon dioxide or silicon nitride. More complicated structures like the strips in a strip sensor are added to other regions or cut out of those. After the regions are defined, the doping of the silicon is set. Beside the constant doping concentration in the bulk, doping profiles can be set with the shape of a gaussian or an error function.

After all parts are in place, contacts can be applied to surfaces or defined regions. These are used to apply external voltage and calculate the current flow through them. Before the mesh is finally generated, regions of interest can be defined, in which the mesh points are narrowed down, e.g. in regions with a large change in the doping concentration.

7.1.3 MODELS AND PARAMETERS USED IN THE SIMULATION

A very important point looking at simulations is the choice of simulation parameters and models. If the parameters and models are not completely given, the simulation is a blackbox, which can simulate anything. The next sections therefore lists the parameters in the simulation, which have been changed compared to the default ones and enlight, which models have been used and why. This should enable further researchers to reproduce any of the results discussed in the later chapters.

7.1.3.1 *Parameters*

Synopsys Sentaurus TCAD uses a set of internally defined parameters for each material. Since this work is dealing with mainly silicon sensors, other materials parameters like SiO2 or aluminum have not been changed. For silicon, the parameters can be changed after the program is forced to write the parameter file for silicon. Usually this file is named `models.par` or, if a parameter is changed in Sentaurus Workbench, `sdevice.par`. Most of the parameters are left untouched. Modified parameters are listed in table 7.1 and explained here:

PERMITTIVITY ϵ_r: The default value in Sentaurus TCAD is $\epsilon_r = 11.7$ [Syn12]. On Wikipedia, almost the same value is found: $\epsilon_r = 11.68$. However, there is no citation given and the value is not considered. In the database of the Ioffe Institute of the University of St. Petersburg, which bases on the findings of Levinstein, Rumyantsev and Shur [LRS96], also $\epsilon_r = 11.7$ [Iof] is found. Measurements by Krupka et al. [K+06] seem to prefer this value.

Looking at the values given by semiconductor industries producing wafers however, Siliconfareast [Sila] and Virginia Semiconductors [Vir02] state a higher value with $\epsilon_r = 11.9$.

The default value ($\epsilon_r = 11.7$) is used in this work.

ELECTRON AFFINITY χ_0: The default value from Synopsys Sentaurus as well as the values from the semiconductor industries is $\chi_0 = 4.05\,eV$ [Syn12][Sila][Vir02]. This value is used.

BANDGAP ENERGY E_g: Synopsys Sentaurus uses $E_g = 1.12\,eV$ as the default value [Syn12]. This can be found also in the Ioffe database [Iof] and several books on semiconductors, e.g. [Dan97].

GENERATION AND RECOMBINATION TIMES: The default values used by Synopsys Sentaurus for the generation and recombination times for electrons τ_e and holes τ_h are very low. During this work it is shown (see section 8.1.3), that they have to be increased to meet the requirements of very clean silicon material. The values given in table 7.1 are just a lower bound.

PERMITTIVITY OF SILICON DIOXIDE AND SILICON NITRIDE: The permittivity of silicon dioxide and silicon nitride used in this work is not changed from the default value [Syn12] of

$$\epsilon_r(SiO_2) = 3.9$$

Table 7.1: Default parameters used in the simulation

Parameter	Used value
ϵ_r	11.7
E_g	1.12 eV
χ_0	4.05 eV
τ_e	$> 10^{-3}$ s
τ_h	$> 10^{-3}$ s

$$\epsilon_r(Si_3N_4) = 7.5$$

These values are also given by [Viro2] and [Sila].

7.1.3.2 *Models*

The models, which are used in the simulation are stated in the `Physics` section of the simulation command file. Options used in this work are given below. If not written otherwise, values and description are after [Syn12].

First of all, the calculation of the fermi level is very important for the simulation of silicon particle detectors. It is activated with the option

```
Fermi
```

It calculates the electron and hole densities correctly according to Fermi-Dirac statistics rather than from Boltzmann statistics.

Several mobility models for the charge carriers are available, which can be applied in a certain parameter range. The following two options are used in this work, preferably the first one:

1. The high-Field saturation model in combination with Philips unified mobility model or
2. the high-field saturation model together with doping dependent carrier mobilities and the carrier-carrier scattering model by Conwell and Weisskopf.

The implementation in the simulation file is found in appendix A.2.1.

HIGH-FIELD SATURATION: High-field saturation is one of the most important models for silicon particle detectors. Because they are quite thin and operate at high voltage, the electric field in the sensor can be very high. Hence, the charge carriers can run into a saturation mobility at high voltages. This is described by the Canali model [CMMO75]

$$\mu(F) = \frac{(\alpha+1)\mu_{low}}{\alpha + \left[1 + \left(\frac{(\alpha+1)\mu_{low}F_{high}}{v_{sat}}\right)^{\beta}\right]^{1/\beta}} \tag{7.1}$$

with the temperature dependent exponent

$$\beta = \beta_0 \left(\frac{T}{300\,K}\right)^{\beta_{exp}} \tag{7.2}$$

The parameter for β_0, β_{exp} and α are given in table 7.2 for electrons and holes respectively.

Table 7.2: Default and used parameters for the Canali model

Parameter	Electrons	Holes
β_0	1.109	1.213
β_{exp}	0.66	0.17
α	0	0

PHILIPS UNIFIED MOBILITY MODEL: Proposed by Klaassen [Kla92], this model unifies the description of majority and minority carriers. It includes temperature dependent mobility, electron-hole scattering, screening and clustering of impurities. Arsenic and Phosphorus behave differently as doping, so it is stated explicitly. Two calibrations for this model are available, Klaassen and Meyer. The Klaassen parameters are used (see [Syn12] for exact parameters).

If the unified model is not used, other options have to be activated for the simulation instead.

DOPING DEPENDENCE: The mobility of the charge carriers is different depending on the doping of the silicon. If not the unified model above is used, one has to account for the different mobility. Synopsys Sentaurus uses the Masetti model [MSS83] as default. The coefficients can be found in the manual [Syn12].

For typical doping concentrations in the bulk of $c = 3 \times 10^{12}\,\mathrm{cm}^{-3}$, the models only differ marginally and are usually only calibrated for higher doping concentrations around $10^{16}\,\mathrm{cm}^{-3}$. For the implants at the frontside or backside, which have a doping of around $10^{19}\,\mathrm{cm}^{-3}$, it can play a role. This however is not the most interesting region in a silicon particle detector, because it is only there to provide a good conductance to the electrode.

CARRIER-CARRIER SCATTERING: Carrier-carrier scattering has to be taken into account for high densities of charge carriers. It can influence the simulation when a lot of charge carriers are generated due to a particle or by impact ionization. The default model is the Conwell-Weisskopf model. Formulas and values are in [Syn12].

A Word on Mobility Degradation at Interfaces:
In the earlier simulations of this work, the statement

```
Enormal
```

can be found in the `Mobility` section. This statement activates the mobility degradation at interfaces. In later simulations, the option was not used any more.

There are two important points to consider:

1. Mobility degradation appears only in layers very close to the surface of another material. Hence the generated mesh should take this into account. A vertical spacing smaller than 0.1 nm is desirable. Because the simulation takes a long time to finish with such a small spacing between the mesh points, one should consider, if it's worth the effort.

2. Since the main part of this work is dealing with signals from the bulk and bulk radiation damage, the mobility degradation at the interface should be negligible. Other effects like surface recombination rates may play a larger role.

RECOMBINATION MODELS: A second part deals with the generation and recombination mechanisms. The Shockley-Read-Hall recombination is used for the description of the generation and recombination of current. The code of the recombination section in the simulation file is listed in appendix A.2.2.

Table 7.3: Default and used parameters of the temperature dependent lifetime.

Parameter	Value
T_α	-3/2
C	2.55

The Shockley-Read-Hall recombination when using Fermi statistics reads:

$$R = \frac{np - \gamma_n \gamma_p n_{i,eff}^2}{\tau_p(n + \gamma_n n_{i,eff}) + \tau_n(p + \gamma_p n_{i,eff})} \tag{7.3}$$

n and p is the electron and hole density. γ is defined as

$$\gamma_n = \frac{n}{N_C} \times e^{-\frac{E_{F,n}-E_C}{kT}} \qquad \gamma_p = \frac{p}{N_V} \times e^{-\frac{E_V-E_{F,n}}{kT}} \tag{7.4}$$

with the occupation number of the valence and conductance band N_V and N_C and the energies of the valence and conductance band E_V and E_C. E_F is the Fermi level.

Of course there are some options available, how the current is generated with different doping concentrations (`DopingDependence`) or when the temperature is changing (`TempDependence`). The doping dependence is modelled by the Scharfetter relation. Since it only influences the recombination in highly doped regions and none of the parameter is changed, the formula and values can be read in [Syn12]. For low doping concentrations in the bulk the maximum lifetime of the charge carriers τ_e and τ_h is used.

To get a correct temperature dependet current in the semiconductor, the lifetimes are modelled to follow either a power law

$$\tau(T) = \tau(300K) \times \left(\frac{T}{300K}\right)^{T_\alpha} \tag{7.5}$$

or an exponential function of the temperature

$$\tau(T) = \tau(300K) \times e^{C(\frac{T}{300K}-1)} \tag{7.6}$$

The parameters for the two equations are given in table 7.3. The values are valid for electron and holes. Both equations describe nearly the same dependence on temperature in the interesting temperature range between 250 K and 300 K. The choice is to use the power law, also for a better comparison between Synopsys Sentaurus and Silvaco Atlas (see section 7.2).

SRH FIELD ENHANCEMENT: Near the electric silicon breakdown field of $E \approx 3 \times 10^5$ V/m, defect-assisted tunneling must not be neglected. This happens "before band-to-band tunneling or avalanche generation" [Syn12]. It can lead to a different behaviour in the total leakage current of the device. The `Hurkx` model has proven to be quite successful simulating silicon particle detectors, therefore this model was chosen in this work. It is enabled by the keyword `Lifetime=Hurkx` in the `ElectricField` statement.

AUGER RECOMBINATION: The `Auger` recombination is not very important for the simulation of silicon particle detectors, because it is only visible for high carrier densities. However it doesn't increase computing time much and is activated for completeness.

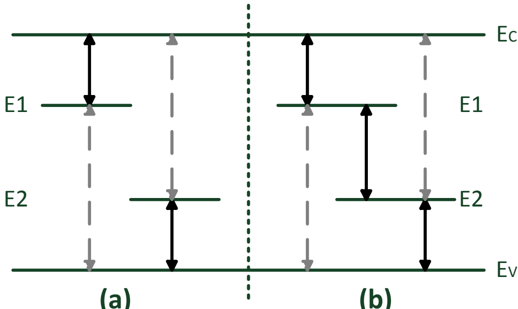

Figure 7.1: Principle of the coupled defect levels: Exchange of charge carriers, electrons and holes, is not only possible between one defect level (E1, E2) and the valence or conductance band, E_V and E_C, (a), but also between the defects themselves (b).

AVALANCHE GENERATION: When it comes to high electric field and charge carriers are drifting very fast in the silicon device, they can hit other charge carriers and create an avalanche. Intrinsically, this is not considered by the Shockley-Read-Hall recombination. Avalanche generation models have to be activated for a simulation of that process (`eAvalanche(vanOverstraeten Eparallel)`). In this case, the van Overstraeten - de Man model is used. The formula can be found in [Syn12].

This model starts at low fields of $1.75 \times 10^5\,V/cm$ and evolves into the high field range of $6 \times 10^5\,V/cm$. The driving force to start avalanche generation is computed as the component of the electric field parallel to the current (`Eparallel`).

Other models and options for driving forces are possible. It has not been studied in detail, how different models affect avalanche generation in different ways, since only the possibility for the generation should not be missing. Most of the simulations are dealing with electric fields way below the breakdown field strength.

COUPLED DEFECT LEVELS: Coupled defect levels (`CDL`) is an option for additional generation of current when traps are introduced in the simulation. So this option only influences the simulation when radiation damage plays a role. The trap levels in the forbidden bandgap between valence and conduction band can now exchange charge carriers between them and not only between the trap and the valence or conductance band. This is expected to happen for quite high concentrations of defects, when the defects are closer together for an exchange of charge carriers. Figure 7.1 illustrates the exchange of charge carriers between traps and the semiconductor bands and the exchange of charge carriers between traps.

There is one caveat: in the parameter file, there is a section dedicated to parameters for coupled defect levels. Since there is a lifetime given and that lifetime is the same as the default value of SRH lifetime for electron and holes, the statment `CDL` generates a lot of current in un-irradiated devices. It should not be used for the simulation of un-irradiated devices.

7.1.4 THE SIMULATION COMMAND FILE

The simulation command file, usually `sdevice_des.cmd`, is the most important file for simulation. It contains all information, which models to use, which parameters to set and the simulation phase space. It is divided into several parts, which are quite self-explanatory.

The code of the simulation command file is found in appendix A.2. The following sections are explained in more detail there:

1. Electrode A.2.3,
2. File A.2.4,
3. Physics A.2.5,
4. Small signal analysis A.2.6,
5. System A.2.7,
6. Plot A.2.8,
7. Math A.2.9,
8. Solve A.2.10,
9. Optics A.2.11,
10. HeavyIon A.2.12
11. Transient A.2.13

7.1.5 ANALYSIS OF THE RESULTS

Simulations obviously create a lot of simulation results stored in different files. These files have to be analyzed, either automatically or by hand. The tools to view and analyze the results are called `Inspect` and `svisual` (or `tecplot` in previous versions than G 2012.06).

In Senauturus Workbench, these tools can be added to automatically extract results from the simulated files and the results are shown next to the corresponding simulation node. In this way, maximum values of electric fields or currents can be determined as well as integrals over the simulated curves.

7.1.5.1 *Inspect*

Inspect is used to create plots of the simulated data: Current – Voltage, Capacitance – Voltage, etc. The data can be exported to several file formats for the use in other visualization tools.

7.1.5.2 *svisual and tecplot*

These tools can be used to view the grid data on the simulation device, e.g. a 2d distribution of the electric field. Cuts along arbitrary axes can be made to view the 1d distribution of any of the saved parameters, which have been defined previously during the simulation. Figure 7.2 shows an example of a 2d doping concentration profile in a strip device with a cut along the y-axis in the middle of the strip.

7.1.6 SIMULATION OF RADIATION DAMAGE

The simulation of silicon particle detectors can be handled with all the instructions explained in the previous sections. One imortant part is still missing: the implementation of radiation damage in the silicon detector. Yet, the simulation cannot deal with real defects like an interstitial atom or vacancies. These defects however create energy levels in the silicon bandgap, which can be built in the simulation. For sensors, which have not been irradiated to high fluences, this approach holds. For higher fluences, defects tend to form clusters. For clusters, it is not easy to specify on exact energy, the defects create. There can be several energy levels or energy levels, which are smeared out. The approach shown here is only an effective simulation, taking into account the most probable values but keeping the system as slim as possible.

An additional effect, that is important for the simulation of silicon strip sensors, is the oxide charge concentration. After irradiation the oxide gets charged positively and attracts electrons at the interface between silicon and silicon dioxide.

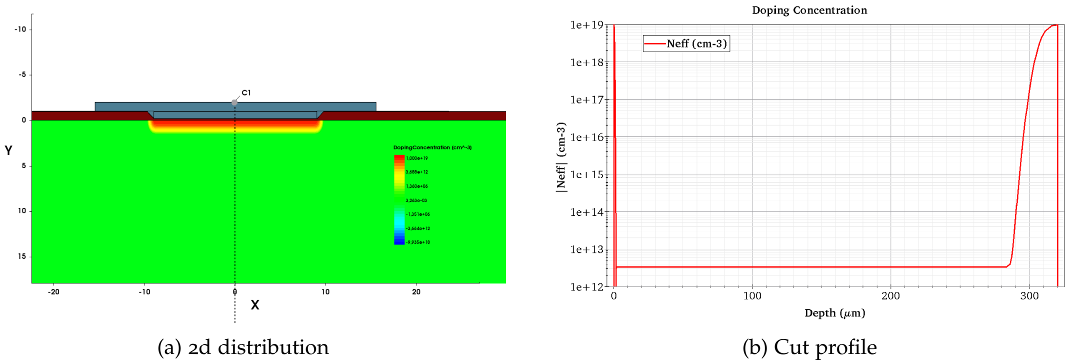

(a) 2d distribution

(b) Cut profile

Figure 7.2: 2d strip sensor showing the doping concentration in the device (a) and a cut through the device showing the doping profile along the y-axis in the middle of the strip.

7.1.6.1 *Implementation of Traps*

Defects in the silicon are called `Traps` in Synopsys Sentaurus. The `Traps` section requires an extra `Physics` section only valid for silicon, in which the traps occur only.

One trap is specified by six parameters:

- donor or acceptor trap,
- the energy level,
- where the energy level is calculated from,
- the concentration of the traps in the bulk,
- electron cross section and
- hole cross section.

The following example shows a trap typically used for the effective 2-defect radiation model (section 11).

```
Physics (material = "Silicon")
{
   Traps
   (
      (
         Donor Level
         fromValBand
         Conc = 1e14
         EnergyMid = 0.48
         eXsection = 1e-14
         hXsection = 1e-14
      )
   )
}
```

7.1.6.2 *Implementation of Interface Charge*

The oxide charge is, for most simulations in this work, not directly implemented as oxide charge as such, but as a projected charge concentration at the interface between silicon and silicon dioxide. Hence the concentration is given per surface area (cm^{-2}).

The oxide/interface charge again requires a separate `Physics` section, only valid for the interface:

```
Physics (MaterialInterface = "Silicon/SiO2")
{
   Traps (FixedCharge Conc = 1e12 )
}
```

7.1.6.3 *Parameters and Models related to Traps*

If Traps come into play, there is an exchange of charge carriers between the traps and the valence or conductance band. If a stationary state is assumend, the occupation of a trap is calculated from the electron capture rate c for an empty trap and the electron emission rate e for a filled trap. In the description of the traps, only the capture rate c or in other words the trap cross section of electrons and holes. The electron occupation f is calculated by equation 7.7. The same is true for the capture and emission of holes.

$$f = \frac{\sum c_i}{\sum(c_i + e_i)} \tag{7.7}$$

Note, that the capture process from the valence band is a different process than the capture process from the conductance band as has to be considered in the sum running over all processes.

The Shockley-Read-Hall recombination rate with traps then reads

$$R = \frac{N_0 v_{th}^n v_{th}^p \sigma_n \sigma_p (np - n_{i,eff}^2)}{v_{th}^n \sigma_n \left(n + n_{i,eff} e^{(E_{trap}/kT)}\right) + v_{th}^p \sigma_p \left(p + n_{i,eff} e^{(-E_{trap}/kT)}\right)} \tag{7.8}$$

where N_0 is the concentration of the traps. $v_{th}^{n,p}$ is the thermal velocity of electrons (n) or holes (p).

The "principle of detailed balance" relates capture and emission rates of a trap. The trap is in equilibrium with the reservoir in a stationary process.

$$e = c \times e^{\left(\frac{E_{trap} - E_F}{kT}\right)} \tag{7.9}$$

E is the energy of the trap and E_F is the Fermi energy of the reservoir. Depending on the energy level of the trap, the trap is either quite filled near the reservoir or almost empty far away from the reservoir.

Going away from a stationary process, the occupation f of a trap changes in time.

$$\frac{\partial f}{\partial t} = \sum_i [(1-f)c_i - fe_i] \tag{7.10}$$

This becomes relevant for a transient simulation, when charge carriers of an induced signal can fill the traps along their way to the electrodes.

For a coupling between the traps, coupled defect levels CDL (described in section 7.1.3.2) can be switched on, to exchange charge carriers between the traps.

7.2 Comparison with Silvaco Atlas

Synopsys Sentaurus is not the only commercial simulation package, which offers a wide range of possibilities for the simulation of silicon devices. Silvaco [Silb] Atlas [Sil13] is a simulation package providing nearly the same features. The usage of both of the simulation packages throughout the community is the motivation for this comparison of the tools.

Of course, there are differences between the simulation packages. Although this work specializes in Synopsys Sentaurus, it is important to point out some of the differences between the

Table 7.4: Standard parameters for the bandgap model in Synopsys Sentaurus, equation 7.11.

Parameter	Value
α	4.73×10^{-4} eV/K
β	636 K
$E_G(0)$	1.1696 eV

packages. These differences can have a very large influence on the simulation results. In other words:

`The results obtained with the standard parameters of Synopsys Sentaurus are definitely different from the results with the standard parameter set of Silvaco Atlas.`

One has to choose carefully, which models to turn on and which parameters to use for a comparable result of the two packages. The following sections point out these differences, show how they influence the values used in the simulation and finally show the impact on the results.

7.2.1 BANDGAP

The first essential point is the silicon band gap at 300 K. There are different parameterizations for the bandgap depending on the temperature of the semiconductor. For Sentaurus [Syn12], the same formula as from the Ioffe database [Iof] is given.

$$E_g(T) = E_G(0) - \frac{\alpha T^2}{T + \beta} \tag{7.11}$$

The parameters for that equation are listed in table 7.4.

The bandgap for silicon at 300 K is respectively:

$$E_G^{Synopsys}(300\,K) = 1.12\,eV$$

In Silvaco Atlas, a slightly different formula is used with the same parameters as in table 7.4.

$$E_G^{Silvaco}(T) = E_G(300\,K) + \alpha \left[\frac{300^2}{300 + \beta} - \frac{T^2}{T + \beta} \right] \tag{7.12}$$

However, this parameterization uses the bandgap energy at 300 K as a reference point and this value is set to

$$E_G^{Silvaco}(300\,K) = 1.08\,eV$$

If the bandgap energy in Silvaco Atlas is not raised, the calculated current is too high. For compatible results with Synopsys Sentaurus, the bandgap energy should be set to 1.12 eV.

7.2.1.1 *Electron Affinity*

Silvaco Atlas also uses a different electron affinity: $\chi_0 = 4.17\,eV$ [Sil13]. This is slightly above the values given in section 7.1.3.1. It may influence the generation of charge carriers by ionization.

7.2.2 SATURATION VELOCITY

In Silvaco Atlas, the same mobility parameterization as in Synopsys Sentaurus is used. Equation 7.1 is used with the same parameters listed in table 7.2, except that for Silvaco Atlas the parameter α is always set to zero.

In equation 7.1, the denominator is dependent on the saturation velocity. Yet, the saturation velocity is parameterized differently in the two simulation packages.

The saturation velocity v_{sat} in Synopsys Sentaurus reads:

$$v_{sat} = v_{sat,0} \left(\frac{300\,\mathrm{K}}{T} \right)^{v_{sat,exp}} \tag{7.13}$$

Different parameters for electrons and holes are used. They can be found in table 7.5.

Table 7.5: Default parameters for the saturation velocity parameterization used in Synopsys Sentaurus (equation 7.13).

Parameter	Electrons	Holes
$v_{sat,0}$	1.07×10^7 cm/s	8.37×10^6 cm/s
$V_{sat,exp}$	0.87	0.52

A different parameterization is used in Silvaco Atlas:

$$v_{sat} = \frac{\alpha}{1 + \theta \times e^{T/T_{nom}}} \tag{7.14}$$

The default parameters for equation 7.14 are declared in table 7.6. It is obvious, that the same parameters are used for electrons and holes. This results in the same saturation velocities for electrons and holes. This however is not observed by Jacoboni et al. [JCOQ77].

Table 7.6: Default parameters for the saturation velocity parameterization used in Silvaco Atlas (equation 7.14).

Parameter	Electrons	Holes
α	2.4×10^7 cm/s	2.4×10^7 cm/s
θ	0.8	0.8
T_{nom}	600 K	600 K

Figure 7.3 shows the comparison of the saturation used the different simulation packages. The saturation velocities for electrons and holes in Silvaco Atlas are the same and have a small slope over the temperature, whereas the saturation velocity in Synopsys Sentaurus is higher for electrons and lower for holes. The slope over the temperature of both charge carriers is larger compared to Silvaco Atlas. Deviations in the simulation are expected in the high-field regimes between the two simulation packages.

7.2.3 CHARGE CARRIER MOBILITY

The two simulation packages calculate a temperature dependent low-field mobility. This temperature dependent mobility is also used in equation 7.1. Although the parameterizations coincide, the default parameters deviate from each other.

The parameterization, valid for both simulators, is:

$$\mu_0 = \mu_L \left(\frac{T}{300\,\mathrm{K}} \right)^{-\gamma} \tag{7.15}$$

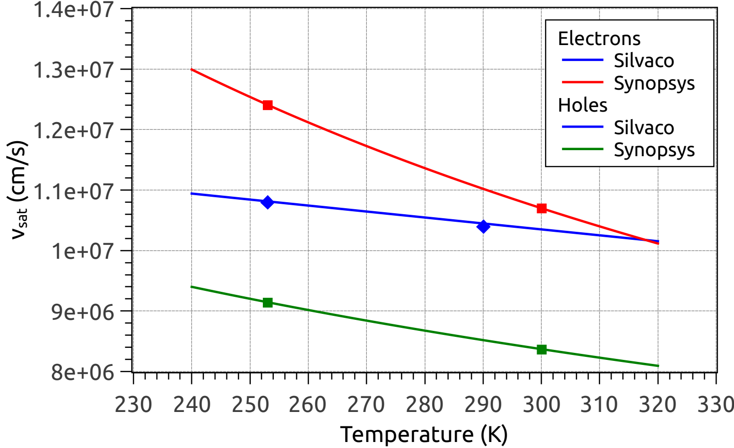

Figure 7.3: Saturation velocities for electrons and holes after the parameterization plotted over the temperature. Silvaco Atlas uses the same saturation velocities for electrons and holes with a small slope over the temperature. The saturation velocities of electrons and holes are very different for Synopsys Sentaurus and rise stronger towards lower temperatures.

The parameters for both simulators can be read in table 7.7.

Table 7.7: Default parameters for the low field mobility models.

	Synopsys Sentaurus		Silvaco Atlas	
Parameter	Electrons	Holes	Electrons	Holes
$\mu_L (cm^2/Vs)$	1417	470.5	1000	500
γ	2.5	2.2	1.5	1.5
Unified models				
$\mu_L (cm^2/Vs)$	1414	470.5	1417	470.5
γ	2.285	2.247	2.285	2.247

Looking at the default parameters, it is clear, that Silvaco Atlas' mobilities for electrons and holes lie closer together and are a rough approximation. In contrast to these number, Synopsys Sentaurus uses the measured values by Jacoboni et al. [JCOQ77]. Nevertheless, the model by Jacoboni et al. is quite old and may need some fine-tuning for very pure silicon used for silicon particle detectors.

When using the Philips unified model (Synopsys Sentaurus) or the Klaassen model (Silvaco Atlas), the two simulators use almost the same parameters, Synopsys Sentaurus has a slightly different tuning for the phosphorus doping, though.

7.2.4 IMPACT IONIZATION

Impact ionization has already been shortly described earlier. In Synopsys Sentaurus, there are several impact ionzation models available, one of them is the Overstraeten de Man-model. This model is also available in Silvaco Atlas, if the exponents of the Selberherr model are set to one.

The impact ionization rate α is written as

$$\alpha(E) = \gamma \times a \times e^{\left(-\frac{\gamma b}{E}\right)} \tag{7.16}$$

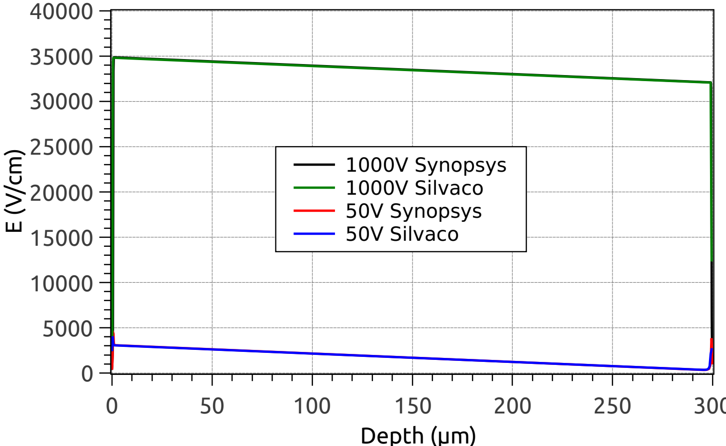

Figure 7.4: Electric field at 300 K for different voltages over the depth of the silicon sensor simulated with the two simulation packages. The difference is barely visible.

with

$$\gamma = \frac{\tanh\left(\frac{\hbar\omega}{2k \times 300}\right)}{\tanh\left(\frac{\hbar\omega}{2kT}\right)} \tag{7.17}$$

The factor $\hbar\omega = 0.063\,eV$ applies for silicon. Default parameters for this model valid for both simulators in this notation can be looked up in [Syn12].

The default impact ionization model in Silvaco Atlas however is not the van Overstraten-de Man model but the Selberherr model, which additionally models temperature dependent effects of the impact ionization rate. Unfortunately, this model is not available in Synopsys Sentaurus, though it has proven to be quite useful for the simlation of avalanche generation.

7.2.5 IMPACT ON THE SIMULATION RESULTS

The different models in the different simulation packages have an influence on the results. The effect of the different default parameters is shown figure 7.5 and figure 7.6, whereas there is negligible difference for the electric field plotted in figure 7.4.

The layout of a diode used in the simulation has not been introduced yet, nevertheless this section shows the impact of the models on a diode with the parameters listed in table 7.8.

As the electric field is calculated as a function of the doping of the device and no radiation damage has been included, the electric fields in the diode are very well in agreement with each other except for some minor meshing differences between the diode models in the two simulators.

In contrast to the electric field, figure 7.5 shows deviations of the mobility at low and high voltages because of the different mobility parameters in the simulation packages. The temperature was chosen to be 300 K for comparison. The electron mobility in Synopsys Sentaurus lies above the charge carrier mobilities for Silvaco Atlas and the hole mobility lies below with a larger slope over the temperature than the mobilities from Silvaco Atlas. At higher voltages, when the mobility is in the high-field regime, the difference becomes more pronounced.

This difference in the mobility is directly transferred to the charge carrier drift velocities seen in figure 7.6. In lower electric fields, the velocity for the same type of charge carrier is the same in both simulators. At higher electric fields, originating from a higher bias voltage, the velocities start to differ. The effect is stronger for the hole drift velocity, electron drift velocities still lie closer together.

Table 7.8: Parameters for the comparison of the simulation packages.

Parameter	Value
τ_e	10^{-4} s
τ_h	10^{-4} s
ϵ_r	11.7
T	300 K
N_{bulk}	$6 \times 10^{11}\,\text{cm}^{-3}$
$N_{junction}$	$10^{19}\,\text{cm}^{-3}$
Junction	Gauss, depth 1 μm
Device size	2d ($1 \times 300\,\mu\text{m}^2$)
Device type	$p^+ - n - n^+$
Voltage at n^+	50 V / 1000 V
areafactor	0

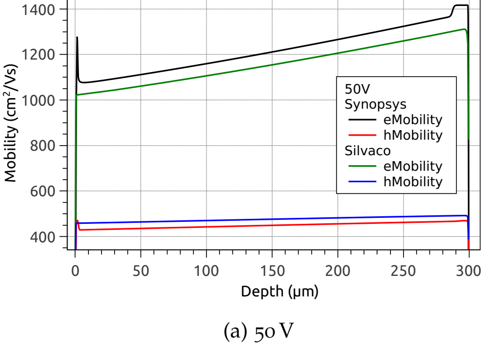

(a) 50 V

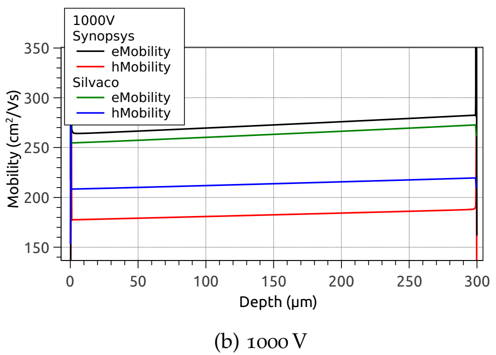

(b) 1000 V

Figure 7.5: Mobility for electrons and holes at 300 K and different voltages over the depth of the silicon sensor. The electron mobility is higher in Synopsys Sentaurus whereas the hole mobility is higher for Silvaco Atlas. This becomes more pronounced at higher voltages.

7.2.6 SUMMARY OF THE COMPARISON

The two simulation packages Synopsys Sentaurus and Silvaco Atlas offer a wide range of models to choose and parameters to set. For most of the models, the simulators can do the same things and just use some different default parameters.

For comparisons between simulation groups, the bandgap in Silvaco Atlas has to be increased to the bandgap used in Synopsys Sentaurus.

Most models explained above use the same formulas to calculate the results. The two simulation packages could be matched by changing the parameters in one or the other simulator to prove this. Because in this work Synopsys Sentaurus has been used exclusively, it has not been done yet.

Unfortunately, there are models, which use different formulas, and cannot be adapted easily to the other simulator. This complicates the comparison and a lot of effort had to be put in here. Hence, radiation models developed in Synopsys Sentaurus cannot be used in Silvaco Atlas with the same set of parameters.

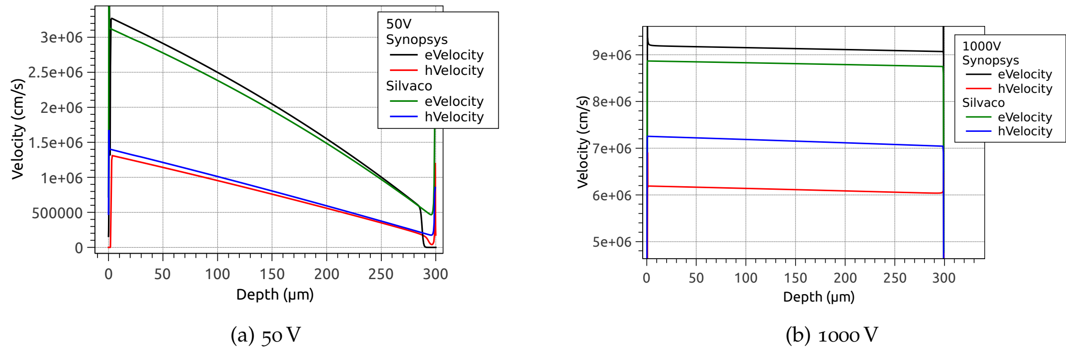

(a) 50 V

(b) 1000 V

Figure 7.6: Drift velocity for electrons and holes at 300 K and different voltages over the depth of the silicon sensor. The drift velocities start to differ at high electric fields and are thus more different at higher voltage. Due to the different mobility, the drift velocities for holes differ more than those for electrons.

Part III

STUDIES

8

ANALYSIS AND SIMULATION OF DEVICES

8.1 Performance of un-irradiated Diodes

All devices fabricated by HPK and labelled with FZ (see section 2.4.2) come with a reduction of the physical thickness of the wafer by deep diffusion. This has already been seen and discussed by Hoffmann [Hof13] and Junkes [Jun11]. There are two effects, which play a role in devices with deep diffusion compared to the ones with a standard backside processing: a shallow increase of the doping towards the backside, which leads to a non-saturating capacitance above full depletion, and additional leakage current in thinner senors, which can be attributed to process induced defects. For a correct description of these devices in the simulation, the doping profiles for each type have been simulated and adapted to measurements.

The complete range of diodes has been simulated except epitaxial material.

8.1.1 Simulation of diodes – diode layout

The diode is a very simple structure compared to silicon strip sensors. Because of the relatively large pad size compared to the surrounding structures, effects of the boundaries can be neglected for investigations of the performance of the diode. This is particularly true, if measurements on the diode have been performed with a connected guard ring.

For this reason, the layout in the simulation can be kept very simple. Thus, the smallest reasonable device has been used: a 2d device with a width of 1 µm. The device is totally homogeneous when cut at a certain depth. The most important quantities for the simulation like depletion voltage, volume generated current and signal generation are calculated very fast. For the comparison with a real diode, the device can be enlarged to a real-size device by just adding an areafactor to the simulation. Picture 8.1 visualizes the diode layout, that is used for these simulations. Under the frontside aluminum layer resides the silicon bulk, limited by the backside aluminum electrode. The doping profiles are discussed in detail in the next section.

For investigations of the boundary effects, a larger device is necessary. Here the influence of a connected guard ring on the depletion voltage can be investigated. Also, the lateral depletion plays a role for the volume generated current. Figure 8.2 shows the layout of a larger diode with pad, guard ring and surrounding structures.

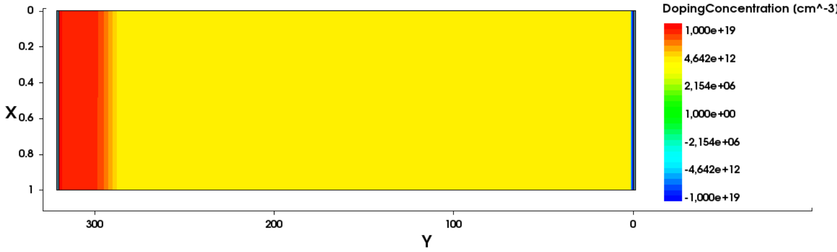

Figure 8.1: Simple 2d diode simulation structure (rotated) with a width of 1 µm. The frontside is at $Y = 0$ µm.

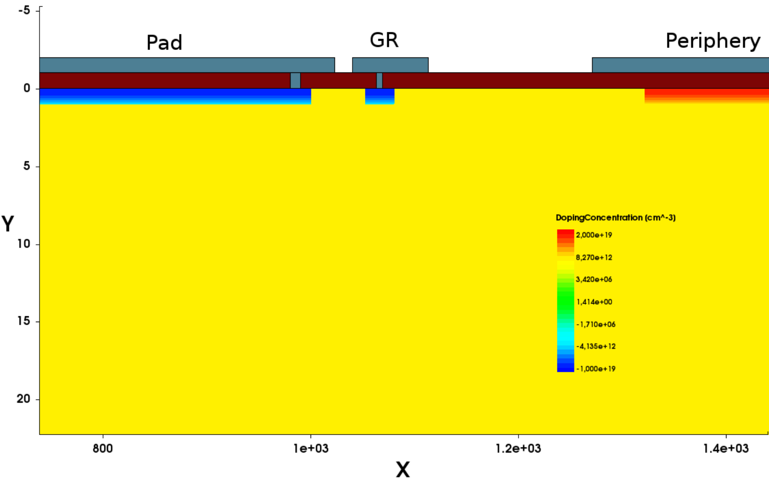

Figure 8.2: 2d diode simulation structure with pad, guard ring (GR) and periphery.

Table 8.1: Full depletion voltage of diodes before irradiation and profile description of the backside implant used for simulation.

Material	V_{fd} (V)	n_{bulk} (cm^{-3})	Erfdepth (μm)	Sympos (μm)
FZ320N	300 ± 5	3.0×10^{12}	31	17
FZ320P/Y	320 ± 5	3.4×10^{12}	33	11
FZ200N	100 ± 10	3.0×10^{12}	115	40
FZ200P/Y	90 ± 10	3.0×10^{12}	125	52
FZ120N	60 ± 10	4.5×10^{12}	198	65
FZ120P/Y	20 ± 10	1.5×10^{12}	215	100
MCz200N	160 ± 5	5.0×10^{12}	3	2
MCz200P/Y	90 ± 5	3.0×10^{12}	3	2
FTH200N	90 ± 5	3.0×10^{12}	4	2
FTH200P/Y	120 ± 5	3.8×10^{12}	4	2

8.1.2 FULL DEPLETION VOLTAGE AND DOPING PROFILE

The full depletion voltage (V_{fd}) of un-irradiated diodes is a function of the doping concentration of the bulk. It is determined using the measurement described in section 5.1.2. Table 8.1 lists the full depletion voltage of the different materials measured in the initial qualification and the corresponding bulk doping concentration, which has been crosschecked with the simulation. For the p-bulk diodes, the same wafers have been used, only the frontside processing differs between p-spray and p-stop. Thus, the same bulk doping concentration is found.

The diodes have been simulated with a gaussian doping profile at the front and a doping profile following an error function from the backside. The simulation can be tuned such, that the end capacitance and the slope of the capacitance matches the experimentally found values. The error function defining the doping profile from the back has to be adjusted such, that it penetrates into the bulk until it reaches the bulk doping concentration ("Erfdepth"). The slope of the error function doping profile can be varied by setting the inflection point ("Sympos"). The values for the various materials are also given in table 8.1.

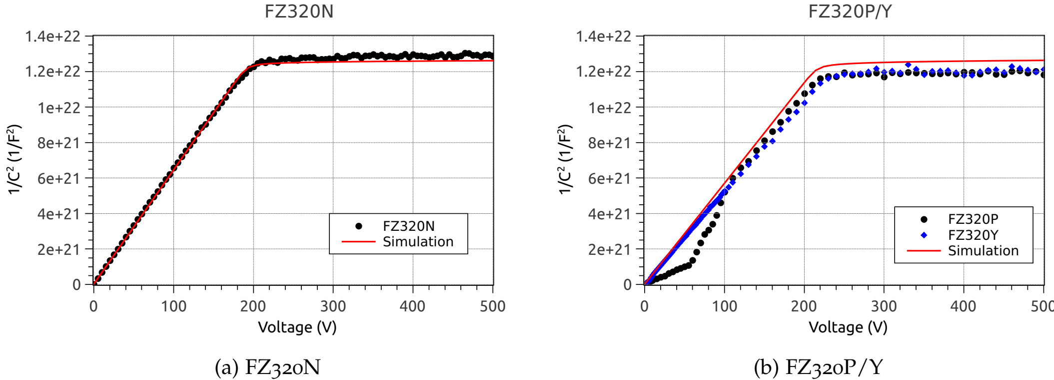

(a) FZ320N

(b) FZ320P/Y

Figure 8.3: Simulated and measured CV of FZ320N (a) FZ320P/Y (b).

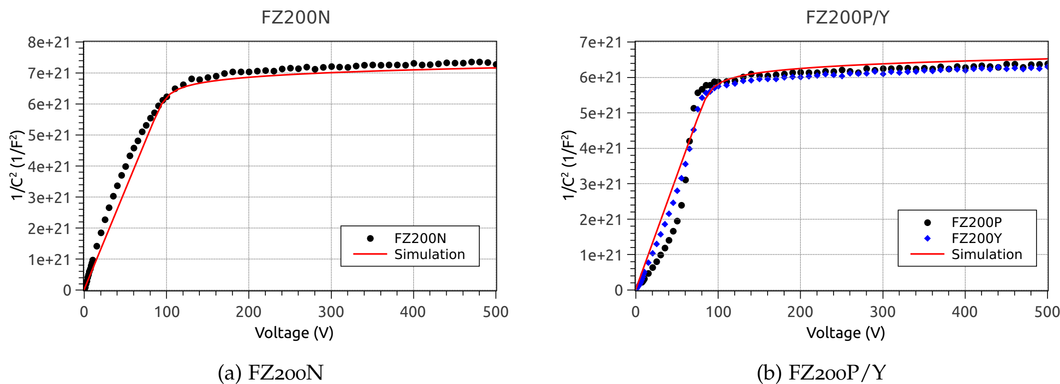

(a) FZ200N

(b) FZ200P/Y

Figure 8.4: Simulated and measured CV of FZ200N (a) FZ200P/Y (b).

The simulated CV behaviour in comparison with the measurement can be seen in the figures 8.3 to 8.6. All simulations and measurements have been carried out at 1 kHz and -20 °C.

As can be seen from figure 8.4 and 8.5, the deeper the dopants are diffused into the material, the shallower is the transition from the bulk doping concentration to the high doping concentration at the backside. This results in a continuously rising end capacitance, which is almost neglibile for the FZ320 diodes, but becomes visible for FZ200 and is most distinct for FZ120.

For FZ320, the simulation matches the measurement nearly perfectly. The rise in the $1/C^2$-curve is very linear, as expected from a constant bulk doping. The kinks in the measurement for the p-stop diodes (P) arise from an imperfect isolation between the pad and the guard ring of the p-stop diodes, which vanishes after depletion.

In figure 8.4, the measurements don't show a nice linear increase. This can be attributed to defects created by the deep diffusion process. They influence the doping profile along the depth of the diodes [Jun11]. The deep diffusion process can create thermal donors, which influence the bulk doping. This can be seen in the FZ120 diodes. The n-bulk diode shows a higher doping concentration in the bulk than the thicker ones. Additional donors raise the intrinsic doping. It is the other way round for the FZ120P/Y diodes: donors in the bulk doped with acceptors actually decrease the overall doping concentration. It is also clear, that these diodes are affected most because they need more time or higher temperatures for the diffusion to penetrate deep into the bulk.

The MCz diodes show a very clear profile. The sensors are physically 200 µm thin and needed a different treatment during the processing. For the 320 µm thick FZ wafers, first the backside processing and then the frontside processing has been done. Because thin sensors cannot be handled during the processing, the 200 µm thick wafers have been processed first on

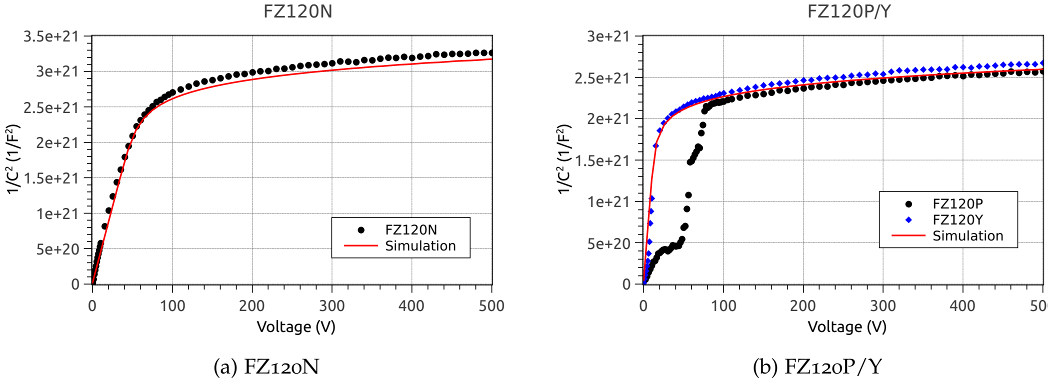

(a) FZ120N (b) FZ120P/Y

Figure 8.5: Simulated and measured CV of FZ120N (a) FZ120P/Y (b).

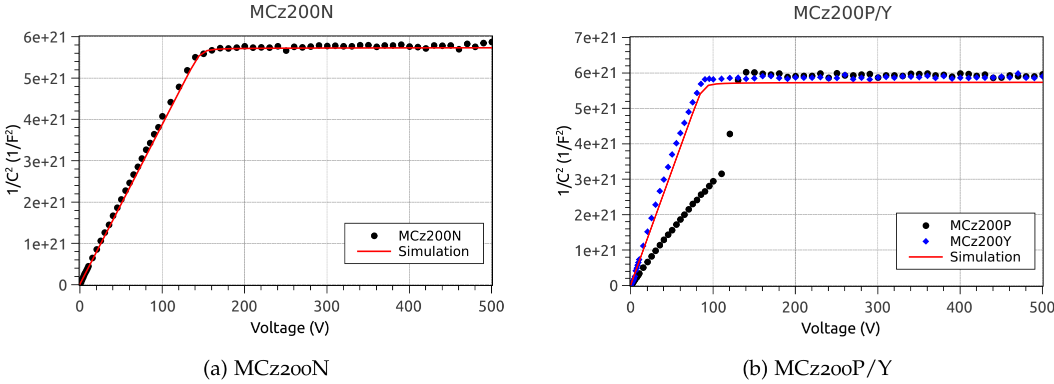

(a) MCz200N (b) MCz200P/Y

Figure 8.6: Simulated and measured CV of MCz200N (a) MCz200P/Y (b).

the frontside. Then they have been thinned from the original thickness (> 200 µm) down to 200 µm and after which the backside implant has been processed. This results in a quite thin backside implant, which can be deducted from table 8.1.

The measurement for MCz200P in figure 8.6 shows a higher depletion voltage than its p-spray isolated counterpart. Again, there is no isolation between pad and guard ring. However, the depletion seems to set in later than for p-spray. This is not understood. Assuming the same MCz wafers have been used and only the isolation technique on the front side differs, the diode with p-spray isolation delivers more reliable results.

The doping profiles used for the simulation of the CV curves can be seen in figure 8.7 and figure 8.8. The difference between the usual backside processing and deep diffusion can be clearly seen: the deep diffusion creates a smooth transition from the bulk doping to the high backside doping, whereas usually a steep and sharp transition creates an abrupt cut and a well defined volume and depletion voltage.

The doping profiles obtained from diodes are most precise, because the frontside is just a pad, there's no segmentation influencing the measured full depletion voltage. The profiles given here are used in all further simulations in this work.

8.1.2.1 *Comparison with measured Doping Profiles*

Not only CV characteristics but also spreading resistance measurements can be a good estimate for the doping profile of devices. Spreading resistance measurements are not a new technique but have been applied for measurements of the doping profile of silicon sensors in high energy physics just recently [D+13].

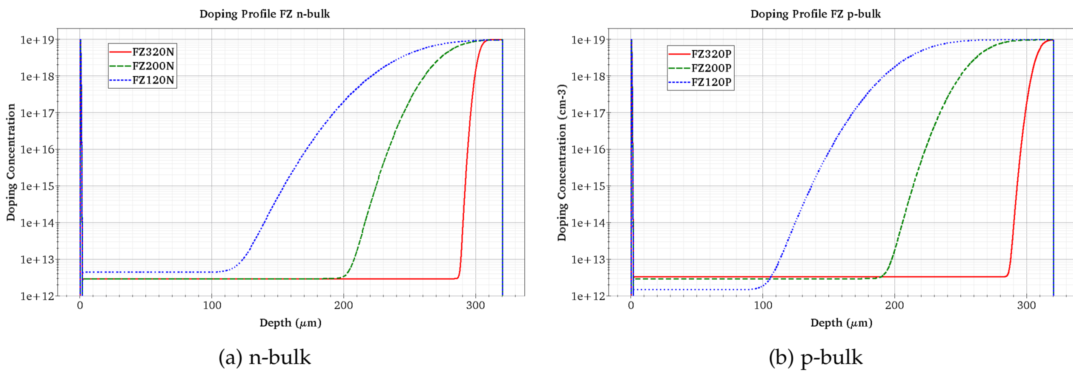

(a) n-bulk (b) p-bulk

Figure 8.7: Doping profile of FZ (a) n-bulk and (b) p-bulk diodes.

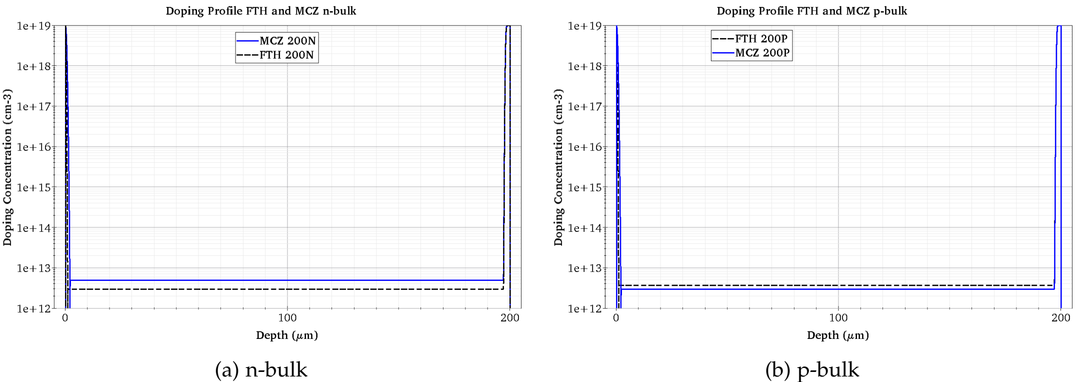

(a) n-bulk (b) p-bulk

Figure 8.8: Doping profile of MCz and FTH (a) n-bulk and (b) p-bulk diodes.

The spreading resistance measurement uses the fact, that the resistance in silicon changes with the doping concentration. The method is a destructive method: silicon devices are bevelled at a very shallow angle. Then two probe needles step across the plane and the resistance between these probes is measured. The angle has te be known very well in order to give the correct depth. The principle of this method is sketched in figure 8.9.

Spreading resistance measurements are nice to get an impression on the shape of the doping profile in the devices. However, the measurement of the absolute doping concentration with this method is not trivial. Correction calculations and cross calibrations have to be done. Another source of errors is the angle with which the devices have been bevelled. The comparison here can show, that the shape of the doping profile can be reproduced very well from CV measurements together with simulation or the spreading resistance measurement. The absolute doping concentration in the bulk is rather best determined with the full depletion voltage of a diode.

Figure 8.10 shows the doping profiles measured by Treberspurg [Tre12] with the spreading resistance method. The doping concentration obtained from the spreading resistance measurement matches quite well the doping concentration obtained by the CV measurement seen in figure 8.11. In comparison with the doping profile used in the simulation, it is obvious, that the simulation does not account for small variations in the bulk as seen in the depth profile of the CV measurement. In the simulation, a mean value for the bulk doping is sufficient for the description of the full depletion voltage. The doping profile implemented on the backside following an error function describes the doping profile from the CV measurement remarkably well. The simulation profile for FZ320 diodes seems to overestimate the active thickness of the diodes. When simulating the CV curve, this can be seen for FZ320P. The active thickness for

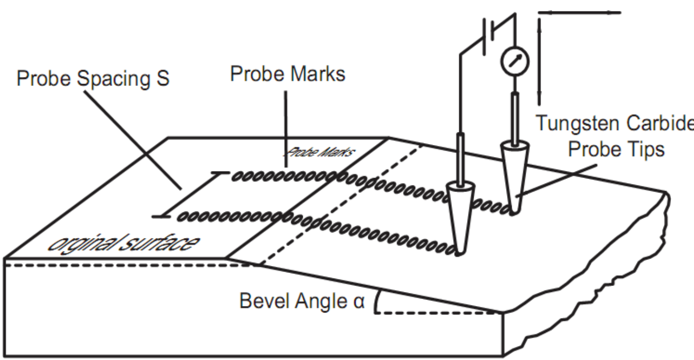

Figure 8.9: Principle of the spreading resistance measurement:
Two probes move on a plane with a bevel angle to the original surface and measure the resistance between them, which changes with the doping concentration. Picture from [D+13].

the bulk could be slightly reduced in the simulation. For the FZ320N diodes, the CV matches quite well the simulated one.

It has been considered to follow the exact doping concentration in the bulk of the diodes. This however means a non-trivial implementation of several doping profiles describing the actual situation. Because the effective doping changes after irradiation, especially after fluences greater than $10^{14}\,n_{eq}/cm^2$, the description with a mean bulk doping concentration is sufficiently precise. The exact shape of the CV curve before irradation cannot be reproduced though.

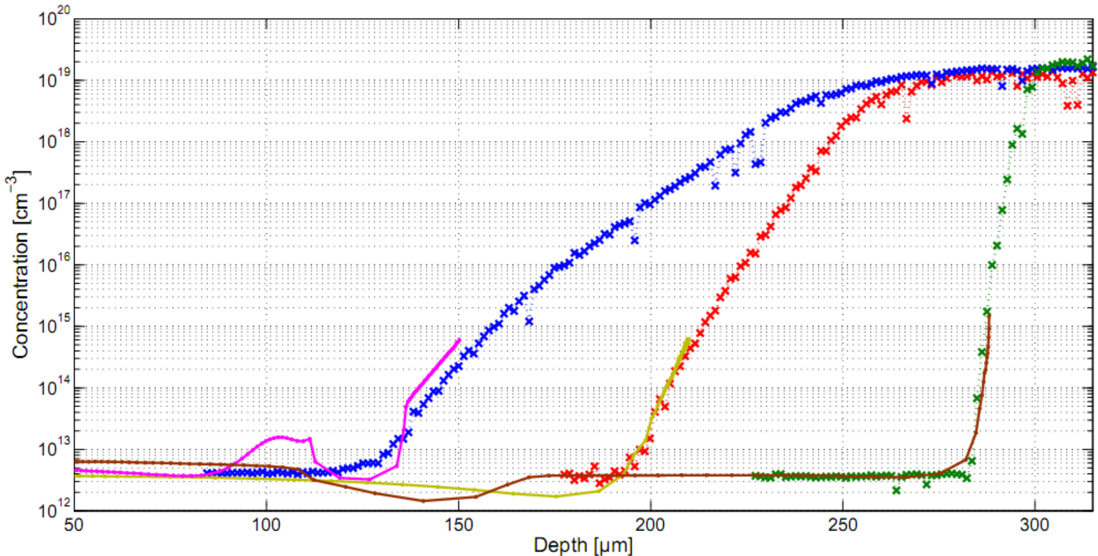

Figure 8.10: Doping profile of FZ p-bulk wafers measured with the spreading resistance measurement (SRP) [D+13] in comparison with the doping profiles obtained from the CV measurement. FZ120P is shown blue (SRP) and magenta (CV), FZ200P is shown in red (SRP) and dark yellow (CV) and FZ320P is visualized in green (SRP) and brown (CV).

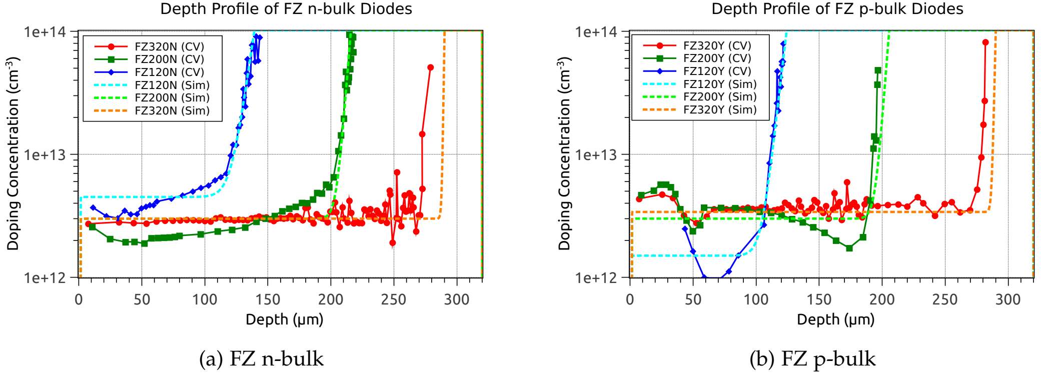

(a) FZ n-bulk

(b) FZ p-bulk

Figure 8.11: The doping profile used in the simulation (dashed line) compared to the doping profile obtained by the CV measurement.

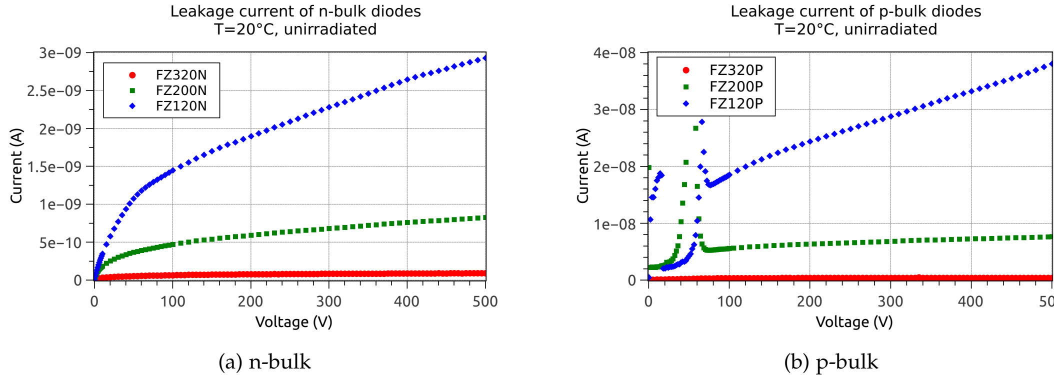

(a) n-bulk

(b) p-bulk

Figure 8.12: Leakage current of un-irradiated diodes with (a) n-bulk and (b) p-bulk at T = 20 °C.

Table 8.2: Parameters for the simulation of the leakage current in un-irradiated diodes. The current is generated according to equation 3.29.

Parameter	Value for n-bulk	Value for p-bulk	Original Values [Syn12]
τ_e	10^{-1} s	10^{-2} s	10^{-5} s
τ_h	10^{-2} s	10^{-2} s	3×10^{-6} s

8.1.3 LEAKAGE CURRENT

The leakage current of un-irradiated diodes is usually very low. Process induced impurities like other atoms, e.g. gold or copper, or process related defects, e.g. defects emerging from the deep diffusion process, largely influence the current. As described in chapter 3.3.6.1, the current scales with the depleted volume if not influenced otherwise. The investigated diodes however show the reverse picture (figure 8.12): FZ320 diodes show the lowest current, whereas FZ120 diodes have the highest measured leakage current. This is due to the mentioned defects created by the deep diffusion process. As Junkes could show [Jun11], the H220K defect is mainly responsible for the high leakage current of FZ p-bulk diodes.

One can also see, that the leakage current of p-bulk diodes is one order of magnitude larger than the current in FZ n-bulk diodes. This leads to the conclusion, that more defects are present in the p-bulk diodes. Because FZ320N/P diodes are very clean of the H220K defect, they have been used to calibrate the simulation. The parameters for the Shockley-Read-Hall (SRH) recombination have been altered to match the leakage current of these diodes. The current in these devices is dominated by the recombination and generation of charge carriers following the SRH statistics. The recombination time for electrons τ_e and holes τ_h define the leakage current. Because the recombination times vary largely over the wafer, a fine-tuning is not necessary, only the order of magnitude should be correct. The measured current of diodes distributed over the wafer as sketched in figure 8.13 can be seen in figure 8.14. The measured current of FZ320N diodes spreads from 1 nA to 2.5 nA just before the breakdown voltage, which is over 900 V for all diodes on the wafer.

Synopsys Sentaurus uses very small recombination times, hence the generated current is too high. Equation 3.29 describes the relation between the recombination time τ and the leakage current. The recombination times have to be increased. The result for n-bulk and p-bulk diodes can be seen in figure 8.15, which uses the parameters in table 8.2 for the simulation. Once fixed, these values have been used throughout the whole work.

On top of that, additional current in thinner diodes is generated by the H220K defect. The effect of the H220K defect has been simulated using the parameters of the defect given

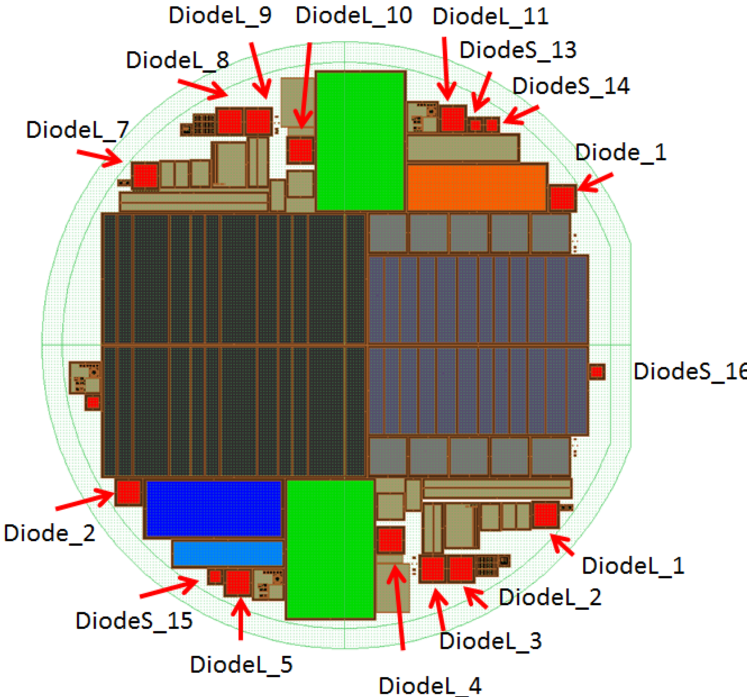

Figure 8.13: Diode distribution and naming scheme on the HPK wafer.

in table 8.3, assuming the most likely configuration found by Junkes. Because the concentration of this defect differs from diode to diode, the same diodes as in [Jun11] have been used for the comparison of the leakage current (FZ200Y_03_Diode_2, FZ200Y_02_Diode_1 and FZ120Y_06_Diode_1).

The electron cross section determined by Junkes seems quite small. The simulation rather suggests a higher electron cross section of the H220K defect. With the modified cross section, the IV curves at 293 K can be simulated. The defect concentration for the two diodes showing a higher current is $3 \times 10^{11} \mathrm{cm}^{-3}$. For the diode showing a lower current, the concentration of $1.5 \times 10^{11} \mathrm{cm}^{-3}$ would yield a higher current at 20% over depletion than the diodes actually show. With a concentration of $0.95 \times 10^{11} \mathrm{cm}^{-3}$ the IV curve can be simulated well. Figure 8.16 shows the measured and simulated IV curves for the three diodes.

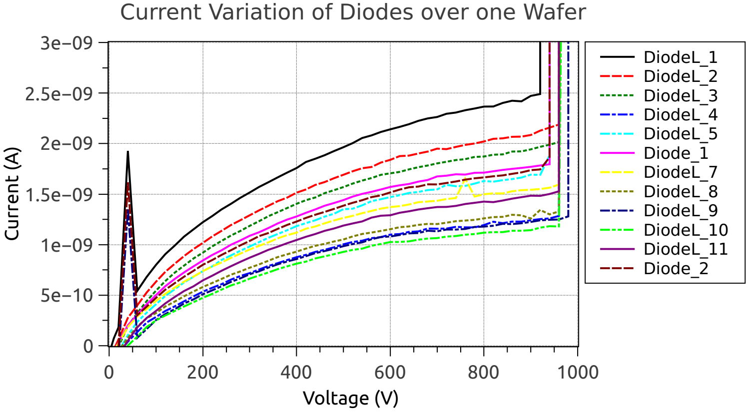

Figure 8.14: Variation of the leakage current of FZ320N diodes over on wafer 1:
The current is largest bottom right and lowest top left.

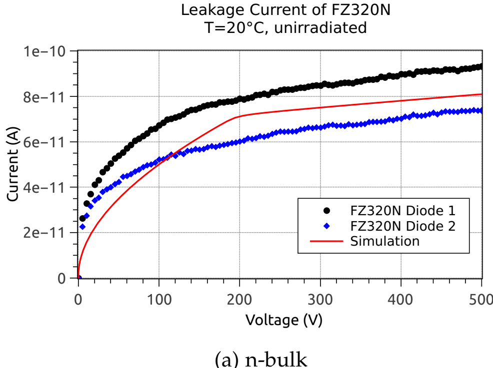

(a) n-bulk

Figure 8.15: Leakage current of un-irradiated diodes with n-bulk. The recombination time has been modified to describe the diodes correctly before irradiation.

Table 8.3: Parameters of the H220K defect.

Parameter	Original Value	Simulation Value
E_G (eV)	$E_V + 0.444$	$E_V + 0.444$
σ_n (cm^2)	1.5×10^{-15}	2.0×10^{-14}
σ_p (cm^2)	5×10^{-14}	5×10^{-14}
[H220K] (cm^{-3})	$\mathcal{O}(10^{11})$	3×10^{11}, 0.95×10^{11}

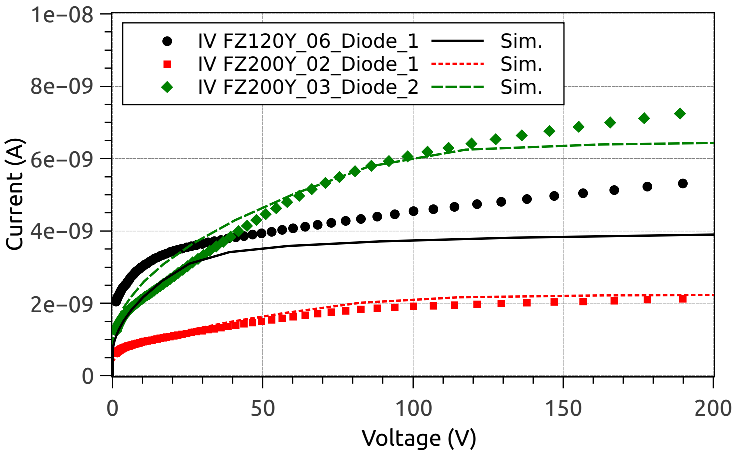

Figure 8.16: Measured and simulated IV of FZ p-bulk diodes showing a high leakage current: *responsible for the high current is most probably the H220K defect, which has been used to simulate the IV of three diodes. The agreement is good for two of the diodes with a defect concentration of* $3 \times 10^{11} cm^{-3}$. *For the diode with a lower current a smaller concentration of* $0.95 \times 10^{11} cm^{-3}$ *has been used.*

8.2 CV Measurements and the Guardring

Capacitance-Voltage measurements have been done since the early days and have been proven to be a useful tool to describe the sensor's performance before and after irradiation in dependence of the bias voltage. The extraction of the depletion voltage is explained in chapter 5.1.2. Yet, there is one critical point in doing this and it is always under discussion among experts: the connection of the guard ring to ground.

There are several arguments supporting one or the other method. Arguments for connecting the guard ring to ground, are the following:

- Measurement of the volume scaled current; the volume is well defined by the surrounding guard ring and additional surface and bulk currents flow through the connected guard ring.
- Measurement of the correct end capacitance; with the end capacitance and the area inside the guard ring, the active depth of the sensor can be calculated. This is useful for an estimation of the collected charge in the sensor.

Arguments against this method are as follows:

- The sensor is not operated in its later operation mode; leaving the guard ring floating leads to a higher breakdown voltage of the sensor.
- An additional needle has to contact the sensor on the guard ring.
- The end capacitance is different from the one measured with guard ring on ground. This leads to a different calculated active depth of the sensor because the area for the measurement is not known very well.

All these points have to be considered, when measuring IV and CV with or without a connection of the guard ring to ground. This chapter is to give hints on which method should be used when.

8.2.1 Active area of diodes

The active area of a sensor is one crucial point in the calculation of the active thickness of the sensor. Because the active thickness d is calculated from the formula for a plate capacitor

$$d = \epsilon_0 \times \epsilon_r \times \frac{A}{C} \tag{8.1}$$

with an area A and a capacitance C, which is measured in the CV measurement, small variations in the area can lead to significant variations in the active depth. Usually, the area is taken from the dimensions of the diode given in the GDS[1] file. The GDS file is used to create the masks, which are again used for the processing of implants and the aluminum layers. Already during the processing and the fabrication of the wafer, there will be differences between the actual structures and the GDS mask due to diffusion. The active area is not known exactly beforehand. Good values are mostly the dimensions of the outermost aluminum edges or the center of the guard ring.

Taking the calculated thicknesses from sensors or diodes [Hof13], a good estimation of the active area for diodes of different thicknesses can be made. Furthermore, the influence of the floating guard ring on the capacitance as well as a correction factor for the calculation of the active thickness with a floating guard ring is presented.

For this analysis, several CV measurements of small and large diodes with and without connected guard ring have been analyzed. The mean capacitance values in the plateau region of the capacitance are taken and plotted over the inverse depth. This can be seen in figure 8.17.

1 Graphical Design Station; data format for layout data of integrated circuits.

Figure 8.17: Determination of the active area of n-bulk diodes. The active area is the slope of the plot capacitance over the inverse depth. The resulting areas differ not only for small and large diodes, but also for measurements with and without the connected guard ring.

Table 8.4: Fit of the active area of diodes.

Measurement	Active Area (mm^2)	Edge Length (μm)	c (F)
DiodeS with GR	4.1021	2025	1.47×10^{-13}
DiodeS w/o GR	4.0361	2009	5.7×10^{-13}
DiodeL with GR	24.6033	4960	3×10^{-15}
DiodeL w/o GR	24.2320	4923	1.32×10^{-12}

First thing to see is, that for thinner diodes, the capacitance values with and without connected guard ring do not differ so much as for thicker diodes. By fitting the different series of points linearly, the active area is identified with the slope of the fit. The intersection with the y-axis can be seen as an additional capacitance, which adds to the total capacitance of the plate capacitor. All deviations from a perfect plate capacitor are absorbed in this constant c. The fit is described by the following formula:

$$\frac{C}{\epsilon_0 \times \epsilon_r} = A \times \frac{1}{d} + c_\epsilon \tag{8.2}$$

If now in return the active thickness of the diode is calcuated, this additional capacitance is the correction factor between the measurement with and without connected guard ring.

$$d = \frac{A}{\frac{C}{\epsilon_0 \times \epsilon_r} - c_\epsilon} = \frac{A}{\frac{C}{\epsilon_0 \times \epsilon_r} - \frac{c}{\epsilon_0 \times \epsilon_r}} \tag{8.3}$$

$$d = \epsilon_0 \times \epsilon_r \times \frac{A}{C - c} \tag{8.4}$$

Table 8.4 shows the fitted values for the active area A and the correction factor c. Of course, the correction factor should be zero for the measurement with connected guard ring, but the measurement error, especially for small capacitances appearing for small diodes, can be large.

At first glance, it is peculiar, that the calculated area of the measurement with floating guard ring is smaller than the area of the measurement with connected guard ring, both for small

Table 8.5: Influence of the additional capacitance occuring in the measurement with floating guard ring.

d (μm)	% of C_{tot}		Corresponding additional area (mm^2)	
	DiodeS	DiodeL	DiodeS	DiodeL
100	11.8	4.9	0.51	1.05
120	16.7	7.1	0.76	1.55
200	22.3	10.4	1.09	2.32
320	28.5	13.0	1.50	2.98

and large diodes. However, when the capacitance of the diode is calculated, an additional capacitance, which is the same for all thicknesses and depends only on the area of the diode, has to be added. This capacitance is the influence of the floating guard ring and the surrounding area, which is not well defined by the connected guard ring. Depending on the thickness of the diode, this can be a significant contribution to the total capacitance of the diode. Table 8.5 shows the contribution to the total capacitance of diodes with different thicknesses.

The additional capacitance, which is present in the measurement with floating guard ring can be converted into an area using again the formula for the plate capacitor. The additional area is increasing from thinner diodes to thicker diodes. This can be explained in the picture of a non-perfect plate capacitor: The thicker the diode is, the more the field lines can extend sideways from the back side to the front, where the area is not limited by the grounded guard ring. The thinner the diode is, the less the electric field lines can escape sideways and the diode is closer to a perfect plate capacitor. This explains, why the difference between measurements with guard ring connected to ground and a floating guard ring almost disappears.

The additional capacitance is of course different for different dimensions of the diode, in this case small and large diodes. Therefore it is necessary to recalculate the correction factor for different layouts. The correction factor cannot be scaled using the area of the diode. Yet, the additional capacitance is an edge effect, therefore it should scale with the edge length of the diode pad. The additional capacitance divided by four times the edge length of the corresponding diode pad indeed gives a value which is nearly the same for small and large diodes.

$$C_{corr,L}/(4 \times l_L) = 5.5 \times 10^{-14}\ F/m \tag{8.5}$$

$$C_{corr,S}/(4 \times l_S) = 6.5 \times 10^{-14}\ F/m \tag{8.6}$$

8.2.2 COMPARISON OF THE DIMENSIONS WITH THE GDS FILE

Having calculated the area of the diode at the front side, which forms the plate capacitor with the back side, it is interesting to compare these values with the dimensions taken from the GDS file. Table 8.6 lists the dimensions of small and large HPK diodes.

It is obvious, that the values of the active area for the measurement with guard ring connected to ground are near the values of the pad of the diode. For the small diode, the value is a little bit larger than the value of the aluminum edge. The edge length for the measurement with floating guard ring is in between the edge length of the pad aluminum and the pad implant.

For the large diode, in the measurement with guard ring connected to ground, the value lies in between the edge of the pad aluminum and the guard ring. The edge length calculated from the measurement with floating guard ring is closer to the edge length of the pad.

Looking at a simulation of a diode, where the guard ring is connected to ground, one can see the electric field lines in the oxide and the very first layers of silicon (see figure 8.18): they run

Table 8.6: Dimensions of HPK diodes taken from the GDS file.

Measured Edge	Length (μm)	Area (mm^2)
DiodeS		
Aluminum Pad	2045	4.18
Implant Pad	2000	4.00
Center GR	2132	4.55
Aluminum outer GR	2225	4.95
Implant outer GR	2160	4.67
DiodeL		
Aluminum Pad	4938	24.38
Implant Pad	4893	23.94
Center GR	5087	25.88
Aluminum outer GR	5242	27.48
Implant outer GR	5177	26.80

from both aluminum contacts of the pad and the guard ring in the region without aluminum. At a certain point, they meet and run perpendicular from the oxide to the backplane. This is an indication, where the separation of the area of the pad and the guard ring happens.

8.2.3 DIRECT CALCULATIONS

Now, that it is clear, that the additional capacitance in a measurement with floating guard ring is not dependent on the thickness of the diode, the extracted values from the previous section can be taken to directly calculate the difference of the measured capacitances with and without a floating guard ring. Table 8.7 shows the mean values of the measured capacitances and their difference.

By calculating the difference, it can be seen, that to first order the difference between the capacitances measured with or without floating guard ring are independent of the thickness. One can take these values for each thickness to state a correction factor for each thickness or take the mean correction factor for each diode type, small or large.

Compared to values in the previous section, the mean difference is equal to the additional capacitance within the calculation errors. This indicates, that the calculated area is reasonable.

The validity region for the correction factor can even be extended, taking into account diodes from the test structures of the CMS production run. These are diodes with a physical thickness of 500 μm and an active thickness of about 485 μm. The difference in capacitances measured with and without the floating guard ring is

$$C_{diff} = C_{float} - C_{GR} = 6.77 \times 10^{-12}\,F - 5.85 \times 10^{-12}\,F = 0.92 \times 10^{-12}\,F$$

This is well in the errors for the large diode, as the dimensions of this diode are nearly the same as for a large diode from the HPK production. This confirms the validity of the correction factor.

8.2.4 COMPARISON OF THE CURVE SHAPES

Having a common correction factor for the conversion of one measurement to the other in hand, the curve shapes of the measurements can be compared. Because of the lateral depletion in the

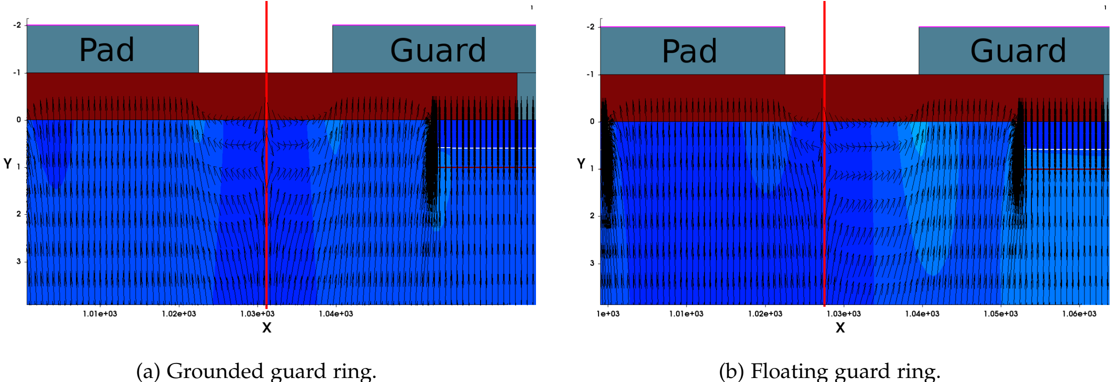

(a) Grounded guard ring.

(b) Floating guard ring.

Figure 8.18: Simulation of a diode with and without guard ring connected to ground at 1000 V bias voltage.
The electric field lines indicate the separation of the pad area and the guard area. In the case of the floating guard ring, the separation occurs closer to the pad on the left side.

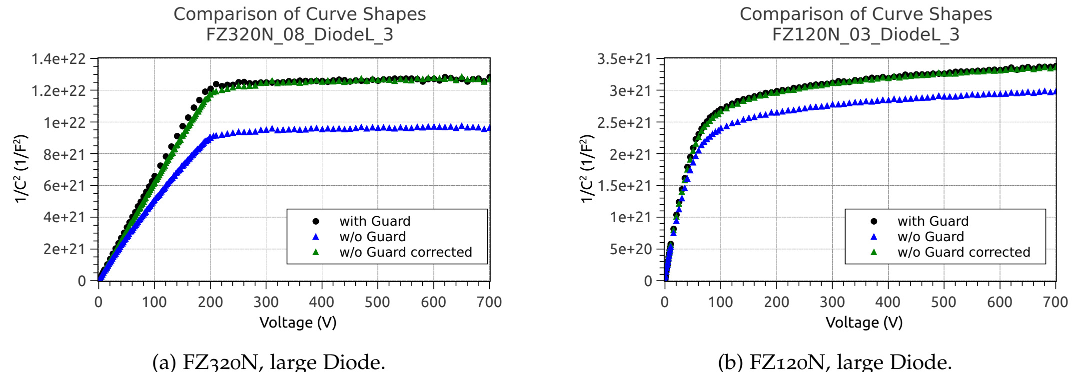

(a) FZ320N, large Diode.

(b) FZ120N, large Diode.

Figure 8.19: Comparison of CV curve shapes of large diodes. The curves measured with floating guard ring have been corrected using the correction factor from table 8.7.

measurement with floating guard ring, it is expected, that the curves do not totally coincide. Figure 8.19 shows two examples of the comparison.

The measurements with floating guard ring have been corrected using the correction factor from table 8.7. Figure 8.19a shows a 320 µm thick diode. In the $1/C^2$-plot, the increase in the values up to the plateau region is very linear when the diode is measured with guard ring on ground. In the measurement with floating guard ring, the increase is not so linear. This can be seen in the corrected curve too, because the values are only scaled globally. The values between the two curves, however, only differ around the kink at the depletion voltage. The effect can be assigned to the lateral depletion, which extends in the region beneath the guard ring. If the guard ring is connected, this effect is not visible, because the guard ring shields this region from the pad.

For the thinner diode in figure 8.19b, a 120 µm thick large n-bulk diode, this effect is rather not visible. The curves agree very well with each other. Yet, due to the deep diffused backside implant, the transition from the linear increase towards the plateau region is very smooth. This exceeds the effect of the lateral depletion.

Table 8.7: Measured capacitances with and without floating guard ring and their difference.

d (μm)	C with GR (pF)	C w/o GR (pF)	Difference (pF)
DiodeS			
100	4.46 ± 0.01	4.83 ± 0.10	0.36 ± 0.11
120	3.07 ± 0.03	3.42 ± 0.09	0.35 ± 0.10
200	2.13 ± 0.04	2.56 ± 0.08	0.43 ± 0.09
320	1.62 ± 0.04	2.00 ± 0.05	0.38 ± 0.06
Mean Difference			0.38 ± 0.17
DiodeL			
100	25.92 ± 0.06	26.86 ± 0.05	0.95 ± 0.08
120	17.56 ± 0.05	18.61 ± 0.17	1.06 ± 0.18
200	11.72 ± 0.10	12.77 ± 0.06	1.05 ± 0.12
320	8.94 ± 0.16	10.20 ± 0.05	1.26 ± 0.17
Mean Difference			1.08 ± 0.20

8.2.5 EVALUATION OF THE DEPLETION VOLTAGE

In the last section, the curve shapes of the two measurements have been compared. In the measurements with floating guard ring, there is a slight slope in the increasing values in the $1/C^2$ vs. voltage plot compared to the measurement with grounded guard ring. This can have an influence on the depletion voltage, because the extraction of the depletion voltage depends on the selection of measurement points for the linear fit in this region. A slope in this region can then lead to a different depletion voltage.

For the comparison of the depletion voltage with and without grounded guard ring, the values for all un-irradiated diodes have been taken from the CMS upgrade database. Table 8.8 lists the depletion voltage for both types of measurements.

As one can see from the listed depletion voltages, the deviations in the measurement are mostly in the order of below 10%. The depletion voltage determined with floating guard ring is not always higher than V_{dep} with grounded guard ring. Mostly, the depletion voltage determined with one method is within the errors of the depletion voltage of the other method. Regarding measurements of p-bulk diodes with p-stop isolation (P), the values can differ more because of the isolation problem already mentioned in section 8.1.2. In summary, it cannot be said, that the measurement with floating guard ring has a systematic influence on the determination of the depletion voltage.

8.2.6 SUMMARY OF THE CV EVALUATION

At the beginning of this chapter, the pros and cons for a measurement with grounded guard ring have been explained. The capacitances of the two measurement methods have been compared and it has been shown, that in the measurement with floating guard ring, an additional capacitance is occuring. This additional capacitance arises from an additional area, which is included in the CV measurement on the pad of the diode. The area in the measurement with grounded guard ring on the other hand is well defined.

The area, one should use for the calculation of the depth of the diode has been discussed. From a global fit of the diode values, this area has an edge length, which lies in between the edge length for the pad and the guard ring in the case with grounded guard ring. For the case

Table 8.8: Depletion Voltage of un-irradiated diodes with and without grounded guard ring.

Diode Type	$V_{dep,GR}$ (V)	$V_{dep,float}$ (V)	Abs. rel. Difference (%)
Epi100N	32 ± 2	34 ± 2	6.9
Epi100P	79 ± 11	73 ± 8	7.2
Epi100Y	69 ± 1	70 ± 3	1.6
Epi50N	5 ± 1	5 ± 0	4.6
Epi50P	21 ± 1	20 ± 0	5.6
Epi50Y	23 ± 3	20 ± 0	13.2
FTH200N	89 ± 4	95 ± 7	6.7
FTH200P	113 ± 7		-
FTH200Y	117 ± 4	117 ± 5	0.3
FZ120N	70 ± 11	70 ± 14	0.3
FZ120P	89 ± 35	83 ± 42	6.4
FZ120Y	27 ± 19	29 ± 19	7.9
FZ200N	99 ± 24	93 ± 14	6.1
FZ200P	79 ± 8	88 ± 9	11.0
FZ200Y	96 ± 32	92 ± 6	3.6
FZ320N	196 ± 5	200 ± 3	2.2
FZ320P	224 ± 6	220 ± 10	1.3
FZ320Y	232 ± 25	231 ± 3	0.3
MCZ200N	134 ± 27	149 ± 8	10.8
MCZ200P	138 ± 14	144 ± 10	4.1
MCZ200Y	99 ± 25	100 ± 10	0.6

with floating guard ring, this area is smaller and much alike the aluminum pad area, but with a constant offset for large diodes of

$$C_{corr} = 1.1\,\mathrm{pF} \pm 0.2\,\mathrm{pF} \tag{8.7}$$

and for small diodes of

$$C_{corr} = 0.38\,\mathrm{pF} \pm 0.17\,\mathrm{pF} \tag{8.8}$$

A very similar value has been calculated from the difference of the capacitance values in the plateau region of the CV curve. This value in turn can be used as a correction factor to convert one measurement into the other measurement.

The curve shape measured with floating guard ring and scaled with the correction factor happens to be not exactly like the curve measured with grounded guard ring. However, they still look very similar. It has been also shown, that the slightly different curve shape does not have an overall systematic influence on the depletion voltage determined with one or the other measurement.

A suggestion for a future measurement with grounded or floating guard ring will not be given here, though. Although a scaling is given here for two diode types, this has to be recalculated, if a different diode layout is used. Furthermore, CV is not the only measurement, which is affected by a grounded guard ring. Rather the difference in breakdown voltage and the volume scaled current should be taken into consideration.

Some of the aspects mentioned above can be avoided using a diode with not only one guard ring. An additional guard ring can be used to shield edge effects in the CV measurement as

well as in the IV measurement, yet operating the device in the usual mode, when the innermost guard ring is connected to the pad. Chapter 9 explains this and the advanced diode layouts in more detail.

8.3 Signals in Diodes

The signal simulation in silicon sensors is of great importance. The signal simulation includes the signal generation by a laser or MIP in a diode or strip sensor. Raw signals as well as signals convoluted by the readout circuit are simulated for the understanding and comparison of TCT signals. The integration of those signals then leads to the charge collection efficiency. The signal generated by a MIP in the simulation can be compared to the signal of an infrared laser, the signal of which is smaller and not distributed uniformly over the sensor.

For both, diodes and strip sensors, the correct areafactor and a proper signal network has to be used. The implementation of the signal simulation with a laser or a MIP and the different networks for the different setups at IEKP and UHH are discussed in the following.

8.3.1 Implementation

The implementation of the signal generation by a laser is described in section A.2.11. The simulation requires the device to be ramped to a certain voltage, at which the laser shot is performed. A transient simulation then mimics the behaviour of the charges generated by the laser. The absorption length varies according to the laser wavelength used. For all following simulations, red refers to a wavelength of 678 nm and infrared to 1060 nm, corresponding to the lasers present in the setup at KIT and UHH. A third wavelength of 880 nm is sometimes used to penetrate deeper into the bulk of the sensor. Figure 8.20 shows the intensity of the three different wavelengths mentioned. The red laser is absorbed in the first few micrometers, 880 nm penetrates deeper into the bulk and light in the infrared wavelength can penetrate the silicion bulk totally, reaching an intensity of about 70% after 320 µm of silicon. This is the reason, why a MIP generates slightly more charges, because its generation of electron-hole pairs is constant over the bulk.

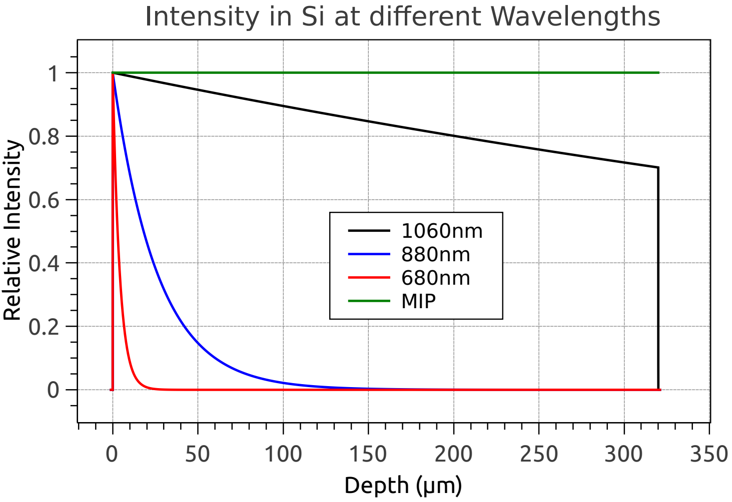

Figure 8.20: Intensity of different wavelengths in silicon, simulated in a 320 µm thick diode. Red light is absorbed in the first few micrometers whereas infrared light can penetrate the bulk. The intensity of a minimum ionizing particle is constant throughout the bulk.

In the simulation grid file, the mesh should be refined around the incident track of the light. If not done so, this can lead to deviations in the generated current in different regions, when the optical generation "leaks" into larger mesh cells.

To generate a MIP signal, the "Heavy Ion" statement can be used (see section A.2.12). In contrast to the charge generated by a laser, the charge generated by a MIP is constant over the bulk.

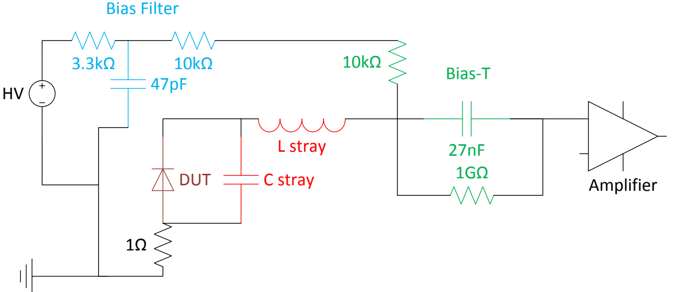

Figure 8.21: Equivalent readout circuit for TCT setups. There is a HV filter and a bias-T, which are common to both setups. The stray capacitance and stray inductance are tuned to fit the curve shape for the setups at KIT and UHH.

8.3.2 SPICE MODELS

For the direct comparison of measured and simulated signals, the readout circuit has to be taken into account. The simulators therefore provide a SPICE simulation, which convolutes the original signal at the device with additional resistances, capacitances or inductances, which are present in a real circuit. For the TCT signals, which are under investigation in this work, the two setups at IEKP and UHH have been modeled. An equivalent circuit for a TCT setup can be seen in figure 8.21.

A stray capacitance and a stray inductance distort the signals in the setup. The bias-T also has an influence on the decoupling of the signal from the HV-line. The bias-T, which is the same for both setups, is well described. The stray capacitance and inductance are different and have to be tuned for each setup to match the measurements. The tuning of the SPICE models is done on a 320 µm thick n-bulk diode. The following parameters are used to describe the readout circuits:

PICOLASER SETUP AT KIT :

- $C_{stray} = 6\,\text{pF}$
- $L_{stray} = 1\,\text{nH}$

TCT SETUP AT UHH :

- $C_{stray} = 2\,\text{pF}$
- $L_{stray} = 15\,\text{nH}$

Additional distortions in the setups can occur because of signal reflections between the diode and the bias-T or between the bias-T and the amplifier. The amplifier is generally not taken into account in the simulations. It can also have a small influence on the signal shape. Yet, the amplifiers used in the setups have a very constant amplification factor up to frequencies of about 1 GHz and hence shouldn't distort the signal too much. The impact of the cabling on the signal shape is much larger and absorbed in the the additional stray capacitance and inductance.

8.3.3 TCT

With the SPICE models in hand, measurement and simulation of TCT pulses with a red laser can be compared. Figure 8.22 shows the comparison between measured signals and the signal from a simulation with the readout network.

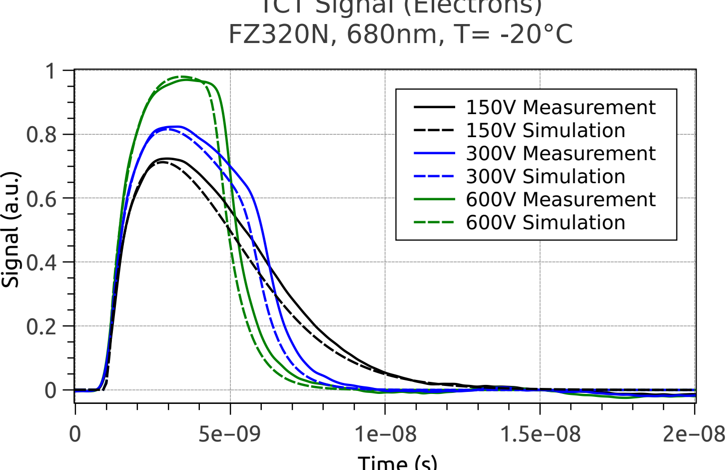

Figure 8.22: Comparison of measured and simulated TCT pulse convoluted with the readout network. *The agreement is very good. The TCT pulse is simulated correctly and therefore the simulator can be used for the prediction of irradiated diodes.*

The signals agree quite well with each other. This shows, that the readout network is understood well enough to compare signals of irradiated diodes with signals from the simulation, where the pulse shape is not known a priori. By directly comparing the signals, additional errors can be excluded.

Comparing the raw signals generated with an infrared laser and a minimum ionizing particle, the signals only differ a bit: scaled to the same peak heights, the laser wins in the total signal at early times; the MIP generates more charge at the back side and so the signal at later times is larger. The comparison of the signals for four voltages is plotted in figure 8.23.

8.3.4 CHARGE COLLECTION EFFICIENCY

Integrating the signals of the simulated pulses, one gets the collected charge. Because the un-irradiated diodes deplete from the front side, the collected charge for signals from a red laser reach the maximum very early, when the bias voltage is raised. The infrared signal however increases proportional to the depleted depth, which is proportional to the square root of the bias voltage. This effect can be seen in figure 8.24a for signals in a 320 μm thick n-bulk diode.

As seen from figure 8.20, different wavelengths of the laser and the minimum ionizing particle have different absorption coefficients in silicon. This leads to a slightly different charge collection. When the device is fully depleted, both, the infrared laser and the MIP generate their maximum number of electron-hole pairs in the device. But because of the exponential drop of the laser's intensity, the total number of generated electrons is lower. Taking for example an un-irradiated FZ320N diode, it depletes from the front side. Because the laser and the MIP start with the same "intensity" at the front surface of the diode, the relative loss of charge in the laser's case is lower. Starting to deplete the device at just over 200 V, a charge collection plateau is reached in both cases with the MIP having generated more charge according to its constant "intensity".

The actual measurements of the charge collection efficiency can be seen in figure 8.24b for a FZ320N diode. Both measurements agree very well with the simulation. The collected charge of the infrared laser rises up to the depletion voltage and shows the same slope as in the simulation. The integrated signal generated by the red laser shows nearly constant behaviour, even before depletion. At higher voltages, the collected charge drops. Parts of the signal can be swallowed by the RC-filter of the readout circuit, because the signals generated with a red laser get larger but also shorter at higher voltages (see e.g. figure 8.22).

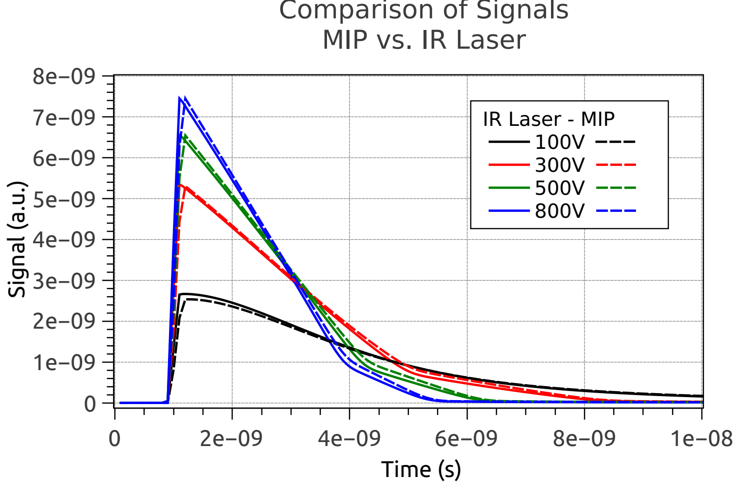

Figure 8.23: Comparison of the signal generated by an IR laser and a MIP in a FZ320N diode: *The signals are scaled to the same peak height. The difference between the signal of the infrared laser and the MIP is almost negligible.*

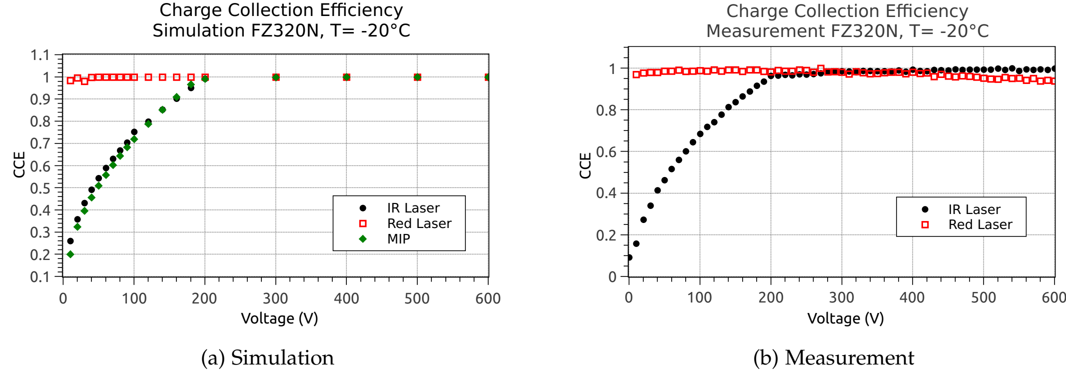

(a) Simulation

(b) Measurement

Figure 8.24: Charge collection of signals generated with lasers of different wavelengths: *The collected charge reaches its maximum very early for the red laser, because the diode depletes from the front side. The signal of the IR laser increases proportional to the depleted depth. The infrared laser and the MIP are in quite good agreement and it is feasible to use the infrared laser to simulate a MIP.*

8.4 Simulation of Silicon Strip Sensors

Silicon strip sensors are – in contrast to diodes – rather sophisticated devices. The geometry of a strip sensor has a significant influence on its qualification parameters and ultimately on its performance as particle detector. It is necessary to understand the parameters of a silicon strip sensor as provided by the manufacturer before one can look at its performance after irradiation. The chapter is dedicated to step through all the qualification parameters, which have to be tuned in the simulation according to the measurements done in the probe station. After the basic parameters have been set, additional parameters like the p-stop or p-spray isolation of the strips in p-bulk devices are reviewed and the most probable configuration for the layout of a future CMS strip sensor is discussed. With respect to later simulations, special attention is payed to strip isolation, necessary because of the oxide charge, which is produced not only during the irradiation but can also occur in not totally perfect silicon oxides grown during the processing.

8.4.1 Layout of Strip Sensors

8.4.1.1 *HPK Strip Sensors*

Not much is initially known about the strip sensors fabricated by HPK. The doping profiles follow the same patterns analyzed by Treberspurg [Tre12]. In the optical analysis it has been seen, that the implanted strips also have a lateral diffusion of less than 1 µm. The strips are rounded around their corners in the bulk. Also the aluminum layer on top of the good quality silicon dioxide layer has a triangular shape towards the metal overhang, which is deposited on a thicker silicon oxide layer. Picture 8.25 shows the layout of one strip, used in the simulation for HPK strip sensors. In addition to a good quality silicon dioxide layer between the strip implant and its aluminum on top, a layer of silicon nitride is implemented. This layer extends about 10 µm perpendicular to the strip, even further than the metal overhang with 6.5 µm.

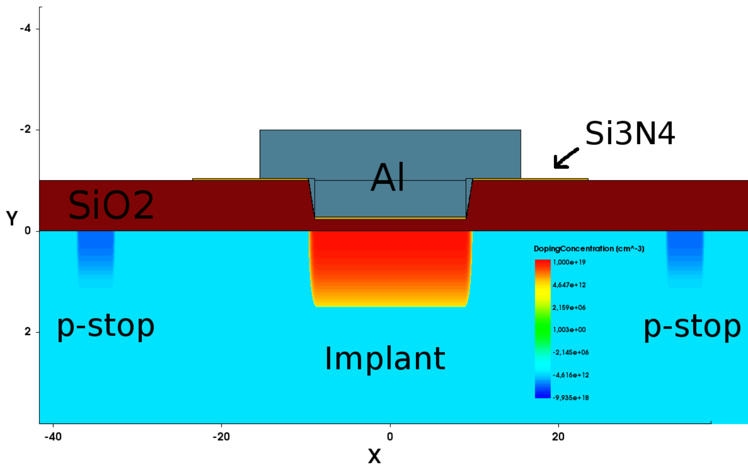

Figure 8.25: Strip sensor geometry of HPK strip sensors:
The implant and the p-stop implants show a lateral diffusion of 0.75 µm. On top of the coupling oxide, a thin nitride layer is deposited, which extends further than the aluminum of the contact. The aluminum over the implant is shaped trapezoidally due to etching.

Table 8.9 summarizes the parameters for the HPK strip geometry. For p-bulk sensors, the additional isolation structures have to be implemented. The optical inspection confirms the layout known from the GDS file. The spreading resistance measurements as well as the num-

Table 8.9: Parameters for the implants of HPK strip sensors.

Parameter	Value
Implant depth	1.5 μm
Implant profile	gaussian
Lateral diffusion	0.75 μm
Silicon oxide thickness	230 nm
Silicon nitride thickness	40 nm
p-spray concentration	5×10^{15} cm^{-3}
p-stop concentration	10^{16} cm^{-3}
p-stop distance from implant	31 μm
p-stop spacing	6 μm
p-stop width	4 μm

Table 8.10: Parameters for the implants of RD50 strip sensors.

Parameter	Value
Implant depth	1.0 μm or 0.5 μm
Implant profile	gaussian
Lateral diffusion	0.75 μm
Silicon oxide thickness	180 nm
P-spray concentration	10^{16} cm^{-3}

bers given by HPK indicate, that the p-stop and p-spray concentration is quite low. The p-stop and p-spray doping is covered in a following section.

8.4.1.2 *RD50 Strip Sensors*

The geometry of RD50 sensors, which are fabricated by Micron and which are under discussion later in this work, is slightly different. The implant at the back side is relatively thin compared to the ones of HPK. About the strip implant not much is known beforehand, in general shallower implants are expected. Yet, they come in different geometries, two of them of special interest with respect to their extreme pitch to width ratio of 0.75 and 0.075. In addition to that, the charge of the implanted ions, phosphorus, has been varied from singly charged ions to doubly charged ions. In the latter case, the implants are shallower, because the stopping power in silicon of doubly charged phosphorus ions is higher. The devices come in p-bulk and p-spray isolation only. In total, four configurations are discussed: deep and shallow implants with narrow and very broad strips.

Table 8.10 summarizes the parameters used for the simulation of RD50 strip sensors.

A silicon nitride layer has not implemented in these strip sensors. The coupling capacitance is directly determined by the coupling oxide thickness.

8.4.2 COUPLING CAPACITANCE

Like in the measurements at the probe station, the coupling capacitance is determined by applying an alternating voltage between the aluminum and the implant strip. If the correct areafactor is used, the coupling capacitance in the measurement and simulation should agree. The oxide thickness of the strip sensors has been optimized to match the measured coupling

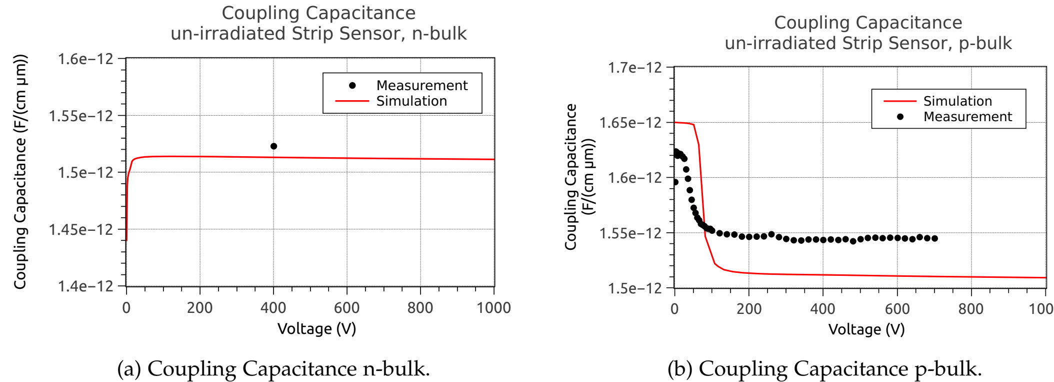

(a) Coupling Capacitance n-bulk.

(b) Coupling Capacitance p-bulk.

Figure 8.26: Coupling capacitance of the simulated strip sensors in comparison with measurements: *The simulated coupling capacitances match very well the measured ones. Even the drop at low voltages for p-bulk strip sensors is reproduced.*

capacitance as this has a great influence on the signal coupling from the DC coupled implant to the AC coupled aluminum strip. The result determined with a frequency of 100 Hz in the simulation and the measurement can be seen in figure 8.26.

The values for the coupling capacitance of the HPK Bstd sensor ranges between 83 pF and 93 pF. With a width of 18 µm and a strip implant length of 32762 µm this results in a normalized value of $1.41\,\mathrm{pF/(cm\mu m)}$ to $1.58\,\mathrm{pF/(cm\mu m)}$. From the simple estimation made with the plate capacitor formula with the values of the oxide and nitride given in table 8.9, a value of

$$C_{\mathrm{Coupling}} = \frac{1}{1/C_{\mathrm{SiO_2}} + 1/C_{\mathrm{Si_3N_4}}} = 1.40\,\mathrm{pF/(cm\mu m)} \tag{8.9}$$

is reached. A slightly higher value is actually the outcome of the simulation. With the geometry of the strips shown in figure 8.25 and 1 cm long strips, the coupling capacitance is 27.1 pF. Normalized to the strip width of 18 µm, this results in 1.51 pF/(cm µm). This value is still well within the measured values from Hoffmann [Hof13].

The deviation from a simple plate capacitor can be explained by the lateral diffusion of the implant and the trapzoidal shape of the aluminum over the implant. Taking the area of the lateral diffusion totally into account, the strip width is 19.5 µm. The normalized value of the coupling capacitance would then read $1.39\,\mathrm{pF/(cm\mu m)}$, which yields almost the desired value.

This shows two things: first, the simple plate capacitor formula is still quite useful for the calculation of the coupling capacitance; and second, the values for the oxide and nitride thicknesses are chosen correctly. Compared to the numbers calculated by Hoffmann [Hof13] for the oxide thickness, the chosen value is about 70 nm less, but there the nitride layer has not been taken into account. Comparing it with the value from Treberspurg [Tre11], the chosen values are at the lower end of the value range. For the overall performance of the simulation however, it is more important to get correct coupling capacitance values instead of taking the absolute values from the optical inspection.

8.4.3 INTERSTRIP CAPACITANCE

The interstrip capacitance is measured at a higher frequency: 1 MHz. This frequency is also used in the simulation. In the simulation however, the interstrip capacitance cannot directly be read off. It has to be calculated from the different contributions of the AC and DC contacts at the strips. The formula for the calculation has been found by Chatterji [C+03] and reads:

$$C_{\mathrm{int}} = C(DC1 - DC2) + C(AC1 - AC2) + C(AC1 - DC2) + C(AC2 - DC1) \tag{8.10}$$

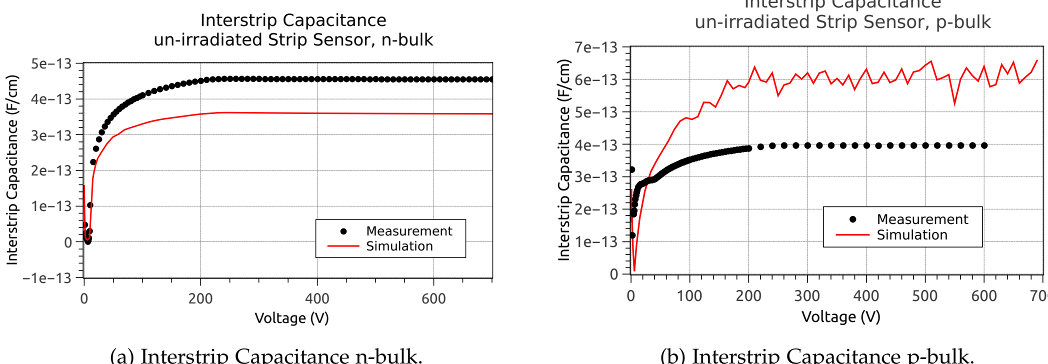

(a) Interstrip Capacitance n-bulk.

(b) Interstrip Capacitance p-bulk.

Figure 8.27: Interstrip capacitance of the simulated strip sensors in comparison with measurements of a FZ320N Bstd sensor:
The measured interstrip capacitance deviates from the simulated interstrip capacitance. The range of the simulated interstrip capacitance is still reasonable though.

In principle it adds all the contributions to the interstrip capacitance, which occur between neighbouring strips, except the coupling capacitance between the AC and DC contact of the same strip. The results for the interstrip capacitance are shown in figure 8.27.

The interstrip capacitance for the shown strip sensors is not so well in agreement as other simulated quantities. The measured interstrip capacitance for the n-bulk strip sensor FZ320N_08_Bstd_2 is higher ($0.45\,\mathrm{pFcm^{-1}}$) than the simulated one ($0.36\,\mathrm{pFcm^{-1}}$). For the p-bulk sensor (FZ320P_04_Bstd_2), it is exactly the other way round; the measured interstrip capacitance ($0.6\,\mathrm{pFcm^{-1}}$) is $0.2\,\mathrm{pFcm^{-1}}$ smaller than the simulated Cint. As observed in the measurement, the simulated Cint for the p-stop strip sensor is higher, although the layout is the same except for the two p-stops in between the strips. Although the interstrip capacitance for the two strip sensors does not totally agree with the simulation, the range of the simulated Cint is still in the correct order of magnitude. Experimentally, large errors (ca. $0.1\,\mathrm{pFcm^{-1}}$) can occur on a single measurement of an interstrip capacitance ramp.

8.4.4 SPICE NETWORK

2d simulations, as done for these strip sensors, are not including structures, which can be found at the end of the strips, namely the bias resistor. The bias resistor has to be included in the simulation of strip sensors manually by adding a readout network. If the bias resistor is not taken into account, the signal coupling, which is a sensitive interplay between coupling capacitance and bias resistor, does not work in the simulation. Figure 8.28 sketches the connection scheme of a strip sensor.

Measurements of the bias resistor can be directly included in the value for the bias resistor in the connection scheme. The values for the bias resistors before irradiation can be found in [Hof13] and are in the range of $1.25\,\mathrm{M\Omega}$ and $2.5\,\mathrm{M\Omega}$, most of the values lying around $1.5\,\mathrm{M\Omega}$. This value has been used as a standard value for the bias resistor. Small changes in the bias resistor value do not much influence the system.

8.4.5 CURRENT IN STRIP SENSORS

Usually, the current of the total strip sensor is measured on the bias ring. As the bias ring is not present in the simulation of a strip sensor, only the current of the single strips can be measured. The current of all strips together sums up to the current through the back plane contact; this is

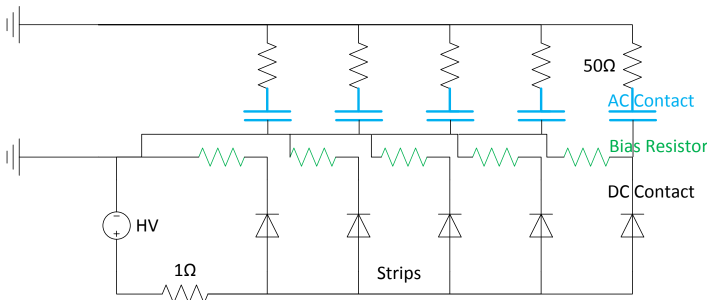

Figure 8.28: Bias network connection scheme of a silicon strip sensor.
The DC contacts are connected to ground via the bias resistor. The AC contacts are connected to ground via a 50 Ω resistor for the readout. Each diode represents one strip, which is connected to the backplane and to high voltage over the backplane contact resistor.

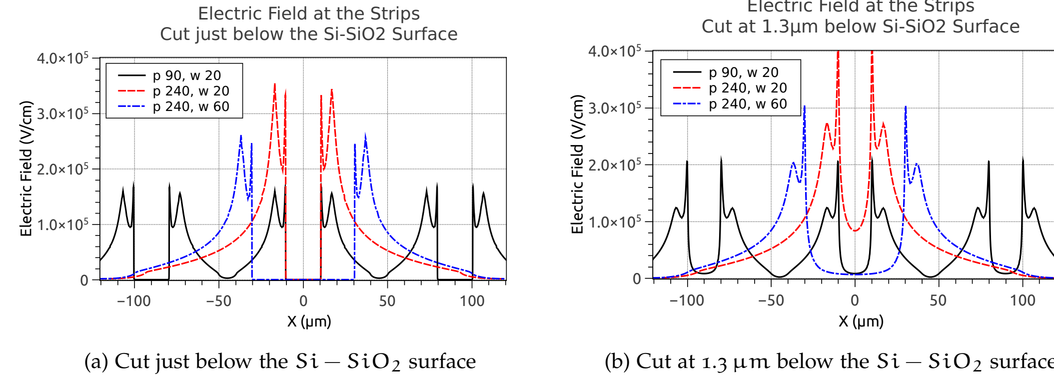

(a) Cut just below the $Si - SiO_2$ surface

(b) Cut at 1.3 μm below the $Si - SiO_2$ surface

Figure 8.29: Electric fields in un-irradiated n-bulk strip sensors at $Q_{ox} = 10^{11}\,cm^{-2}$ and 1000 V:
the fields are highest at the corner of the strip implants. For large pitches and small strip widths, electric fields get higher.

equal to a total current measured on the bias ring. Boundary effects regarding the guard ring cannot be considered, though.

8.4.6 ELECTRIC FIELD AT THE STRIPS

Depending on the initial oxide charge and the strip isolation, the electric fields at the strips of the sensor are influenced. For a stable operation, the electric field at the strips should not be too high. The strip sensors are analyzed with respect to their maximum electric fields before irradiation and a preference is given at the end of this section.

Two extreme pitches, 90 μm – the most probable future pitch for the 2S-module – and 240 μm, are simulated. For the strip width, 20 μm is chosen as the most likely strip width and 60 μm as the maximum strip width fitting in for 90 μm pitch sensors.

8.4.6.1 *N-Bulk Sensors*

Considering an interface charge of $Q_{ox} = 10^{11}\,cm^{-2}$ at the $Si - SiO_2$ interface for a good oxide, the resulting electric fields at the strips at a bias voltage of 1000 V are shown in figure 8.29.

Two cuts parallel to the surface are made to compare the electric fields at the spots with highest electric field. A cut just beneath the $Si - SiO_2$ interface shows, that the high electric fields occur directly at the edge of the implant (e.g. at 10 μm for width $w = 20$ μm) and at the aluminum overhang, 6.5 μm away from the implant. The electric field reaching out from the aluminum overhang of the aluminum strip is still quite high in the silicon region, but most of the electric field is absorbed in the silicon dioxide layer between the aluminum and the silicon bulk.

A cut at 1.3 μm below the $Si - SiO_2$ interface shows, that even higher electric fields occur at the corner of the implants. These fields also depend slightly on the shape of the implant. Having chosen a quite realistic scenario with an implant depth of 2.2 μm and a lateral diffusion of 0.75 μm, these spots define the highest electric field present in the n-bulk sensor.

Both pictures only show the configurations of (p90, w20), (p240, w20) and (p240, w60). The device with pitch 90 and width 20 is not converging in the simulation; very high electric fields between the very close strips are likely the reason.

8.4.6.2 *P-Bulk Sensors*

Oxide charge plays a very important role for silicon strip sensors, when it comes to the isolation of the strip implants. The isolation is only necessary for p-bulk devices, as already mentioned. Measurements of the oxide charge in the HPK oxide by Bernard-Schwarz [BS11] indicate a very good oxide quality and therefore a very low concentration of oxide charges. For n-bulk MOS structures a concentration of $(1.8 \pm 0.6) \times 10^{10}\,\text{cm}^{-2}$ [BS11] has been obtained and for p-bulk a concentration fo $(6.2 \pm 1.3) \times 10^{10}\,\text{cm}^{-2}$ [BS11] has been found.

The oxide charges in the simulation are implemented as a 2d projection of the oxide charge to interface between the silicon dioxide and the silicon bulk; the concentration is given in cm^{-2}. A usual concentration of oxide charges is $10^{11}\,\text{cm}^{-2}$. Considering a high quality oxide, this value can decrease down to $\mathcal{O}(10^{10}\,\text{cm}^{-2})$.

The p-stop geometry of the HPK strip sensors is known very well. The two p-stops are placed near the center between two strips with a distance of 6 μm between them. Their width is 4 μm. The placement in the center is the right choice for low electric fields in p-bulk sensor, as figure 8.30a shows. If the p-stops are placed closer to the strip, the electric field at the p-stop implant increases very much. For a FTH200P sensor, they can even exceed the critical field strength of 3×10^5 V/cm, if the p-stop doping concentration is chosen quite high. The p-stop concentration in the HPK sensors is generally quite low, but the isolation is still working. For the simulations, a p-stop doping concentration of $c = 10^{16}\,\text{cm}^{-3}$ is preferred.

The p-spray isolation does not require any structuring, however again the concentration and the diffusion into the bulk depend on the individual process. Figure 8.30b shows the influence of the doping concentration and the depth of the p-spray on the electric fields near the strip implants. The maximum electric fields are reached for a high doping concentration and deep implant depth. Measurements by Treberspurg [Tre11] show, that the HPK sensors rather have a shallow p-spray doping depth near 0.2 μm and a low doping concentration of $5 \times 10^{15}\,\text{cm}^{-3}$ or lower.

For the standard configuration listed in table 8.9, the electric field at the strips at two different depths can be seen in figure 8.31. The highest electric fields are located near the strip junction at the depth of 1.3 μm. Higher electric fields are also present near the p-stop implant at 35 μm and at the aluminum overhang at 24.5 μm. Note that the pitch of this device is only 80 μm. The electric fields for this device are not high at all.

8.4.7 CHARGE COLLECTION EFFICIENCY

The charge collection efficiency is one of the most important criteria for particle tracking sensors. The design of the strip sensor should be such, that all charge created by a MIP is collected at the strips, independent of the particle's traversing position. Of course, the minimal charge is

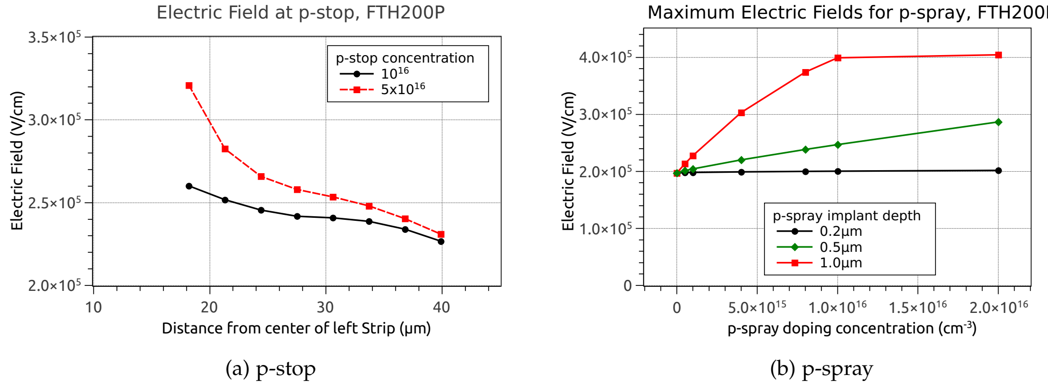

(a) p-stop (b) p-spray

Figure 8.30: Maxmimum electric fields in a FTH200 p-bulk sensor with p-stop or p-spray isolation: *The electric fields increases with higher doping concentrations for both isolation techniques.* Simulations from [Str12].

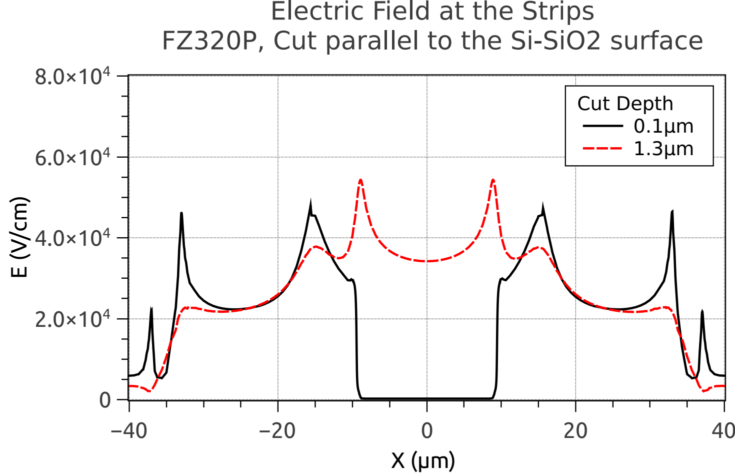

Figure 8.31: Electric fields at the strips for a FZ320P strip sensor (Pitch 80 μm): *The simulation shows the highest electric field at the junction at a depth of 1.3 μm. Still high fields are located at the p-stop at 35 μm. The overall field strength is not critical at all.*

created and collected, if the particle hits the sensor perpendicular to the surface. If the particle hits in the center of one strip, this strip collects almost all of the charges created by the particle. If the particle's position moves towards the neighouring strip, the neighbouring strip collects more and more of the particle's created charge. The total deposited charge is then the sum of the collected charge by the two single strips, it is called cluster charge.

The cluster formation and charge sharing between the two strips is defined by the interstrip resistance and interstrip capacitance. The simulation may not describe the perfect shape of the eta function but it can show general trends regarding the charge sharing and cluster formation depending on the strip sensor design. In this section, the charge collection of a n-bulk and p-bulk strip sensor is shown with the future pitch of the 2S-module of 90 μm. According to the current width to pitch ratio, $w/p = 0.225$, the strip width is $w = 20$ μm.

The simulation of the charge collection efficiency uses the "heavy ion" model to generate charges. The particle track is chosen to be perpendicular to the strip sensor surface. The particle's hit position is varied from the center of one strip (left strip at position 0 μm) and the center between two strips (45 μm, right strip at 90 μm). For the simulation, a device with five strips is used to consider effects including the neighbouring strips.

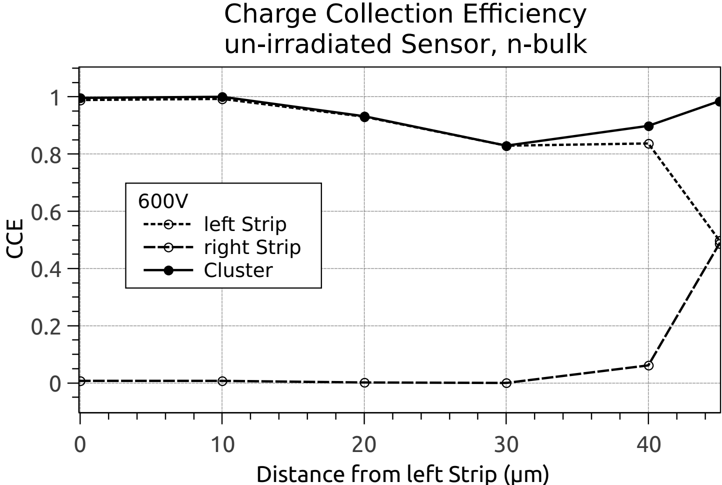

Figure 8.32: Charge collection efficiency of a un-irradiated n-bulk strip sensor with pitch 90 μm geometry: *In the center of the strip, 100% of the charge is collected. At 30 μm, 15% less charge is collected. At the center of the pitch, each strip collects 50% of the signal.*

The induced signals on the AC strips of the strip sensor are recorded, integrated and normalized to the highest collected charge. The integration of the signals is done over the full range of the simulated 20 ns time window. Mostly, the induced signals on the AC strips are negative in n-bulk, however undershoots can appear in the signals, when the charge is first drifting towards the strip and then drifting away from the strip again. The integrated charge can be zero.

Figure 8.32 shows the charge collection efficiency of an un-irradiated n-bulk strip detector. Near the left strip at position 0 μm, all of the particle's created charge is collected by the left strip. In the center between the two strips, the charge is split between the two strips, each strip collecting 50% of the signal. However, already 5 μm away from the center between the two strips, one strip collects about 90% of the charge. For particles hitting the sensor perpendicular to the surface and the strips, the cluster size is mostly one for binary readout.

The simulated collected charge shows the known picture for particles crossing the sensor in the center of one strip and in the middle between two strips. The cluster charge is 100%, collected either by a single strip or 50% by each neighbouring strip. Between the highly doped strip region from 0 μm to 10 μm and the center of the pitch at 45 μm, the collected charge drops. This has not been seen in the test beam so far. However, the simulation has been checked with three different layouts, including a refinement of the mesh around the charge created by the MIP and an overall refined mesh. No difference has been observed between the simulations. It may be, that some charge is lost due to the fixed charges at the $Si - SiO_2$ interface.

For a binary readout, the loss in charge does not affect the efficiency. There is only little charge sharing between the strips in the simulation, which can be positive for binary readout, since the collected signal is not split between the strips up to 40 μm and a signal loss because of the applied threshold is less likely. The situation can change for an irradiated sensor; this is discussed in section 12.2.2.1.

The signals, which have been integrated to get the collected charge, can be seen in figure 8.33. For the left strip, which is near to the particle's hit position, all signals are negative and don't show any undershoot. On the right strip on the other hand, the undershoot of most signals is as large as the positive peak. This means, that the integrated charge is zero for those positions, where the particle hits the sensor near one of the strips. Only near the center between the two strips, the overall collected charge is gaining. In the perfect center between the two strips, it is obvious, that the two induced signals are the same for both strips.

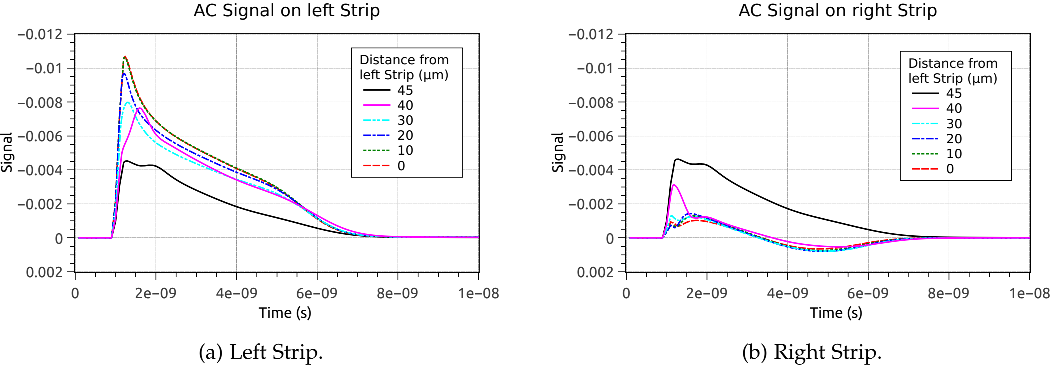

(a) Left Strip.

(b) Right Strip.

Figure 8.33: Signals induced in the left and right strip of a un-irradiated FZ320N strip sensor: *Signals near the left strip don't show any undershoot, whereas the undershoot on the right strip is very large and the integrated charge is almost zero.*

8.4.8 EDGE-TCT

Like the Transient Current Technique, the edge Transient Current Technique has been invented to probe the electric field in silicon strip sensor. First measurements have been done by Kramberger [K+10]. A laser generates charge carriers in the silicon strip sensor. The laser beam enters the sensor from the sensor edge and is focused beneath one strip in the sensor. Usually, only one strip of the sensor is bonded to the readout electronics, which is the same as for the TCT. The transient signals induced in the AC strip can be recorded and used to reconstruct drift velocity and electric field in the sensor at different depths.

The electric field in a strip sensor is different from the electric field in a diode near the strips at the front surface. Usually, inducing a signal will lead to different currents in the strips near the hit, this is because of the weighting field in a strip sensor. The current can be described as

$$I_{e,h}(t) = Ae_0 N_{e,h} exp\left(-\frac{t}{\tau_{eff(e,h)}}\right)\left[\vec{v}_{e,h}(t) \times \vec{E}_w(t)\right] \tag{8.11}$$

Generating electron-hole pairs with the laser parallel to the surface leads to signals on all strips. The sum of the signals from all strips is then the weighting field of a diode, $\vec{E}_w(t) = 1/d$, (see section 5.2.3). The equation above simplifies to

$$I_{e,h}(t) \approx Ae_0 N_{e,h} exp\left(-\frac{t}{\tau_{eff(e,h)}}\right)\frac{\vec{v}_{e,h}(t)}{d} \tag{8.12}$$

Other than with the grazing technique [C+05], which only measures the induced charge, the prompt current is measured with edge-TCT to gain a lot more information.

Edge-TCT measurements are not possible at the IEKP, therefore the signals resulting from edge-TCT are simulated. Corresponding measurements have been done at CERN [Gar12]. Signals are generated with an infrared laserbeam, which hits the sensor at different depths from the sensor edge and is 10 µm wide. In figure 8.34, the laser beam at a depth of 100 µm in the silicon strip sensor is sketched.

The signals in the five-strip device are read out on the AC strip of the center strip. The signals of a FZ320P sensor at different depths can be seen in figure 8.35. The locally created charge cloud is separated in electrons and holes. Electrons drift to DC strips at the front side, the holes drift to the back side. Hence the signal is an overlap of the contributions from electrons and holes. If the red laser generates the signal near the front or back side, the signal looks very

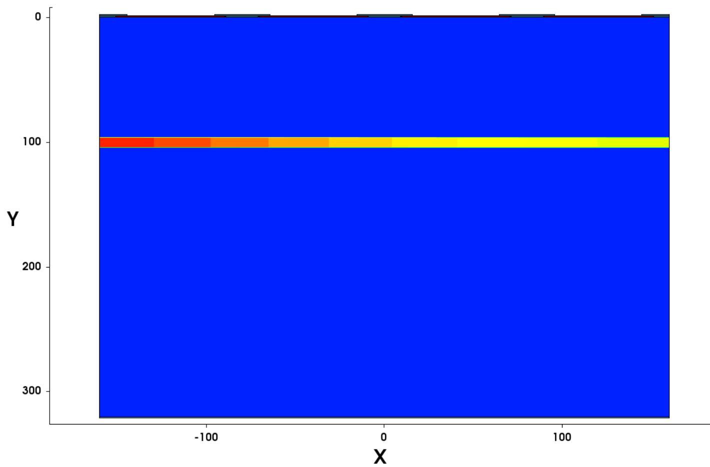

Figure 8.34: The infrared laser beam penetrates the strip sensor from the edge of the sensor.

much like the TCT signal of a red laser in a diode. In the center of the device, both electrons and holes contribute to the signal according to their distance to the electrode.

At 20 μm a very short signal from the electrons drifting to the strip overlaps with a lower and longer signal from the drifting holes. Further away from the strip, the drift distance for the holes is shorter and the hole signal gets shorter; in contrast, the electrons have to drift longer to the strip and the electron signal gets longer. At 280 μm the signal looks again very much like the electron signal in a p-bulk diode.

A FZ320N strip sensor measured with edge-TCT can be seen in figure 8.36. At short distances to the collecting strip, the signal mainly consists of electrons drifting the back overlayed with a short signal from the holes, which are collected at the strip. Going away from the strip, the signal broadens, because the contribution of the hole current to signal increases. Since electrons have a larger drift velocity, the pulses at short distance to the strip are shorter and the contribution of the electron and hole current are not as distinct as for the p-bulk sensor. The signal induced at the back side of the sensor however shows a clear peak for the electrons and a long contribution from the hole current. Due to the readout chain, the signals are distorted.

The implementation of the edge Transient Current Technique in the simulation can help to understand the experimental results obtained with this method, since the technique is quite new and signals in irradiated detectors can be more complicated.

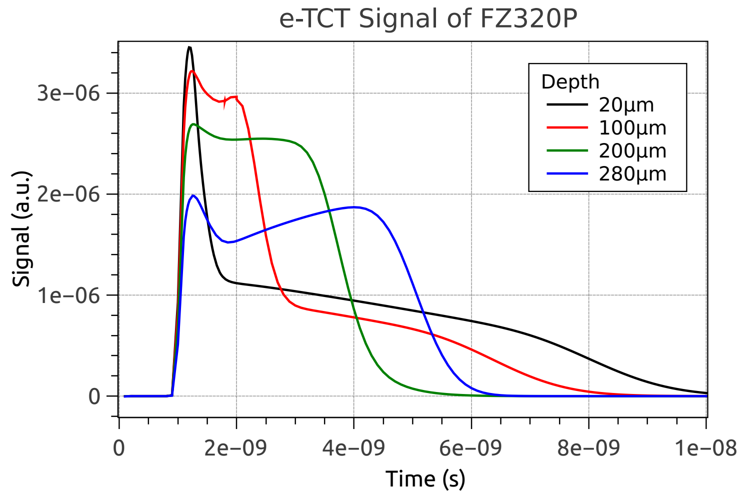

Figure 8.35: Simulated edge-TCT signal in a FZ320P strip sensor:
The contribution of electrons and holes drifting through the sensor can be seen.

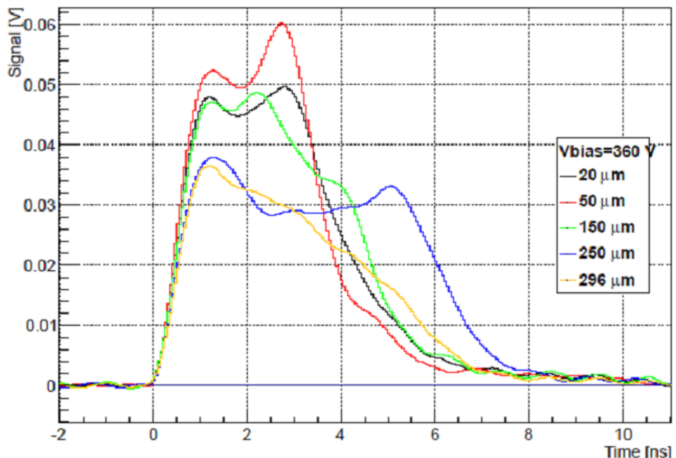

Figure 8.36: Measured edge-TCT signal in FZ320N strip sensor:
At short distances to the strip, mainly the electrons drifting to the back side contact can be seen. At larger distances from the strip, the hole signal contributes significantly. From [Gar12].

9

ADVANCED DIODE DESIGN

The diode design used on the wafers of the HPK Campaign with p-stop isolation do not have a p-stop isolation between the pad and the single guard ring. As it has been shown in sections 8.1.2 and 8.1.3, this leads to ugly results in the IV and CV measurements performed with a connected guard ring. Before depletion sets in, the guard ring and the pad are connected because of the missing isolation and a charge accumulation layer at the surface.

In this way, edge currents distort the picture of the IV measurement done on the pad. If the two needles connecting to guard ring and pad are not exactly at the same potential (ground), even a small difference in the potential (1 mV) can lead to quite high surface currents between pad and guard ring exceeding the currents from the bulk.

This effect is also reflected in the CV measurement. Here the capacitance shows quite high values (low values in the $1/C^2$-plot) until depletion is reached. Thus, the usual technique to determine the depletion voltage cannot be used. The voltage, at which pad and guard ring are isolated, tends to be higher than the depletion voltage of the usual technique.

In this chapter, new designs of diodes are presented. They have been designed in this work to fulfill the requirements of the qualification procedure and the needs for TCT measurements (small capacitance, high breakdown voltage). The diodes have been integrated on the wafer production at ITE Warsaw in 2012 [Str12] and parts of the new designs on a wafer production run at CNM Barcelona. First, an overview of and a motivation for the different designs is given. The different designs are simulated and their performance with respect to IV and CV measurements is analyzed. The most successful designs have then been implemented on the wafers by M. Printz (IEKP, KIT) [Str12]. The produced diodes are measured in the probestation and the results are compared to the predictions of the simulation. Conclusions on an advanced design are drawn at the end of this chapter.

9.1 Layouts

The original HPK diode design for p-bulk wafers fabricated with p-stop isolation technology works without a p-stop between the pad and the guard ring. This leads to the mentioned aberrations from the expectations. For high voltage operation however, the design works flawlessly.

Starting from this functional design, several options have been defined with the emphasis on a well-defined bulk volume needed for exact measurements of the volume generated current as well as a defined pad area for the calculation of the diode's thickness.

9.1.1 Guard rings

The guard ring of the HPK diodes is not foreseen to be connected to ground in high voltage operation mode. Connecting it to the ground decreases the breakdown voltage significantly. In order to get a well-defined area for the measurements, connecting the guard ring is absolutely necessary. Hence, to extend the scope of the measurements to high voltages, designs with more than one guard ring are considered. The minimal option is a diode with two guard rings, more guard rings are possible, of course. For the TCT measurements, which are performed without guard rings connected, more guard rings lead to a higher capacitance though, which is less favorable for the signal.

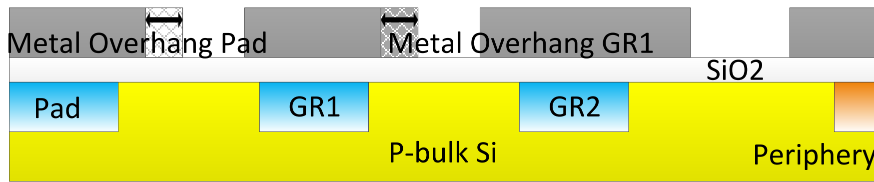

(a) Different metal overhang of the diode pad and inner guard ring.

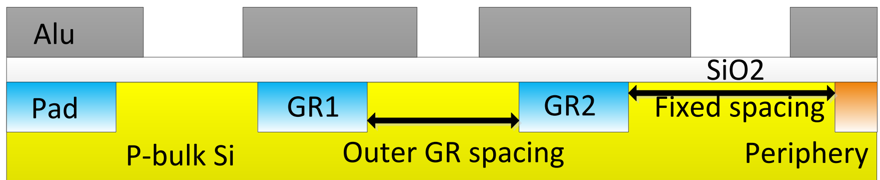

(b) Different spacings of the outer guard ring to the inner guard ring

Figure 9.1: Cut through various diode geometries with two guard rings. The aluminum overhang (grey) of the pad and the inner guard ring are varied and different spacings of the outer guard ring are tested.

Two guard rings offer the possibility to connect one guard ring to ground and leave the outermost guard ring floating. In this way, the high voltage operation is ensured and the pad area is restrained by the inner guard ring. Yet, there is no point in a design with two guard rings, if there is no p-stop isolation implemented, as there would still be a connection between the structures before depletion. Several geometries with different aluminum overhangs and distances between the two guard rings are considered. Different options for the p-stop isolation are explored on top of that.

The basic geometry designs are depicted in figure 9.1. The geometry variations are summarized in table 9.1.

Picture 9.1a shows different metal overhangs of the pad and the inner guard ring. The metal overhang has an influence on the breakdown voltage of the diode. If the metal overhang is too small, the large electric field occuring at the corner of the metal over the silicon dioxide coincides with the large electric field appearing at the edge of the implant and leads to an early breakdown. On the other hand, the aluminum overhang should not be too large because of space consumption.

In picture 9.1b, different spacings of the outer guard ring to the inner guard ring are sketched. The outer guard ring is shifted further out. Because the outer guard ring is always floating, it acts as an mediator between the high potential region at the periphery and the grounded region at the pad and inner guard ring. Shifting the outer guard ring and the periphery further out is more space-consuming but should be more tolerant to high voltage.

An option with five guard rings instead of only two guard rings has been implemented on the production wafers to compare breakdown performance.

9.1.2 ISOLATION

To isolate the guard rings from each other or the pad, p-stops can be placed between the doping regions of the pad or the guard ring. A certain fraction of the potential will drop at the p-stop, thus one has to be careful placing the p-stop isolation looking at breakdown voltage. Several different scenarios are possible and sketched in figure 9.2:

Table 9.1: Variation of parameters for the advanced diode design. Default parameters are written in bold.

Varied Parameter	Chosen Values
Metal overhang pad (µm)	**22.5**, 40
Metal overhang inner guard ring (µm)	12.5, **32.5**, 40
Outer guard ring spacing (µm)	**62**, 80, 100
p-stop (pad - inner guard) distance[1] (µm)	12, 23, 31

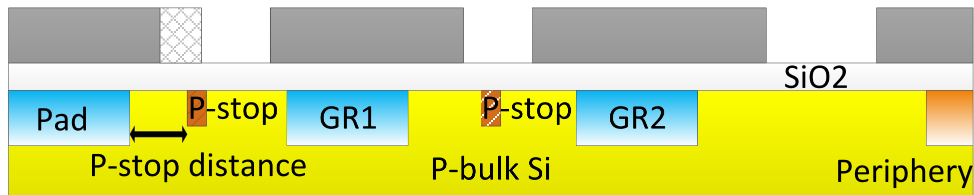

Figure 9.2: Options for the placing of the p-stop. There can be a single p-stop between pad and inner guard ring at two different positions or two p-stop, one between pad and inner guard, the other one between the two guard rings. If the metal overhang of the pad is large and the p-stop is placed near the pad, the metal overhang covers the p-stop.

No p-stop:
: This option has not been included to compare the performance of the diode to the standard HPK diode without any p-stop isolation.

p-stop between pad and guard:
: When looking at the problem naively, only one p-stop isolation is required, namely between the diode pad and the inner guard ring. This ensures the electrical separation of the two structures – the diode should work as desired. Figure 9.2 shows the different implementations for this p-stop: the width of the p-stop is always 6 µm. The distance from the center of the p-stop to the pad is called *p-stop distance*. The values that are used can be found in table 9.1.

  One interesting option arises, when looking at figure 9.2: if the p-stop is placed near the pad and the aluminum overhang is large, the p-stop lies below the aluminum of the pad. The electric field at the p-stop should be reduced by this design.

p-stop between the two guard rings:
: A p-stop can also be placed between the inner and outer guard ring. The distance of the center of the 6 µm wide p-stop to the inner guard ring is always set to 30 µm. Because a single p-stop at this position does not ensure the desired operability, only the option with both p-stops is considered.

9.2 Simulations

The different layouts described in section 9.1 have been simulated. Subject to further analysis are those layouts, which are the most interesting ones in terms of operation and comparison. Breakdown values are identified as the maximum voltage, the simulation reaches before it does not converge any more. Capacitances are analyzed in addition to determine the influence of the p-stop isolation on the measurement.

The simulation device has the different geometries listed in table 9.1. The pad implant is 20 µm wide, for the guard rings, the standard geometry of the HPK diodes has been taken:

- Implant width: 18 μm.
- Metal overhang towards pad: 12.5 μm.

p-stop structures implemented in the simulation are 6 μm wide and have a gaussian shape in depth; the concentration of the p-stop implant is $10^{16}\,\mathrm{cm}^{-3}$ having the same concentration as the bulk at the depth of 1 μm. The value $10^{16}\,\mathrm{cm}^{-3}$ has been chosen, because simulations of Printz showed, that this concentration is sufficient to isolate the structures [Str12].

The distance from the outermost implant of a guard ring to the implant of the periphery has always been set to 240 μm, with a metal overhang of the outermost guard ring of 32.5 μm and a metal overhang of the periphery of 50 μm. These values have shown good high voltage performance in the HPK layout.

The configurations with more than one p-stop do not converge in their current configuration and have been disregarded. Leaving alone this difficulty, more than one p-stop does not improve the desired measurement performance.

9.2.1 BREAKDOWN

First of all, a closer look at the diodes without any p-stop is taken. This already gives hints on the breakdown performance of the different geometries. Implementing a p-stop changes the field configuration near the surface. Higher electric fields can appear, which negatively influences the breakdown performance. Because the "breakdown" voltage has been set as the convergence limit of the simulation, the values might differ very much from reality. The simulated breakdown voltages reflect the expected trends for real devices, but cannot give quantitative results. The functionality has to be confirmed by measurements.

9.2.1.1 *Influence of the spacing between inner and outer guard ring*

The outer guard ring serves as a mediator between the high voltage potential at the periphery and the grounded inner guard ring or the pad. The spacing between the inner grounded guard ring and the outer floating guard ring can have a major influence on the breakdown voltage of a diode. The spacing between the two guard rings has been varied, together with the metal overhang of the pad and the metal overhang of the inner guard ring.

From the simulations it turns out, that an increased spacing between the two guard rings does not improve the breakdown performance. The default configuration with a spacing between the two guard rings of 62 μm works best, deviations may lead to an earlier breakdown.

For the p-stop variations, only the two extremes, a spacing of 62 μm and 100 μm are investigated.

9.2.1.2 *Influence of the p-stop placement*

The p-stop placement depends very much on the metal overhang of the pad. Either the p-stop is placed between the metal overhangs of pad and guard (p-stop distance 31 μm, pad overhang 22.5 μm) or just beneath the extended pad overhang (p-stop distance 23 μm or 13 μm, pad overhang 40 μm).

DEFAULT GR SPACING: All simulations continue up to 1000 V except one configuration: a small p-stop distance to the pad implant with the metal overhang of the pad running over it decreases the breakdown to 531 V.

100 μm GR SPACING: The breakdown performance decreases for two out of the three configuarions. Only the p-stop placed between the metal overhangs reaches 1000 V. The other configurations break at around 370 V.

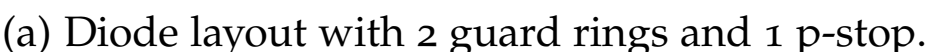

(a) Diode layout with 2 guard rings and 1 p-stop.

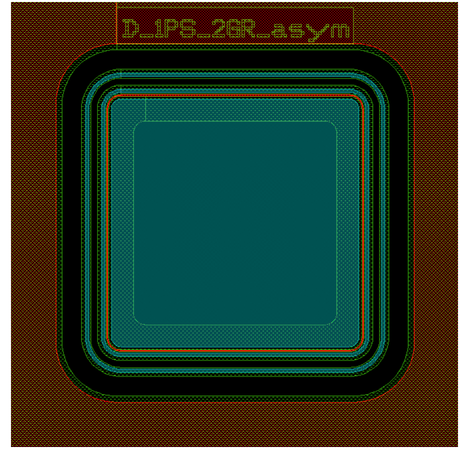

(b) Diode layout with 2 guard rings and 1 p-stop, the outer guard ring is shifter further out.

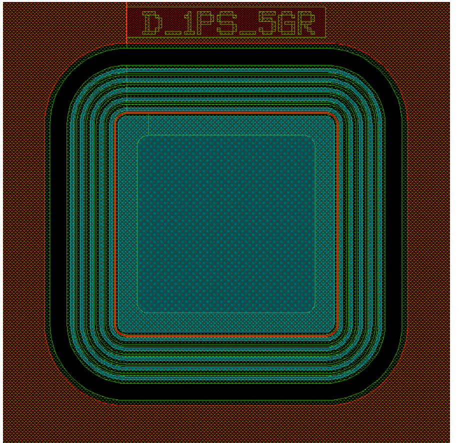

(c) Diode layout with 5 guard rings and 1 p-stop.

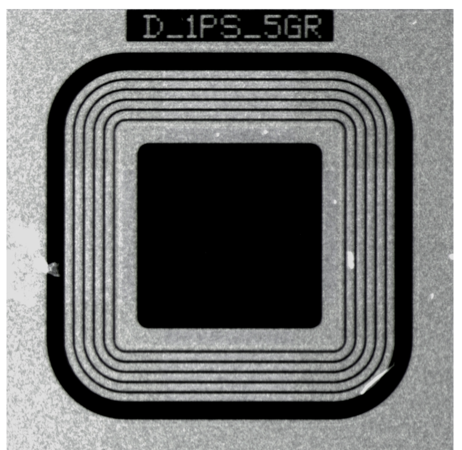

(d) Picture of a diode with 5 guard rings and 1 p-stop.

Figure 9.3: Advanced diode layouts placed on the production wafers at ITE Warsaw and CNM Barcelona. There is always one p-stop between the pad and the inner guard ring, ensuring isolation at low voltages. The p-stop is shown in red, the n^+-implant and the aluminum are shown in greenish colors.

9.3 Layouts on the Wafer

The layouts in figure 9.3 have been placed on the wafer produced at ITE Warsaw and CNM Barcelona.

The name on the diode, seen in picture 9.3b, describes the structures: the number of guard rings is specified by *GR* and the number of p-stop implants is stated by *PS*. *Asym* indicates, that the spacing of the two guard rings is different from the spacing between pad and inner guard ring. “D_1PS_5GR” is describing a diode with 5 guard rings and a single p-stop between pad and inner guard ring.

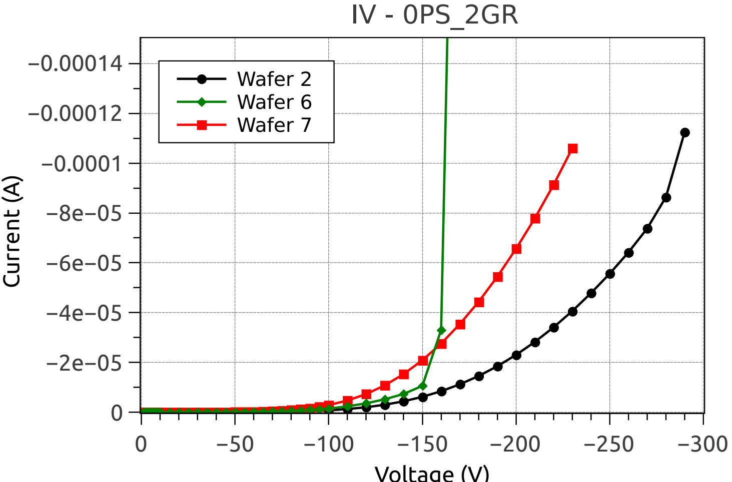

Figure 9.4: Current of the diode with two guard rings and no p-stop isolation on three different ITE wafers.

9.4 Measurements (ITE)

In a first step, the IV of the diode with two guard rings and no p-stop has been measured on the wafers from ITE. As it turns out, the current of the diode on some wafers is so high, that it terminates after a few volts. The diodes on wafer 2, 6 and 7 could be measured and are seen in figure 9.4. The breakdown on wafer 6 occurs much earlier than on wafer 2 and 7, so only the two latter wafers are measured and analyzed further.

The diodes have been measured in the probe station at 20 °C. The frequency for the capacitance measurement is 1 kHz. The guard ring has not been connected in any of the measurements.

9.4.1 Current

The current of all diodes show quite large values already at low voltages. The volume generated bulk current is in the order of $10^{-5}\,\mathrm{A/cm^3}$ already at 50 V, this is two orders of magnitude larger than the current in the HPK diodes.

As it can be seen in figure 9.5, all the different diodes on wafer 2 show the same behaviour. After 100 V the current increases strongly until the breakdown occurs between 230 V and 300 V. The same picture is observed on wafer 7. Here the initial current is a lower, however the breakdown occurs already at 170 V and 180 V for two diodes.

9.4.2 Capacitance

Figure 9.6 shows the inverse squared capacitances for the wafers 2 and 7. The diodes' capacitance is quite small for the diodes are quite small. The diodes group in three different capacitance values. Diodes with 2 guard rings appear to have the same capacitance, disregarding the p-stop isolation. The diode with five guard rings has a larger area, therefore it shows a higher capacitance. The diode with only one guard ring (1GR) and the diode with the p-stop beneath the aluminum of the pad (uAlu) both show strange low values. This fact could not be explained by the simulation. However, on both wafers, the high capacitance for the diode 1PS_uAlu has been measured. This indicates, that this configuration is not desirable. For the operation in the Picolaser Setup, a smaller capacitance is favored.

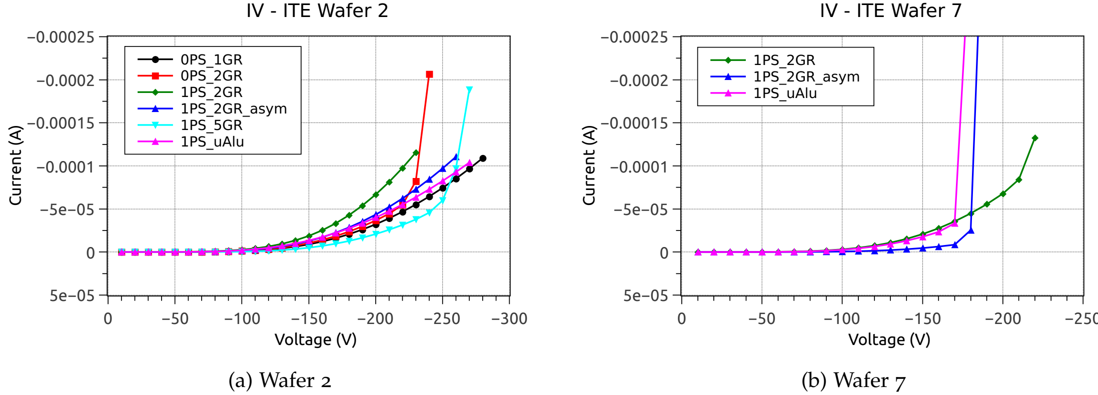

(a) Wafer 2 (b) Wafer 7

Figure 9.5: Current of different diodes placed on the ITE wafer:
The current of all diodes is in good agreement. The overall current is very high and the breakdown occurs between 230 V and 300 V. Wafer 7 shows lower current but also earlier breakdowns.

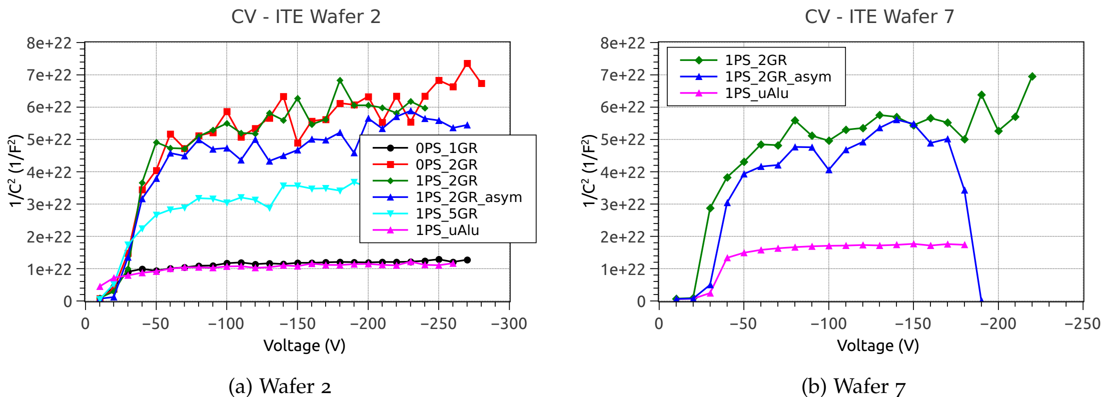

(a) Wafer 2 (b) Wafer 7

Figure 9.6: Inverse squared capacitance of different diodes on the ITE wafer:
The depletion voltage is roughly the same for all diodes. The diodes with p-stop beneath the aluminum, the diode with only one guard ring and the diode with five guard rings have a higher capacitance.

The depletion voltage for diodes with two guard rings on wafer 2 is $V_{depl} = 45\,V \pm 5\,V$, the diodes with a higher capacitance show slightly lower depletion voltages. On wafer 7, the depletion voltages are about $V_{depl} = 40\,V \pm 10\,V$. The bulk doping of these p-bulk wafers can be calculated only roughly to be $N_{Bulk} \approx 6 \times 10^{11}\,cm^{-3}$, which fits quite well with the given values from ITE for the resistance of the wafers (measured by `Topsil Semiconductor Materials A/S`): $13 - 14\,k\Omega cm$.

9.4.3 RESISTANCE BETWEEN PAD AND GUARD

To investigate the isolation power of the implemented p-stop on the diodes, the resistance between the diode pad and the guard ring (R_{PG}) can be measured. The better the p-stop isolates, the higher the resistance. The resistance is supposed to increase with higher voltage, because the electron accumulation layer below the oxide is reduced.

Figure 9.7 shows, that the resistance is very low between the pad and guard ring for almost all measured diodes. This means, that the isolation is very poor. A dependence on the wafer can be seen too. Wafer 2 seems to isolate better with higher voltages, the resistance for the two diodes on wafer 7 shown here is always lower and has a more shallow slope.

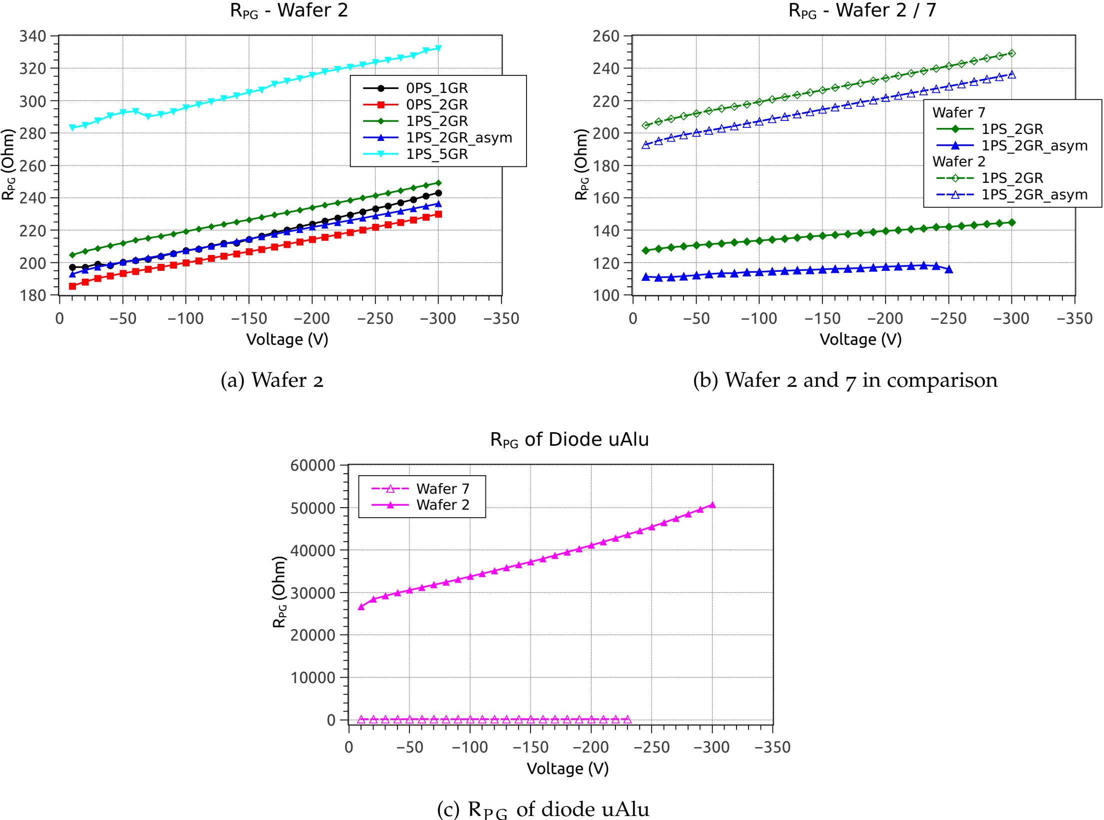

(a) Wafer 2

(b) Wafer 2 and 7 in comparison

(c) R_{PG} of diode uAlu

Figure 9.7: R_{PG} measurements on diodes on the ITE wafer:
The resistance between pad and guard ring is very low, this indicates, that there is no isolation between the structures. Wafer 2 seems to isolate a bit better. The diode with the p-stop just beneath the pad aluminum shows a high resistance value.

One positive exception has been found for the diode with the p-stop beneath the pad aluminum (1PS_uAlu). The resistance is at least $R_{PG} = 30\,k\Omega - 50\,k\Omega$, but still too low for a good isolation.

9.4.4 CONCLUSION ON ITE DIODES

The diodes produced by ITE with different implementations of two guard rings and p-stop placements have been measured. It turns out, that the current is quite high, which usually comes from impurities during the production process or the production itself. Because all diodes break before 300 V is reached, a conclusion about breakdown performance of the different layouts is not possible.

The capacitance measurements show a depletion voltage which lies around $40\,V - 50\,V$. This is in good agreement with the wafers' resistivity claimed by Topsil.

The resistance measured between pad and guard ring of the different diodes reveals, that there is no isolation between pad and guard on any diode. The most probable explanation is, that the doping concentration of the p-stop implant has been chosen too low.

Regarding the high currents and the low doping concentration of the p-stop, the performance of the different layouts has to be probed in a further production. The layout D_1PS_uAlu however is not considered any more because of its high measured capacitance.

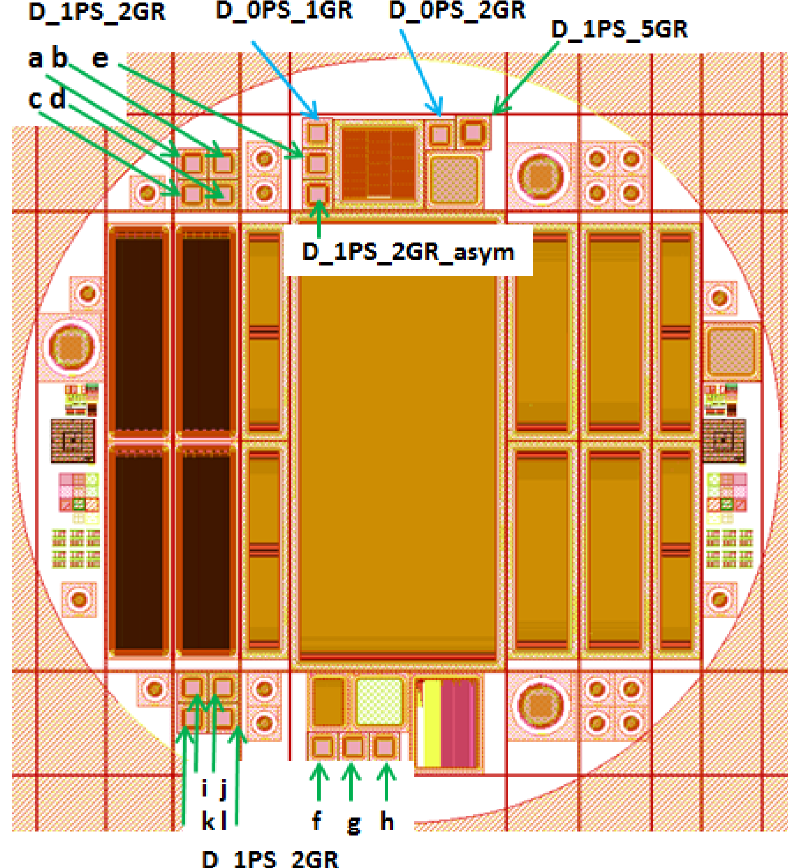

Figure 9.8: Layout of the CNM wafer. The position of the measured diodes is marked.

9.5 MEASUREMENTS (CNM)

After the production of wafers at CNM, a first wafer has been tested to prove the functionality. All diodes placed on the wafer are operational. Most of the diodes are layouted as a diode with two guard rings and one p-stop isolation between the pad and guard ring (D_1PS_2GR). In addition to these diodes, a diode with only one guard ring and no isolation is present (D_0PS_1GR), as well as a diode with two guard rings and no isolation (D_0PS_2GR), a diode with five guard rings and p-stop isolation (D_1PS_5GR) and a diode with a larger guard ring spacing and p-stop isolation (D_1PS_asym).

The position of the different diodes on the CNM wafer is depicted in figure 9.8.

The total current of the diodes, shown in figure 9.9, measured with guard ring is dependent on the position of the diodes on the wafer. For comparison, only the diodes D_1PS_2GR (a – l) are examined. The grouping of the diodes is very much visible. Diodes a – d show almost the same current, diode e exhibits a lower current. The group of diodes in the bottom center of the wafer (f – h) shows the highest current, which is a factor two more than the other diodes.

The last group in the bottom left of the wafer (i – l) is split in two groups. The upper diodes show very low currents, whereas the lower diodes show double the leakage current. This effect is not very clear, because the diodes are positioned very close together. However, the leakage current can increase due to processing or handling at certain positions.

Indicated by the saturation value of the leakage current above 40 V, all diodes can be operated at least up to three times the depletion voltage and still show quite a low volume current $\mathcal{O}(10^{-6}\,\mathrm{A/cm^3})$ at 20 °C.

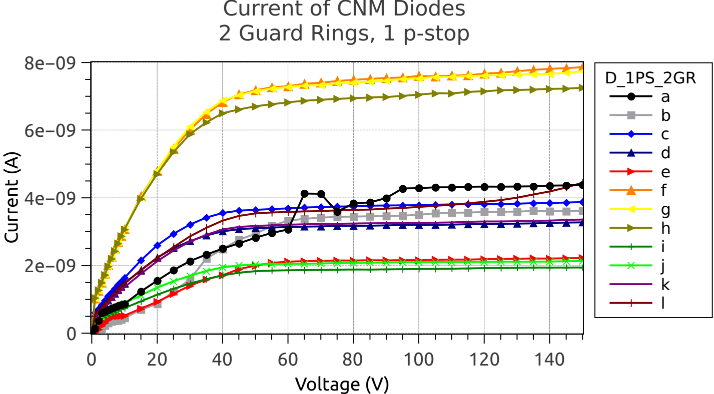

Figure 9.9: Current of diodes with two guard rings and one p-stop across the CNM wafer: *The current of diodes close together on the wafer is nearly the same. The diodes are mostly grouped by their position on the wafer.*

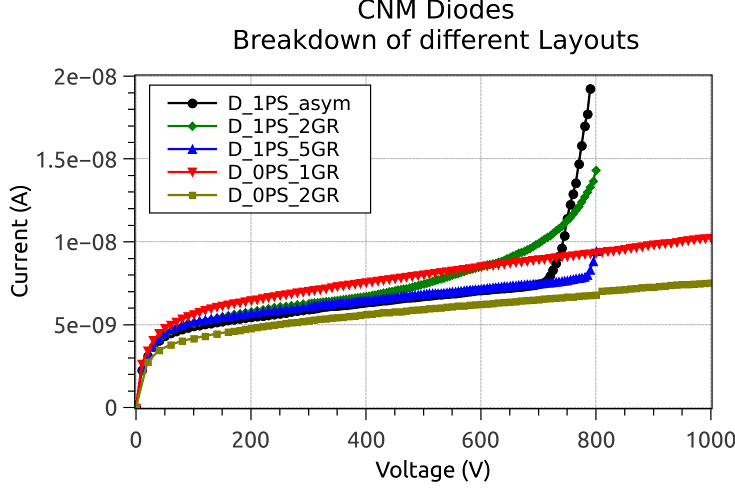

Figure 9.10: Breakdown behaviour of the different diode layouts on the CNM wafer: *Diodes with p-stop between pad and guard break at 800 V.*

9.5.1 BREAKDOWN

All types of diodes on the CNM wafer show a very good breakdown behaviour, which can be seen in figure 9.10. Guard rings are floating for this measurement. The classical diode with only 1 guard ring as well as the diode with 2 guard rings and no p-stop isolation structures reach 1000 V. As soon as there is a p-stop isolation between the pad and the first guard ring, the breakdown voltage decreases. Still, all diodes show a low current up to 800 V.

From the layouts with p-stop isolation, the diode with five guard rings shows the best performance. The current is not influenced by any other effects than the bulk current up to the breakdown at 800 V.

The diode D_2GR_asym, where the second guard ring has a larger spacing to the first guard ring, also shows a good behaviour, however the breakdown already starts at 700 V.

All diodes of the type D_1PS_2GR show a larger increase in the leakage current at higher voltages than the other diodes, but are also operational up to 800 V.

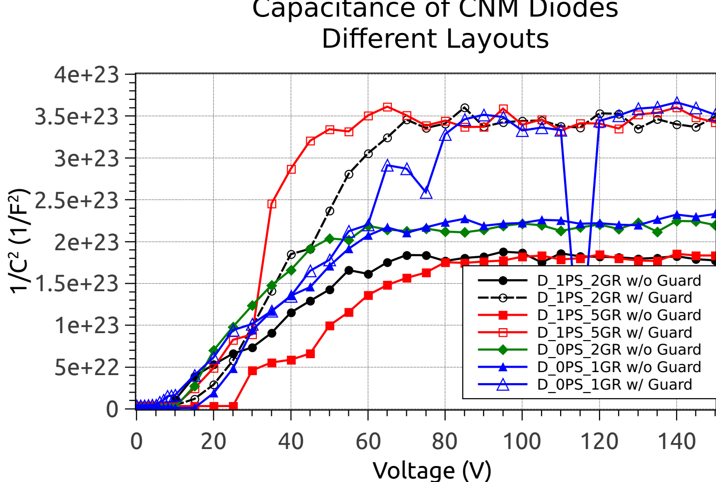

Figure 9.11: Capacitance of different diode layouts on the CNM wafer:
Diodes measured with guard ring reach the same end capacitance because of the same active area. With floating guard ring, diodes without p-stop isolation between pad and guard ring show a higher $1/C^2$ *value.*

9.5.2 CAPACITANCE

The capacitance of all diodes is measured at 20 °C and at 1 kHz. Due to the small capacitance of the diodes, the values are fluctuating because of the experimental measurement limits in figure 9.11. Diodes measured with guard ring show the same end capacitance. This is expected because of the same active area of all diodes, when the guard ring is connected to ground. If the guard ring is left floating, $1/C^2$ shows lower values for diodes with a p-stop isolation. This means, that the p-stop isolation is introducing an additional capacitance to the diodes. However, the absolute difference of the capacitance is quite small. The best option for TCT measurements would be to connect the guard ring to ground for a lower capacitance of the pad.

The depletion voltage of the diodes is different for different layouts and dependent on the guard ring connection. There is no clear trend visible, but all diodes fully deplete between 60 V and 80 V. This corresponds to a resistivity of the wafers of about roughly 14 kΩcm.

9.5.3 RESISTANCE BETWEEN PAD AND GUARD

From the optical inspection seen in figure 9.12, the p-stop placement between the pad and first guard ring can be seen on diodes with p-stop isolation in comparison with diodes without p-stop isolation.

To confirm the proper operation of the p-stop isolation, the resistance between the pad and first guard ring is measured. The results are shown in figure 9.13. The guard ring and the pad are very well isolated, as soon as there is a p-stop in between both structures. On the diode without any isolation structure, R_{PG} is very low before the full depletion voltage and the structures cannot be considered isolated. Only after depletion, the R_{PG} is in the same range as for the other diodes.

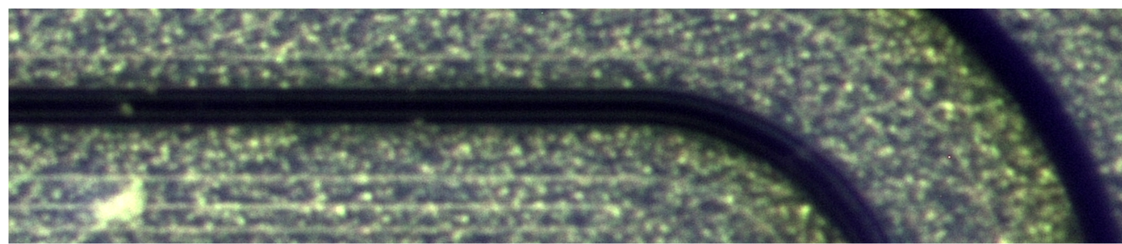

(a) With p-stop isolation

(b) Without p-stop isolation

Figure 9.12: Optical inspection of CNM diodes:
The p-stop isolation on diodes can be seen very well with the microscope.

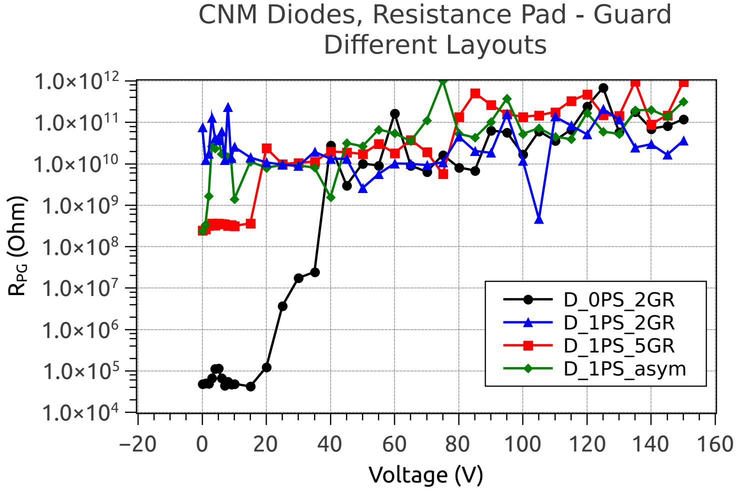

Figure 9.13: Resistance between pad and guard ring (R_{PG}) of diodes on the CNM wafer:
All diodes with p-stop isolation between pad and guard ring show a high resistance, the structures are isolated.

9.6 Conclusions

Diodes on p-bulk wafers need an isolation structure between the different doping regions of the pad and the guard rings, otherwise the doping regions are shorted at low voltages due to an electron accumulation layer at the $Si - SiO_2$ interface. This shortcut disturbes the capacitance measurements in the probe station below the depletion voltage. To provide a better functionality for the electrical tests in the probe station as well as for TCT measurements, not degrading the high voltage performance of the diodes, first simulations have been carried out. Promising layouts have been implemented on wafers fabricated at ITE Warsaw and CNM Barcelona.

The principle idea is to isolate the diode pad and the guard ring to ensure low voltage operability for IV and CV measurements with guard ring. To prevent early breakdowns due to the grounded guard ring, a second floating guard ring takes care of the high voltage functionality. Because of the electron accumulation layer at the $Si - SiO_2$ interface in p-bulk diodes, the pad and guard rings are shorted, unless a p-stop isolation is introduced between the pad and the first guard ring. This provides a defined area, thus a defined volume for exact current measurements as well as a for a good estimation of the wafer thickness and doping profile from CV measurements.

Simulations of various layouts have shown, that one p-stop isolation between the diode pad and first guard ring is sufficient to maintain isolation at low voltages. The p-stop should be placed between the metal overhangs of the structures. The configuration with a smaller metal overhang towards the pad and a larger metal overhang towards the periphery works best. Shifting the second guard ring away from the first guard ring does not improve the high voltage performance.

Measurements on diodes from the ITE wafers showed a depletion voltage around 50 V and quite high leakage currents. All diodes are working, the design with a p-stop placed underneath the metal overhang of the diode pad is ruled out because of a higher capacitance, though. The resistance measured between pad and guard ring reveals, that there is no or not sufficient p-stop isolation on the wafer. A conclusion on the functionality of the design cannot be drawn from these diodes.

Diodes from the CNM wafer show an overall good quality. The volume generated current is low and the depletion voltage is around 50 V. All diodes are operable up to at least 800 V. The desired design with p-stop isolation shows an earlier breakdown compared to the classical design, but beyond the range of interest. Diodes with p-stop isolation also show a slightly higher capacitance with two floating guard rings. The resistance measurement between pad and guard ring clearly shows the working p-stop isolation, hence the volume is very well defined even at low voltages. The three designs show quite equal performance. Regarding space consumption and functionality, the simplest design D_1PS_2GR is recommended.

10

SENSOR WITH INTEGRATED PITCH ADAPTER

A new sensor design, which includes the pitch adapter adapting the pitch of the sensor to the pitch of the readout chip directly on the sensor has been developed. At one edge, a specially desigend pitch adapter region is implemented. The "sensor with integrated pitch adapter" can save material budget in the tracker since no extra pitch adapters, introducing additional material in the tracker region, are needed. To test the new design, this sensor is included on the wafers of the HPK Campaign.

Two basic approaches exist to investigate a sensor featuring a pitch adapter: the pitch adapter in the first and only metal layer and the pitch adapter in a second metal layer, decoupled from the first metal layer by a thick silicon oxide. For the later implementation, several wafers have been processed with a second metal layer. The devices, on which this pitch adapter is included, are the *Baby Standard* sensors (Bstd) in the second metal layer and the *Baby Pitch Adapter* sensors (BPA) in the first metal layer.

They have already been subject to investigations in [Kor11] and [Ebe11]. More detailed investigations on these structures and corresponding simulations are to follow in the next sections.

10.1 Integration on first Metal Layer

The sensor with integrated pitch adapter in the layout of the first metal layer is not very different from a standard sensor design. The sensor differs only in the last 2240 µm of the sensor at one edge, where the strips are read out. The aluminum strip, usually running over the strip implant, stops and narrow aluminum lines route to the readout pads at a smaller pitch. Figure 10.1 shows the pitch adapter region of the BPA. Although the region occupies only 8% of the total surface area of the BPA, it influences the performance of the sensor significantly.

Current-Voltage measurements and Capacitance-Voltage measurements have been performed as usual; there is no difference to a usual standard sensor. Also the strip parameters bias resistance, pinhole and strip leakage current don't show any peculiarities.

10.1.1 BPA: Coupling Capacitance

The plate capacitor, formed by the aluminum strip running over the strip implant, indicates the quality of the signal coupling from the implant to the readout strip. Because the aluminum strip is not running over the total implanted strip, the coupling capacitance is less than usually expected. The difference is mainly geometrically explained: on some strips, the narrow aluminum routing strip follows the implant much longer than on other strips, where the routing line crosses severals strips at a certain angle. Figure 10.2 shows the coupling capacitance measured on a FZ320N BPA sensor.

The outermost strip is the strip with shortest aluminum strip over the implant. Taken from the GDS file, the aluminum strip is 29924 µm long. The longest aluminum strip, taking the routing into account, is 31864 µm. However, in the last 1940 µm, the routing strip is only 10 µm wide except for the two readout pads, which are even 58 µm wide. The coupling capacitance of the longest aluminum strip calculated from these numbers should therefore be 4% more than that of the shortest aluminum strip. This agrees quite well with the deviations found

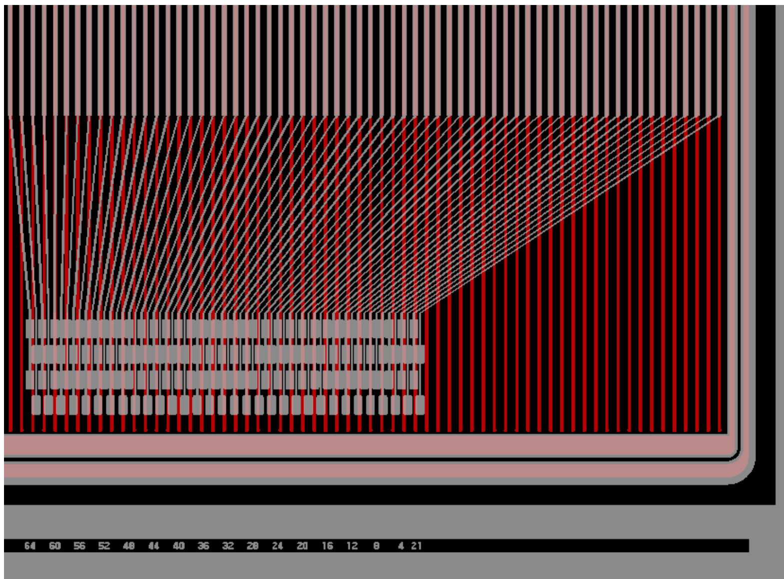

Figure 10.1: **B**aby **P**itch **A**dapter integrated on the first metal layer:
The aluminum strip running over the implant strip ends at some point and narrow aluminum routing strips adapt the pitch of the sensor to the readout pads for the electronics.

in figure 10.2. The routing of strip number 60 and 69 cover the implant of that strip and the coupling capacitance is highest with a 3.6% larger capacitance than the other strips.

10.1.2 BPA: Interstrip Capacitance

The interstrip capacitance, an indication for the signal coupling to neighbouring strips, is very different from a standard sensor. In figure 10.3 it rises from the outer strips towards the inner strips, peaking at strip 59 and 70. The very inner strips show again a very low interstrip capacitance; this is due to the small overlap of routing lines and readout pads of neighbouring strips. In the region, where many routing lines overlap with the implants of the strips, the coupling to the neighbours is higher. The increase of the interstrip capacitance is much more severe than the increase of the coupling capacitance in figure 10.2. The maximum increase for C_{int} is almost 180% of the values in the outer region. This can have an effect on the signal as shown in the next section.

How the overlap of the routing lines and the readout pads over different strip implants influence the interstrip capacitance can be seen in figure 10.3b. One needle is placed on a distinct AC strip and the coupling capacitance to neighbouring DC is measured at 1 MHz, the frequency at which the interstrip capacitance is usually measured. The picture is very interesting: the capacitance is of course largest, if the coupling between AC and its own DC contact is measured. Depending on the overlap of the aluminum and readout pad of the neighbouring strip, an additional capacitance of at most 2 pF is measured. The capacitance of strip 61 to strip 60 for example is very low, because there is no aluminum overlap. The capacitance from strip 61 to strip 62 however, shows a capacitance of 2 pF; the readout pad and aluminum routing of strip 62 is mostly lying directly over the implant of strip 61.

In the case of no overlap of the routing lines of other strips, the interstrip capacitance is at the level of a baby standard sensor.

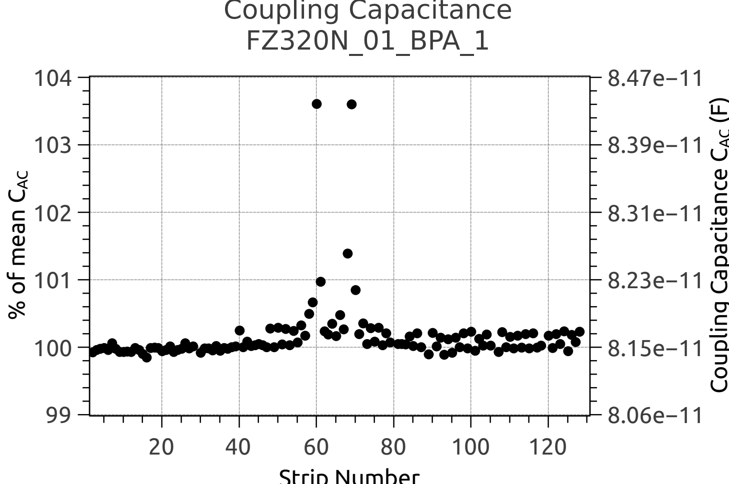

Figure 10.2: Coupling Capacitance of a FZ320N BPA sensor:
Most of the strips show the same coupling capacitance except some strips in the center of the pitch adapter region, where the routing line lies directly over the same implant as the aluminum readout strip.

10.1.3 BPA: SIGNALS

In most of its area, the design of the BPA is not different from a standard sensor and so the signals don't differ, as showed by Kornmayer [Kor11]. Because the BPA differs from a standard sensor in the pitch adapter region, the behaviour of the signals generated in that region is of interest. A strontium-90 source has been placed over this region at four positions over one half of the BPA (strip 1 to 64). These four runs have been combined and analyzed to get the signal and signal to noise ratio [Kor11]. In figure 10.4a one can see, that the total cluster signal from strip 10 to 25 collects the right amount of electrons generated in a 320 μm thick sensor. Again in the region with many crossing routing lines, the cluster signal drops to 15000 collected electrons; this corresponds to a signal loss of about 35%. With less crossing routing lines in the central region of the pitch adapter senor, the collected charge rises again.

Because the signal drop is dominating in the region from strip 30 to 55, also the signal to noise ratio drops (figure 10.4b). The noise in the sensor (figure 10.5a) is quite homogeneous over the strips.

The very outer strips are rarely hit by the source and suffer from low statistics. Note that there is a slight loss of signal from strip ten to 25.

In the previous section, it has been mentioned, that the coupling capacitance can affect the signal distribution on the strips. This can be nicely seen in figure 10.5b. The average of hit strips is increasing towards the center of the pitch adapter region, where also the interstrip capacitance is largest.

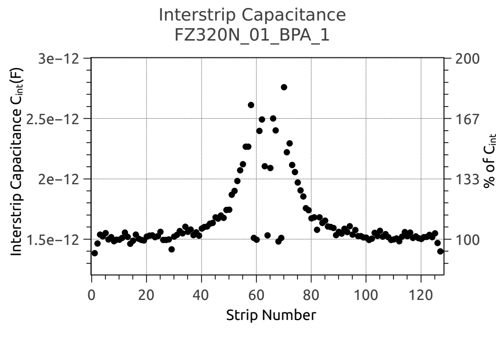

(a) Interstrip Capacitance

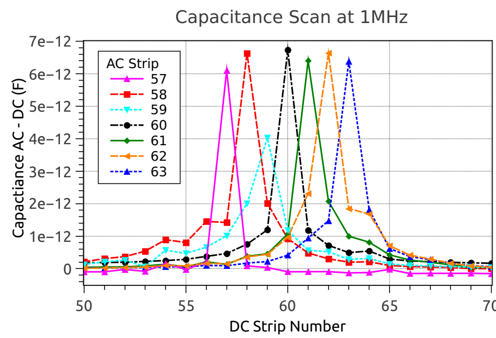

(b) Capacitance between an AC and neighbouring DC strips at 1 MHz

Figure 10.3: Interstrip Capacitance of a FZ320N BPA sensor:
The interstrip capacitance rises towards the center of the pitch adapter region. Because the interstrip capacitance is measured to its right neighbour, the overlap of the routing and the corresponding readout pad increases towards the center of the pitch adapter region. In the center, where there are no readout pads over the strips, the interstrip capacitance is again low. The additional coupling can be approximately determined by measuring the capacitance between one AC strip and the neighbouring DC strips. The capacitance is maximal for the same strip and large for strips with a large aluminum overlap.

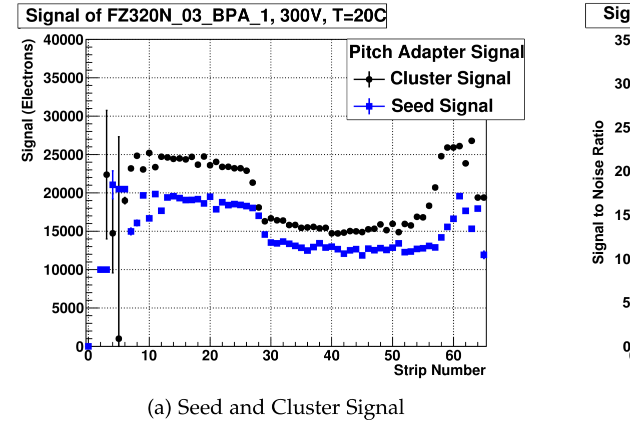

(a) Seed and Cluster Signal

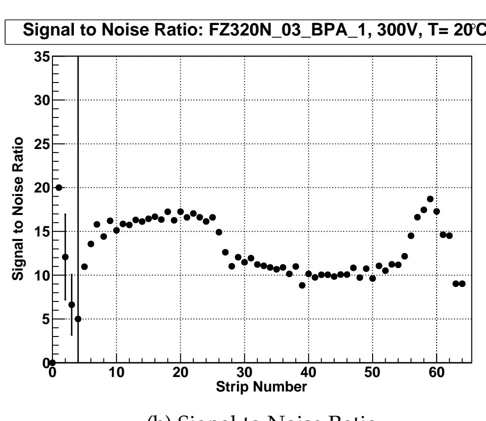

(b) Signal to Noise Ratio

Figure 10.4: Signals and signal to noise ratio of a BPA sensor in the pitch adapter region:
Both, the cluster and the seed signal are as expected in the region without any crossing routing lines. In the region with many crossing strips (strip 30 to 60) the signal decreases from 24000 electrons down to 15000 electrons. This also decreases the signal to noise ratio in this region.
Data from Kornmayer [Kor11].

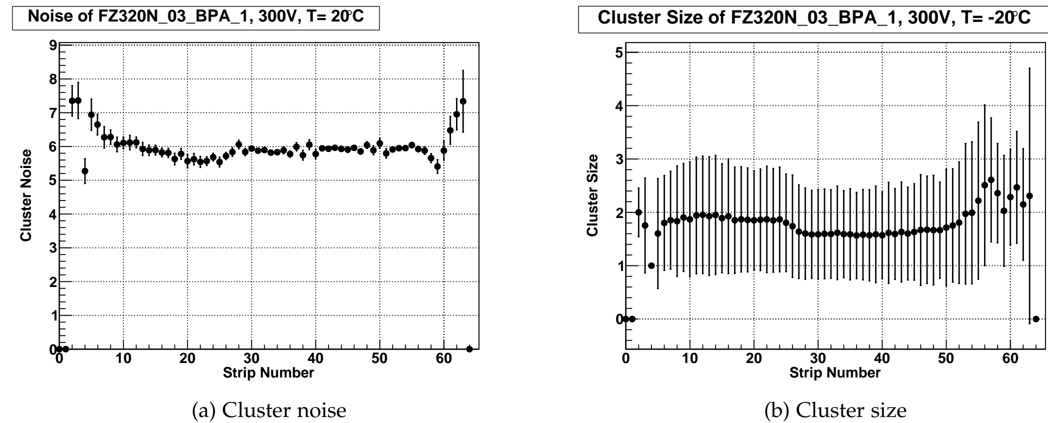

(a) Cluster noise

(b) Cluster size

Figure 10.5: Cluster noise and cluster size measured on the BPA:
The noise is quite homogeneous over the sensor. Only near the sensor edge, the noise is higher due to lower statistics. The effect of the increased coupling capacitance is visible in the cluster size of the signal. The cluster size is larger in the region with large interstrip capacitance.

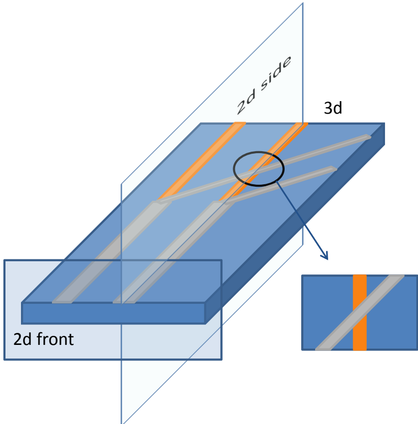

Figure 10.6: Sketch of a simulation device of a BPA:
The best choice for a 2d simulation of a BPA is to cut the device along one strip, featuring the standard strip region and the pitch adapter zone with crossing routing lines.

10.1.4 SIMULATION OF BPA

To get a deeper understanding of the signal loss in the region of the pitch adapter on the BPA, simulations have been carried out. Now the difficulty for the simulation is to do the coupling to the neighbouring strips as well as the crossing routing lines. Picture 10.6 sketches the different possibilities for a simulation.

The best choice to simulate the coupling to the neighbouring strips along with a signal would be a 3d simulation. This simulation however is too time-consuming and too memory-intensive already with only two adjacent strips. A usual 2d simulation, which cuts the device perpendicular to the strips cannot show the signal coupling or signal loss due to the routing lines.

The only 2d simulation, which can handle both aspects reasonably, is to cut the device along one strip. On the right hand side of the device shown in figure 10.7, the standard aluminum coupling strip is seen. On the left hand side, the pitch adapter region is implemented: four pads to account for the staggered readout pads, and up to 20 narrow aluminum lines, which represent the routing lines of different strips. Three configurations are under investigation:

- four pads with 20 routing lines,
- ten routing lines,
- one routing line.

For the simulation device, a profile obtained in chapter 8.1.2 for FZ320N has been used. The 1 μm thick aluminum layer is on top of the thin coupling oxide. For the oxide, the same thicknesses as in section 8.4.2 have been used. The total device is exactly 3 cm long. Only in the left part, 2 mm are occupied by the pitch adapter region seen in figure 10.7.

10.1.4.1 *Coupling Capacitance*

Clearly, the coupling capacitance for the simulation device is defined geometrically. For the simulation, a slightly smaller value for the coupling capacitance is used, which comes from the silicon oxide thickness of 230 nm plus a 40 nm thick silicon nitride layer. The simulation device explained above features a strip, where the aluminum of the actual strip is shortest and most routing lines cross.

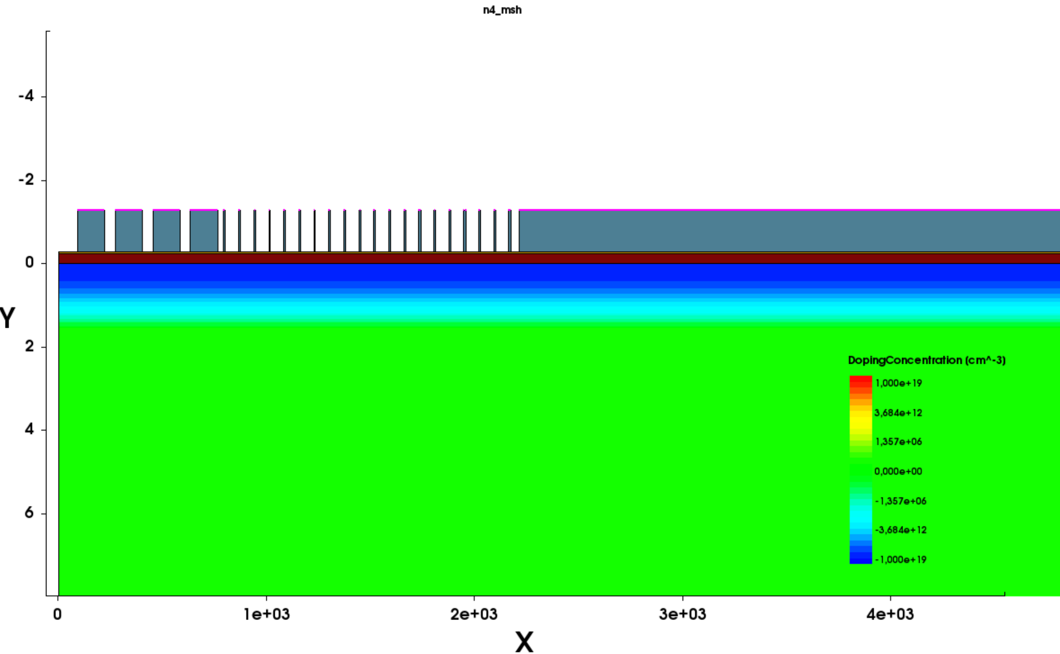

Figure 10.7: 2d simulation model of the BPA:
The cut is along the strip. On the right side is the standard sensor region and on the left side is the pitch adapter region with four larger readout pads and several narrow routing strips of other strips crossing the simulated strip.

A value of 69 pF is high enough to obtain a correct signal coupling to the actual readout strip, yet the measured value is 12 pF larger. Deviations from the measured value can come not only from a different oxide thickness but also from a slightly different strip length or the metal overhang, which cannot be considered in this 2d simulation.

10.1.4.2 *Signal Simulation on the BPA*

For the simulation of a signal, the optics section in Synopsys Sentaurus has been used with a wavelength of 1060 nm, that is an infrared laser. To see the influence of the pitch adapter region in the sensor, several positions along the X-axis have been chosen for a laser shot: from 500 µm to 3000 µm in the pitch adapter region with steps of 500 µm and at 20000 µm to compare with the behaviour of a standard sensor. To speed up the simulation, a quite coarse mesh has been chosen, only around the interesting region of the pitch adapter and the laser shot the mesh is refined. The signal can now be read out on each of the aluminum contacts including the routing strips. In this way, the signal coupling to neighbouring strips due to the routing line can be analyzed.

To compare with measurements, the signal on the AC pad of the strip is integrated over the readout time.

Plot 10.8a shows the simulated signals measured on the AC pad with 20 crossing routing lines and four readout pads. Beginning with position 20000, the signal is the same as at laser position 3000. These signals are generated in the standard region of the sensor, where the AC strip is placed over the implant, where the signal is collected. With increasing distance from the AC pad, from position 2500 to 500, the signal height decreases and the signals get longer. Also, the starting position of the signal is shifted to later times. Depending on the readout chip, a short signal collection time can decrease the signal.

In figure 10.8b the integrated signal is shown versus the laser shot position. The integration time is 50 ns. The simulated configuration with four readout pads and 20 crossing routing lines

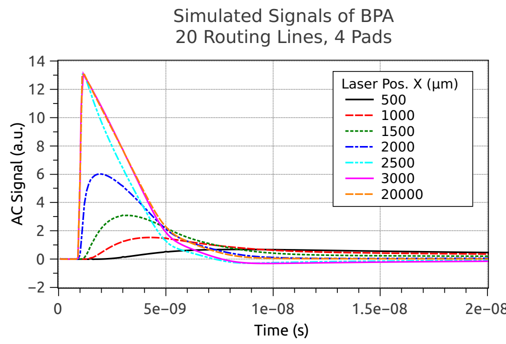

(a) Signals on the AC strip with 20 routing lines and 4 pads.

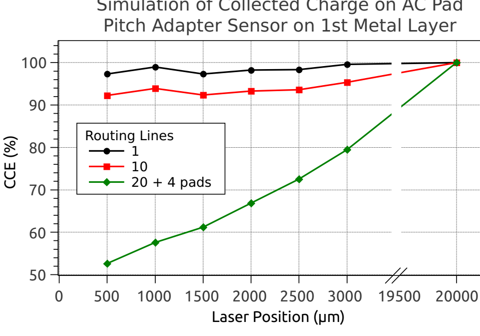

(b) Collected Charge on the AC pad.

Figure 10.8: Simulation of laser signals on the BPA sensor:
The laser generates signals at different positions from the sensor edge. With 20 routing and 4 pads, the signals get lower and slower with increasing distance from the aluminum readout strip. With less routing strips crossing the implant in the pitch adapter region, the collected charge increases.

clearly shows a signal loss in the pitch adapter region depending on the distance to the AC strip. Also the signal at position 3000, which is already beneath the AC strip, still shows a decreased signal because of the coupling to the routing lines.

With less crossing routing lines, that is either ten or only one routing line, almost no signal is lost. With ten routing lines, the signal does not even drop below 90% efficiency.

The simulation can explain the measurements results obtained in figure 10.4a. The signal collection in the area with only few routing lines is quite good. With an increasing number of routing lines from strip 10 to 25, there is a slight decrease in the signal. This is also seen in the simulation: a small number of routing lines does not decrease the signal significantly.

If many routing lines cross the implant of one strip and additional readout pads of other strips are placed over a strip implant, the signal is decreased. Taking the average charge collection in the pitch adapter region, a drop of 35% can be explained very well by the simulation with 20 routing lines and four readout pads.

10.2 Integration on second Metal Layer

To correct the misbehaviour of the pitch adapter sensor integrated on the first metal layer, wafers with a second metal layer have been ordered. The pitch adapter is implemented in the second metal layer of the baby standard sensors. This Double Metal Pitch Adapter sensor (DMPA) has the layout of a standard sensor in the first metal layer. The readout pads and the routing lines of the pitch adapter are processed in the second metal layer, decoupled from the first metal layer by an about 1.3 μm thick silicon oxide. Vias connect the aluminum strips in the first metal layer to the routing lines in the second metal layer. The pitch adapter region of the DMPA can be seen in figure 10.9.

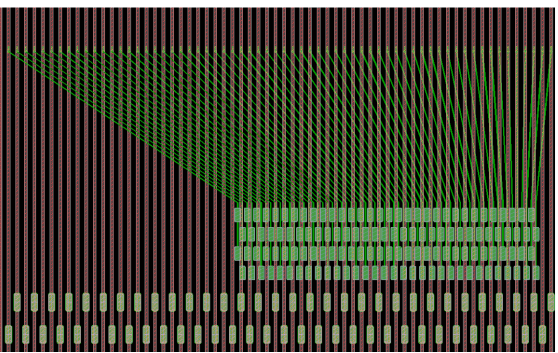

Figure 10.9: Double Metal Pitch Adapter integrated on the second metal layer:
The aluminum strips over the implants cover the whole strip; the routing lines to adapt the pitch of the sensor to the readout are in a second metal layer, decoupled from the first metal layer by a thicker silicon oxide.

Figure 10.10 shows the qualification measurements done on a FZ200 DMPA sensor. All measurements are very good. IV, CV, strip leakage current, interstrip resistance, bias resistance, pinhole and coupling capacitance don't show any deviations from a standard strip sensor. The interstrip capacitance shows the same pattern seen on a BPA sensor. Because the sensor has 256 strips, two pitch adapters are implemented on the DMPA, so there are two peaks visible in figure 10.10h.

The overall picture shows, that the fabrication of a sensor with a second metal works and leads to results, which are comparable to sensors with only one metal layer.

The coupling capacitance, which increased in the pitch adapter region for the BPA, is very homogeneous for the DMPA for geometrical reasons. All strip implants are totally covered by an aluminum strip, so there are no deviations for geometrical reasons.

One exception is the interstrip capacitance. Although the pitch adapter is only implemented in the second metal layer, the capacitance to neighbouring strips is still higher in the region with many routing strips. The effect of the larger interstrip capacitance has only geometrical reasons. The routing strips are closer together in the pitch adapter region and again cross several other strips, this time, however, only aluminum strips and the spacing of the oxide with 1.3 μm is much larger than on the BPA.

10.2.1 DMPA: Interstrip Capacitance

Like in section 10.1.2, the capacitance from one AC strip to several DC strips has been measured at 1 MHz in figure 10.11. Of course, the maximum of each curve is at the point, where the AC strip and its corresponding DC strip is measured. The capacitance of all neighbouring strips is always below 2 pF. In contrast to the BPA, the capacitance of the neighbour strips is distributed more homogeneously and not so much dependent on the geometrical overlap of the aluminum routing lines. The effect of the increasing capacitance towards the measured AC strip is due to decreased spacing between the strips in the pitch adapter region.

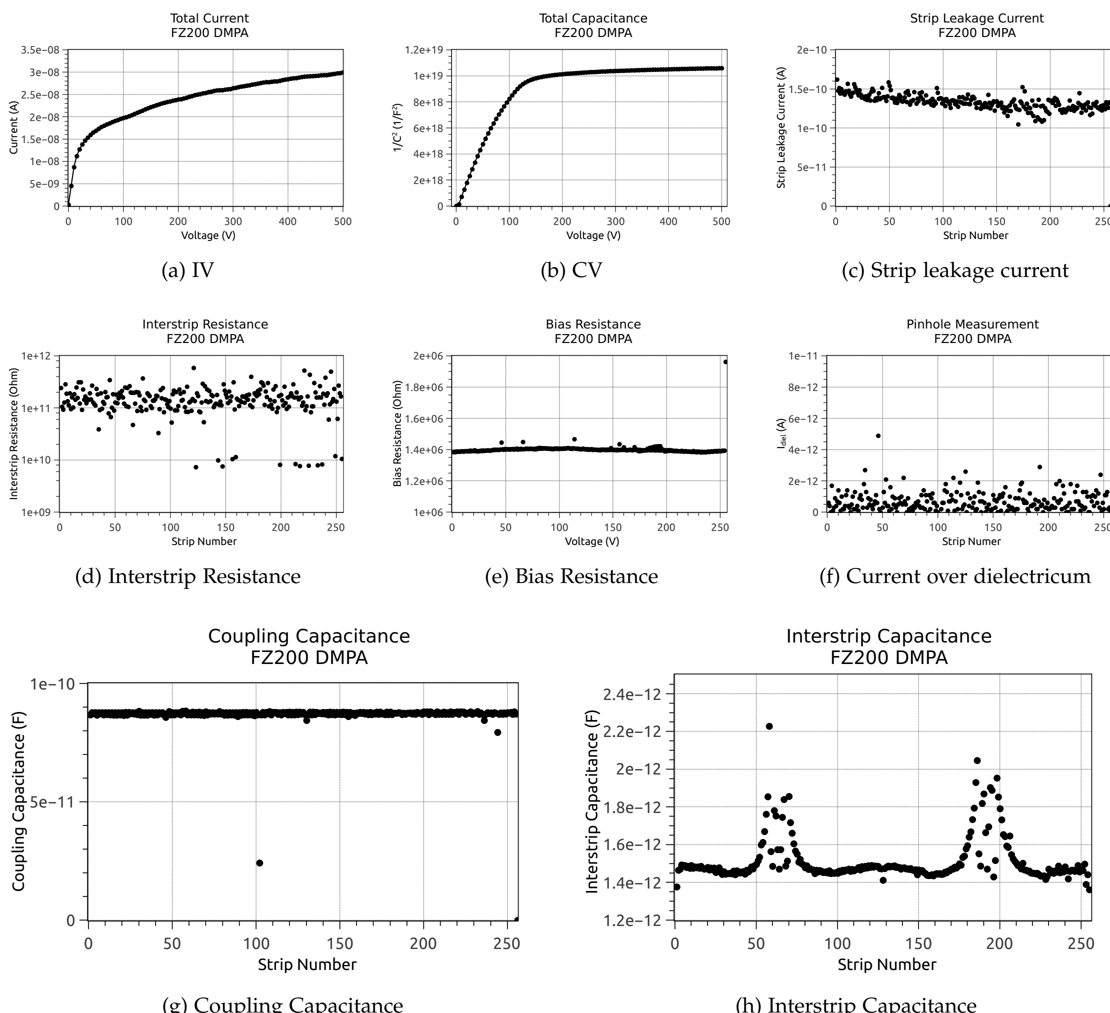

(a) IV (b) CV (c) Strip leakage current

(d) Interstrip Resistance (e) Bias Resistance (f) Current over dielectricum

(g) Coupling Capacitance (h) Interstrip Capacitance

Figure 10.10: Qualification of the double metal pitch adapter sensor:
All measurements are good and don't show any peculiarities. The interstrip capacitance shows the same behaviour as the BPA. As the sensor has 256 strips instead of 128, two pitch adapters are implemented on the sensor.

The overall capacitance of the maximum value between the AC and corresponding DC strip is higher compared to the BPA. This is explained by the fact, that the AC metal strip of the DMPA runs all over the DC strip and therefore has a larger coupling capacitance than the BPA, whose DC strip is shorter to leave space for the pitch adapter routing region.

10.2.2 DMPA: SIGNAL MEASUREMENTS

The double metal pitch adapter sensors have been measured in the strip readout system at the IEKP just like the BPA. Again, one is interested in the signal in the pitch adapter region, hence the source has been placed over this region. Figure 10.12 shows the performance of the DMPA in this region.

Assuming the DMPA to be about 220 µm thick according to the deep diffusion profiles in chapter 8.1.2, it can collect about 17600 electrons. This is exactly the number of electrons, which is collected when looking at the cluster signal. The signal on the seed strip is a bit lower with only about 15000 electrons. The signal is quite constant over the pitch adapter region, there is no signal loss in the region, where many routing strips cross the readout strips. Some

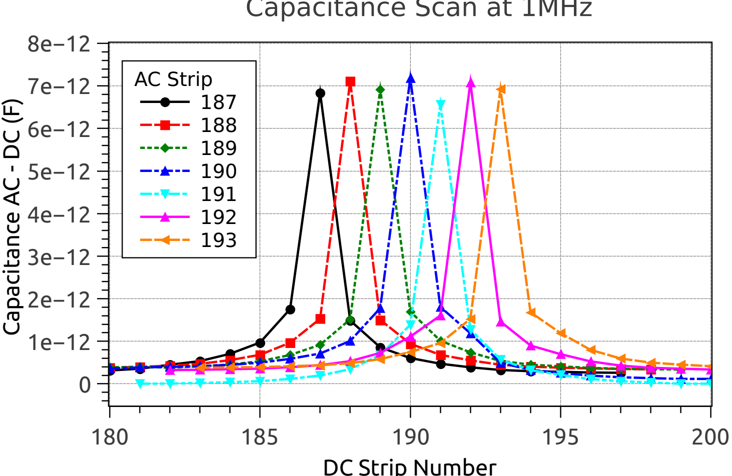

Figure 10.11: Capacitance between AC and DC at 1 MHz for several strips:
The maximum measured capacitance is of course between the AC and corresponding DC strip number. Like in the case for the BPA, the capacitance is higher for neighbouring strips but drops quickly with increasing distance. Unlike the BPA, the capacitance is symmetryically distributed and below 2 pF for the neighbours.

irritations are found in the center of the pitch adapter region: here the signal seems to be lower for some strips. However the errors are quite large and it may suffer from insufficient statistics, for several source runs have been combined to obtain the signal over a large number of strips.

The signal to noise ratio in figure 10.12b shows exactly the same behaviour as the signal in figure 10.12a. It is constantly high at about 17 with some small deviations in the center of the pitch adapter region. Still almost all the strips show a signal to noise ratio which is well above ten.

Although the interstrip capacitance rises in the pitch adapter region for the DMPA too, the cluster size obtained from the measurements is very flat. This means, that the coupling to the neighbouring strips is not as large as expected from the interstrip capacitance. This is in contrast to the BPA cluster size, which increases also with increasing interstrip capacitance. The difference for the signal coupling between the two sensors is, that the routing lines in the first metal layer can directly couple to the underlying implant and collect a considerably large amount of the signal; whereas the routing lines of the DMPA are in the second metal layer and cannot directly couple to any implant. The capacitive coupling between the strips is suppressed in contrast to the coupling of the routing line with implant strip.

10.2.3 SIMULATIONS

The double metal pitch adapter sensor has been simulated in the same way as the BPA: a 2d simulation has been used and the device has been cut along one strip. Instead of implementing several routing lines in the first metal layer, the AC coupled aluminum strip cover the whole sensor. On top of this aluminum strip, a 1.3 µm thick silicon dioxide separates the routing lines from the AC readout strip. One can directly derive, that the coupling of the signal to one of the routing lines in the second metal layer should be much smaller than for the BPA. This is confirmed in figure 10.13, where the coupling of the signal in the pitch adapter region to several routing lines in comparison to the coupling to the AC strip is shown.

Signals have been generated again in different regions of the DMPA: in the pitch adapter region with routing lines in the second metal layer and in the standard region, where there is no second metal layer present. No significant dependence of the signal collected on the

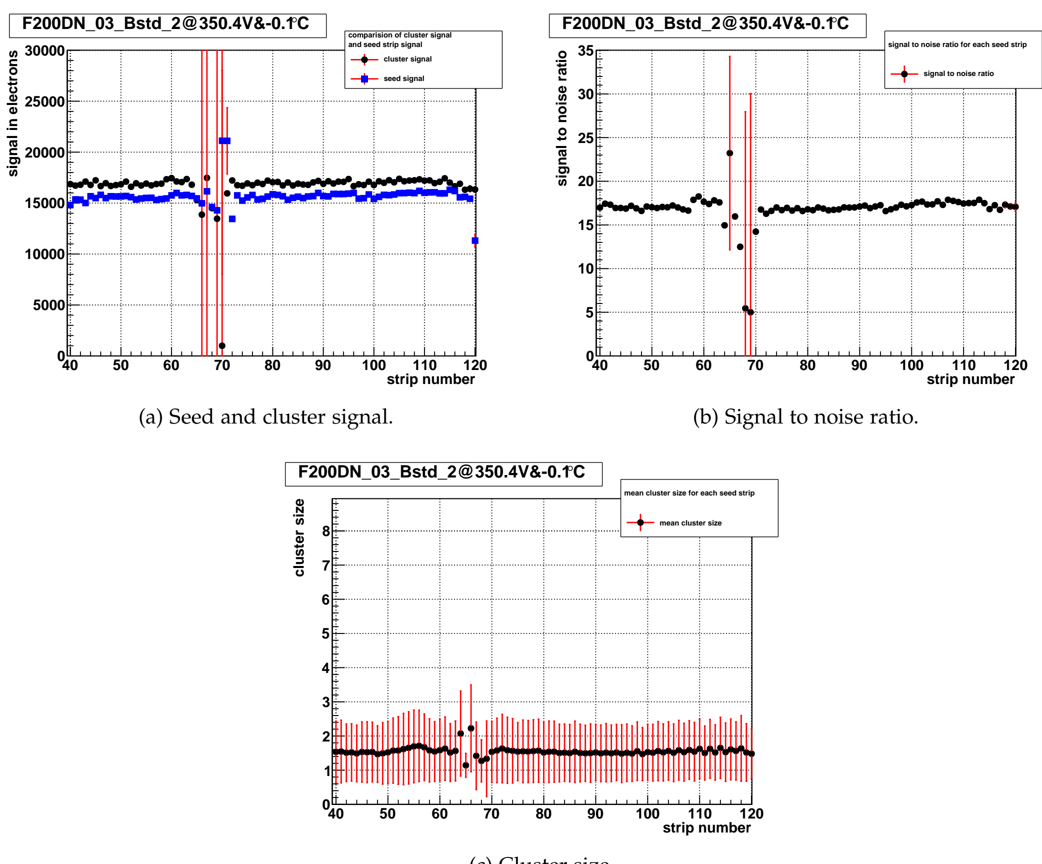

(a) Seed and cluster signal.

(b) Signal to noise ratio.

(c) Cluster size.

Figure 10.12: Measurements performed on the DMPA in the pitch adapter region: *Seed and cluster signal don't show any loss in the pitch adapter region in contrast to the BPA. A constant noise over the sensor leads then to a flat signal to noise ratio. Although the interstrip capacitance is higher in the pitch adapter region, the clustersize is constant over the sensor with a small exception in the center of the PA region.*

AC strip is observed at the different locations. This again confirms the superior signal quality, when the routing is implemented on the second metal.

10.2.4 SUMMARY

Measurements and simulations on the DMPA show, that the coupling of the routing lines to neighbouring strips is still present. However, the signal coupling is mostly suppressed because the strips are totally covered by their aluminum readout strip. The signal loss of the BPA in the pitch adapter region is cured by adding the functionality of the pitch adapter in the second metal layer, which is more decoupled from the first metal layer by a thick oxide.

The concept of the double metal pitch adapter has proven to be successful. Yet, wafers with a second metal require more processing steps and additional masks. The fabrication of those sensors is more costly and not all vendors offer the possibility for a second metal layer on the sensor. The influence of the quite thick silicon dioxide layer on the performance and signal coupling after irradiation is not clear yet.

If one wants to save the material of an external pitch adapter on glass substrates in the tracker region, the DMPA is clearly preferred over the BPA. On the other hand, the pitch adapter can be included directly on the hybrid as it is foreseen for the future modules for the

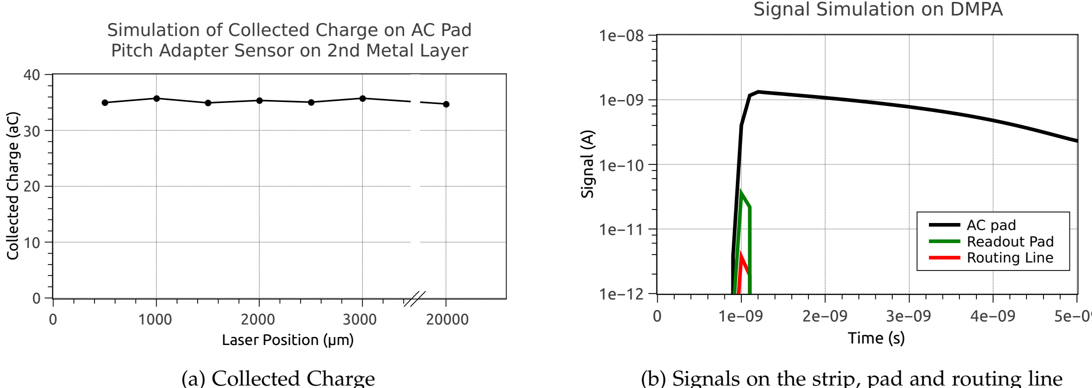

(a) Collected Charge

(b) Signals on the strip, pad and routing line

Figure 10.13: Simulation of signals on the DMPA:
The signal on the AC strip is very large compared to the signal coupling to the readout pads or routing lines. The collected charge is not dependent on the position of the laser.

CMS Tracker. With this option, no additional material is introduced in the tracker and the sensor's performance cannot be influenced negatively.

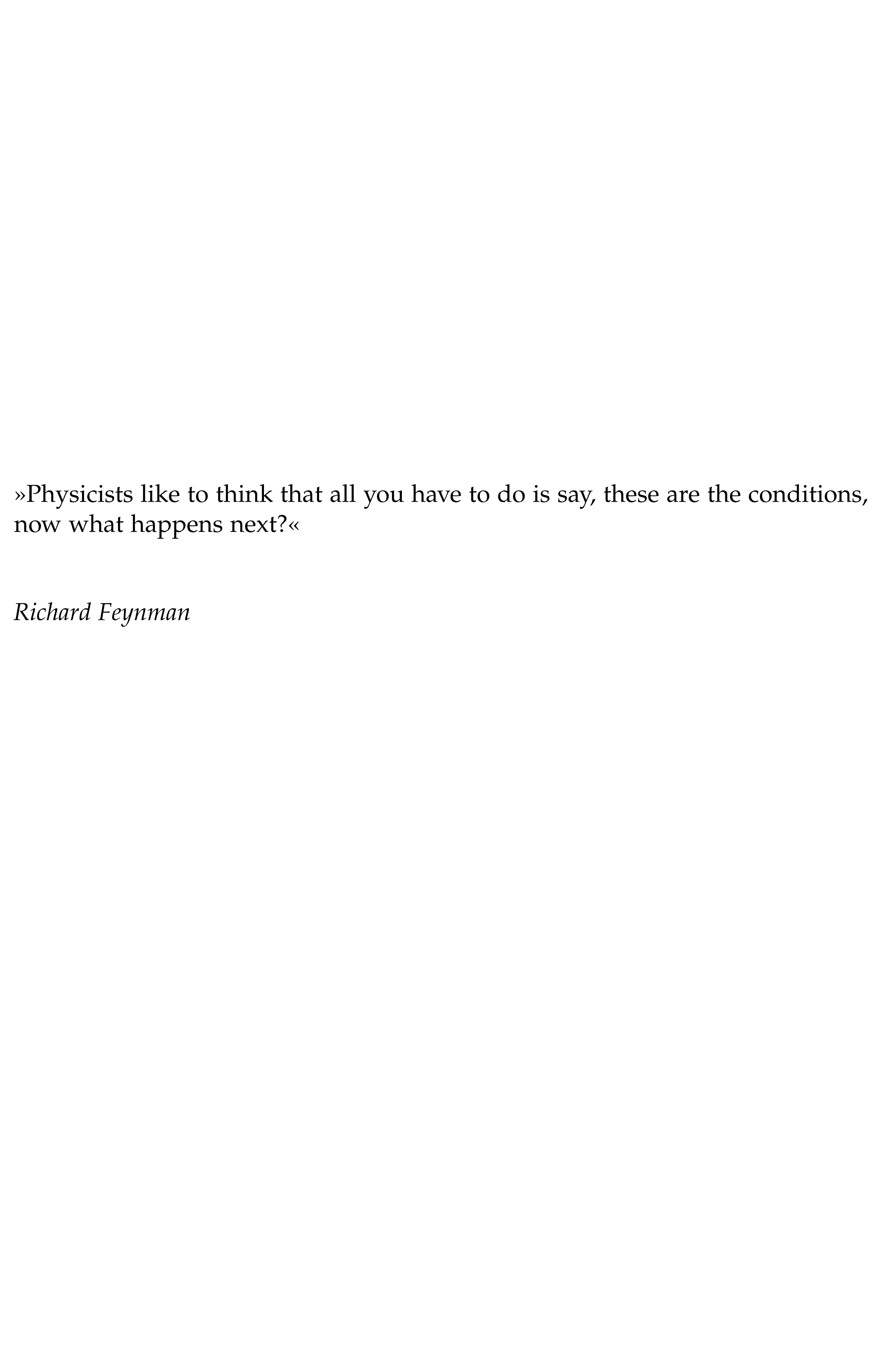

»Physicists like to think that all you have to do is say, these are the conditions, now what happens next?«

Richard Feynman

Part IV

IRRADIATED SILICON SENSORS

11

TWO-DEFECT MODEL

In this chapter, the development of an effective two-defect radiation damage model for Synopsys Sentaurus is described in detail. The data basis is provided by lots of measurements done in the framework of the HPK Campaign. The data obtained from diodes – IV, CV, TCT and CCE – as well as the data from mini strip sensors contribute to this model.

The model is not aimed to describe the leakage current and the depletion voltage after irradiation only, but to provide additional useful information about the electric field after irradiation. Therefore, TCT measurements are used as an important input for the determination of the parameters of the model.

The first part of this chapter characterizes the measured samples and sets the data basis for development of the model. Subsequently, the tuning of the two-defect model to match leakage current and depletion voltage is described. Especially the adaption of the TCT pulses plays an important role; the influence of the different parameters of the model is discussed. The electric fields resulting from the simulation of diodes are compared to other radiation damage models, which have been developed – in contrast to this new model – to describe sensors with respect to current, depletion voltage and sometimes charge collection efficiency only. The important feature of the tuned model is, that it can describe the so called "double peak", which is appearing in the TCT measurements. Resulting from the electric fields, the drift simulation is compared to the measured TCT pulses. In a last step, the charge collection efficiency of the diode in the simulation and measurement with respect to the fluence is characterized.

The effective two-defect radiation damage model is used in the following chapters to simulate an irradiated sensor and analyze its performance with special interest in the performance in a future CMS Tracker after the upgrade of the LHC.

11.1 Measurement Data

All sensors and diodes are irradiated with one particle first, before they undergo the mixed irradiation. The measurements between these irradiations serve as the basis for particle dependent models, although this is not necessarily expected from the NIEL hypothesis.

The data shown here is measured at $T = -20\,^{\circ}C$ with a frequency of 1 kHz for CV.

11.1.1 CURRENT

Mostly, the diodes show a linear correlation between the measured current and fluence, independent of the irradiated particle type. The current is normalized to the volume of the diodes to calculate the current related damage factor α for all diodes after irradiation. The fit over all measured data points results in an alpha-value of

$$\alpha(-20\,^{\circ}C) = (8.5 \pm 0.2) \times 10^{-19}\,A/cm^3. \tag{11.1}$$

This value is very close to the alpha-value from Moll [Mol99] scaled to $-20\,^{\circ}C$: $\alpha = 8.8 \times 10^{-19}\,A/cm^3$. The value can be a little bit smaller than expected, the current has been taken directly at the depletion voltage. Because the alpha-value for mini sensors from the HPK Cam-

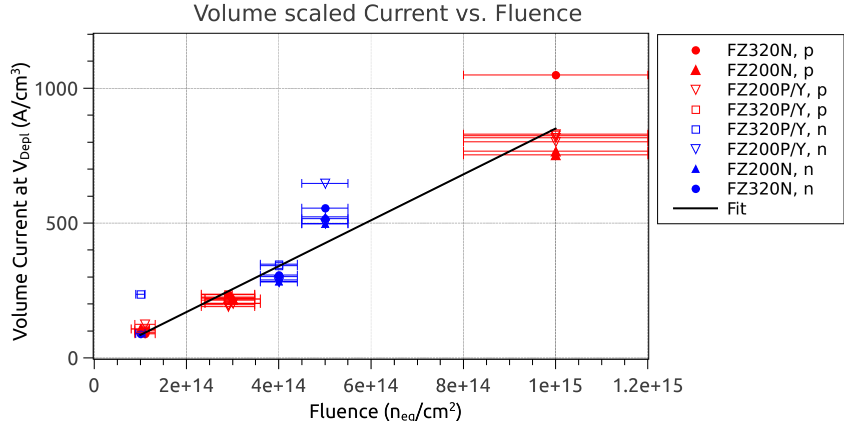

Figure 11.1: Measured volume scaled current for 320 µm and 200 µm thick n-bulk and p-bulk diodes.

paign is a little bit larger, in general the Moll values for the current related damage parameter have been used. For these values, also the annealing behaviour is known.

The current for diodes irradiated to $5 \times 10^{14}\, n_{eq}cm^{-2}$ is a little bit higher. The diodes have not been annealed after transport for 10 minutes at 60 °C, wich results in a higher current. There are two points, which do not fit into the picture: a neutron irradiated p-bulk diode at $10^{14}\, n_{eq}cm^{-2}$ and the proton irradiated diode at $10^{15}\, n_{eq}cm^{-2}$. The reason may be, that the guard ring has not been connected correctly, thus the measured volume current results in a higher value.

11.1.2 FULL DEPLETION VOLTAGE

For the development of a radiation damage model for the simulation, depletion voltages from sensors and diodes have been used to increase statistics. To compare the depletion voltage of segmented sensors with diodes, a correction formula is used [B+02]

$$V_{depl} = V_{depl,Diode}\left[1 + 2\frac{p}{d} \times f\left(\frac{w}{p}\right)\right] \tag{11.2}$$

where "f is a universal function which is numerically approximated by" [B+02]

$$f(x) = -0.00111x^{-2} + 0.0586x^{-1} + 0.240 - 0.651x + 0.355x^2 \tag{11.3}$$

The depletion voltages versus fluence for the different samples (sensors are corrected to diodes) are illustrated in figure 11.2.

On all measured depletion voltages, an error is given, which results from the fit of the slopes to the $1/C^2$ curves, as described in section 5.1.2. Only the depletion voltage of samples irradiated with one particle type is plotted, an initial annealing after irradiation of 10 minutes at 60 °C included.

At first glance, it can be seen, that the depletion voltage of p-bulk samples is higher after the same fluence than for n-bulk samples, as it is expected from the *type inversion*. Also, the depletion voltage of thinner samples is lower. When looking at the data points from proton irradiated and neutron irradiated samples, one can guess, that a single slope won't fit all data points. The proton irradiated samples consistently show a lower depletion voltage than the neutron irradiated ones. This is not described by the NIEL-hypothesis, which treats all particles the same, but can occur in samples with sufficient oxygen concentration, as shown by the RD50 collaboration [RD5]. Hence it is only justifiable to treat the two different irradiations in a different way. Nevertheless it is still assumed, that the depletion voltage is proportional to the fluence for each of the particle types.

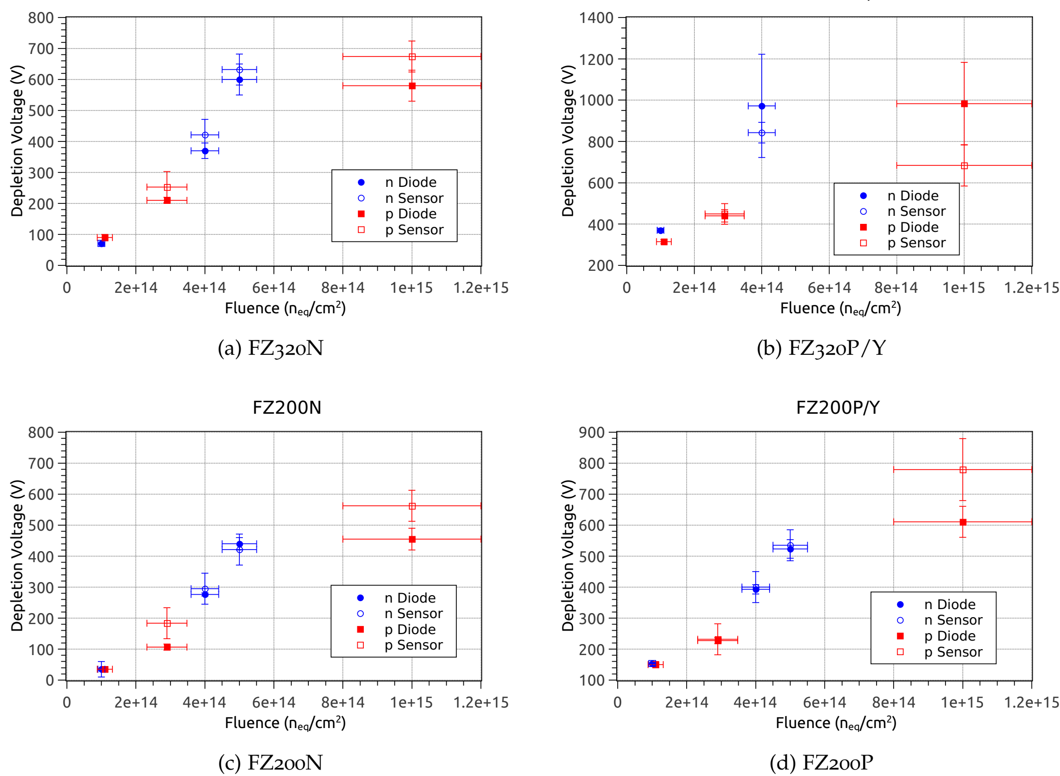

(a) FZ320N (b) FZ320P/Y

(c) FZ200N (d) FZ200P

Figure 11.2: Depletion voltage of FZ diodes, irradiated with only one particle type after 10 min at 60 °C annealing time.
A voltage above 1000 V could not be applied; depletion voltages above 1000 V are not shown here.

11.2 Model Building

Many options to establish a defect model are possible. A very general way is offered by the recipe given here. At first, the leakage current plays the most important role, as it influences the occupation of the traps and hence the space charge. This in turn can modify the electric field and depletion voltage. Not only IV and CV, but also the TCT pulses are needed to determine the six parameters, which are fully describing the two-defect radiation damage model. The EVL model has proven to be able to simulate device performance and doubly peaked electric field (see section 5.2.6). It is used as a basis for the development of the two-defect radiation damage model describing devices of the HPK Campaign. The original values are listed in table 11.1.

The energy level in the bandgap of the chosen two defects is such, that they can generate leakage current due to their proximity to the middle of the bandgap on the one hand, on the

Table 11.1: Parameters of the original EVL model [E+04].

Parameter	Donor	Acceptor
Energy (eV)	$E_V + 0.48$	$E_C - 0.525$
Concentration (cm^{-3})	$1\,cm^{-1} \times F$	$1\,cm^{-1} \times F$
$\sigma(e)$ (cm^2)	10^{-15}	10^{-15}
$\sigma(h)$ (cm^2)	10^{-15}	10^{-15}

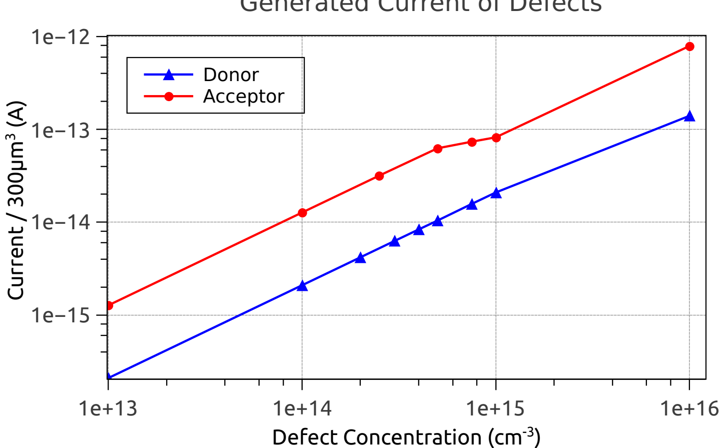

Figure 11.3: Concentration dependence of the current generated by the two defects of the EVL model: *the generated current is simulated separately for the two defects. The acceptor generates more current than the donor at the same concentration.*

other hand they are still able to create space charge by being occupied by charge carriers. The filling of the defects is dependent on the current, which is controlled by the cross sections of electrons and holes. More space charge can be introduced by raising the concentration of the defects in the bulk.

Lying not too close to the conduction or valence band and not too close to the center of the bandgap, even the trapping of charge carriers can be modeled, as will be shown later.

11.2.1 PARAMETRISATION OF THE LEAKAGE CURRENT

The leakage current after irradiation is independent of the particle type and well parametrized by Moll [Mol99]. The measurement data fits well within the parametrized values, hence it is justified to use the theoretical α-value for the determination of the leakage current in the simulation.

Defects in the simulator always act as both types of defects: current generators and space charge generators, depending on their energy level in the silicon bandgap. Thus it has been chosen to implement the current by using the two defects of the EVL model and not to use any other approach. In this way, other elements such as additional defects in the bandgap for the generation of leakage current cannot distort the electric field in the device and influence the trapping time of the charge carriers.

The leakage current generated by the two defects in the simulation is dependent on two main factors: the concentration of the defects and the cross section of electrons and holes of the specific trap.

The dependence on the defect concentration is pictured in figure 11.3. Only one defect is simulated at the time with both cross sections of electrons and hole set to $\sigma = 10^{-14}\,\text{cm}^2$. If the concentration of the acceptor is too high, the device does not deplete any more up to 1000 V and the volume generated current is lower accordingly.

A systematic scan varying the cross sections of the two defects at a fixed concentration of the defects has been performed. The simple 2d simulation diode with the correct doping profile has been used for this purpose. Both defects are implemented in the simulation with a fixed concentration of $c_{test} = 1 \times 10^{14}\,\text{cm}^{-3}$. This value is reasonable because the concentration of the defects will be around this concentration. Then one of the four cross sections, electron cross section of the donor, hole cross section of the donor, electron cross section of the acceptor or hole cross section of the acceptor have been varied over some order of magnitude around the starting value. Because the current is too low with the original cross section, they have been

Figure 11.4: Influence of the cross sections on the current in the simulated diode: *Only one of the cross sections of a defect is largely influencing the current. Current is generated by the electron cross section of the donor and the hole cross section of the acceptor. The other cross sections have only a minor influence.*

raised from $\sigma = 10^{-15}\,\mathrm{cm}^2$ up to $\sigma = 10^{-12}\,\mathrm{cm}^2$. Only one cross section is varied at a time, all others are set to $\sigma = 10^{-14}\,\mathrm{cm}^2$.

The resulting current when varying the cross sections according to the given description can be seen in figure 11.4.

The current is taken at 1000 V, values for which the device is not depleted (this is true for the three points at large hole cross section of the acceptor), are not taken into account for the parametrization. The slope of the generated current versus the corresponding cross sections are fitted.

$$I/(c_{test} \times \sigma_{electron,donor}) = 2.07 \times 10^{-15}\,\mathrm{Acm} \tag{11.4}$$

$$I/(c_{test} \times \sigma_{hole,donor}) = 4 \times 10^{-20}\,\mathrm{Acm} \tag{11.5}$$

$$I/(c_{test} \times \sigma_{electron,acceptor}) = 1 \times 10^{-17}\,\mathrm{Acm} \tag{11.6}$$

$$I/(c_{test} \times \sigma_{hole,acceptor}) = 1.268 \times 10^{-14}\,\mathrm{Acm} \tag{11.7}$$

The value $I/(c_{test} \times \sigma)$ is substituted by $X_{e/h,don/acc}$ in the course of this section. The ultimate goal is now to calculate the concentration of the traps, which has to be put in the simulator at given cross sections and fluence to always generate the correct current. Because the equation has ambiguous solutions with respect to the donor and acceptor concentration, the donor concentration is expressed as a fixed ratio of the acceptor concetration. The value is chosen manually.

$$c_{don} = r \times c_{acc} \tag{11.8}$$

The resulting acceptor concentration, expressed in terms of parametrized current X and the desired current $I \approx \Delta I = \alpha \times \mathrm{Vol.} \times F$ reads

$$c_{acc} = \frac{\alpha \times \mathrm{Vol.} \times F}{r \times (X_{e,don} \times \sigma_{e,don} + X_{h,don} \times \sigma_{h,don}) + (X_{e,acc} \times \sigma_{e,acc} + X_{h,acc} \times \sigma_{h,acc})}$$

Figure 11.5: Estimation of removable donors during neutron or proton irradiation with the Hamburg Model.

(11.9)

Just by choosing the current, the cross sections and the ratio between donor and acceptor concentration, the correct volume scaled current is generated in the simulation device. Many values for ratio r and the cross sections are possible. To fix these values, further input from the depletion voltage and TCT curves is needed.

11.2.2 DONOR REMOVAL

During the hadron irradiation process, donor removal is expected to happen for n-bulk devices. The electrically active phosphorus joins a radiation induced vacancy and forms an electrically inactive VP-defect. This lowers the donor concentration in the bulk. The effect is more pronounced in irradiations with charged hadrons. In samples irradiated with protons, the depletion voltage suggests a donor removal of about 50%, whereas for irradiations with neutrons only few donors are removed (10%) [W+96].

The effect of the donor removal can be well described by the simulation. During the irradiation process, mostly the acceptors dominate, the so called *type inversion* occurs at lower fluences. Because the phosphorus is distributed quite homogeneously throughout the bulk, it is very unlikely, that all phosphorus dopants will be deactivated. Thus, after a certain fluence, depending on the initial bulk doping, the donor removal is finished. This can be implemented in the simulation very easily: after a fluence of $F = 10^{14}\, n_{eq}cm^{-2}$, the donor removal is assumed to be finished and the bulk concentration of phosphorus can be lowered by the expected amount of removed donors.

Figure 11.5 shows the Hamburg-Model with and without donor removal. To match the different depletion voltages for proton and neutron irradiation, a different damage factor has been used for the two models shown. Nevertheless, it can be seen, that the neutron irradiation is very well compatible with the model, when only 10% of the donors are removed from the bulk. For the protons however, the curve only matches, if 50% of the donors are removed during the irradiation.

11.2.3 FULL DEPLETION VOLTAGE

Since there isn't any recipe to model the full depletion voltage out of the box, a systematic scan over the increasing defect concentration has been done. One has to be careful with the sign

Figure 11.6: CV curves of proton irradiated FZ320N diodes. The agreement between simulation and measurement is fairly good.

of the change of the effective doping concentration. The measurement data shows, that FZ n-bulk diodes undergo *type inversion* after irradiation. Therefore, the depletion voltage has to drop first and increase again with higher fluence. The drop of depletion voltage is modeled by donor removal and by introducing more donors than acceptors in the simulation. This makes sure, that the device is type inverted after a fluence of $F_{eq} = 10^{14}\, n_{eq}cm^{-2}$. For an affirmation of the *type inversion* of the diode, one can have a look at the electric field, after the depletion voltage is modeled correctly.

In a first iteration, the depletion is adapted for the FZ320N diodes. In the next step, the obtained models are applied to the other diodes. Simulated and measured CV curves for proton irradiated FZ320N diodes are compared in figure 11.6. Although the shape of the inverse squared capacitance versus voltage is slightly different between the simulation and measurement, the slope at lower voltages could be reproduced. At $F = 10^{15}\, n_{eq}cm^{-2}$ for example, $1/C^2$ drops at very low voltages, rises slowly until about 300 V and then increases faster up to the depletion voltage at about 600 V.

For the proton model, the depletion voltage of the three available fluences at 253 K has been tuned separately. For higher fluences, more donors have to be introduced to make up for the relatively low depletion voltage at $F_{eq} = 10^{15}\, n_{eq}cm^{-2}$.

For the neutron model, the situation is easier, since the introduction rate of donor to acceptor is constant and can be interpolated linearly over the measured fluence range.

Figure 11.7 shows the depletion voltage of the four simulated types of diodes.

Taking a closer look at the comparison of measured and simulated depletion voltage, the neutron model shows a low depletion voltage at $F = 10^{14}\, n_{eq}cm^{-2}$. To reach a higher depletion voltage, a separate tuning for each of the curves can be considered as well as donor removal for the irradiation with neutrons.

Looking at figure 11.8, the neutron model describes the depletion voltages measured at $-20\,°C$ and 1 kHz for both thicknesses very well. The depletion voltage around 1000 V for 320 µm thick p-bulk diodes and sensors is not so easy to determine and has a large error.

The proton model, developed and tuned for FZ320 n-bulk diodes originally, still works for FZ320 p-bulk diodes. At the low fluence at $10^{14}\, n_{eq}cm^{-2}$, the simulated depletion voltage is higher than the measured one, at $10^{15}\, n_{eq}cm^{-2}$ the depletion voltage matches V_{depl} of the sensor, the depletion voltage of the diode is larger. For the thinner p-bulk, the proton model describes the depletion voltage of the lower two fluences quite well, but deviates significantly for both, sensor and diode at $10^{15}\, n_{eq}cm^{-2}$.

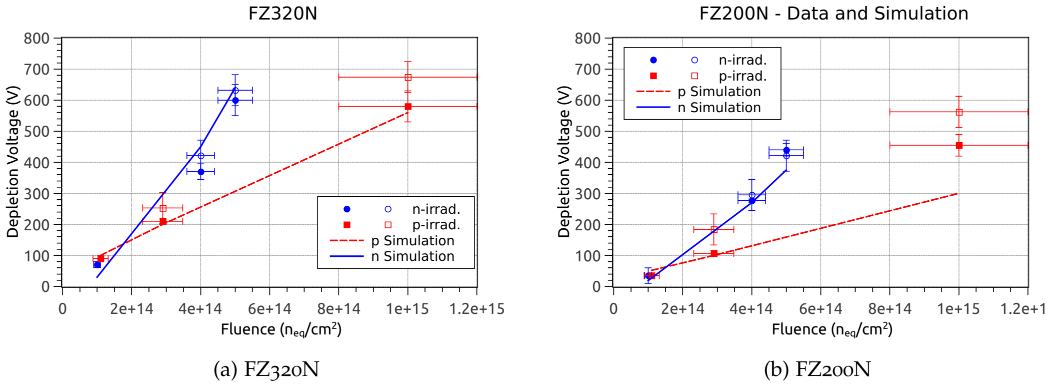

(a) FZ320N (b) FZ200N

Figure 11.7: Simulated and measured depletion voltage of FZ320 and FZ200 n-bulk diodes in comparison. *The simulated depletion voltage agrees quite well within the errors. For the thinner diodes, the proton model deviates at the high fluence.*

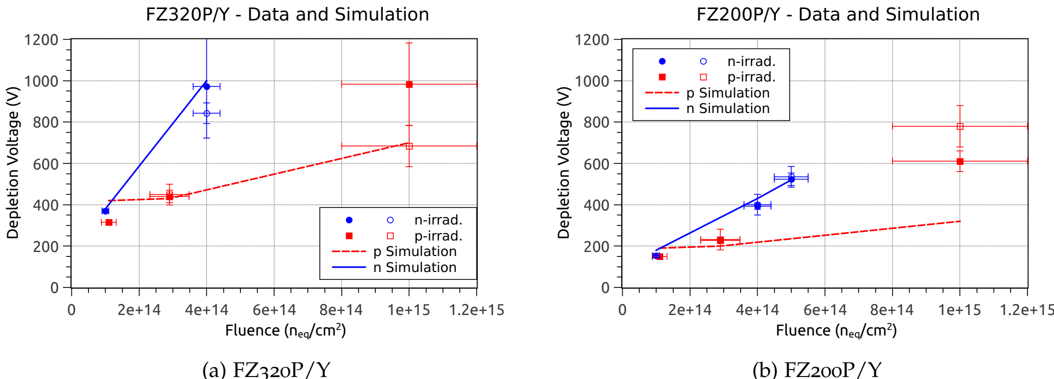

(a) FZ320P/Y (b) FZ200P/Y

Figure 11.8: Simulated and measured depletion voltage of FZ320 and FZ200 p-bulk diodes in comparison. *The simulated depletion voltage agrees quite well within the errors. For the thinner diodes, the proton model deviates at the high fluence.*

11.2.4 NEUTRON MODEL

The neutron data can be described quite easyly with an introduction rate of the donor and the acceptor. This means, that the concentration of the defect is directly proportional to the fluence without any correction. To get the correct depletion voltage for this natural introduction rate, cross sections for electrons and holes for both, donor and acceptor, are equal at $\sigma = 1.2 \times 10^{14}\,\mathrm{cm}^2$. The concentration for the donor is always 90% of the concentration of the acceptor. The introduction rate for the acceptor is $\eta = 1.55$, yet for convenience in table 11.2 the concentration is given as a function of the fluence.

11.2.5 PROTON MODEL

The proton model has been tuned for each of the three fluences to match the depletion voltage for FZ320N as well as the current of course. Afterwards, the drift simulation is used to determine the cross sections for electrons and holes for the donor and the acceptor in the simulation. The drift simulation is described in the next chapter.

After all three fluences are matched independently, a linear fit is applied to describe the concentration of the defects. Because of the relatively low depletion voltage at $F = 10^{15}\,n_{eq}\mathrm{cm}^{-2}$, the concentration of the donor is increasing more rapidly than the concentration of the acceptor,

Table 11.2: Two-Defect model for neutron irradiation.

Parameter	Donor	Acceptor
Energy (eV)	$E_V + 0.48$	$E_C - 0.525$
Concentration (cm^{-3})	$1.395\,cm^{-1} \times F$	$1.55\,cm^{-1} \times F$
$\sigma(e)$ (cm^2)	1.2×10^{-14}	1.2×10^{-14}
$\sigma(h)$ (cm^2)	1.2×10^{-14}	1.2×10^{-14}

Table 11.3: Two-Defect model for proton irradiation.

Parameter	Donor	Acceptor
Energy (eV)	$E_V + 0.48$	$E_C - 0.525$
Concentration (cm^{-3})	$5.598\,cm^{-1} \times F - 3.949 \cdot 10^{14}$	$1.189\,cm^{-1} \times F + 6.454 \cdot 10^{13}$
$\sigma(e)$ (cm^2)	1.0×10^{-14}	1.0×10^{-14}
$\sigma(h)$ (cm^2)	1.0×10^{-14}	1.0×10^{-14}

leading to a negative correction factor for the donor. This means, that the model can only be applied after type inversion. This model is only valid above $F = 10^{14}\,n_{eq}cm^{-2}$.

As it turns out from the drift simulation, the cross sections for electrons and holes for the effective defect levels are equal at $\sigma = 10^{-14}\,cm^2$.

The proton model in table 11.3 is established on measurement data taken at $T = -20\,°C$ and thus only valid at this temperature. For the a temperature dependent model, see section 11.8.

11.3 The Double Peak Transient Current Pulses

In the last sections, the tuning of the concentration of the defects to match the leakage current and the depletion voltage has been described. From the current point of view, it is not obvious, how the double peak shape of the transient current pulses evolves from the simulation model. We particularly look at the proton model in detail.

The general description of the double peak electric field has been given in chapter 5.2.6.

In the un-irradiated device, the electric field is a function of the constant doping in the silicon sensor. Due to irradiation, the acceptors and donors are introduced, summed up by the two effective defects in the two-defect model. As it is obvious from table 11.3, more donors than acceptors are introduced. At about $1.0 \times 10^{14}\, n_{eq} cm^{-2}$, the concentration of both defects is the same. At $1.0 \times 10^{15}\, n_{eq} cm^{-2}$, the concentration of the donor is four times higher than the concentration of the acceptor. This, of course, affects the electric field, because the occupied donors and acceptors contribute to the space charge.

Yet, only a minor fraction of the introduced donors and acceptors contribute to the space charge, since only about 1 % to 10 % are ionised. The ionisation fraction is a function of the energy level in the bandgap. The donor is farther away from the conduction band ($E_C - 0.64\, eV$), thus it is less probable for an electron to occupy the donor level. The acceptor is a little bit closer to the valence band ($E_V + 0.595\, eV$) and a larger fraction is ionised.

The whole concentration of the defects contributes to the generated leakage current, as it has been shown in section 11.2.1, with mainly one of the two available cross sections for electrons and holes. Because in each slice of the silicon sensor, the same amount of charge carriers are generated, the electron current sums up at one electrode, the current of the holes sums up at the opposite electrode. The occupation of the donor and acceptor in the defect model are also affected hereby, since the probability is higher to be occupied, if more suitable charge carriers are available to occupy the state.

Looking at an n-bulk sensor, the electrons drift to the back, the holes drift to the front. Hence, the occupation of the donor is higher at the front, the occupation of the acceptor is higher at the back. Having the same concentrations at $1 \times 10^{14}\, n_{eq} cm^{-2}$, the acceptor dominates due to its larger occupation. The device is type inverted and not much of the electric field is found at the front side. At higher fluence, the donor introduction is higher and more of the electric field is found at the front. This is the reason for the double peak electric field in irradiated sensors, simulated with either defect model. The effect is more pronounced for the proton model. The electric fields can be found in detail for n-bulk and p-bulk diodes in section 11.5.

The charge carriers are forced to drift according to the electric field. In a transient simulation with a red laser, mainly one charge carrier generates the recorded signal. The one type of drifting charge carriers is very dependent on the trapping time, or, in the simulation, dependent on the mentioned remaining free cross sections of the two defects: the hole cross section of the donor and the electron cross section of the acceptor. These are tuned to match the TCT pulses. The simulation for n-bulk diodes can be seen in full detail in section 11.4.

An overall picture is given in the overview for the fluence of $F = 10^{15}\, n_{eq} cm^{-2}$ in figure 11.9. Beginning with the electric field configuration for different voltages in figure 11.9a, the charge carriers have to move according to the electric field. In the transient simulation, electrons are generated with a red laser on the front and drift towards the back side. Holes don't contribute much.

The cloud of moving electrons can be seen for two example voltages in figures 11.9b and 11.9c. At low fields, the electrons are decelerated and trapped more easily. The convolution of trapping and deceleration can be seen very clearly at 600 V. At 1000 V, the electric field is much higher in the center of the sensor and the electrons are not so much decelerated.

The measurement and the simulation in comparison with the measurement of the electron TCT pulses in the 320 μm thick n-bulk diode irradiated to $10^{15}\, n_{eq} cm^{-2}$ is visualized in figures 11.9d and 11.9e.

Finally, the charge collection efficiency is simulated with an infrared laser, generating charge carriers throughout the whole bulk of the diode. This is valid method to simulate a minimum-ionising particle, as shown in section 8.3.4. The comparison of the overall shape is in good agreement, the efficiency can be simulated within 20 % agreement (figure 11.9f. The charge collection efficiency of all fluences is shown in section 11.7.

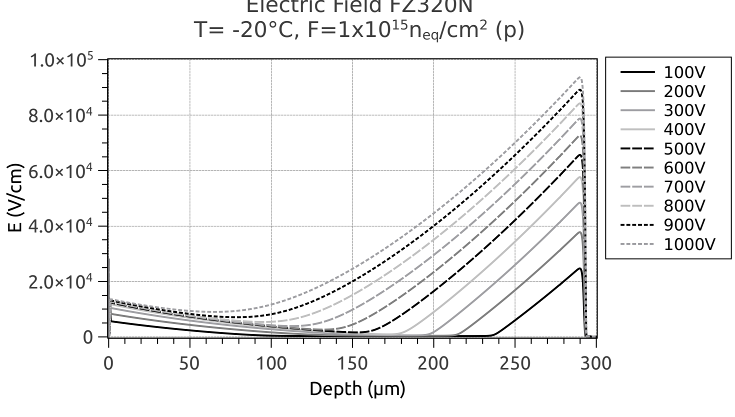

(a) Electric fields for different voltages

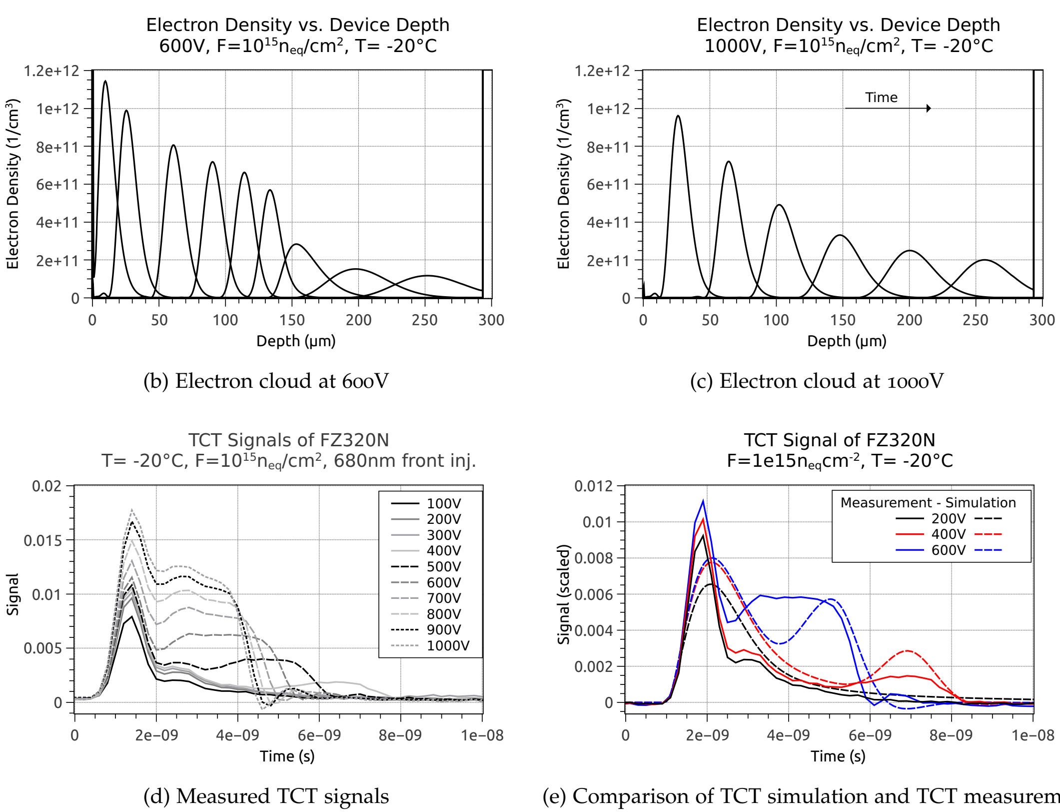

(b) Electron cloud at 600V

(c) Electron cloud at 1000V

(d) Measured TCT signals

(e) Comparison of TCT simulation and TCT measurement

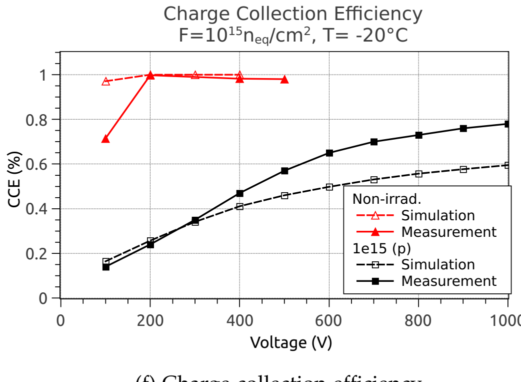

(f) Charge collection efficiency

Figure 11.9: Summary of obtained results for $F = 10^{15}\, n_{eq} cm^{-2}$:
Measured and simulated TCT signals are shown and compared. The electric field is obtained from the simulation. The electron cloud in the simulation moves according to the electric field from $0\,\mu m$ *to* $300\,\mu m$.

11.4 Transient Current Pulses

Simulating the current-voltage or the capacitance-voltage characteristics with the effective two-trap model is the basic work and the first check, if the provided model meets the requirements of an irradiation damage model for the simulation. But there are several things, which have not been taken into account by just simulating these two parameters, amongst them the electric field in the device and the trapping time.

As mentioned in the previous section, the cross sections of the proton defect model have been tuned such, that they match the measured transient pulses. The transient current pulses (TCT signals) are very sensitive to the electric field in the device. The electric field in the simulation is very much influenced by the space charge, which is created by the donor and the acceptor in the bulk. The space charge is created by the trapped charges of the donor and the acceptor and, besides the concentration, dependent on the cross sections of electrons and holes of the donor and acceptor.

The trapping, as the second important parameter for the shape of the transient pulses, is also influenced by the cross sections of the two defects. In the two-defect model, mainly the cross sections, which do not much influence the current through the device, are responsible for the shape of the transient signal. The parameters listed in table 11.3 are already tuned.

Measurements on proton irradiated diodes and the simulation results from the proton model are compared in this section. Unless declared otherwise, all TCT signals of irradiated diodes have been generated with a red laser and have been recorded with the picolaser setup at $-20\,^{\circ}$C after the diodes have been annealed for 10 minutes at $60\,^{\circ}$C. The drift simulation has been carried out with the standard parameters given in chapter 7.1.3.1. The influence of some simulation parameters on the signal shape is discussed in the course of this section.

11.4.1 Measurement and Simulation Results

Beginning from the lowest fluence of $1.1 \times 10^{14}\ n_{eq}cm^{-2}$, the TCT signals generated with a red laser and the corresponding simulation of a FZ320N diode simulated with the proton model can be seen in figure 11.10.

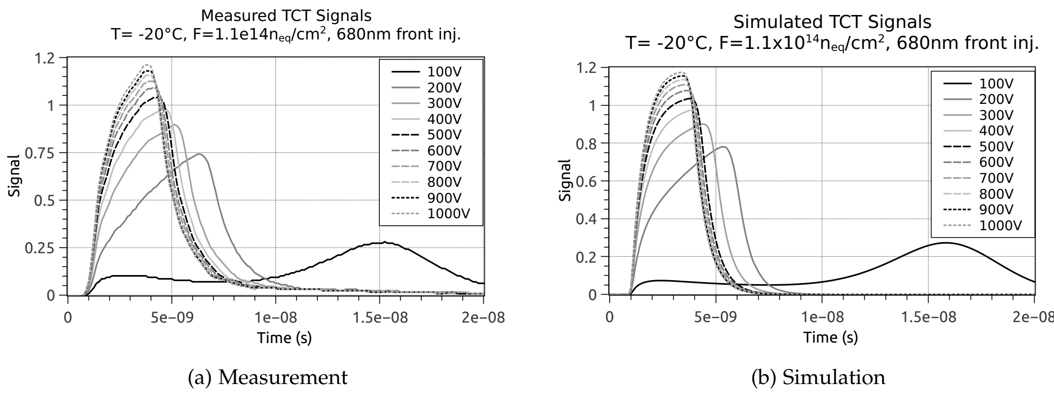

(a) Measurement (b) Simulation

Figure 11.10: Measurement and Simulation of TCT signals at $F = 1.1 \times 10^{14}\ n_{eq}/cm^2$ irradiated with protons:
A double peak is visible for 100 V, merging to one peak in the type inverted diode at higher voltages.

At 100 V, the model has been tuned to match the measurement. The simulation at higher voltages and fluence have been done with exactly the same parameters. Comparing the simulation and the measurement, the simulation agrees best at 100 V. At higher voltages, the simulation pulse shows the same peak heights and almost the same shape as the measured pulse. The simulated pulse length however is shorter. This effect can have several reasons: one of them has

already been seen in section 8.3.3. The simulated signal is slightly shorter than the measured signal. Yet, in the simulation of the irradiated diode, the effect is more visible.

Because the pulse shapes agree quite well, the electric field is considered to be correct. It is shown in the following section. For the pulse shape, the drift velocity, the saturation drift velocity and the mobility at $T = -20\,^{\circ}C$ play an important role. None of these parameters has been measured exactly for silicon sensors irradiated to very high fluences. Minor changes can affect the pulse shape, which is discussed later.

From the TCT signal, the electric field and the depletion behaviour can be deducted. At low voltages, there is only a small peak at early times and a larger peak at later times for 100 V, when the red laser generates charges at the front side. Here, the *type inversion* can be seen very well. The larger electric field is at the back side of the device but there's also field at the front side – a double peak is formed. In the middle of the device there is a zone with a low electric field and thus the electrons drift slowly through the bulk. Considering a trapping time correction for the pulses, more electrons would be left at later times and the second peak would be even larger.

At higher voltages, the second peak and the first peak melt, the low field zone in the middle of the device vanishes. Yet, the *type inversion* of the diode is still clearly visible (compare table 5.2). The signal becomes higher and shorter, indicating that in the 320 μm thick diode, the saturation velocity has not been reached and the drift velocity is still proportional to the electric field. This is a fact, that can be exploited to reconstruct the electric field other than from the simulation.

Going to the higher fluence of $2.9 \times 10^{14}\,n_{eq}cm^{-2}$, measurement and simulation are shown in figure 11.11. The measurements at this fluence show one typical characteristic, which is not present in the measurement at $1.1 \times 10^{14}\,n_{eq}cm^{-2}$: at the beginning of the pulse, there is a sharp overshoot of the signal, followed by a small undershoot in the plateau region, and a second undershoot after the drop-off of the signal. The reason is the different measurement setup – the diode has been measured at the University of Hamburg.

Again, at low voltages, the signal presents itself as a double peak signal. Due to the higher depletion voltage, the second peak of the signal is not yet visible at 100 V, but only at 200 V. At higher voltages, the first peak and the second peak merge and form one single pulse. The typical type inverted shape is also seen in this measurement. At 500 V and higher, the signal is almost forming a plateau. Due to the readout network distortions, the shape before 2 ns is not so clear however.

The simulation shows very much the same picture. Compared to the measurements, the signal at 100 V is a little bit higher than in the measurement. The pulse lengths in the simulation is almost fitting the measured ones. One crucial difference is the different readout network used for the simulation. Whereas the diode has been measured at UHH, the simulation has been done with the readout network at IEKP. This leads to the very different shape between 1 ns and about 2 ns. The very high inductance in the readout network at UHH is responsible for the first spike in the signal, the higher stray capacitance in the IEKP network used for the simulation is responsible for the slower rise time of the signal.

Nevertheless, the overall shape of the signals is reproduced quite well, as it is pointed out in figure 11.12 for 100 V and 200 V. At 100 V, the measured curve shows an exponential decrease, the simulation already shows a small second peak after 17 ns. This position of this peak is very sensitive to the fluence and the defect cross sections in the simulation. If the fluence is chosen a bit higher, keeping in mind that the experimental error on the fluence is about 20%, the peak vanishes completely at 100 V. At 200 V, the signal shape of the simulated signal matches very well the shape of the measurement; again the signal is 1 ns too short, partly because of the already mentioned short signal in the un-irradiated case. The first sharp overshoot of the signal due to the readout network is not correctly simulated, but can also be considered as an experimental error.

The measurement and three representative voltages for the comparison with the simulated signal are shown in figure 11.13 for the highest fluence irradiated with protons, $10^{15}\,n_{eq}cm^{-2}$.

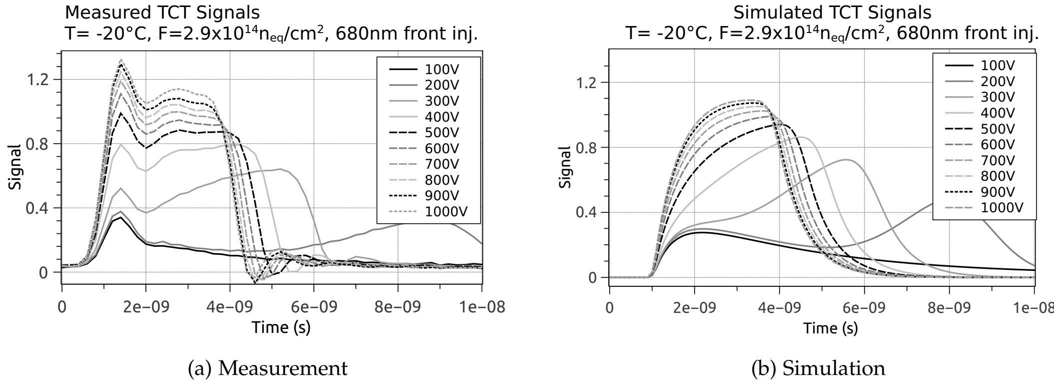

(a) Measurement (b) Simulation

Figure 11.11: Measurement and Simulation of TCT signals at $F = 2.9 \times 10^{14}\, n_{eq}/cm^2$ irradiated with protons:
The overall shape of the signal is reproduced in principle, the difference in the signal at the first few nanoseconds arises due to a different readout network used.

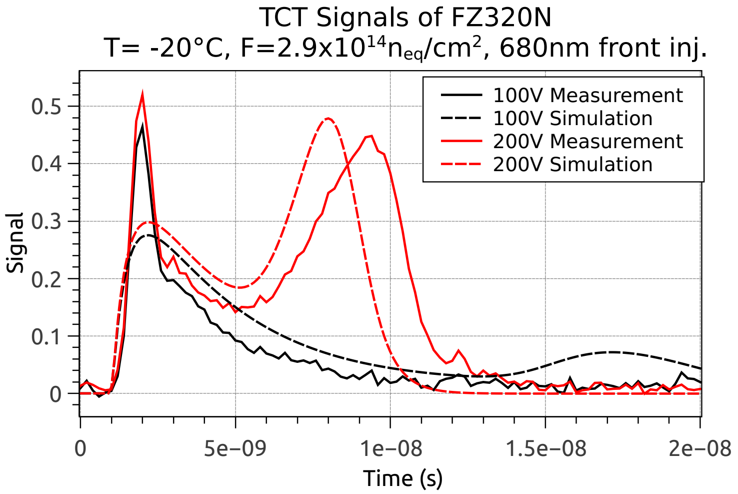

Figure 11.12: Comparison of TCT signals at $F = 2.9 \times 10^{14}\, n_{eq}/cm^2$ (p):
The signal shape matches quite well, the pulse length is slightly too short in the simulation.

The diode is again measured at UHH, therefore the overshoot in the signal in the first few nanoseconds is visible again.

The measurements at voltages from 100 V to 1000 V still show a double peak shape. As seen at the lower two fluences, the higher the depletion voltage, the later the second peak is showing up in the signal. Here, the second peak is only clearly visible at 400 V. But also trapping comes into play at this high fluence. The injected electrons decrease exponentially and after only 4 ns (see next section), $1/e$ of the original number of electrons can contribute to the current and the peak height at later times. Over 600 V, the two peaks start to merge again to form a single peak. Because of the high first peak, the device's type inversion is not so clearly visible. But because of the trapping effects, which decrease the second peak and the type inversion appearing at lower fluences, the device can still be considered type-inverted.

Comparing measurement and a simulated signal of a FZ320N irradiated with protons to $10^{15}\, n_{eq}cm^{-2}$, the pulses agree with each other almost perfectly at 200 V. At 400 V, the simulation seems to overestimate the second peak a little bit. A slightly different trapping between measurement and simulation can cause this effect. At 600 V, the simulated signal shows a valley between the two distinct peaks. In the measured curve, it is difficult to see, if there are

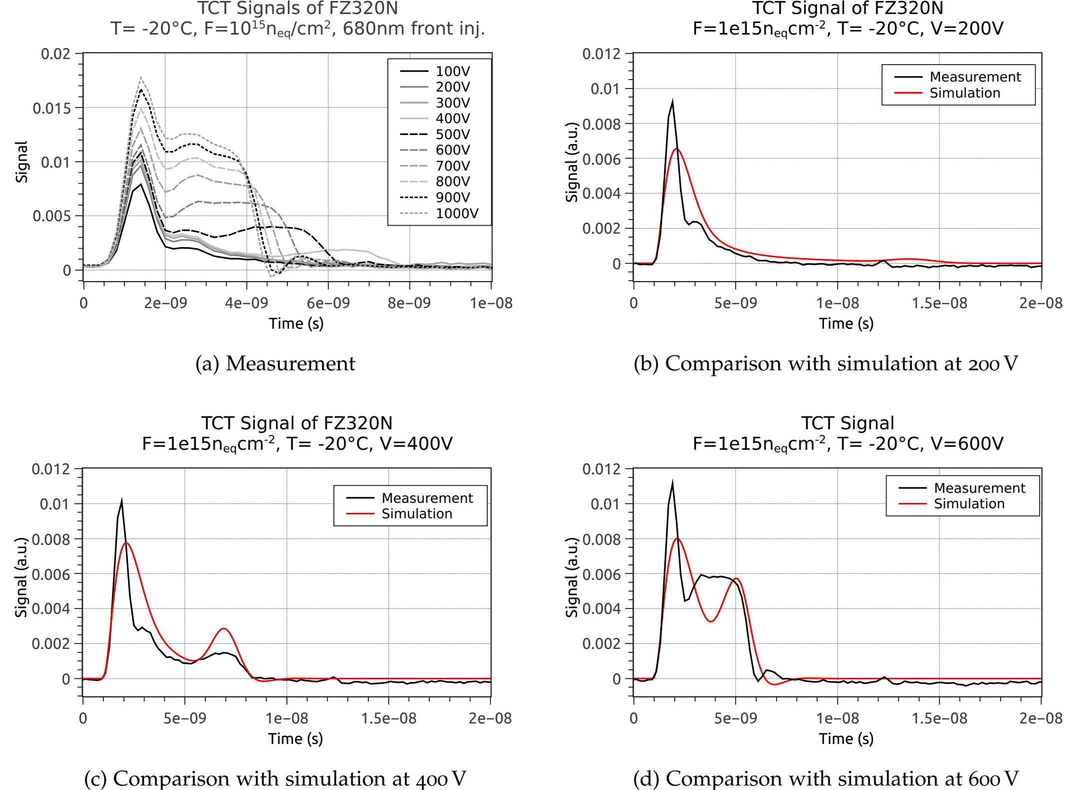

(a) Measurement

(b) Comparison with simulation at 200 V

(c) Comparison with simulation at 400 V

(d) Comparison with simulation at 600 V

Figure 11.13: TCT signals and comparison with simulation at $F = 10^{15}\ n_{eq}/cm^2$ (p): *The simulation describes the experimental results very well. At 400 V, the second peak is slightly overestimated, for 600 V, the measurement cannot really distinguish between the two peaks any more.*

really two distinct peaks or if the overshoot and the following undershoot are caused by the readout network. Still, the pulse height and the pulse length agree very well.

11.4.2 Influence of saturation velocity

At $F = 10^{14}\ n_{eq}cm^{-2}$, the TCT signals in the simulation appear to be too fast at voltages higher than 100 V. The same behaviour is seen for the signals at $F = 3 \times 10^{14}\ n_{eq}cm^{-2}$. Because the signals appear to be correct for the lower voltages, a minor variation of the saturation velocity could lead to the correct signal lengths.

The "standard" saturation velocity used by Synopsys Sentaurus is $v_{sat,e} = 1.07 \times 10^7\ cm/s$ for electrons and $v_{sat,h} = 8.37 \times 10^6\ cm/s$ for holes. Because the signal in the FZ320N diodes is caused by electrons drifting through the bulk, a change of the saturation velocity of holes does not influence the signal.

In figure 11.14, the saturation velocity of electrons has been varied to lower and higher values to see a trend. The two plots represent low and high voltages.

For a higher saturation velocity ($v_{sat,e} = 1.3 \times 10^7\ cm/s$), the signal shape is even closer to the desired one. But, because of the higher drift velocity, the pulse is even shorter than before. If the saturation velocity is decreased, the pulse length can be increased to the desired value. But the longer pulse duration comes with the drawback of a different signal height or signal shape, which is too flat in the region from the beginning of the pulse to its maximum value.

Decreasing the saturation velocity has also the disadvantage, that the pulse is affected even at low voltage. At 100 V, the higher saturation velocity does not influence the TCT pulse so much, but at a lower saturation velocity, the second peak of the pulse is shifted to later times.

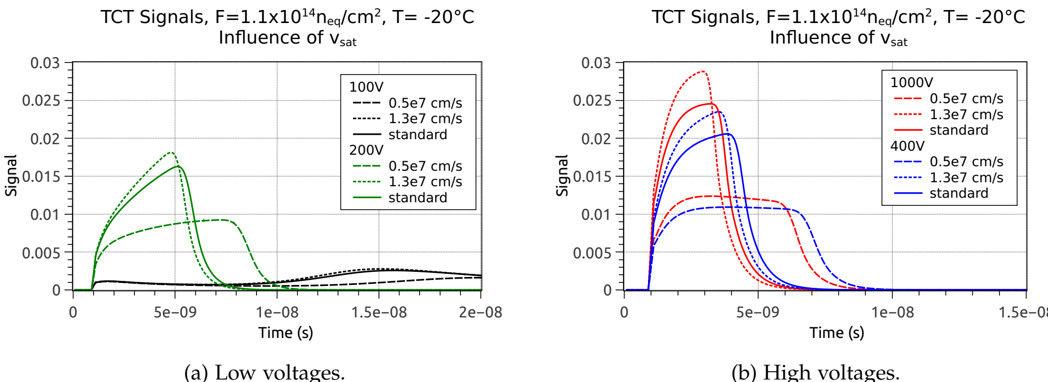

(a) Low voltages. (b) High voltages.

Figure 11.14: Influence of the saturation velocity on the TCT pulse:
V_{sat} mostly affects the pulses at higher voltages, but shows a different pulse shape.

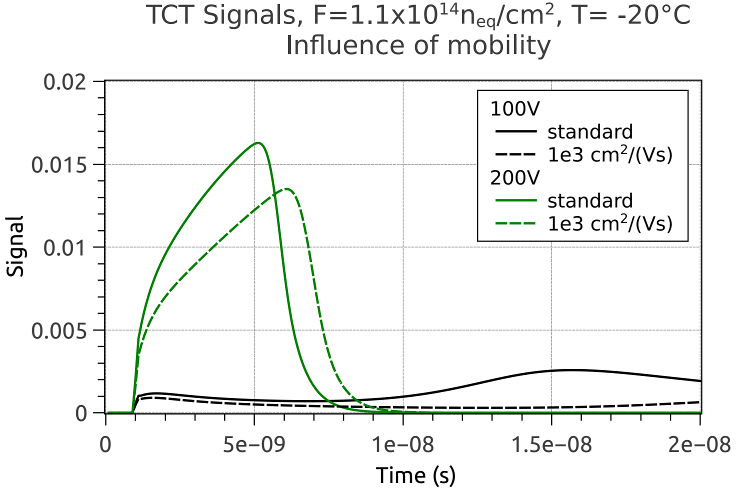

Figure 11.15: Influence of the mobility on the TCT pulse:
The pulse length can be changed by changing the mobility. This affects all voltages, though.

Because the whole picture is disturbed by decreasing the saturation velocity, a major change of the saturation velocity cannot solve the problem of the short TCT pulses at higher voltages in the simulation.

11.4.3 INFLUENCE OF MOBILITY

Another possibility to influence the pulse length is the mobility of the charge carriers. In this case, the mobility of electrons is varied. To achieve a longer pulse, the mobility of the electrons has to be lower than the standard mobility of Synopsys Sentaurus ($\mu_e = 1.414 \times 10^3\ \text{cm}^2/(\text{Vs})$). But decreasing the mobility has the disadvantage, that it affects the pulses at all voltages right from the start.

In figure 11.15 the influence of the mobility decreased to $\mu_e = 10^3\ \text{cm}^2/(\text{Vs})$ is visualized. The simulated signal at 200 V can really be extended to the measured pulse length. But as expected, also the second peak at 100 V is shifted to later times.

Usually, the mobilities used by Synopsys Sentaurus are taken from well measured models and have been tested in several other applications. There is no obvious reason, why the mobility should be decreased by at least 30% to match the current pulses of irradiated diodes. Of course,

defects can act as a barrier for charge carriers, but such a decrease does not only affect those pulses at higher voltage, but also the pulses at lower voltage.

The best result may be achieved by only slightly decreasing the mobility in irradiated diodes and increase the saturation velocity, to match the pulses. A variation within 10% is reasonable, since the used parameters have not been measured for very pure silicon detectors irradiated to very high fluences. The electric field, which influences the pulse length and peak shape most, is more sensitive to the defect occupation, generated space charge and trapping time. From this point of view, an effective two-defect model may not describe all pulses at all voltages perfectly.

11.5 Electric Fields

The TCT pulses shown in the previous section are caused by charge carriers drifting through the silicon bulk with a drift velociy proportional to the electric field, if the saturation velocity has not been reached. The electric field in a diode after irradiation is very different from the electric field before irradiation. The electric field is not linear any more and can grow from the back side, if it is *type inverted*.

The electric field is a direct outcome of the simulation, when the device is ramped to certain voltage. A cut along the depth of the diode provides the electric field as a function of the depth from the front side.

11.5.1 FZ320N

The electric fields for the FZ320N diode, which are the basis for the TCT simulations in the last section, are shown in figure 11.16. The fields are plotted for the three fluences from 100 V to 1000 V.

$F = 1.1 \times 10^{14}\, n_{eq} cm^{-2}$: At 100 V, the electric field is almost only at the back side, falling nearly linearly to front. Between 0 μm and 50 μm the field is almost zero, slightly increasing towards the front. This field explains very well the TCT pulse shape in figure 11.10. After the electrons experience a small electric field and are accelerated, they decelerate towards the bulk. When they reach the region with a higher electric field closer to the back side, they are accelerated again, forming a second peak before they leave the device at the back side.

At higher voltages, the higher field is always found at the back side of the diode, falling nearly linearly to front side. Higher electric fields let the electrons drift faster. The TCT signals show an increasing behaviour and get shorter with higher voltages.

$F = 2.9 \times 10^{14}\, n_{eq} cm^{-2}$: With three times more fluence as before, the electric field is pulled stronger to the back side. At low voltages, only little field is left in the bulk. But the electric field is always increasing again to the front side, which is then seen as the typical double peak structure in the TCT signal. The lowest electric field at this fluence is shifting from around 160 μm towards the front side as the voltage is increased from 100 V to 500 V. After 500 V, the field is getting more and more linear, and so the TCT is more and more constant including the convolution with the trapping time.

$F = 10^{15}\, n_{eq} cm^{-2}$: At the highest simulated fluence, the electric field shows two peaks at all voltages. Even more than at $F = 2.9 \times 10^{14}\, n_{eq} cm^{-2}$, the electric field is located at the back side. In the bulk, very low electric fields are present, even for high voltages. But also here, the field is increasing again towards the front side. Because more charge carriers are trapped at a higher fluence, the double peak at low voltages is not so visible in the TCT pulses. Many charge carriers are lost, until they reach the high field region at the back side, e.g. 240 μm at 100 V. The second peak in the TCT pulse does simply not show up.

At high voltages, the simulated TCT pulse still shows a double peak, following the electric field.

11.5.2 P-bulk Diodes

The proton model has been tuned especially for FZ320N diodes, but is still valid for FZ320P material. The most likely choice of material for the new CMS Tracker is p-bulk silicon. Therefore, the electric fields for p-bulk silicon diodes are shown here. To figure out, which thickness may be preferrable, both 320 μm and 200 μm thick diodes are investigated.

For the FZ320P diodes, shown in figure 11.17, the situation is quite the same as for the FZ320N diodes. The most obvious difference is, that the p-bulk diodes are not *type inverted*, but still deplete from the front side. This fact is most fortunate for the charge collection in higher irradiated diodes and sensors. Because of the high electric field at the front side, where the strips are located in a strip sensor, electrons are collected very fast. If there is a low-field region at the back of the device, some charge may be lost. However, the faster drift of electrons and the high electric field at the front side make the p-bulk material intrinsically more radiation hard with respect to charge collection compared to n-bulk material.

The electric fields for the three fluences tend to show the same behaviour as the electric fields for the n-bulk devices, but mirrored. There are minor differences in the field shape, because of the doping concentration before irradiation. Acceptor removal has not been considered in this case.

At the lowest fluence, the fields are still quite linear at higher voltages, showing only low electric fields at the back side below 500 V. But also for p-bulk devices, the electric field is not totally zero, but increasing slightly towards the back side. At $F = 2.9 \times 10^{14}\, n_{eq} cm^{-2}$, the fields tend to be parabolic, below 600 V they show low electric fields at the back. The highest electric fields at the front side are present for the highest fluence. Here the fields are dropping towards the center of the bulk and increase a little bit towards the back side.

For FZ200P diodes, the electric field – shown in figure 11.18, is a little bit different. Because of the lower bulk depth, the overall electric field is higher. For $F = 1.1 \times 10^{14}\, n_{eq} cm^{-2}$ the field is almost linear throughout the bulk and higher for the same voltage as the field in the 320 μm thick diode. For three times the fluence, the field gets more parabolic again, but only for 200 V it shows a low electric field in the bulk near the back side. At the highest simulated fluence, at the highest voltages, the double peak in the electric field is not as pronounced as for the thicker diode. Also here, at low voltages the field is quite low in the middle of the bulk, but increasing strongly towards the back.

With respect to charge collection, the higher electric fields in the thinner devices should be positive; thinner devices probably loose less signal due to low electric fields compared to thicker devices.

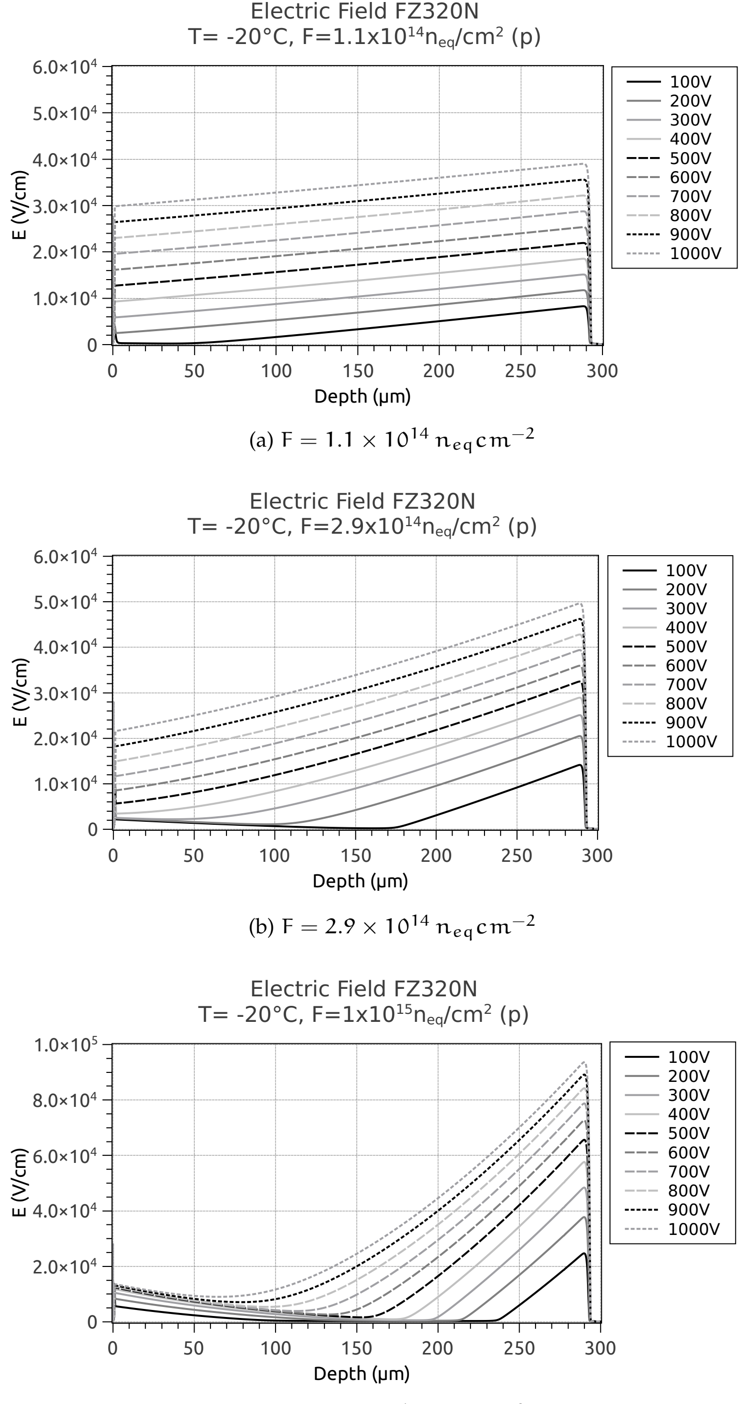

(a) $F = 1.1 \times 10^{14}\ n_{eq}cm^{-2}$

(b) $F = 2.9 \times 10^{14}\ n_{eq}cm^{-2}$

(c) $F = 1 \times 10^{15}\ n_{eq}cm^{-2}$

Figure 11.16: Electric fields in a FZ320N diode at different fluences simulated with the proton model: *At lower fluences ($10^{14}\ n_{eq}cm^{-2}$) the electric field is larger at the back side, but still quite linear at higher voltages. At higher fluences, the electric field is pronounced at the front and at the back side.*

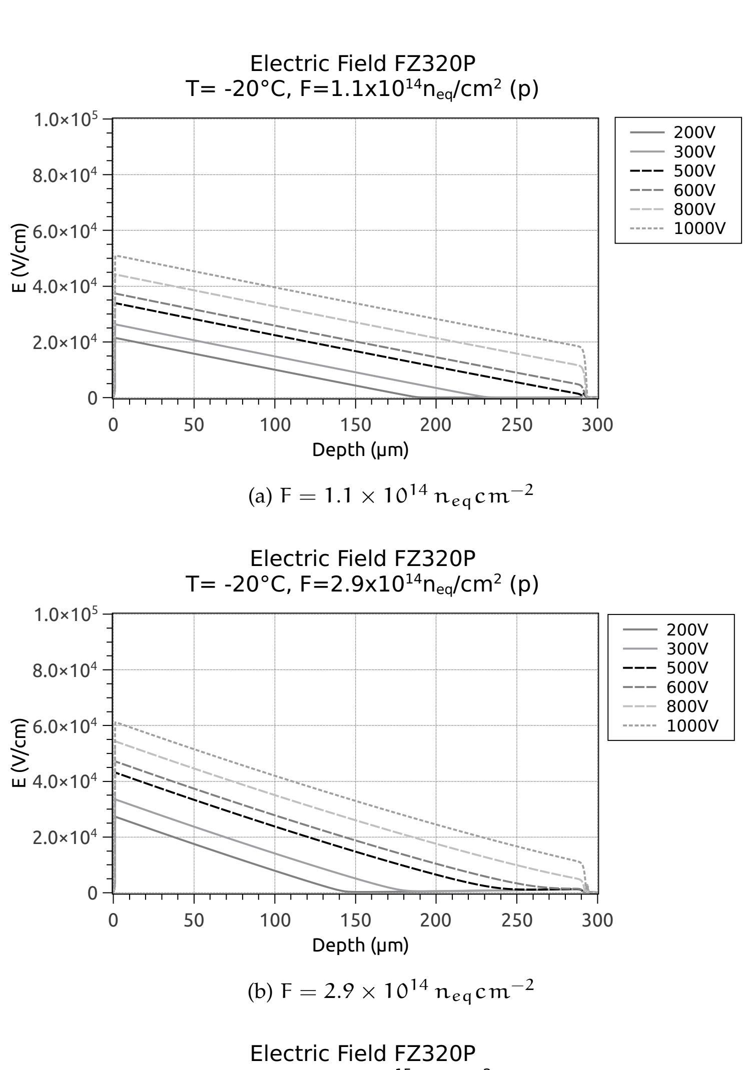

(a) $F = 1.1 \times 10^{14}\ n_{eq} cm^{-2}$

(b) $F = 2.9 \times 10^{14}\ n_{eq} cm^{-2}$

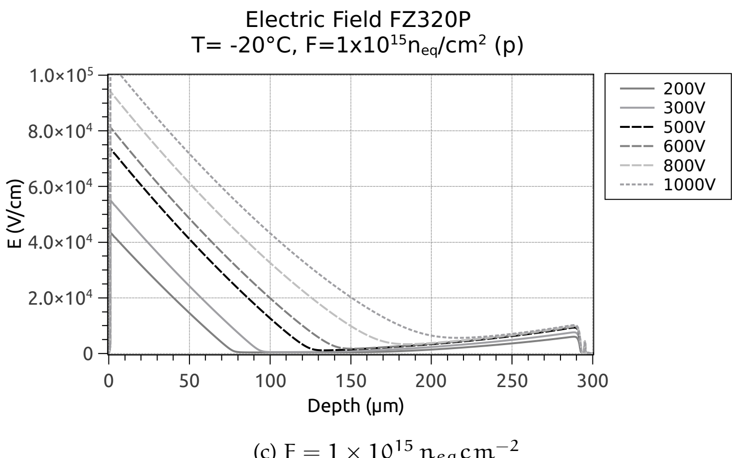

(c) $F = 1 \times 10^{15}\ n_{eq} cm^{-2}$

Figure 11.17: Electric fields in a FZ320P diode at different fluences simulated with the proton model: *The electric field shape is very much the same as for the n-bulk diodes, but mirrored. The high electric fields are at the front side.*

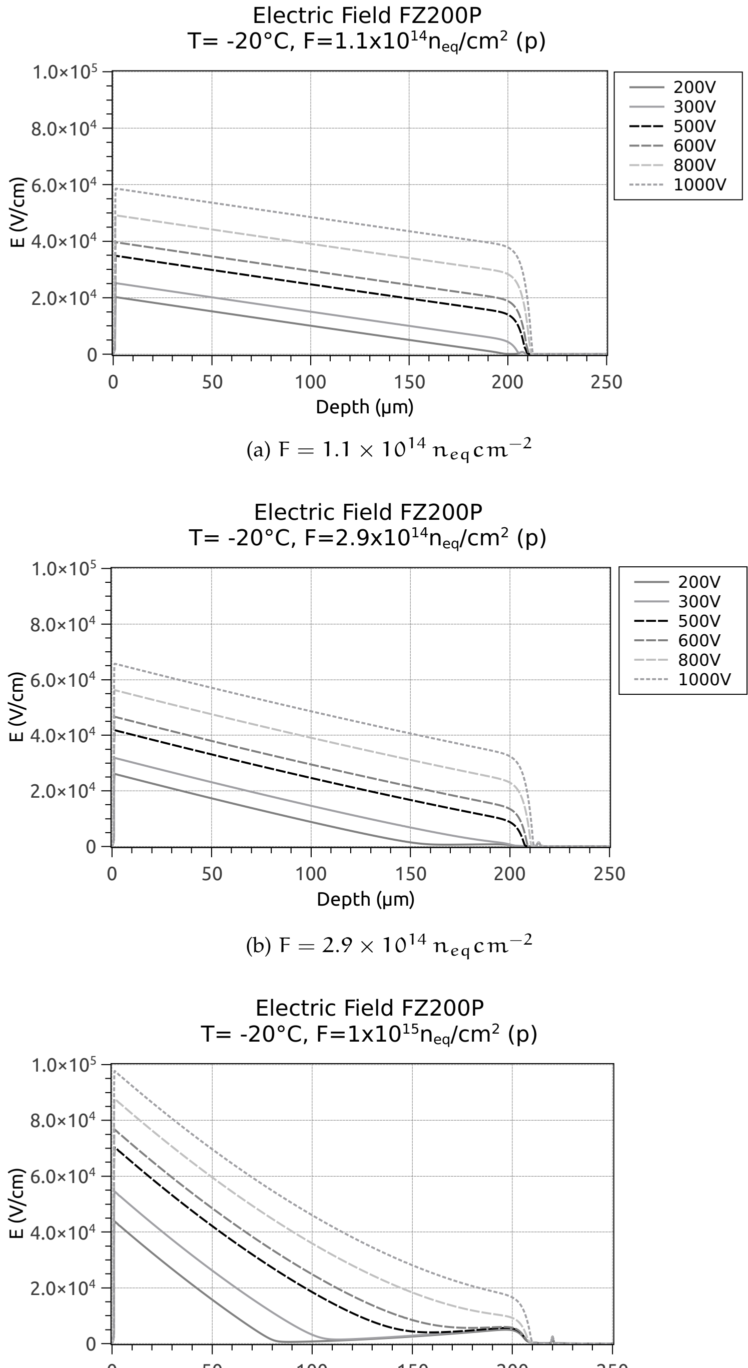

(a) $F = 1.1 \times 10^{14}\ n_{eq} cm^{-2}$

(b) $F = 2.9 \times 10^{14}\ n_{eq} cm^{-2}$

(c) $F = 1 \times 10^{15}\ n_{eq} cm^{-2}$

Figure 11.18: Electric fields in a FZ200P diode at different fluences simulated with the proton model: *The fields are higher compared to the thicker diodes. The double peak is not so pronounced.*

11.6 Trapping

Trapping is one of the most important factors, influencing the performance of irradiated silicon detectors. Due to trapping of charge carriers by defects in the silicon, the collected charge is reduced. The trapping time τ describes the typical lifetime of charge carriers in irradiated silicon. The trapping time is an effective quantity to specify the quality of the silicon material with respect to radiation damage. The trapping time of electrons or holes can be determined from TCT pulses. This has already been shown in 1993 by Kraner [KLF93].

A quantity, which describes the trapping dependence of the fluence is β:

$$\frac{1}{\tau} = \beta \times F. \tag{11.10}$$

If trapping is assumed to be proportional to the number of created defects, β should be constant over a wide fluence range.

First, this section shows the experimentally obtained trapping times. Secondly, a new method to calculate the trapping time from the simulation is presented. Thirdly, the results are discussed in context with other publications on the trapping time.

11.6.1 Experimental results

For the experimental determination of the trapping time for the FZ320N diodes, three diodes at different fluences are investigated. The TCT signal of n-bulk diodes generated with a red laser on the front side is created by drifting electrons. Since the FZ320N diodes have a quite deep diffusion of the highly doped region on the back, only the electron trapping time can be determined.

To compare the trapping time with the simulation, an effective trapping time is assumed. The method used to estimate the trapping time τ from the TCT pulses is the Charge Correction Method [K+02a]. The method works as follows: the collected charge of the device is reduced by the capturing of electrons drifting through the bulk. To correct for the capture of electrons, the pulse is corrected with an exponential. The time, at which the pulse starts is at t_0. At later times, more of the signal is lost and with the trapping time τ, the signal correction is larger at later times.

$$I_{corr.} = I \times \exp\left(\frac{t - t_0}{\tau}\right) \tag{11.11}$$

After full depletion, the collected charge should be constant as a function of voltage. The electrons drift faster at higher voltages and the signal is faster. Less electrons are trapped and shorter signals are not corrected so much with the trapping time. The integrated TCT signal, which is the collected charge, is corrected with the trapping time in a way, that the collected charge is constant above the full depletion voltage. At the correct trapping time, the collected charge versus voltage has a slope of zero; a larger trapping time leads to a positive slope, a smaller trapping leads to an overcorrection of the signals and ends up in a negative slope for the corrected charge.

The results for the electron trapping time are listed in table 11.4. These diodes have been irradiated with protons only.

If the trapping times are converted into the beta-factor, a fluence independent indicator for the trapping in silicon, it is obvious, that the trapping largely varies in the investigated diodes. At the fluences around $10^{14}\ n_{eq}cm^{-2}$, the Charge Correction method should be quite robust. At $10^{15}\ n_{eq}cm^{-2}$, it is difficult to obtain a trapping time, because the depletion voltage is quite high and only few voltage steps are left to fit a slope. The small trapping time furthermore leads to large corrections in the curve, which is an additional source of errors. The error on the trapping is estimated as the deviation, which does not lead to a significant change in the

Table 11.4: Electron trapping times of FZ320N diodes, $T = -20\,°C$.

Diode	Fluence ($n_{eq}cm^{-2}$)	τ_e (ns)	$\beta(10^{-16}\,cm^2/ns)$
FZ320N_08_DiodeL_05	1.1×10^{14}	17.8 ± 0.3	5.1 ± 1.0
FZ320N_01_DiodeS_14	2.9×10^{14}	13.0 ± 0.3	2.7 ± 0.5
FZ320N_03_DiodeS_16	1.0×10^{15}	1.1 ± 0.1	9.1 ± 2.0

almost zero slope of the fit on the collected charge plateau. The error for β includes the error on the fluence and is calculated with:

$$\Delta\beta = \sqrt{\left(\frac{\partial\beta}{\partial\tau}\right)^2 (\Delta\tau)^2 + \left(\frac{\partial\beta}{\partial F}\right)^2 (\Delta F)^2}. \tag{11.12}$$

11.6.2 SIMULATED TRAPPING TIME

After the TCT pulse has been simulated, the charge correction can be applied to these pulses, too. However, there is another possibility to determine the trapping time in the simulation. The simulator knows very well, how many charges are drifting through the diode at each time. As an example, a FZ320N diode simulated with the proton defect model at three fluences, $1.1 \times 10^{14}\, n_{eq}cm^{-2}$, $2.9 \times 10^{14}\, n_{eq}cm^{-2}$ and $10^{15}\, n_{eq}cm^{-2}$ is considered.

In figure 11.19 it is shown, how the electrons drift through the diode. The electrons, generated by the laser pulse at 1 ns start to drift according to the electric field. For 300 V, the situation is very clear; the well defined electron cloud is moving through the diode and smears out at larger times because of diffusion. At about 4 ns, the TCT pulse has reached its maximum and drops. This is the point, at which the electrons start to leave the diode.

At 100 V, again the electrons start to drift. However, due to the quite low electric field at 100 V, the electron cloud moving through the device is not moving as a whole, but the peak is shifting very slowly towards to the back side of the diode and decreases, while the electrons are spread all over the diode. At 20 ns, not all of the generated electrons have left the diode, so the electron density is not totally vanishing.

The trapping time can now be estimated during the drift of the full electron cloud. The TCT pulse is the best time estimator for that. From the laser shot at 1 ns up to the point at which the electrons leave the diode– this is the maximum in the TCT pulse – the electron density can be integrated over the depth of the device. The resulting total number of electrons is visualized in figures 11.20 and 11.21.

It is obvious, that the total number of electrons is decreasing slowly up to the point, where they reach the back side of the diode. Before this point, the decrease of electrons can be attributed to the trapping of charge carriers due to the defects in the diode.

The trapping time is obtained from a simple exponential

$$e = e_0 \times \exp\left(-\frac{t - t_0}{\tau}\right) \tag{11.13}$$

where the initial number of electrons e_0 is reduced during the drift through the diode, starting at time $t_0 = 1\,ns$, with a probability $1/\tau$. There is a significant offset of electrons present in the device, if the total number of electrons is considered, which is in the order of $10^{10}\,e$. The fit range for the exponential is given by the maximum of the TCT pulse and is marked in the plot. Of course, for higher voltages the pulse is faster and hence the fit range is smaller. For each voltage, the trapping time is fitted separately. Table 11.5 lists the trapping time for different voltages in steps of 100 V. It is clear, that the trapping time in the simulator is not dependent on the bias voltage. Therefore, the average over the voltage is given as simulated trapping time.

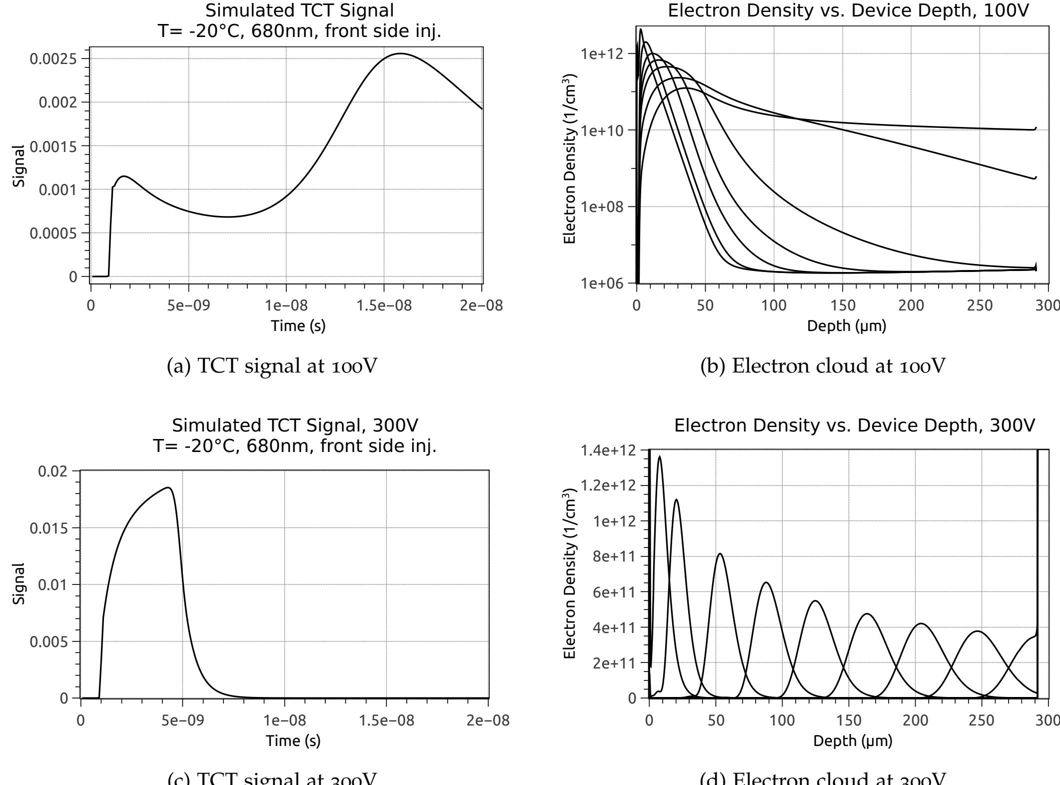

(a) TCT signal at 100V

(b) Electron cloud at 100V

(c) TCT signal at 300V

(d) Electron cloud at 300V

Figure 11.19: Simulation of the signal evolution in the diode at $F = 10^{14}\,n_{eq}cm^{-2}$: *the electrons generated at the front side move through the device. At higher voltages, the cloud is more defined than at low electric fields.*

To validate the trapping times determined by this method, the simulated TCT pulses can be corrected by the trapping time found and integrated to get the total collected charge. Figure 11.22 shows the corrected TCT pulses for the FZ320N diode at $F = 10^{14}\,n_{eq}cm^{-2}$ and the integral of the TCT pulses as simulated and correct. It is clear, that the integral of the corrected TCT pulses show a constant value, as it is expected from an effective trapping time, whereas the pulses as simulated show an increase. The values at 100 V suffer from an incomplete simulation of the TCT pulse, the integral misses some charge. Picture 11.23 shows, that a smaller trapping time leads to larger corrections at later times in the TCT signal. This affects the integrated signal much stronger than at lower fluences and the increasing charge with higher bias voltage again shows a constant value after the correction with the trapping time. Hence figures 11.22 and 11.23 make clear, that the approach to determine the trapping time via the total number of electrons in the simulation is a valid method.

11.6.3 DISCUSSION ON TRAPPING TIMES

The experimental trapping times are not very linear over the fluence, as the β-factor in table 11.4 shows. Taking a look at the calculated values from the trapping time extracted from the simulation, $\beta(1.1 \times 10^{14}\,n_{eq}cm^{-2}) = 3.2 \times 10^{-16}\,cm^2/ns$, $\beta(2.9 \times 10^{14}\,n_{eq}cm^{-2}) = 2.7 \times 10^{-16}\,cm^2/ns$ and $\beta(10^{15}\,n_{eq}cm^{-2}) = 2.4 \times 10^{-16}\,cm^2/ns$, they show the tendency to decrease with higher fluence. At higher fluences, less charge carriers are trapped than expected from the increase in fluence.

Comparing with values from Kramberger [K+02a] at $-10\,°C$ and beneficial annealing (10d at RT): $\beta(Neutrons) = 4.1 \times 10^{-16}\,cm^2/ns$, $\beta(Pions) = 5.7 \times 10^{-16}\,cm^2/ns$, $\beta(Protons) =$

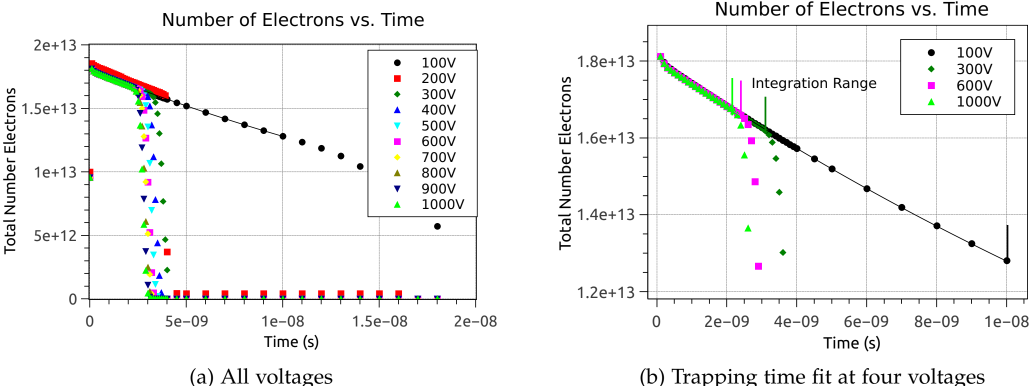

(a) All voltages (b) Trapping time fit at four voltages

Figure 11.20: Fit of the trapping time for a FZ320N diode simulated at $F = 10^{14}\,n_{eq}cm^{-2}$.
The fit range is marked in the right plot. At this point, the electron cloud moving through the diode starts to leave the device.

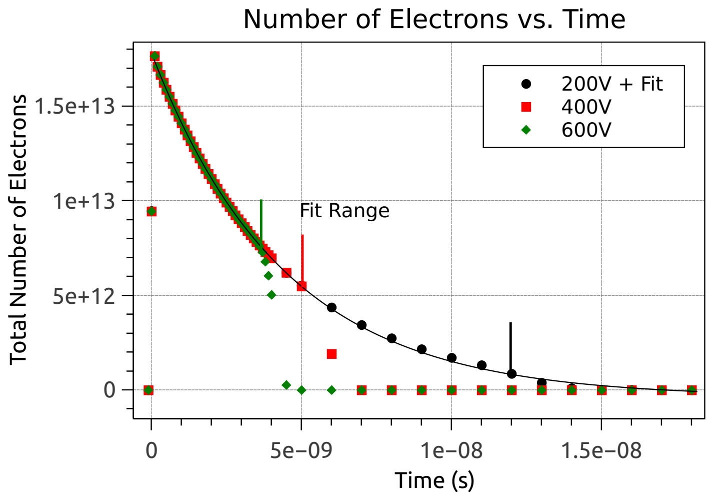

Figure 11.21: Fit of the trapping time for a FZ320N diode simulated at $F = 10^{15}\,n_{eq}cm^{-2}$.
The exponential drop in the total number of electrons due to trapping is clearly visible at this fluence. The fit range is marked.

$5.6 \times 10^{-16}\,cm^2/ns$, $\beta(\text{Neutrons}) = 4.2 \times 10^{-16}\,cm^2/ns$ [K+02b], the experimental value for $F = 1.1 \times 10^{14}\,n_{eq}cm^{-2}$ is well within the errors. It has to be considered though, that the values from Kramberger are at a higher temperature and more beneficial annealing. Especially the beneficial annealing can increase the electron trapping time [K+07]. The simulation also results in a larger trapping time. The reason for the larger trapping time in the simulation may be the shorter TCT pulse (see figure 11.10). In a shorter pulse, less charge carriers are able to be trapped.

At $2.9 \times 10^{14}\,n_{eq}cm^{-2}$, the measured trapping time is larger than the expected value, but very close to the simulated τ_e. At the highest fluence, the trapping time obtained from the simulation is larger than the experimentally obtained value. The simulation overestimates the second peak in the TCT signal in figure 11.13, which requires less correction and thus leads to a larger trapping time. Because it is more difficult to get a precise trapping time at larger fluences, it is not clear, if the trapping is still proportional to the created defects.

Because the experimental method to determine trapping times from the TCT pulses is not very accurate, the simulation can hint to the correct range of the trapping time of the charge carriers. Here, the two-defect model has been tuned to match the TCT pulses at several fluences,

Table 11.5: Electron trapping time from the simulation at different voltages. The error on all fits is smaller than 0.1 ns.

Voltage (V)	$\tau_e(10^{14}\,n_{eq}cm^{-2})$ (ns)	$\tau_e(3\times10^{14}\,n_{eq}cm^{-2})$ (ns)	$\tau_e(10^{15}\,n_{eq}cm^{-2})$ (ns)
100	29.1	12.6	4.2
200	26.6	12.6	4.2
300	28.6	12.7	4.2
400	28.4	12.7	4.2
500	28.5	12.6	4.2
600	28.3	12.6	4.2
700	28.1	12.6	4.2
800	28.1	12.6	4.2
900	28.1	12.6	4.3
1000	28.1	12.6	4.3
Avg.	28.2 ± 0.6	12.62 ± 0.03	4.24 ± 0.01

small trade-offs had to be accepted. For comparison and prediction, the method to calculate the trapping time from the simulation can be a very useful tool. If the TCT pulses can be simulated even more accurately with a better tuning of the trap model, the accuracy of the simulation can be boosted even more. An effective description over a larger fluence range is then lost, though.

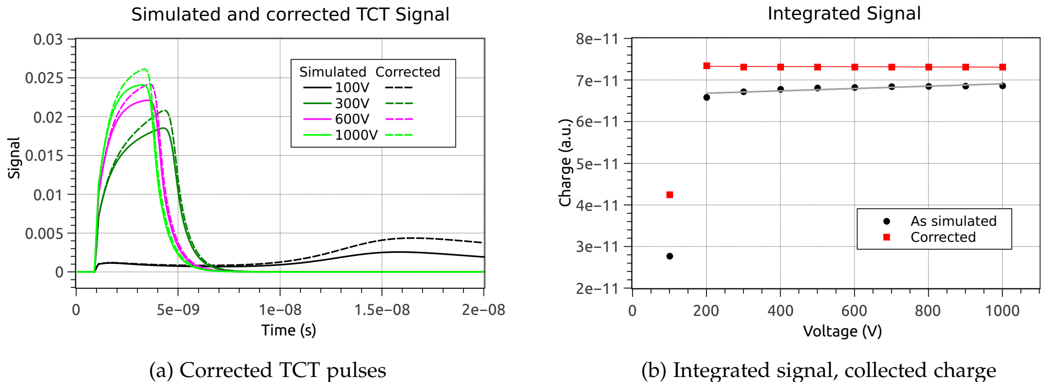

(a) Corrected TCT pulses

(b) Integrated signal, collected charge

Figure 11.22: Simulated TCT pulses with and without trapping time correction and integrated signals at $F = 10^{14}\, n_{eq} cm^{-2}$:
The correction with the trapping leads to higher maxima in the TCT signals. Therefore the integrated signals with correction are larger and show a constant value as expected from an effective trapping time.

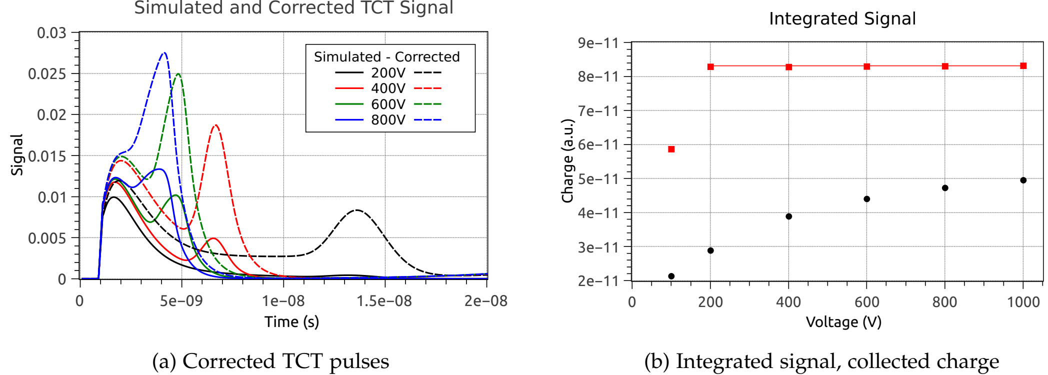

(a) Corrected TCT pulses

(b) Integrated signal, collected charge

Figure 11.23: Simulated TCT pulses with and without trapping time correction and integrated signals at $F = 10^{15}\, n_{eq} cm^{-2}$:
The correction with the lower trapping time affects the signal much stronger. Especially the peaks at later times are more pronounced. The integrated signal, gaining more and more charge before the correction, again shows a constant value after correction.

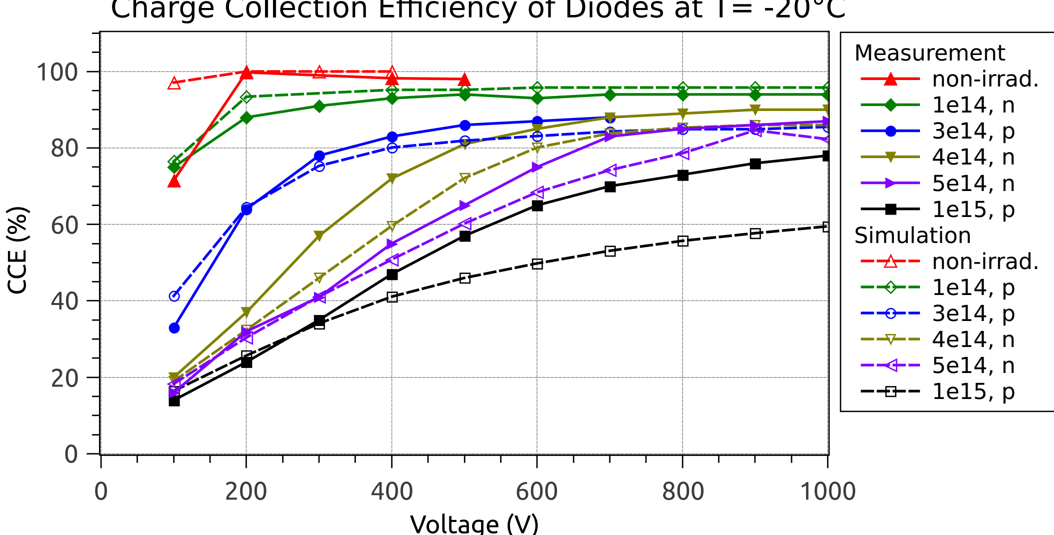

Figure 11.24: Charge collection efficiency of FZ320N diodes at $T = -20\,°C$ and several fluences (proton and neutron irradiation):
The CCE is simulated quite well, only at $F = 10^{15}\,n_{eq}cm^{-2}$ *the measured CCE values are higher.* Data partly from [Poe13].

11.7 Charge Collection Efficiency

With respect to the sensor performance in a possible CMS Tracker upgrade scenario, charge collection efficiency is one of the most interesting points. The simulation of charge collection efficiency for diodes can give a hint on the collected charge in sensor, however, the different geometry and the influence of oxide charges and strip couplings will give lower signal in sensors.

In this section, the collected charge of diodes is simulated and compared to the experimental results obtained with the picolaser setup. To determine the collected charge in diodes, signals are generated with an infrared laser. In the simulation, the optical generation with an infrared wavelength (1060 nm) is used. The optical absorption of infrared light in silicon is explained in section 5.2.1 and the implementation in the simulation in section A.2.11.

The collected charge normalized to the charge collected by an un-irradiated FZ320N diode can be seen in figure 11.24. Although the simulation is able to give the correct depletion voltage for the un-irradiated diode, the collected charge generated with an infrared laser is too high before full depletion.

The charge collection efficiency of diodes irradiated to $2.9 \times 10^{14}\,n_{eq}cm^{-2}$ and $4 \times 10^{14}\,n_{eq}cm^{-2}$ is taken from Poehlsen [Poe13]. For the irradiated diodes at $F = 10^{14}\,n_{eq}cm^{-2}$ and $2.9 \times 10^{14}\,n_{eq}cm^{-2}$, the shape of the CCE matches very well between measurement and simulation. The neutron irradiated curves at $4 \times 10^{14}\,n_{eq}cm^{-2}$ and $5 \times 10^{14}\,n_{eq}cm^{-2}$ differ 10% at most between 300 V and 600 V, and 500 V and 800 V respectively. They eventually reach the high voltage efficiency within less than 5% difference.

At the largest fluence however, $F = 10^{15}\,n_{eq}cm^{-2}$, the charge collected in the simulated diodes seems to be 20% lower at high voltages. The depletion voltage cannot be the reason for the deviation, since the difference in CCE remains at 20% even at 1000 V. A different detrapping of the defects at higher voltages and higer fluences or field dependent trapping may possibly be the case, which is not considered in the simulation (see section 11.6). A deviation from the desired fluence or a miscalibration of the laser intensity cannot be excluded. To account for the higher CCE, $\sigma_h(\mathrm{Don.})$ and $\sigma_e(\mathrm{Acc.})$ can be changed to achieve a higher CCE, carefully paying attention not to spoil the shape of the TCT pulse.

Table 11.6: Proton Model for $T = 0\,^{\circ}C$.

Parameter	Donor	Acceptor
$\sigma(e)(cm^2)$	0.954×10^{-14}	1.65×10^{-14}
$\sigma(h)(cm^2)$	1.65×10^{-14}	0.954×10^{-14}

11.8 Temperature Dependence of the Proton Model

So far, all the simulations, IV, CV, TCT and CCE, have been simulated at $T = -20\,^{\circ}C$. The cross sections of both irradiation models are tuned to match the current at this temperature. To make the well tuned proton model more robust, other temperatures have to be considered. For all the irradiated diodes, data at $T = 0\,^{\circ}C$ is available.

LEAKAGE CURRENT: For the current at 273 K, the current related damage rate is $\alpha = 7.8 \times 10^{-18}\,A/cm$. If the parameters at 253 K of the proton model are used, the current at 273 K is slightly too high. To correct for this and to obtain the correct current temperature scaling (see section 3.3.6.2), the cross sections mainly responsible for the current (σ_e(Don.) and σ_h(Acc.)) have to be decreased slightly. Both of these cross sections are set equal again and are reduced from $\sigma = 1.0 \times 10^{-14}\,cm^2$ to $\sigma = 0.954 \times 10^{-14}\,cm^2$.

DEPLETION VOLTAGE: Experimentally, the depletion voltage at 273 K measured at 1 kHz is a little bit lower than the depletion voltage at 253 K and 1 kHz. At a fluence of $1.1 \times 10^{14}\,n_{eq}cm^{-2}$, the simulation with the given concentrations of the proton model results in a depletion voltage near the measured depletion voltage. The concentrations of the defects at different fluences – the introduction rate – is not changed.

TRANSIENT CURRENT: The measured TCT pulses at $0\,^{\circ}C$ do not look very different from the pulses measured at $-20\,^{\circ}C$. The pulses of both temperatures are plotted in figure 11.25. Because space charge and trapping is temperature dependent in the simulation and the silicon bandgap at 273 K is smaller, the generated space charge and trapping of charge carriers is different. To get the same pulse shape at two different temperatures, the two cross section, which do not influence the current, have to be modified. Simulations at $F = 1.1 \times 10^{14}\,n_{eq}cm^{-2}$ show, that both cross sections, σ_h(Don.) and σ_e(Acc.) have to be raised from their original value ($\sigma = 1.0 \times 10^{14}\,cm^2$) to $\sigma = 1.65 \times 10^{-14}\,cm^2$. This means, that more charge carriers can be trapped in these defects.

The resulting trap model for $T = 0\,^{\circ}C$ is listed in table 11.6. The energy of the two defects as well as the fluence dependent concentration are kept the same. The cross sections of electrons and holes for the donor and the acceptor are adapted to the new temperature.

The picture of the different cross sections is very convincing: the cross sections for the current are not very different from those in table 11.3. A slight adaption because of the bandgap is reasonable. The larger cross sections for electrons and holes also fit in the picture: at a higher temperature charge carriers can be trapped more easily because the defects are more reactive.

For the fluence of $1.1 \times 10^{14}\,n_{eq}cm^{-2}$, the simulated CV curve as well as the simulated TCT pulse at $0\,^{\circ}C$ can be seen in figure 11.26. They fit very well to the measured curves.

11.9 Annealing Time

The irradiation damage models for the simulation presented here are established for a single annealing time only. All data from the investigated diodes and strip sensors in this work is collected at 10 minutes at $60\,^{\circ}C$ annealing time, which is the initial annealing time for all samples in the HPK Campaign. This corresponds to about two days annealing at room temperature and describes the “just irradiated” scenario for test sensors or the sensors in the future CMS

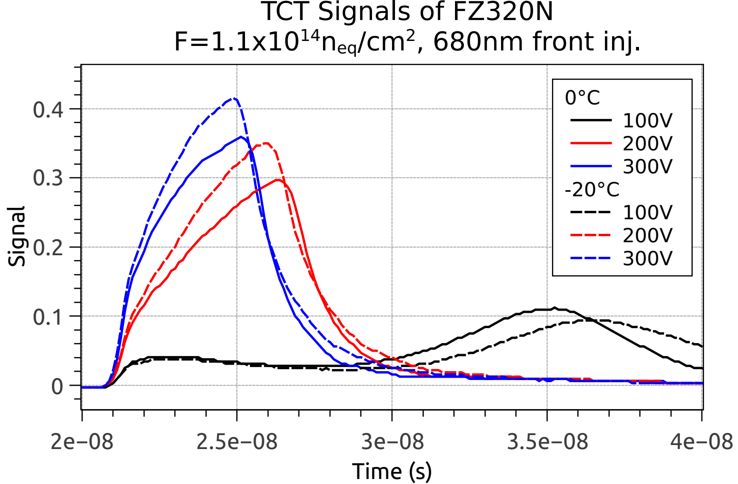

Figure 11.25: TCT signals at $T = 0\,°C$ and $T = -20\,°C$ in comparison: *The TCT pulses do not differ much at these two temperatures.*

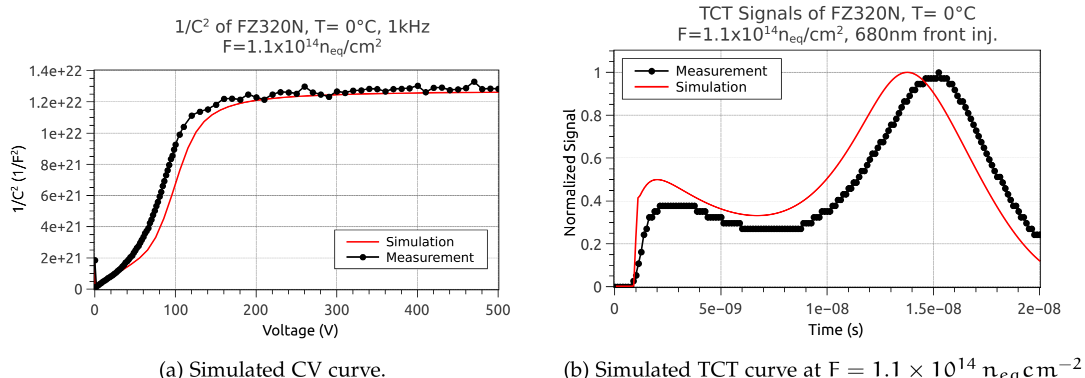

(a) Simulated CV curve.

(b) Simulated TCT curve at $F = 1.1 \times 10^{14}\, n_{eq} cm^{-2}$

Figure 11.26: Simulated CV and TCT curve at $T = 0\,°C$ with the adapted proton model.

Tracker, which are operated at $-20\,°C$ with only few maintenance hours. For a lower leakage current of the sensors and a better charge collection collection of the sensors depending on its type, the sensors can be annealed.

The annealing of the devices can be estimated either via an interpolation with the Hamburg-Model or a change of the parameters of the effective two-defect model. Because the Hamburg-Model only describes the annealing of the leakage current and the depletion voltage, the values for the charge collection efficiency have to be taken from the experimental values.

For a better estimation of the collected charge and depletion voltage after irradiation and annealing, the introduction rates of the donor and the acceptor in the two-defect model should be altered. Because the annealing process can also affect the interplay between the defects and because the leakage current is lower after annealing, the cross sections of the defects have to be altered, too.

The HPK Campaign presents the unique opportunity to expand the effective two-defect model to include the parameter annealing time. However, this exceeds the possibilities of this thesis and will not be pursued further here.

11.10 Summary and Discussion

In this chapter, an effective two-defect model for silicon detectors irradiated to HL-LHC fluences has been established on the basis of [E+04] and has been presented in its modified version. First, measurement results show, that it is legitimate to assume different damage models for proton and neutron irradiation because of the different slope of the depletion voltage as a function of fluence. It has been shown, that the current of the two-defect model can be well parametrized according to the current related damage parameter by Moll [Mol99], taking into account concentrations and cross sections of the two defects.

Furthermore, the effective two-defect model for protons has been used to simulate TCT pulses and the cross sections have been modified such, that the TCT pulse shape can be reproduced very well. As the double peak structure of the TCT pulses show, the electric field in the bulk is quite low and increases towards both sides. With the defect model in hand, the electric field can be exctracted from the simulation and not only from the reconstruction with TCT pulses [V+07]. In addition, the radiation damage model for the bulk can be applied to other geometries like silicon strip sensors.

A new method to extract the trapping time – a very important parameter for the basic material investigation of radiation hardness – has been presented and compared to experimental results. Here, the simulation lacks some fine-tuning but is able to forecast the general trend.

Again in the transient simulation for the charge collection efficiency, the model can predict very well the charge loss in silicon diodes.

Additional factors influencing the simulation have been discussed in the course of this chapter: the dependence of the model on simulation parameters like saturation velocity and mobility, the dependence on temperature and annealing time. Because measurements almost show the same pulses at $0\,^{\circ}\mathrm{C}$ and $-20\,^{\circ}\mathrm{C}$, the cross sections of the trap model had to be modified at the higher temperature.

There have been several other attempts to establish a radiation damage model including several effects like leakage current, depletion voltage and charge collection efficiency. The models using one, two or three traps shown by Petasecca et al. ([PMPP06], [P+06], [P+05], [PMP05]) require different parameters for different fluences.

The model shown by Chiochia et al. [C+05] and Swartz et al. [S+06] already take into account the double peak electric field in heavily irradiated silicon detectors. Due to the double peak electric field, the meaning of the effective doping concentration and depletion voltage are questioned [C+06]. Also, the meaning of "type inversion" can be understood as the change of the high electric field from the front to the back side of the sensor. The charge collection of measurements compared to simulation fits very well for these models, which also use the two defects described by Eremin [E+04].

However, none of these radiation damage models for the simulation take into account the information from the Transient Current Technique. This unique opportunity is given by the HPK Campaign, sensors and diodes are irradiated to the same fluences. The TCT pulses in diodes provide more information about the electric field and trapping in silicon sensors, although the grazing angle technique [C+05] can also hint on the electric field in the sensor bulk. The model developed for diodes in this chapter can be applied to the strip sensors, in which the electric fields after irradiation are very important for their performance.

The effective two-defect model in this thesis describes not only a single or several aspects of irradiated silicon sensors but combines them to one model. Leakage current, depletion voltage, transient pulses and charge collection are provided in a coherent way. The universal approach keeps the cross sections for the defects constant at one temperature and concentrations are introduced as linear dependencies of the fluence.

With the two-defect model of this thesis, the measured results of diodes and sensors from the HPK Campaign can be predicted and reproduced very well.

Note that the model is valid for highly irradiated sensors only ($F > 10^{14}\, n_{eq} cm^{-2}$) and has been tuned for Synopsys Sentaurus.

12

IRRADIATED STRIP SENSORS

The effective two-defect radiation damage model is powerful in predicting the performance of diodes after irradiation, as it has been shown in the last chapter. The model is now applied to silicon strip sensors to analyze electric fields and charge collection efficiency after irradiation. One more important ingredient comes into play when discussing strip sensors: the oxide charge concentration. Near the strips on the front side of the strip sensor, the oxide charge can completely alter the electric fields and even influence charge collection efficiency. For irradiated sensors in the simulation, a comparison is done between a configuration with low oxide charge ($10^{11}\,cm^{-2}$) and higher oxide charge concentration ($7 \times 10^{11}\,cm^{-2}$ or $10^{12}\,cm^{-2}$).

The pitch of the strip sensors has been chosen to be 90 μm, the most probable future pitch of the sensors for the phase II tracker upgrade.

This chapter is dedicated to predict and compare the performance of irradiated silicon strip sensors in the measurement and simulation.

12.1 Electric Fields at the Strips

Depending on the oxide charge, large electric fields can appear at the strips of silicon strip sensors. The two-defect radiation damage model is applied to silicon strip sensors in the simulation to investigate the formation of high electric fields, which can be the cause for breakdown or noise in the sensors.

The sensors are examined with view on different surface damage. Two interface charge concentrations are considered to compare between bulk damage only and radiation damage covering severe bulk and surface damage.

12.1.1 N-BULK SENSORS

`Neutron irradiation:`

In the case of neutron irradiation, mainly bulk damage is created. This case is simulated at a fluence of $F_{eq} = 5 \times 10^{14}\,n_{eq}cm^{-2}$ and interface charge concentration of $Q_{ox} = 10^{11}\,cm^{-2}$ with the neutron two-defect model. This case is compared to a high interface charge concentration at $Q_{ox} = 10^{12}\,cm^{-2}$. The resulting electric fields at two cuts parallel to the surface are shown in figure 12.1. The cuts are made at 100 nm below the $Si - SiO_2$ interface and 1.3 μm below the interface; this is at the junction of the 1.5 μm deep gaussian-shaped doping profile of the strip.

As it can be seen, the electric fields are higher, when less interface charge is present. The highest electric fields are found at the edge of the strip just beneath the $Si - SiO_2$ interface. The fields at the corner of the strip implant are, compared to the un-irradiated case, not so high any more.

An additional strip pitch of 240 μm is investigated here, which is an extremly large pitch and which is intended to show the trend for sensors with a larger pitch. In the comparison of the two pitches, 90 μm and 240 μm, the larger pitch again shows higher electric fields for both interface charge concentrations and strip widths. Larger implant widths always tend to show lower electric fields at the strip edge and especially at the strip corner. The smaller pitch of

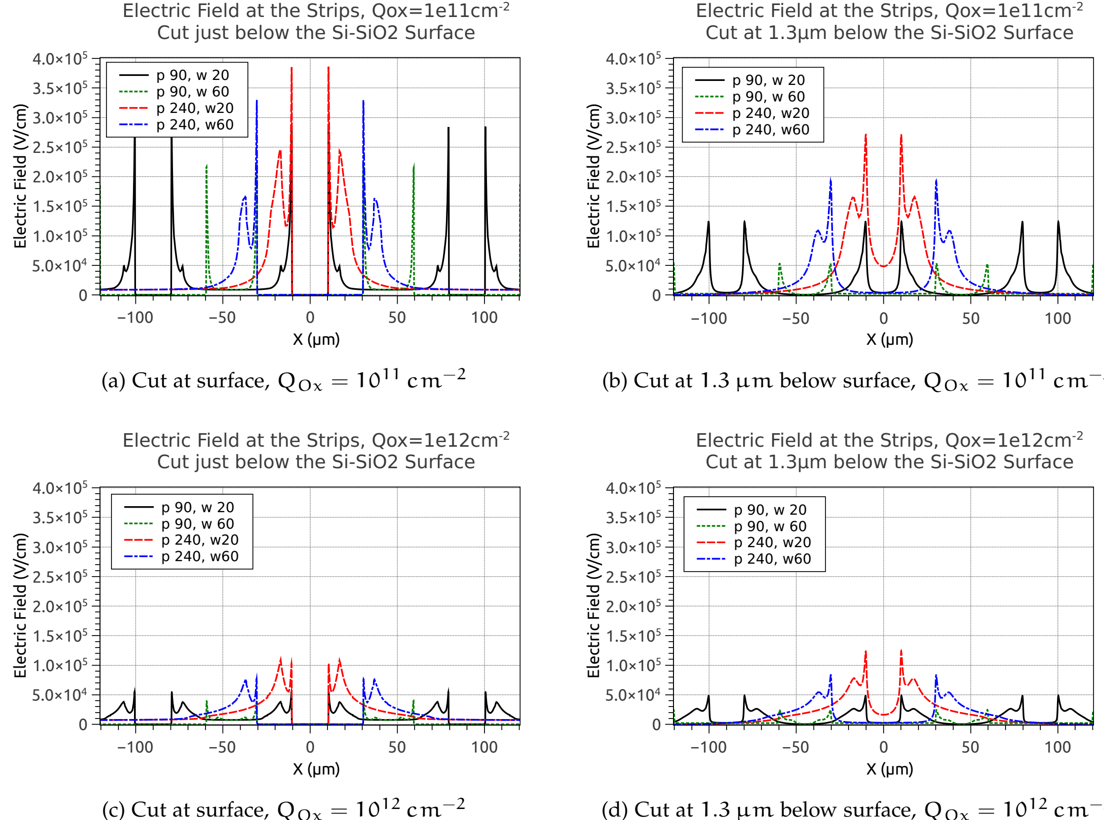

(a) Cut at surface, $Q_{Ox} = 10^{11}\,\text{cm}^{-2}$

(b) Cut at 1.3 µm below surface, $Q_{Ox} = 10^{11}\,\text{cm}^{-2}$

(c) Cut at surface, $Q_{Ox} = 10^{12}\,\text{cm}^{-2}$

(d) Cut at 1.3 µm below surface, $Q_{Ox} = 10^{12}\,\text{cm}^{-2}$

Figure 12.1: Electric fields at the strips, simulated with the neutron model at $F_{eq} = 5 \times 10^{14}\,n_{eq}\text{cm}^{-2}$ and two different interface charge concentrations.

90 µm shows the same tendencies mentioned above; the direct comparison with 240 µm shows, that the electric field at the strip edge is smaller at the same strip width.

When comparing the two interface charge concentrations, it is obvious, that the electric fields are much smaller for a high interface charge. In the case of $Q_{ox} = 10^{11}\,\text{cm}^{-2}$, the electric fields seem to be critical for the large pitch at 1000 V since the field peaks above 3×10^5 V/cm, the breakdown field strength in silicon. All other configurations operate in a safe regime regarding the electrical field strength.

`Proton irradiation:`

Depending on the proton particle energy, not only bulk damage is created, but in the case of 23 MeV protons a lot of oxide charge is created too. This influences the electric field in the bulk in addition to the bulk damage by the protons. The electric fields at 1000 V for low oxide charge ($Q_{ox} = 10^{11}\,\text{cm}^{-2}$) and high oxide charge ($Q_{ox} = 10^{12}\,\text{cm}^{-2}$) are shown in figure 12.2.

For a low oxide charge concentration, the electric fields do not exceed 3×10^5 V/cm for all configurations. The sensor with pitch 240 µm of course shows the highest electric fields for the smallest strip width. The field of the desired pitch of 90 µm at the strip implant and at the metal overhang just reach 10^5 V/cm.

The electric field increases very much, if the oxide charge is raised to $10^{12}\,\text{cm}^{-2}$. This is the more likely case after proton irradiation. The electric fields increase very much and exceed 3×10^5 V/cm for three out of the four configurations. Also the pitch 90 µm and width 20 µm sensor shows these high fields near the silicon-silicon dioxide interface. At the junction at a depth of 1.3 µm, the fields are a little bit lower.

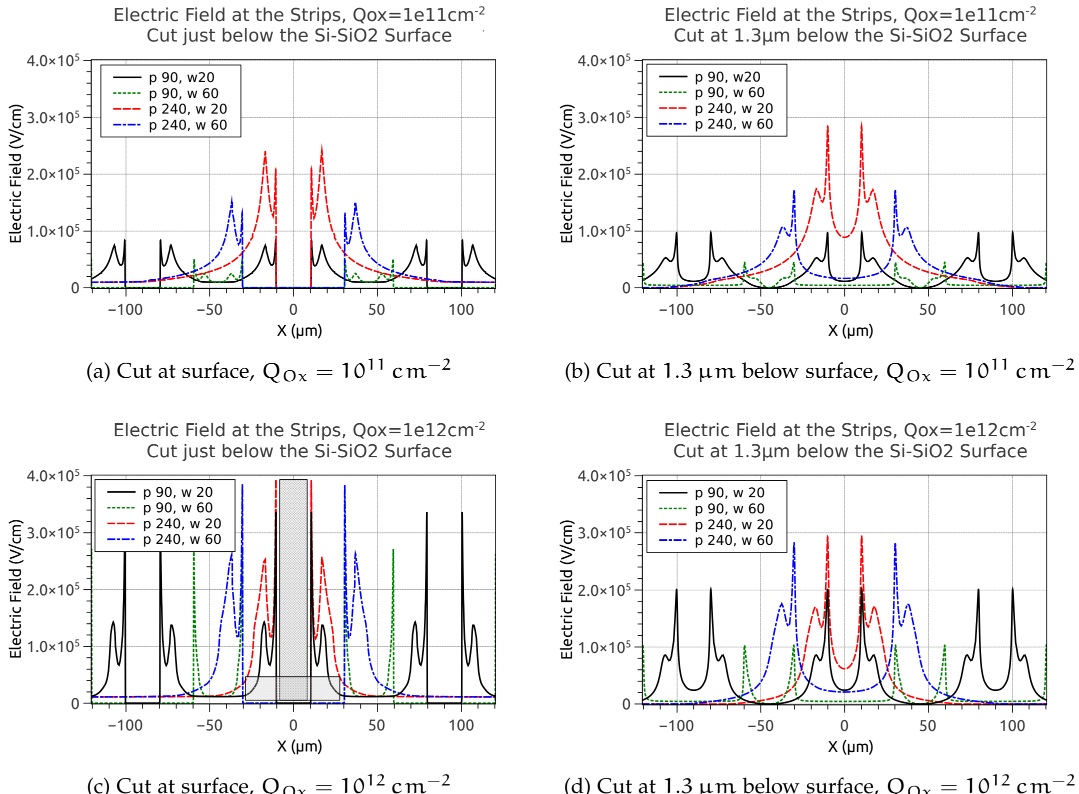

(a) Cut at surface, $Q_{Ox} = 10^{11}\,cm^{-2}$

(b) Cut at 1.3 μm below surface, $Q_{Ox} = 10^{11}\,cm^{-2}$

(c) Cut at surface, $Q_{Ox} = 10^{12}\,cm^{-2}$

(d) Cut at 1.3 μm below surface, $Q_{Ox} = 10^{12}\,cm^{-2}$

Figure 12.2: Electric fields at the strips in a n-bulk sensor simulated with the proton model at $F = 10^{15}\,n_{eq}cm^{-2}$, 1000 V and two interface charge concentrations.

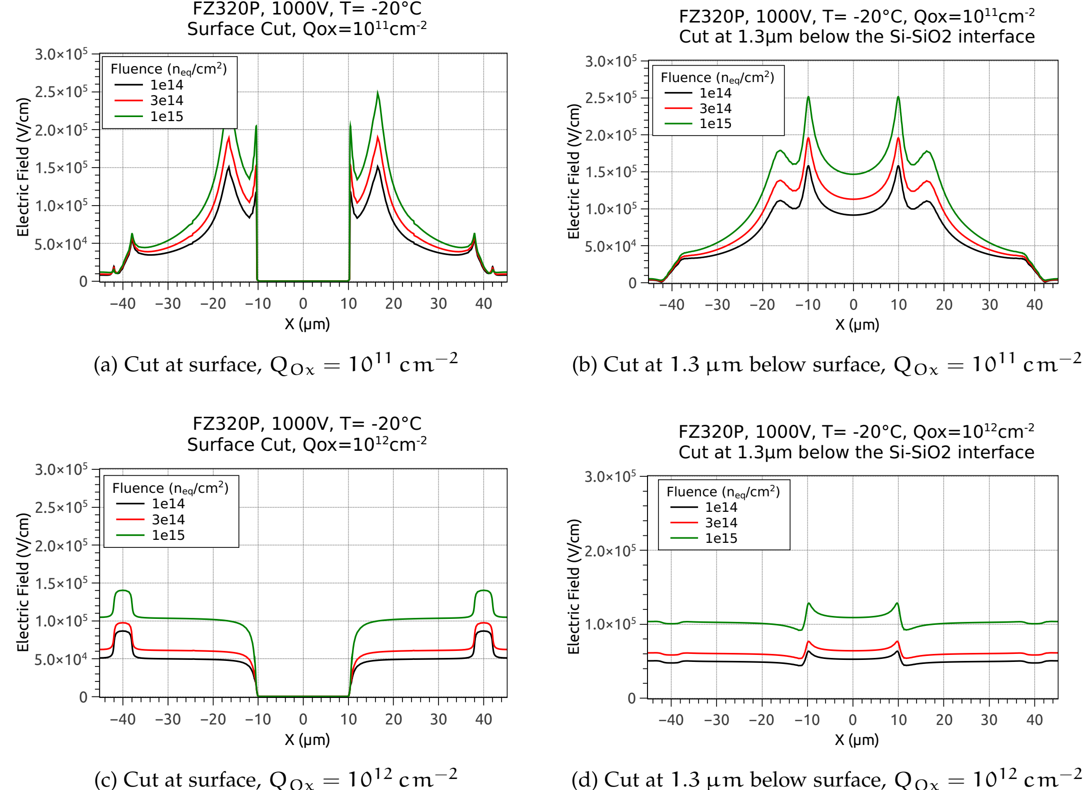

(a) Cut at surface, $Q_{Ox} = 10^{11}\,\mathrm{cm}^{-2}$

(b) Cut at 1.3 µm below surface, $Q_{Ox} = 10^{11}\,\mathrm{cm}^{-2}$

(c) Cut at surface, $Q_{Ox} = 10^{12}\,\mathrm{cm}^{-2}$

(d) Cut at 1.3 µm below surface, $Q_{Ox} = 10^{12}\,\mathrm{cm}^{-2}$

Figure 12.3: Electric fields at the strips in a p-bulk sensor with p-stop isolation simulated with the proton model at 1000 V, different fluences and two interface charge concentrations.

The comparison of the electric fields at the strips between the two models and a low or high interface charge reveals several important points: in the case of neutron irradiation, electric fields tend to decrease with increasing oxide charge. In the case for the protons it is the other way round. Higher electric fields occur with higher oxide charge. Since the proton irradiation creates more oxide charge, it is obvious, that the strip sensors are more prone to micro discharges because of high electric fields. However, because the neutron irradiation does not create a lot of oxide charge, the electric field at the strips is still quite high in the case of the neutron irradiation, which does not exclude an erroneous behaviour of these strip sensors.

12.1.2 P-BULK SENSORS

As p-bulk silicon sensors are favored for the phase II CMS Tracker upgrade, the radiation damage model is used to evaluate the electric fields in these kind of senors. The electric fields for different fluences and different oxide charge concentrations have been simulated using the proton model. The pitch and the width of the sensors is chosen to be near the design of the future sensors for the CMS phase II Tracker upgrade with p-stop isolation.

Because the material budget in the CMS Tracker plays an important role and the silicon sensors contribute a significant part to the material in the Tracker, also the electric fields of 200 µm thin sensors have been simulated and are compared to the field configuration in thicker sensors after irradiation.

The electric fields near the strips – two cuts are made parallel to the silicon-silicon dioxide interface – shows an increase with fluence in figure 12.3. Yet, none of the peaks occuring at the strip implant and at the metal overhang for a low oxide charge exceeds $3 \times 10^5\ \mathrm{V/cm}$.

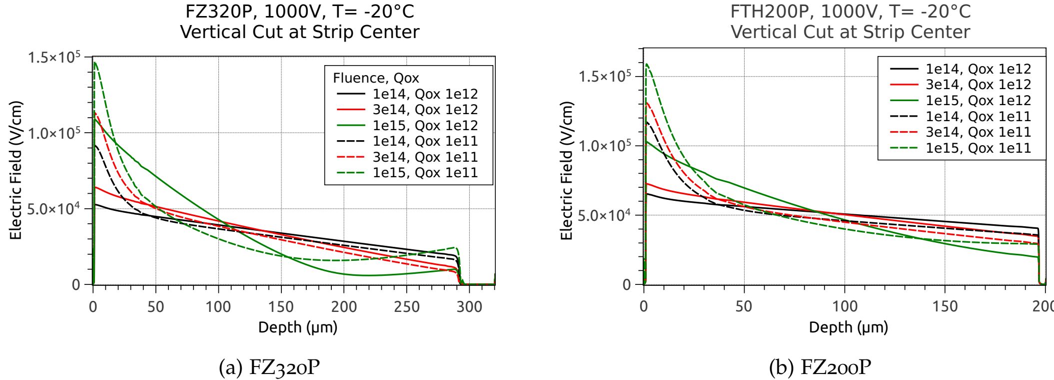

(a) FZ320P

(b) FZ200P

Figure 12.4: Electric fields in the bulk for a FZ320P and a FZ200P strip sensor at 1000 V, two different oxide charge concentrations and three fluences.

The situation gets even more comfortable, if the oxide charge is increased to $10^{12}\,\mathrm{cm}^{-2}$. The electric fields near the strip implants vanish completely because of the conducting electron accumulation layer. The p-stops are visible as peaks in the electric field. The electric fields at the junction at the depth of $1.3\,\mu\mathrm{m}$ is still visible, but also here the peaks are not very high.

This is a strong indication, that the p-bulk sensors, if desigend properly, are intrinsically more radiation hard with respect to the development of high electric fields.

Now that the material is very likely to be reduced in a future tracker, the electric fields in thinner sensors are of interest. Figure 12.4 shows the electric fields at different fluences and at two different oxide charges at 1000 V in the bulk of the sensor. For a low oxide charge concentration, the field increases towards the strips. The cut along the depth of the sensor is done in the center of a strip, even higher fields can occur at the strip edge. With higher oxide charge, the electric field near the strip is decreasing. At the same time, the field in the bulk has to compensate for this and increases a little bit. At the highest simulated fluence, $F = 10^{15}\,n_{eq}\mathrm{cm}^{-2}$, a double peak shape is visible.

The field strength at the strips is very much the same for the two different thicknesses. Thus, the fields in the bulk are higher in the thinner sensor. Higher fields in the bulk can positively influence the collected charge in thinner sensors, which can be an additional advantage of thinner sensors.

Like for the FZ320P sensor, the electric field configuration at the strips at two different cuts below the silicon-silicon dioxide interface has been simulated. These can be seen in figure 12.5. The black curves for the FTH200P sensor represent the same parameter settings as for the FZ320P sensor. The electric field at the lower oxide charge and a fluence of $F = 10^{15}\,n_{eq}\mathrm{cm}^{-2}$ are quite high, but nearly the same as for the FZ320P sensor at the same fluence. At the higher oxide charge concentration, again the electric fields agree very well between the $200\,\mu\mathrm{m}$ and $320\,\mu\mathrm{m}$ thick sensors.

A second configuration of the sensor design is shown in figure 12.5: the peak p-stop concentration has been increased from $10^{16}\,\mathrm{cm}^{-3}$ to $10^{18}\,\mathrm{cm}^{-3}$. The resulting effect on the irradiated device with low oxide charge is almost neglibile. At the p-stop, higher electric fields are forming, which are still lower than the high fields at the strips, though. The high p-stop doping concentration and a high oxide charge concentration can cause problems. Due to the electron accumulation layer, an electric field at the strip implant cannot build up and the total electric field is located at the p-stop. Due to the high doping concentration, the p-stop's isolation is very good and the electric field cannot be distributed between the strips. The high fields at the p-stop can lead – like in the case for n-bulk detectors – to a local breakdown or micro discharges near the p-stop. Therefore, a high p-stop doping concentration should be avoided in highly irradiated sensors with a larger concentration of positive oxide charges. HPK strip

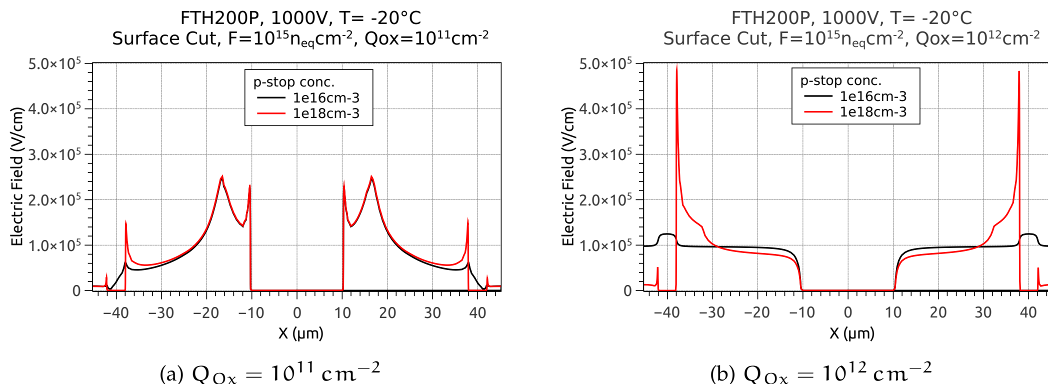

(a) $Q_{Ox} = 10^{11}\,cm^{-2}$

(b) $Q_{Ox} = 10^{12}\,cm^{-2}$

Figure 12.5: Electric fields at the strips for a FZ200P sensor with two different p-stop concentrations at $F = 10^{15}\,n_{eq}cm^{-2}$:
Very high electric fields can occur at the p-stop after irradiation, if the p-stop concentration is chosen too high.

sensors come with a moderate p-stop doping, which ensures isolation before irradiation and still works sufficiently after irradiation, but does not lead to a bad high voltage performance after irradiation.

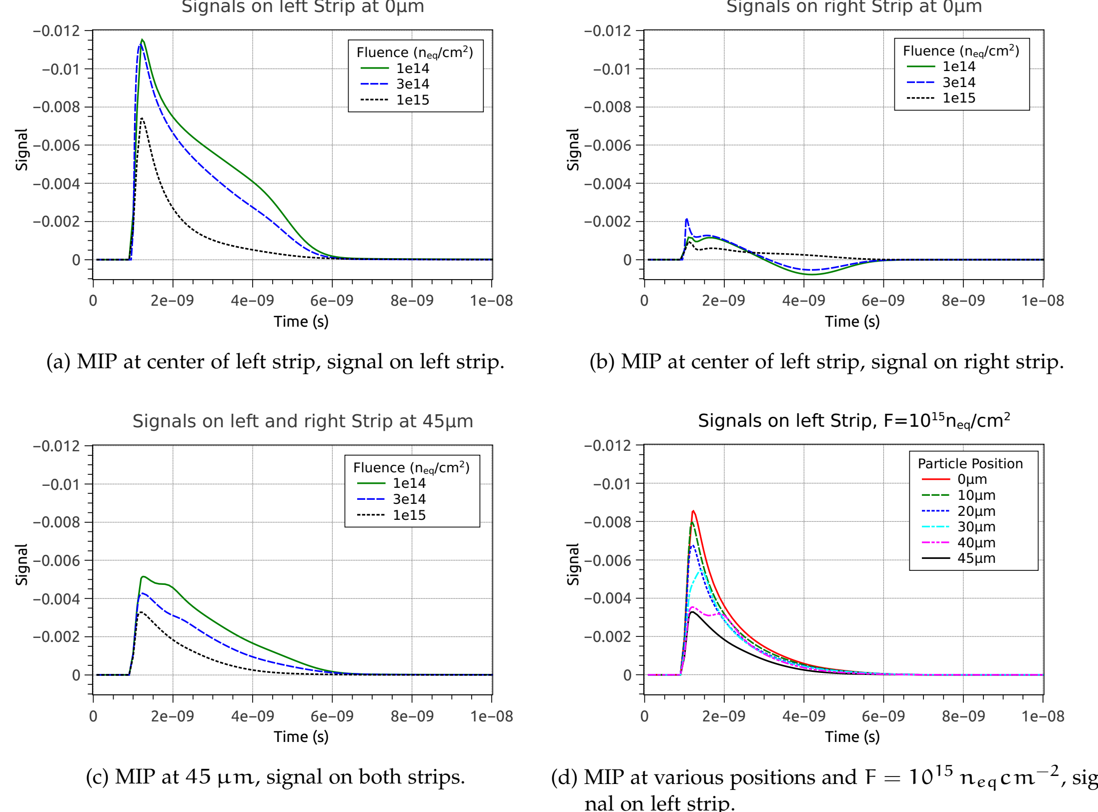

(a) MIP at center of left strip, signal on left strip.

(b) MIP at center of left strip, signal on right strip.

(c) MIP at 45 μm, signal on both strips.

(d) MIP at various positions and $F = 10^{15}\, n_{eq} cm^{-2}$, signal on left strip.

Figure 12.6: Signals of two strips in an irradiated strip sensor with the particle hit position at the center of the strip and the middle between two strips. Simulation with the proton model and $Q_{ox} = 10^{12}\, cm^{-2}$.

12.2 Signal Simulation in irradiated Strip Sensors

Electric fields are very important for the high voltage performance of irradiated sensors. After irradiation, charge collection efficiency is the most important quantity.

To estimate the performance of the strip sensors after irradiation, the proton model for irradiated silicon sensors is applied to 320 μm thick strip sensors and a simulation with signals from particles is performed. The simulated data is compared to the charge collection efficiency of n-bulk and p-bulk sensors at different fluences.

Because electric fields are varying on the surface of a silicon strip sensors, as it was explained in the previous section, the charge collection efficiency can vary depending on the particle's hit position on the sensor. This is also investigated in this section.

12.2.1 Transient Signals

The signals for the transient simulation in silicon strip sensors uses the "heavy ion" model provided by Synopsys Sentaurus. This model can be tuned to simulate a MIP traversing the sensor and creating charge constantly throughout the bulk. Only tracks perpendicular to the sensor surface have been simulated.

The transient signals shown in figure 12.6 are simulated at three different fluences, $10^{14}\, n_{eq} cm^{-2}$, $3 \times 10^{14}\, n_{eq} cm^{-2}$ and $10^{15}\, n_{eq} cm^{-2}$, with the proton model. For the particle hit position in the center of the left strip, the signals are shown for both, the left and the right strip. On the left strip, the signal decreases with higher fluence. On the right strip, the

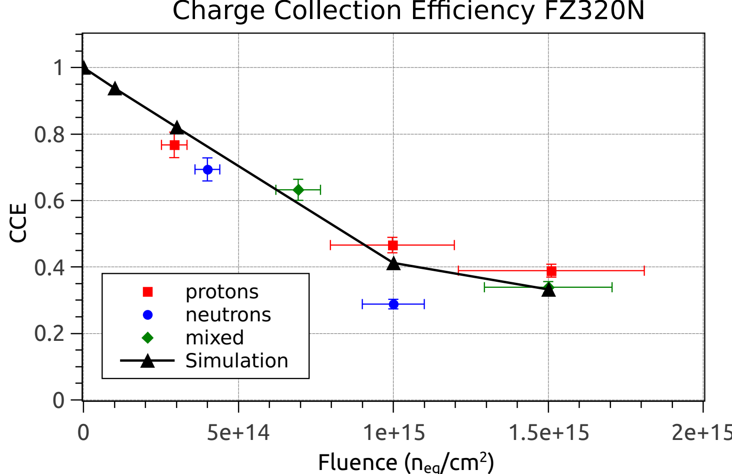

Figure 12.7: Comparison of experimental and simulated CCE for FZ320N measured at −20 °C. The proton model (at 1000 V) has been used for the simulation. Measured data at 900 V partly from [Hof13] and [Fre12].

signals are very small compared to the left strip, if the particle hits at the left strip. Nevertheless, there is a signal induced in the right strip. For the lower fluences - like in the un-irradiated case - there is a positive and a negative contribution, which add to almost zero. With increasing fluence, the integrated signal gets larger; the right strip collects more and more of the total signal.

If the particle crosses the strip sensor in the middle between the two strips, the signals are the same for both strips. Compared to the particle position zero, the signal is divided by two. Again, with increasing fluence, the signal decreases.

Figure 12.6d shows the signals at different MIP positions at a fluence of $10^{15}\,n_{eq}cm^{-2}$. Clearly, the signal decreases as the particle's hit position moves away from the strip. At 40 µm, there are two peaks in the signal, one peak coming from charges directly drifting to the strip, the second arising from charges, first drifting to surface and then drifting to the DC strip of the left strip, because this strip is closer than the right strip. In addition, the p-stop is placed around 40 µm, which deflects the charges drifting to towards the p-stop.

12.2.2 CHARGE COLLECTION EFFICIENCY

The charge collection efficiency is calculated from the simulated signals on the AC strip in strip sensors. The signal in the center of the strip is integrated and compared to the signal generated in an un-irradiated sensor. The simulation data is compared to experimental data, partly measured by Hoffmann [Hof13] and Frech [Fre12]. Because the simulation is tuned for an annealing time of 10 minutes at 60 °C, only the data points with this annealing time or close to it have been considered. The CCE of sensors irradiated with neutrons and protons (mixed irradiation) is larger due to double the annealing time, which increases the charge collection because of beneficial annealing. All measured CCE values are obtained at a voltage of 900 V. The simulation uses a voltage of 1000 V. At these high voltages, no change in the collected charge can be expected for the lower fluences and only a minor change for higher fluences.

The comparison of simulated and measured CCE for FZ320N sensors is shown in figure 12.7. Within the experimental errors, the simulation can describe the collected charge for n-bulk sensors very well. All irradiated efficiencies have been simulated with an oxide charge of $10^{12}\,cm^{-2}$. A slightly lower oxide charge can increase the simulated CCE.

The same picture for simulation and experimental data is seen for the FZ320P sensors (see figure 12.8). The measured CCE values for all fluences except the mixed irradiation match

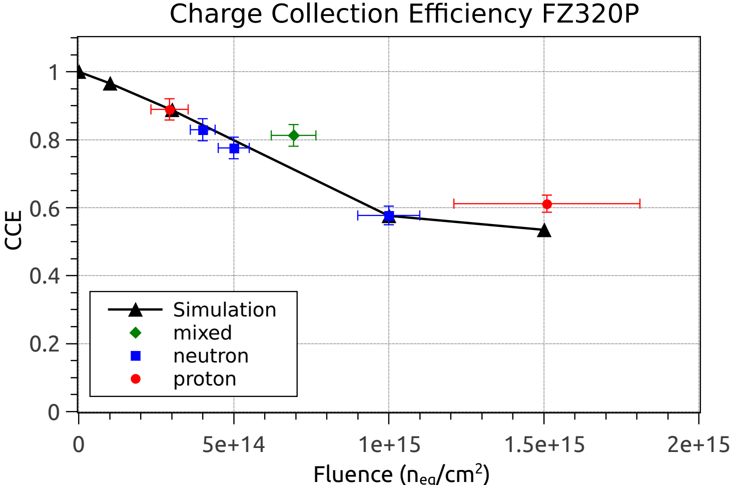

Figure 12.8: Comparison of experimental and simulated CCE for FZ320P measured at −20 °C. The proton model (at 1000 V) has been used for the simulation. Measured data at 900 V partly from [Hof13] and [Fre12].

almost exactly the simulated CCE. An oxide charge of 7×10^{11} cm^{-2} has been used for the simulation of CCE in p-bulk sensors.

The simulation of charge collection efficiency in irradiated silicon strip sensors and the comparison with data is a full success for the developed irradiation damage model in this thesis. Designs of different strip sensors and their performance after irradiation can be predicted very reliably, both for n-bulk and p-bulk sensors.

12.2.2.1 *Position dependent CCE*

Contrary to diodes, the charge collection in strip sensors doesn't need to be constant over the segmented strip region. The electric fields are not homogeneous between the strips and the charges are collected at the DC electrodes of the strips. The induced signals on the AC strip can be very different, when the particle hits either the center of a strip or between the strips.

The collected charge as function of the particle's hit position between the strips has been simulated and is analyzed here. Only one half of the sensor's pitch of 90 µm is simulated. Position 0 µm is in the center of the left strip, 10 µm is just at the edge of the left strip and 45 µm is in the middle between the two strips collecting most of the signal. For the analysis, the collected charge of two out of the five strips is presented. The signal is generated near the third strip (left strip) and the fourth strip (right strip). For the cluster charge, the signal of both strips is summed up. For the normalization, the collected charge is divded by the highest collected charge, in this case the charge of the un-irradiated sensor at position zero.

The results for the n-bulk sensor are presented in figure 12.9. Beginning from the un-irradiated case, the sensor collects the full charge directly at the strip. At a distance of 20 µm from the strip onwards, some charge is lost. For the discussion of this effect see section 8.4.7. In the middle between the strips, some charge is lost between the two strips. At the lowest available fluence, 10^{14} n_{eq}cm^{-2}, the cluster efficiency drops to about 95% in the center of the strip. Again some charge is lost between 20 µm and 40 µm. At the higher fluences, this effect is levelled out, the total collected charge drops from the strip center to pitch center.

With higher fluences, the right strip collects more and more signal of the total cluster charge. This effect can arise from a lower interstrip resistance as well as from a higher interstrip capacitance after irradiation.

The charge loss between the strips is visualized again in figure 12.11. The lost charge is calculated as the relative difference between the collected charge at position 0 and position 45.

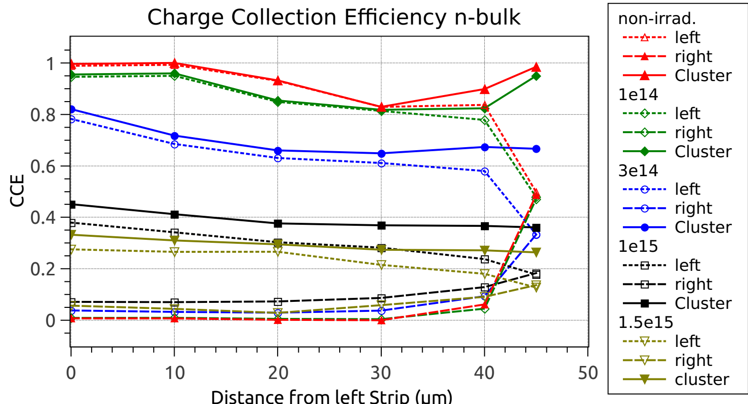

Figure 12.9: Simulated charge collection efficiency for irradiated n-bulk sensors dependent on the MIP hit position. The proton model at 1000 V and $Q_{ox} = 10^{12}\,\mathrm{cm}^{-2}$ has been used.

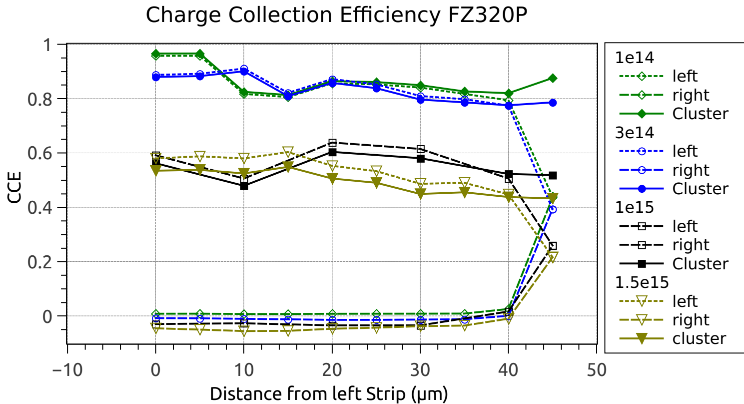

Figure 12.10: Simulated charge collection efficiency for irradiated p-bulk sensors dependent on the MIP hit position. The proton model at 1000 V and $Q_{ox} = 7 \times 10^{11}\,\mathrm{cm}^{-2}$ has been used.

The charge collection efficiency in figure 12.9 is shown for an oxide charge of $10^{12}\,n_{eq}\mathrm{cm}^{-2}$. Additionally, the charge loss for a low oxide charge is shown. With increasing fluence, the charge loss rises up to 20% at $10^{15}\,n_{eq}\mathrm{cm}^{-2}$. At lower fluences, the lost charge decreases, more drastically for a lower oxide charge. Without irradiation or at low fluences, the charge loss is in the range of a few percent, which cannot be detected in a real strip sensor.

The p-bulk sensor shows quite the same behaviour. The charge collection efficiency drops with increasing fluence. Again, up to 7% efficiency is lost, when the charge is generated further away from the strip, increasing a little bit at the center of the pitch for $10^{14}\,n_{eq}\mathrm{cm}^{-2}$, but decreasing for higher fluences. In contrast to the n-bulk sensors, where the right strips collects more and more signal at higher fluences, the integrated signal on the right strip shows a negative charge, which decreases the cluster charge a little bit. With higher fluence, the negative signal increases. An influence of the p-stop isolation on the collected charge at 40 μm cannot be seen in the curves, only a general trend of a lower CCE towards the center of the pitch is visible.

Again the charge loss in the center of the pitch is calculated and shown in figure 12.11. For the p-bulk sensor, only an oxide charge of $7 \times 10^{11}\,n_{eq}\mathrm{cm}^{-2}$ has been used in the simulation. The charge loss is quite constant over the whole fluence range. Starting from 9% at $10^{14}\,n_{eq}\mathrm{cm}^{-2}$, the charge loss shows a maximum at $3 \times 10^{14}\,n_{eq}\mathrm{cm}^{-2}$ and decreases to about 8% at $10^{15}\,n_{eq}\mathrm{cm}^{-2}$. This indicates, that the charge loss in p-bulk sensors with p-stop isolation is not that distinct.

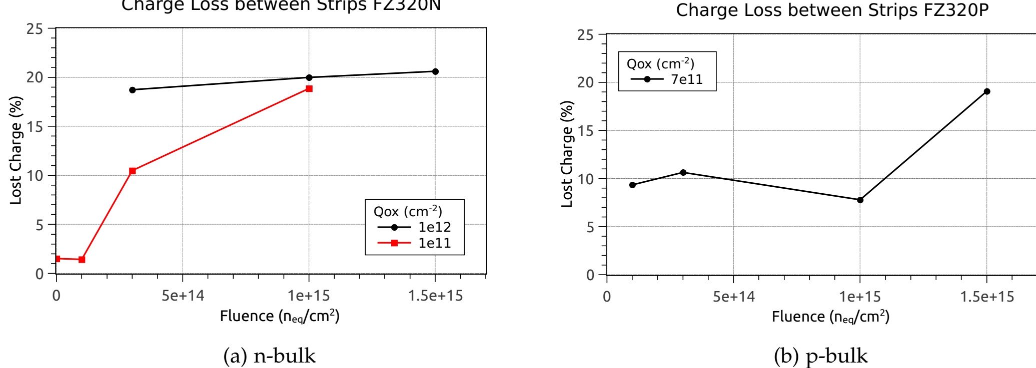

(a) n-bulk

(b) p-bulk

Figure 12.11: Charge loss between the strips for irradiated strip sensors as a function of fluence. The simulation uses the proton model at 1000 V and the oxide charge stated in the plots.

12.3 Charge Multiplication in Silicon Strip Sensors

Charge multiplication is nowadays a well-proven effect, which can enhance the collected charge in highly irradiation sensors and even diodes [C+13],[L+10a], [C+10], [M+10]. Special sensors by the RD50 group [RD5] have been designed to analyze, which geometry affects the charge multiplication [B+13]. The effect may be utilized to enhance signals in heavily irradiated sensors in HL-LHC scenarios.

Charge multiplication has also been seen by Altan et al. [A+13] on the same structures. To fortify the experimental results, these strip sensors with a geometry copying the layout of the dedicated RD50 sensors have been simulated and analyzed with special view on the charge multiplication. A signal simulation has not been performed on these structures, however the total current in the device, the electric field at the strips and the impact ionization can explain the dependence of the charge multiplication on the oxide charge and strip geometry. For all simulations, the proton model (table 11.3) has been used.

Note, that charge multiplication in the simulation is strongly model dependent and requires tuning to the experimentally observed values. For the following simulations, the impact ionization model by van Overstraeten and de Man (see section 7.1.3.2) is used. Since only few sensors have been investigated, simulations are only able to reveal the general trend.

12.3.1 Dependence on Oxide Charge

To investigate the dependence on oxide charge, the current in the strip sensor and the electric field in the standard configuration is simulated. The pitch is 80 μm and the strip width is 6 μm. The oxide charge is varied from a low concentration (10^{11} cm^{-2}) over a medium concentration (5×10^{11} cm^{-2}) to a high concentration (10^{12} cm^{-2}). The fluence investigated in the simulation is $F = 10^{15}\,n_{eq}cm^{-2}$ and the neutron model is used, since a difference between neutron irradiated sensors with low and high oxide charge has been observed [A+13].

The current, which is an indicator for the beginning of the charge multiplication and comes with a soft breakdown or at least with an increase in leakage current of the sensor, is shown in figure 12.12. The sensor with a low oxide charge has a lower current at low voltages but shows an early increase in the current. At high oxide charge concentration, the leakage current is higher at low voltages and the soft breakdown occurs at higher voltages.

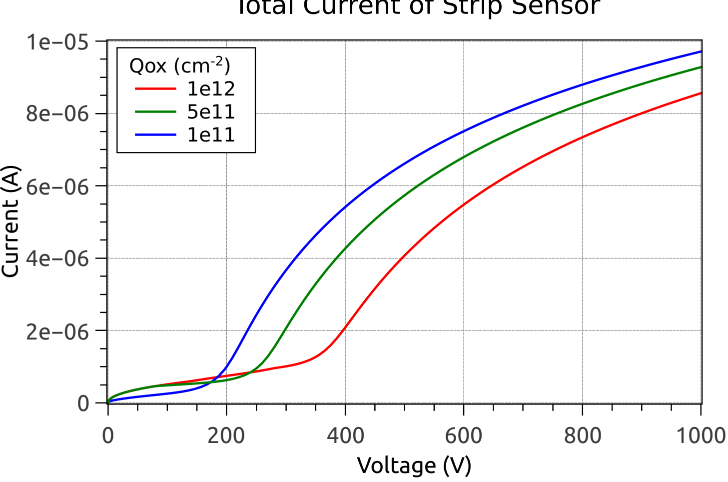

Figure 12.12: Simulated current in a strip sensor with RD50 geometry and a strip width of 6 μm at $F = 5 \times 10^{15}\,n_{eq}cm^{-2}$ and three different oxide charge concentrations at −20 °C:
The current and soft breakdown behaviour is strongly dependent on the oxide charge concentration.

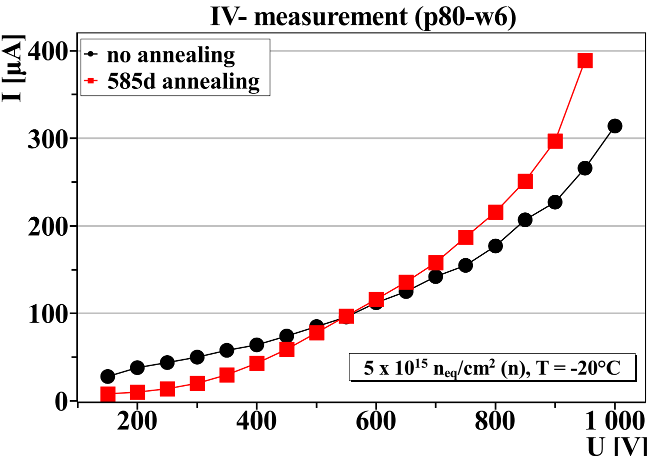

Figure 12.13: Measured current in a RD50 strip sensor with 6 µm wide strips irradiated with neutrons to $F = 5 \times 10^{15}\, n_{eq} cm^{-2}$:
After a long annealing time, an increase in current can be seen. The increase occurs simultaneously when charge multiplication is present in the sensor. Data from [A+13].

This behaviour can be seen for a measured RD50 sensor with a small strip width of 6 µm. At high voltages the increase in current for the annealed sensor is much larger than the current for the sensor, which is not annealed. The next section also shows, that the increase in current occurs when the senors also shows charge multiplication.

The electric field shown in figure 12.14 reflects this behaviour. The higher the oxide charge concentration is, the lower is the electric field near the strips. The cut is made in the center of a strip, the electric fields are higher at the junction edge. Because the electric field exceeds 3×10^5 V/cm, the current in the device increases due to the local enhancement of charge carriers.

Although the simulation cannot reproduce the results shown by Altan [A+13] correctly, the trend is clearly visible. Sensors irradiated with neutrons only have less oxide charge and show a higher charge multiplication. If the devices are exposed to gamma irradiation or are irradiated with protons, more oxide charge is created and the sensor shows less or no charge multiplication.

12.3.2 DEPENDENCE ON STRIP GEOMETRY

Experimental results show, that the strip geometry can play an important role for the charge multiplication. Narrow strips strongly show charge multiplication, whereas wide strips do not show any effect, even at high irradiation. Figure 12.15 shows the an annealing study of the charge collection efficiency of sensors with narrow and wide strips irradiated with protons or neutrons to a fluence of $5 \times 10^{15}\, n_{eq} cm^{-2}$. For long annealing times, the increase in the collected charge for neutron irradiated sensors with narrow strip widths is obvious.

The effect of the charge multiplication is simulated on the dedicated RD50 sensors with narrow and wide strips and can be seen in figure 12.16. Narrow strips are only 6 µm wide, wide strips are 60 µm wide, which is almost the total pitch of 80 µm.

The electric fields near the strips at a cut 1 µm below the silicon surface are plotted for these two strip widths and two different oxide charge concentrations. The sensors with a low oxide charge concentration both show quite high electric fields at the junction (being at 3 µm for narrow strips and at 30 µm for wide strips) and are almost equal. For higher oxide charge concentrations, the electric fields are a little bit lower at the junction of the wide strips. However, the electric field alone cannot explain the difference in the impact ionization rate shown in figure 12.17.

Figure 12.14: Simulated electric field near the surface cut in the center of one strip for various oxide charge concentrations at 1000 V and $F = 5 \times 10^{15}\, n_{eq} cm^{-2}$:
The electric field at the frontside decreases with higher oxide charge concentration.

The impact ionization rate namely shows a large difference between the two different strip widths. It is largest for the narrow strips at a low oxide charge concentration. The wide strips only show one third of the impact ionization rate of the narrow strips, being very low for higher oxide charge. Also the narrow strips' impact ionization rate decreases with higher oxide charge.

The effect is strongly dependent on the charge carrier density near the strips. Because the electric fields are strongly focused to the strips at low oxide charges and the charge carriers (in this case electrons in p-bulk sensors) are collected by the DC strips, the electron density at the junction corner is very high for the narrow strips. This strongly supports impact ionization. Wide strips collect electrons almost all over the surface. The current density is not that high. Thus, the impact ionization rate in the interplay with the electric field suppress charge multiplication at wide strips.

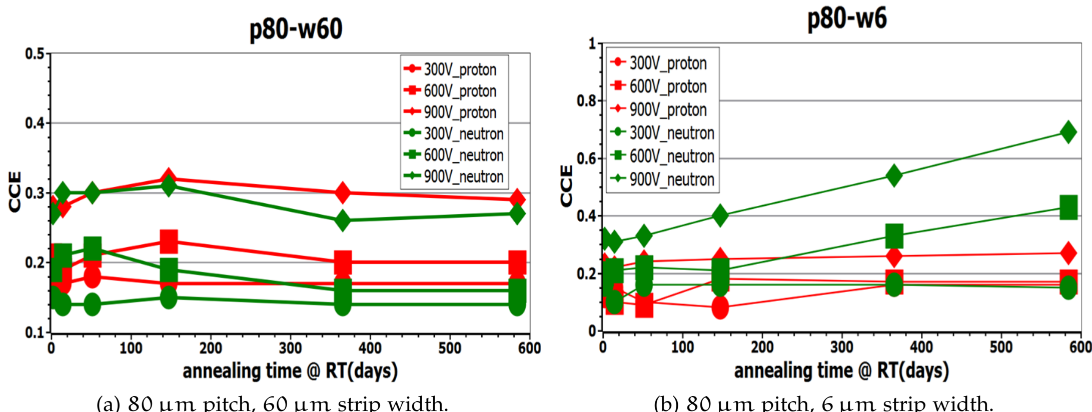

(a) 80 µm pitch, 60 µm strip width.

(b) 80 µm pitch, 6 µm strip width.

Figure 12.15: Measured CCE versus annealing time on dedicated RD50 strip sensors irradiated with neutron or protons to $5 \times 10^{15}\, n_{eq} cm^{-2}$ at three different voltages ($T = -20\,°C$):
At large annealing times and high voltages, charge multiplication is observed for neutron irradiated sensor with small strip width. Proton irradiated sensors or the neutron irradiated sensor with wide strips do not show this effect. From [A+13].

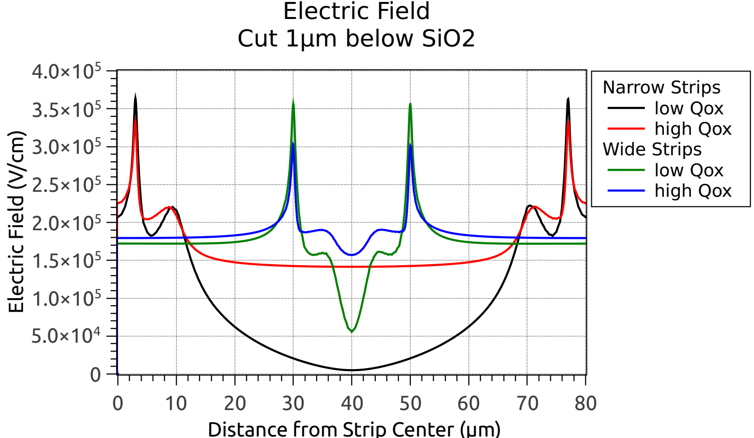

Figure 12.16: Electric field at the strips for $F = 5 \times 10^{15}\, n_{eq} cm^{-2}$ for low and high oxide charge and broad and narrow strip widths, $T = -20\,°C$. Shown is the detail of the pitch 80 µm strip sensor extending from the center of the strip to the center of the neighbouring strip. The strip corner of the left strip for the narrow strip width is therefore found at 3 µm and for the wide strip at 30 µm.
The electric field is highest for narrow strips and low oxide charge.

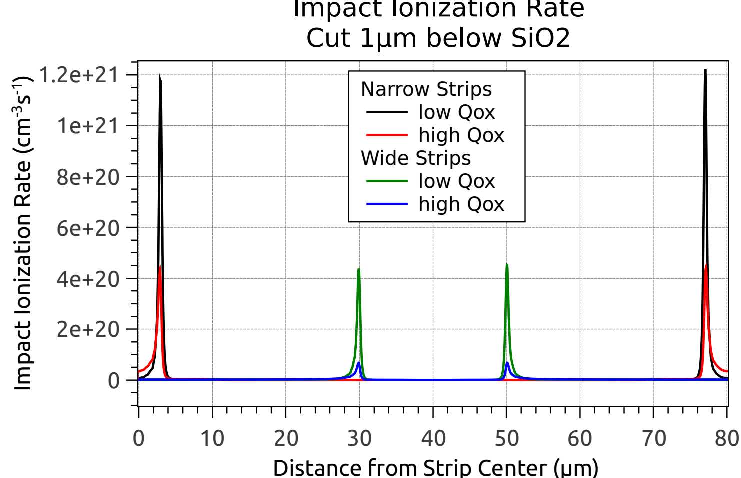

Figure 12.17: Impact ionization rate for different strip widths and oxide charge concentrations at 1000 V, $F = 5 \times 10^{15}\, n_{eq} cm^{-2}$ and $T = -20\,°C$:
Narrow strips at a low oxide charge concentration show a large impact ionization rate whereas wide strips at a high Q_{Ox} *show much less impact ionization.*

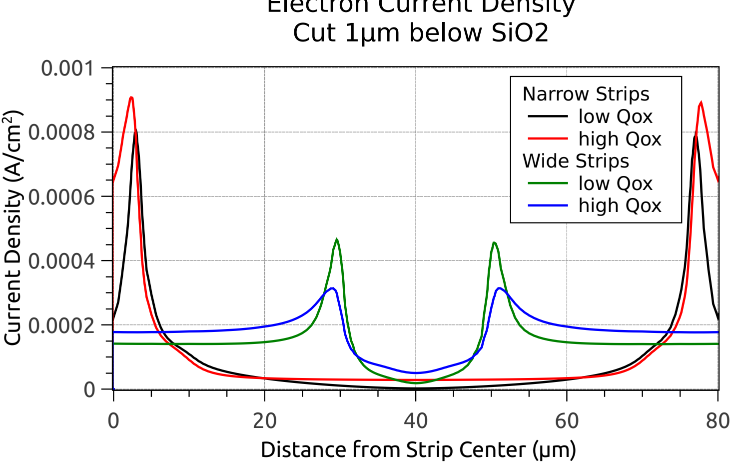

Figure 12.18: Electron density at the strips for different strip widths and oxide charge concentrations at 1000 V, $F = 5 \times 10^{15}\, n_{eq} cm^{-2}$ and $T = -20\,°C$:
Because all charge carriers are collected at the DC strips, the electron density is much higher for narrow strips.

12.4 Conclusion

This chapter has shown, that radiation damage in silicon strip sensors is an interplay between bulk damage and surface damage. The bulk damage has been simulated with the effective two-defect model, which has been developed and well-tuned in the previous chapter. The surface damage has been implemented as interface charge between the silicon and silicon dioxide layer.

The electric fields simulated with the proton model show a different behaviour for the two different bulk dopings: In the case of n-bulk, the electric fields get higher at the strip edges with higer oxide charge; in the case of p-bulk, the electric fields get lower with higher oxide charge. Since radiation damage in the CMS Tracker does not occur as bulk damage only, p-bulk sensors tend to be more favorable in terms of electric fields.

For p-bulk sensors it has been shown, that the electric field configuration does not change very much, if the sensors are thinned from 320 μm to 200 μm. Only the electric field in the bulk is larger, which is not problematic at any point. If the p-stop isolation is used for the p-bulk sensors, very high electric fields at the p-stop can result from a high doping concentration of the p-stop. A p-stop concentration around 10^{16} cm^{-3} should be considered.

The simulated charge collection efficiency in strip sensors showed a very good agreement to measurement data taken with the *baby standard* sensor of the HPK Campaign in the IEKP strip sensor readout system (ALiBaVa). The simulation has shown, that some charge is lost, when the crossing particle hits the sensor in the middle between two strips in contrast to to the hit position in the center of the strip, where all the charge is collected. This is the case for n-bulk as well as p-bulk sensors. It may be reduced with a different geometry of the strips. The effect has to be confirmed by testbeam measurements.

The geometry of the strips is also affecting the charge multiplication effect, which enhances the collected charge. Narrow strips and shallow implants favor the appearance of this effect whereas broad strips and deep implants counteract charge multiplication. Oxide charges, induced by ionizing radiation, also dampen the effect.

The charge multiplication is the best example of the interplay between bulk and surface damage, greatly affecting the performance of a silicon strip sensor. Other quantities are also influenced by the interplay between bulk and surface damage like electric fields, strip isolation (p-stop, p-spray) or charge loss between the strips. If both damage components are correctly taken into account in the simulation, not only diodes but also silicon strip sensors can be simulated to a good accuracy and predictability. Hence the developed model once again has proven to be a mighty tool for the development of radiation hard silicion strip sensors for the application at the HL-LHC.

Part V

SUMMARY

13

SUMMARY

The upgrade of the Large Hadron Collider to the high luminosity Large Hadron Collider (HL-LHC) after 2022 requires new radiation hard sensors for the CMS Tracker to keep up with the increase in the number of particle tracks and fluence. Within the campaign to identify the new sensor material baseline for the phase II CMS Tracker upgrade, many devices like diodes and mini sensors have been irradiated with neutrons and protons to HL-LHC fluences and their properties have been tested before and after irradiation.

For the investigation of the radiation hardness of the materials, a picolaser setup has been built in the course of this thesis, allowing the testing of diodes with the Transient Current Technique (TCT) in the environment of the future application. Cold, dry and stable measurements are possible in a temperature range from -30 °C to +80 °C and three different laser wavelengths from infrared to red are available for TCT and charge collection efficiency (CCE) measurements.

A major part of this thesis incorporates simulations to reflect the behaviour of un-irradiated and irradiated silicon sensors and to predict the performance of new designs after irradiation. The simulation framework and the used models and parameters have been discussed extensivly.

The measurements done on un-irradiated diodes and sensors from the HPK Campaign are used to model the doping profiles of the devices. The agreement between simulation and measurements on the un-irradiated devices is very good. The deep diffusion doping profiles for devices with thinner active areas has been modeled successfully. The strip parameters of the sensors such as coupling capacitance and interstrip capacitance have been reproduced in the simulation as well. The obtained profiles in the simulation are used later on as the basis for irradiated devices.

Diodes of the HPK Campaign on p-bulk wafer processed with the p-stop isolation technique suffer from the disadvantage of a missing isolation between pad and guard ring with respect to the capacitance-voltage measurement. The depletion voltage is quite difficult to determine and the doping profile cannot be obtained from this measurement because of surface currents between pad and guard ring. Diode designs with more than one guard ring, an isolation between the pad and the first guard ring and a good high voltage stability have been investigated: first with simulations, secondly with a production done at ITE Warsaw and thirdly with a production at CNM. With respect to functionality and space consumption, a small diode with two equally spaced guard rings and the p-stop being placed between the pad and the first guard ring is recommended as a good design.

A new design for sensors, the sensor with integrated pitch adapter, has been reviewed with respect to the signal loss in the pitch adapter region of the sensor. Simulations, in agreement with measurements, have shown, that the signal is coupling to the metal routing lines in this region. The problem can be solved by placing all routing lines in a second metal layer on top of the standard metal layer, separated by a thicker silicon oxide. First of all, it has been proven, that the fabrication of wafers with a second metal layer is working. Secondly, the coupling to the routing lines is very much reduced due to the thicker isolation between routing lines and readout strips. Simulations strongly support the implementation of routing lines in a second metal layer.

The measurement data of diodes and sensors of the HPK Campaign has given the unique opportunity to establish a simulation model for highly irradiated sensors in the range of $F =$

$10^{14}\,n_{eq}cm^{-2}$ up to $10^{15}\,n_{eq}cm^{-2}$ and beyond. Therefore, an effective two-defect model has been used and fit to measurement data. Not only current and depletion voltage have been considered, but also charge collection efficiency and data from the Transient Current Technique. This allows for a more precise tuning of the concentration per fluence and cross sections of the donor and acceptor than ever before. The models are listed in tables 11.3 and 11.2.

With the simulation of the transient current pulses in diodes, the simulation allows for the extraction of trapping times, a parameter describing the radiation hardness of the silicon material very well. With the method described in chapter 11.6, the simulation can qualify the trapping time obtained from experimental methods or obtain even more exact results.

Furthermore, with the effective two-defect model in the simulation one can get an insight in the electric field in the bulk of an irradiated detector. After irradiation, n-bulk sensors "type-invert", which just paraphrases that the electric field is higher at the back side of the detector than at the front side, where it has been higher before irradiation. Depending on the ratio of donors and acceptors created during irradiation, the electric field is higher at the front side and the back side than in the bulk. This causes the so-called double peak in the TCT measurements. The effective two-defect model presented here is able to describe the observed double peaks very well. The electric field obtained from the simulation is higher at the back side for n-bulk diodes and higher at the front side for p-bulk diodes. In both types, the electric field is quite low opposite the high field region, rising again towards the electrode. The charge collection, also dependent on the electric field in the diode, is described to a certain extent. Both simulation and data show a quite linear decrease in the collected charge with fluence up to $10^{15}\,n_{eq}cm^{-2}$ decreasing more slowly for higher fluences. The effective defect model has been developed for T=-20 °C. An adaption of the model for 0 °C had been necessary: The hole cross section of the donor and the electron cross section of the acceptor had to be modified in order to account for the slightly different trapping.

In a last step, the predictive power of the model has been tested with irradiated silicon sensors. The charge collection of silicion strip sensors agrees very well with data measured with a strip sensor readout system. The charge collected on the strips is not only dependent on the fluence, but also on the particle's hit position on the sensor. Between the strips, the simulation shows a decrease in the collected charge, both for n-bulk and p-bulk sensors. The effect seems to be 10% stronger for n-bulk sensors.

Electric fields in highly irradiated sensors are a critical issue and the simulation has shown a substantial difference between n-bulk and p-bulk silicon strip sensors. The electric fields in n-bulk sensors after a fluence of $10^{15}\,n_{eq}cm^{-2}$ are very high and close to breakdown electric field of silicon whereas the fields in p-bulk sensors stay quite low near the strips. Only if the p-stop concentration is chosen too high, critical fields could occur at the p-stop isolation structures at higher fluences.

One important point has to be considered, yet: radiation damage in silicon sensors is an interplay between bulk damage (modeled by the effective two-defect model) and surface damage (modeled by the implementation of oxide charges). In an HL-LHC irradiation scenario, also surface damage comes into play. The collected charge is dependent on the oxide charge concentration, modifying the electric fields at the strips.

The effect of charge multiplication, occuring in sensors irradiated with neutrons only, which introduce mainly bulk damage but not surface damage can be predicted by the simulation. The effect only occurs at low oxide charge concentrations and is dependent on the geometry. Narrow strips enhance the effect, broad strips at the same pitch do not show the effect. Despite the larger signal in the sensors, the noise due to the larger leakage current can revert the picture. Whether charge multiplication is a useful effect is questionable, simulations can help to find a good operating regime, though.

In summary, an effective two-defect radiation damage model for highly irradiated silicon sensors with great predictive power has been established.

Outlook

The established effective two-defect model is able to describe many effects by now. One important parameter for the operation of silicon sensors is not considered so far: Annealing. The effect of annealing can be implemented in the effective two-defect model by providing concentrations not only as a function of fluence but also as a function of annealing. The cross sections of the two defects will have to be changed as a function of annealing time. Including annealing time in the model, one can directly simulate the impact of annealing on depletion voltage and charge collection and do not need to rely on the Hamburg-Model only.

Progressing towards a real defect model based on measured defects, including energy levels, concentrations and cross sections, would be another step forward to the predictability of silicon sensors.

Part VI

APPENDIX

SIMULATION FILES

A.1 The Device File

A short introduction to the most common commands is given in this section. The file containing the directives to generate the simulation device is usually named `sde_dvs.cmd`. The following commands are used in the definition of a simple diode structure after the description in section 8.1.1 in 2d. Thus, the z-coordinate is always set to zero.

The starting point is the definition of areas filled with material. A rectangular silicon bulk is generated by

```
(sdegeo:create-rectangle (position X0 Y0 0) (position X1 Y1 0) "Silicon" "bulk")
```

The shape is drawn by `sdegeo:create-rectangle` with the positions of two opposing corners of the rectangle given by positions in the xy-plane: (X0,Y0) and (X1,Y1). The material is set to "Silicon" and the region is assigned the name "bulk". The same statement can be used to add silicon oxide ("SiO2"), silicon nitride ("Si3N4") or aluminum ("Aluminum") layers.

The doping of the silicon bulk is set by the following statement:

```
(sdedr:define-constant-profile "constant_doping" "PhosphorusActiveConcentration" 3e12)
```

The command `sdedr:define-constant-profile` defines a constant doping of the silicon and this doping is named "constant_doping". It uses phosphorus as a dopant ("PhosphorusActiveConcentration") with a concentration of $3 \times 10^{12}\,\text{cm}^{-3}$.

After that, profiles for regions with different dopings can be defined, e.g. for the frontside or backside implants:

```
(sdedr:define-gaussian-profile "gauss_profile" "BoronActiveConcentration" "PeakPos" 0 "
    PeakVal" 1e19 "ValueAtDepth" 3e12 "Depth" 1.5 "Erf" "Factor" 0.5)
```

This command defines a doping profile with a gaussian shape (`sdedr:define-gaussian-profile`), named "gauss_profile" and, contrary to the bulk, doped with boron ("BoronActiveConcentration"). The gaussian is described by the parameters "PeakPos", which sets the peak position of the gaussian; "PeakVal", which sets the maximum doping concentration; "ValueAtDepth", which gives the concentration at the "Depth". Both "PeakPos" and "Depth" are given in micrometer. At the edges of this 1d profile, the profile can be chamfered with an error function ("Erf"), reaching into the bulk perpendicular to the actual profile by a "Factor" of the "Depth".

An error function (`sdedr:define-erf-profile`) can be used equivalently, using a slightly different syntax though:

```
(sdedr:define-erf-profile "erf_profile" "BoronActiveConcentration" "SymPos" 20 "MaxVal" 1e
    19 "ValueAtDepth" 3e12 "Depth" 40 "Erf" "Factor" 0.5)
```

The maximum doping concentration is depicted with "MaxVal" in this profile type, the inflection point of the error function is set with "SymPos". All other parameters can be inherited from the gaussian profile.

Now the doping profiles have been defined, they have to be placed and assigned to a region. Usually, only silicon is doped. The silicon "bulk" is assigned the constant doping profile ("constant_doping"):

```
(sdedr:define-constant-profile-region "place_const" "constant_doping" "bulk")
```

Because the width of the doping profiles often doesn't extend over the whole surface, they can be set to start from previously defined surfaces, so called reference windows. In 2d, this is a "Line" with a starting position and an end position (named "ref_win" here):

```
(sdedr:define-refeval-window "ref_win" "Line" (position X0 Y0 0) (position X1 Y1 0))
```

Placing the gaussian profile at this line so that it extends into the bulk, is done by linking the "ref_win" to "gauss_profile" in the placement command:

```
(sdedr:define-analytical-profile-placement "place_gauss" "gauss_profile" "ref_win" "Both" "
    NoReplace" "Eval")
```

After the basics of the device are configured, contacts are assigned to the readout electrodes. Placing the contacts, it is necessary to avoid choosing corners of the device as starting points on a surface. There are two surfaces next to the corner and the contact might be ambiguously defined. The contacts are assigend to a surface finding the point next to the given one (X0,Y0) in the command:

```
(sdegeo:define-contact-set "contact1" 4 (color:rgb 0 0 1) "##" )
(sdegeo:set-current-contact-set "contact1")
(sdegeo:define-2d-contact (list (car (find-edge-id (position X0 Y0 0)))) "contact1")
```

Here the contact is firstly created, secondly selected and thirdly assigned to a surface. The name "contact1" is used in the simulation file to find the corresponding contact in the device file.

Having placed the contacts, the mesh of the device can eventually be generated. Only the least possible number of mesh points is created, if not stated otherwise. To narrow down the mesh points for a better convergence and better results of the simulation, refinements of the mesh can be made with a minimum cell width of xmin, ymin and a maximum cell width of xmax, ymax

```
(sdedr:define-refinement-size "RefinementDefinition_1" xmin ymin xmax ymax)
```

either in certain regions defined by a reference window (see above)

```
(sdedr:define-refinement-placement "RefinementDefinition_3" "RefinementDefinition_3" "
    refine")
```

or depending on large changes in the doping concentration of the silicon area

```
(sdedr:define-refinement-material "RefinementPlacement_1" "RefinementDefinition_1" "Silicon
    " )
(sdedr:define-refinement-function "RefinementDefinition_1" "DopingConcentration" "
    MaxTransDiff" 0.5)
```

The device with its mesh is automatically generated and saved with a filename compatible to Sentaurus Workbench by

```
(sde:build-mesh "snmesh" " " "n@node@_msh")
```

The device model is ready for simulation.

A.2 The Simulation Command File

A.2.1 Mobility Models

The first mobility model is used for most of the simulations in this work.

1.
```
Mobility
(
   eHighFieldSaturation
   hHighFieldSaturation
   PhuMob( Phosphorus Klaassen )
)
```

2.
```
Mobility
(
   DopingDep
   eHighFieldSaturation
   hHighFieldSaturation
   CarrierCarrierScattering (ConwellWeisskopf)
)
```

A.2.2 RECOMBINATION MODELS

The following recombination model options are used in this work for the simulation:

```
Recombination
(
   SRH
   (
      DopingDependence
      TempDependence
      ElectricField(Lifetime=Hurkx DensityCorrection=none)
   )
   Auger
   eAvalanche (vanOverstraeten Eparallel)
   hAvalanche (vanOverstraeten Eparallel)
   CDL
)
```

A.2.3 ELECTRODE

The electrode section connects the electrodes, which have been defined in the device file, to virtual simulation electrodes, at which high voltage can be applied and the current can be measured.

```
Electrode
{
   {Name="contact1" Voltage=0.0}
   {Name="contact2" Voltage=0.0}
}
```

The name has to be the same as the contact name in the device file. The `Voltage` command defines the electrodes with a voltage boundary condition. The initial voltage for the simulation is set to zero. The voltage can be ramped up in the course of the simulation.

These contacts should be connected to ground or a voltage source. A floating contact can be simulated by setting a very small voltage (intial guess) and a defined current. If the contact is floating, the current should be zero.

```
{Name="contact1" Voltage = 1e-3 Current = 0}
```

A.2.4 FILE

In the file section, all relevant file settings for input and output are set. If a parameter file is served, its name has to be given in the file section. The device file is required by the Grid statement. Output files for all the current analysis is set by Current. If at any point the status of the device with all its variables is saved, it is saved in the file handled by Plot.

```
File
{
   Grid    = "@tdr@"
   Current = "@plot@"
   Plot    = "@dat@"
   Parameter = "@parameter@"
}
```

When using Sentaurus Workbench, the code above automatically generates the input and output files for a given set of parameters. The variables enclosed by @ are the default node names from swb.

A.2.5 PHYSICS

In the Physics section, all the models explained above are set.

```
Physics
{
   areafactor = 1e6
   Temperature = 293
}
```

Furthermore in this section, the simulation temperature (in Kelvin) is set. Additionally, an areafactor can be defined. This areafactor extends a 2d device model in the third dimension. The depth of the device in 2d simulation is assumed to be 1 μm. The device is thus extended along the z-axis by the factor (in μm) of the areafactor.

All models given in Physics are valid for the whole device.

A.2.6 DEVICE IN A SMALL SIGNAL ANALYSIS

If an AC analysis of the device is performed, that is often the case when simulating silicon particle detectors, the device is connected to an external circuitry. In principle, several devices could be connected to one circuit. Therefore, the definition for one device, that is the Electrode, the File and the Physics section, are enclosed by a device statement.

```
device Diode
{
   Electrode{...}
   File{...}
   Physics{...}
}
File
{
   ACExtract = "@acplot@"
}
```

After the devices are connected to circuit, the files to save the simulations, which belong to the circuit, are managed in an extra File section outside the device statement. Here the outcome of the AC analysis is stored in a file with the default name given by swb.

A.2.7 SYSTEM

If the device is connected to an external eletrical circuit, the `System` section has to be inserted. In the system section, the simulation device is conncted to a voltage source, to resistors, capacitors or inductors. The Syntax is very much like the Syntax used for Spice.

```
System
{
   Diode diodesystem ("contact1"=front "contact2"=back)
   Vsource_pset v (back 0) {dc = 0}
   Resistor_pset r (front 0) {resistance = 50}
   Capacitor_pset c (front 0) {capacitance = 1e-9}
   Inductor_pset i (front 0) {inductance = 1e-10}
}
```

The first command assigns new names for the Diode in the system *diodesystem* with new names for the previously defined contacts "contact1" and "contact2", now named *front* and *back*.

The second command applies a high voltage source to the *back* contact. The applied voltage is initially set to zero.

The next two statements connect the *front* contact to ground via a resistor, a capacitor and an inductor with values given in Ohm, Farad and Henry.

A.2.8 PLOT

In the `Plot` section, simulated variables to be saved to a file at a given simulation step are chosen. Examples for variables are electron and hole current, space charge, the doping concentrations in the bulk, charge carrier mobilities and avalanche generation rates. For an exhaustive overview of all the possible commands, see [Syn12].

A standard choice of observables to store is given here:

```
Plot
{
   eCurrent/Vector hCurrent/Vector Current/vector
   eDensity hDensity
   ElectricField ElectricField/Vector
   eEparallel hEparallel
   Potential SpaceCharge
   Doping DonorConcentration AcceptorConcentration
   Auger eAvalanche hAvalanche AvalancheGeneration
   eMobility hMobility
   SRHRecombination
   EffectiveBandGap
   HeavyIonCharge HeavyIonGeneration
   OpticalIntensity OpticalGeneration
   CDL CDL1 CDL2 CDL3
}
```

A.2.9 MATH

The `Math` section controls, how the equations on the grid points are solved. There are some solvers available, the fastest algorithm used here is `pardiso`. `Number_of_Threads` is the maximum number of threads, which can be computed on different CPU cores. One Synopsys Sentaurus license can maximally simulate on four cores. If not enough licenses are available, the simulation falls back to serial execution, which takes much longer.

The accurateness of the computation is set by the number of digits, 5 is a good choice between accuracy and computation time. The maximum number of iterations, the solver tries

to converge to a solution is set by `Iterations`. After the maximum number of iterations is reached, the solver tries to find a solution for a smaller step width or finishes the simulation without a solution, if the step width is too small. The parameters for the step width is set in the `Solve` part.

Other commands given here are useful, for their exact functionality is refered to [Syn12].

```
Math
{
   Method = pardiso
   Number_of_Threads = 4
   Extrapolate
   Derivatives
   RelErrControl
   Digits = 5
   Notdamped = 50
   Iterations = 15
   RecBoxIntegr (1e-2 10 1000)
}
```

A.2.10 SOLVE

In the `Solve` part, finally the ultimate parameters are set, to which the device has to be ramped. In the following example, the voltage on the back contact is ramped from 0 V to 1000 V, while the current through the electrodes is calculated and an AC analysis is done.

First, a solution for the intial state has to be found. That is done by solving the poisson equation for all grid points. Then equations for the contacts and the charge carriers are solved.

In the `Quasistationary`, the actual ramping process takes place. The goal is defined by `Goal`, here the Parameter (dc) referring to the voltage source (v) applied to the back contact of the device is ramped to 1000 V. The goal is simultaneously the step at 100%. All steps are written as a factor of 100%, a stepsize of 0.01 results in steps of 10 V. If all equations for one step are solved successfully, the stepsize is increased by the factor of `Increment` until `MaxStep` is reached. Otherwise the stepwidth is reduced by the factor of `Decrement`. If the minimum stepwidth is reached, the simulation fails.

In the `ACCoupled` command, several parameters for the AC analysis are given. Several frequencies between a start and an end frequency can be analyzed. Because the AC analysis uses its own solver, which is set in `ACSubMethod("Diode")`, the number of iterations can be set differently to the usual iterations for a voltage step. Any capacitance occuring between a contact written in `Node(...)` is calculated. Certain parts of the circuit can even be left out by `Exclude()`.

In curly braces, the equations to be solved to ramp the device to 1000 V are written down. The poisson equation along with the equation for the charge carriers, electron and hole, have to be solved to get the current. If an AC analysis is performed, the contact connecting the device to the circuit and the circuit itself have to be computed too.

If one is interested in the variables stated in the `Plot` section, they can be stored (`Plot`) at a certain `Time` in the simulation, e.g. at 100 V (Time = 0.01) and 1000 V (Time = 1). A new file is generated each time, the simulation reaches the command.

```
Solve
{
   Coupled (iterations=50) {Poisson}
   Coupled (iterations=15)
   {
      Poisson
      Electron
      Hole
```

```
      Contact
   }
   Quasistationary
   {
        InitialStep=1e-6
        Minstep   = 1e-7
        MaxStep   = 1e-2
        Increment = 2
        Decrement = 4
        Goal
        {
                Parameter = v.dc
                Voltage=1000
        }
   }
   ACCoupled
   (
        StartFrequency=1e3
        EndFrequency=1e6
        NumberOfPoints=4 Decade
        Iterations=15
        Node(front back)
        Exclude(c)
        ACMethod=Blocked
        ACSubMethod("diodesystem")=ParDiSo
        ){
           poisson
           electron
           hole
           contact
           circuit
        }
        Plot (FilePrefix = "@tdrdat@" Time=(0.01;1) NoOverwrite)
}
```

A.2.11 OPTICS

An `Optics` section can be implemented, to generate charge carriers by optical absorption in silicon. This is useful for a transient analysis - the evolution of the generated signal in time.

`Optics` is to be implemented in the physics section. There are subsections for the optical generation of the charge carriers and where the excitation takes place. In the mostly used example below, a short laser pulse with a single wavelength is injected in the device. The shape of the pulse is a gaussian (chosen by `WaveTSigma`) with a sigma of 50 ps. The maximum of the gaussian is at 1 ns.

The option `Scaling = 0` is very important for the transient simulation. This options switches on the illumination only during the transient simulation, not while ramping the voltage.

`Wavelength` sets the wavelength of the laser in μm. The `Intensity` is set in W/cm^2. An illumination window can be defined in several ways, here a `Line` with a width of 10 μm is chosen, pointing in the y-direction with an angle of zero degrees from the y-axis starting at the origin.

Grid points have to be chosen, where charge carriers are excited. This is done along the center of the defined window L1 for the whole region, which is in the window.

The real and imaginary part of the complex refractive index is used to calculate the absorption of the light in silicon. Value pairs for certain wavelengths can be found in the parameter file for silicon. The absorption for other wavelengths is interpolated from these values.

```
Optics
(
   OpticalGeneration
   (
      ComputeFromMonochromaticSource()
      TimeDependence
      (
        WaveTime = (1e-9, 1e-9)
        WaveTSigma = 50e-12 *# gaussian
      )
      Scaling = 0
   )
   Excitation
   (
      Wavelength = 0.68 *# um
      Intensity = 0.06 *# W/cm2
      Window("L1")
      (
         Origin = (0,0)
         XDirection = (1,0,0)
         Line( Dx = 10 )
      )
      Theta = 0  *# Angle from positive y-axis (in 2D)
   )
   OpticalSolver
   (
      OptBeam
      (
         LayerStackExtraction
         (
            WindowName = "L1"
            WindowPosition = Center
            Mode = ElementWise
         )
      )
   )
   ComplexRefractiveIndex
   (
      WavelengthDep(real imag)
   )
)
```

A.2.12 HEAVY ION

The heavy ion command can be used instead of the optics section to simulate charge created by a traversing particle. The direction of flight and the incident location can be defined along with the time, at which the particle passes. `Length` gives four points, between which the scaling factors `Wt_hi` are applied to the charge deposited per micrometer defined by `LET_f`. The distribution is usually set to be gaussian and calculated in Picocoulomb. This command is easier to use than the optics section described above; to imitate the laser signal in a transient measurement, the available options are not sufficient.

```
HeavyIon
(
   Direction=(0,1)
   Location=(0.5,0)
```

```
   Time=1e-9
   Length=[0 0.001 350 350.001]
   Wt_hi= [1.0 1.0 1.0 1.0]
   LET_f= [0 8.7e-6 8.7e-6 0]   # 1.282E-5/2.5e7*0.68
   Gaussian
   PicoCoulomb
)
```

A.2.13 TRANSIENT

The transient command is used in the `Solve` section to look at the evolution of signals in time after the voltage is ramped to the desired value beforehand.

```
NewCurrentPrefix ="trans_"
Transient
(
   InitialTime = 0
   FinalTime = 20e-9
   MinStep = 1e-17
   MaxStep = 1e-10
)
{
   Coupled
   {
      Poisson
      Electron
      Hole
      Circuit
   }
   Plot (FilePrefix = "@tdrdat@" Time=(1e-9;5e-9;10e-9) NoOverwrite)
}
```

Because the current is saved in both, the voltage ramp and transient analysis, a new current file should be created. This is done by the command `NewCurrentPrefix ="trans_"`. All files belonging to the transient simulation will get the prefix "trans_".

The current in the transient is then simulated from an initial time to a final time of 20 ns in the example above. MinStep and MaxStep are factors in terms of the final time. For the transient, the same equations are solved as for the voltageramp. Variables stated in the `Plot` section can be saved at chosen times during the transient.

If the simulation device is connected to a circuit, the transient is also simulated with the applied circuit.

B

Measurement Specifications

Many institutes are involved in the measurements of the HPK campaign. Therefore, general regulations and specifications about the measurements have been defined. In general, two different options for the devices have been specified: the initial qualification and the performance after irradiation.

B.1 Probe Station

On diodes, sensors and most other structures, IV and CV curves can be recorded. Before irradiation, the following scenarios apply:

Diodes

Diodes are to be measured at +20 °C, 0 °C and -20 °C. While for all temperatures, the frequency for the CV measurement is chosen to be 1 kHz, at -20 °C the diode should additionally be measured at 455 Hz.

All the measurements are performed with grounded guard ring as well as with floating guard ring. If the guard ring is connected to ground, the current over the guard ring can be measured and stored, too.

The maximum voltage for un-irradiated samples is 500 V, if the guard ring is connected to ground, and 700 V otherwise. The voltage steps are 1 V from 0 V − 10 V, 5 V in the range from 10 V − 100 V and 10 V up to the maximum voltage allowed.

Sensors

The measurements on the un-irradiated sensors are performed at +20 °C only, with grounded and with floating guard ring. The same maximum voltages as for diodes are allowed: 500 V for measurements with grounded guard ring, 700 V otherwise. The voltage steps are chosen to be same as for the diodes.

For the un-irradiated sensors, a strip scan at 600 V is foreseen as a quality check. This includes R_{int}, R_{poly}, C_{int}, C_{AC}, I_{leak} and I_{diel}. The guard ring is not connected.

After irradiation, the structures show higher leakage currents. Thus, the measurements are mostly performed cold only. The following directions apply:

Diodes

Diodes' IV and CV is measured at 0 °C and -20 °C. CV at both temperatures is performed at 1 kHz, at -20 °C the additional 455 Hz are applied.

The maximum voltage for irradiated diodes is 1000 V, the current limit is hardware-based 1 mA. The same voltage steps as for un-irradiated diodes are valid.

Sensors

Sensors are measured at -20 °C only. IV and CV are performed with grounded and with floating guard ring up to 1000 V.

The voltage steps 1 V (0 V − 10 V), 5 V (10 V − 100 V) and 10 V (100 V − 1000 V) apply for IV, CV and strip ramps.

In the irradiated case, strip ramps on at least two strips should be done. On a specific strip, R_{int}, R_{poly}, C_{int}, C_{AC}, I_{leak} and I_{diel} are recorded over voltage.

B.2 TCT and CCE Measurements

For TCT and CCE measurements, more general regulations apply, because the setups are more different here.

The minimum requirements on the system are:

- Laser wavelengths for TCT: 650 nm to 680 nm (red); 880 nm from the back if not possible with red.
- Laser wavelenght for CCE: >1000 nm.
- Laser intensity: <100 MIPs. Stable at 5%.
- Laser repetition frequency: 200 Hz.
- Sampling rate of oscilloscope: $\geqslant 5$ GS/s.
- Averaging over waveforms: 512.

The time window should be at least 50 ns.

All measurements on the diodes are done without connected guard ring.

Before irradation, some diodes of the same type should be measured as reference at +20 °C, 0 °C and -20 °C. The voltage should be ramped in steps of 10 V up to 700 V.

In the irradiated case, the maximum voltage is 1000 V and the measurement at +20 °C is dropped.

For the analysis of the charge collection efficiency, a monitor diode is measured along with each sample to normalize the measured charge. The collected charge of a diode after irradiation divided by the collected charge of un-irradiated diode of the same type is stored in the database. By comparing the monitor charge of the measurements, the uncertainty of the charge collection efficiency should be within 5%.

C

MEASUREMENT DEVICES

C.1 Probestation

- Keithley 6517A for high voltage supply and primary current measurement,
- LCR Meter: HP 4284A,
- Keithley 617 for additional current measurement,
- HP 6614C for low voltage supply,
- TDK-Lambda Gen20-38 for peltier power,
- IO-Warrior control for switching relays,
- 12 V power supply for relays.

For more information refer to [Hof13].

C.2 ALiBaVa

- ALiBaVa system [MH10],
- strip sensor readout setup [Fre12], [Pfi10],
- ISEG high voltage power supply,
- Hamamatsu photomultiplier,
- High voltage supply for photomultiplier,
- Scintillator.

C.3 Picolaser Setup

- High voltage source: Keithley 2410.
- Bias-T: *Picosecond* Model 5531 High Voltage Bias Tee (risetime 35 ps, bandwidth 10 GHz).
- Amplifier: *Miteq* AM 1309 (51 dB amplification, flat to 1 GHz).
- Oscilloscope: *Tektronix* TDS 5104B (bandwidth 1 GHz, 5 GS/s).
- Laser: *Advanced Laser Systems* PiLas. 679 nm, 880 nm and 1055 nm.

D

THE IEKP DATABASE

D.1 Structure

The IEKP database consists of several tables linked by a unique identifier. The structure is sketched in figure D.1. Higher order tables have less entries than lower order tables (data tables). The summary of tables with several entries for one id, needed to identify the status of a measurement from another table, are processed on request the so called *views*. These are available for irradiation, annealing and location.

The entries of the tables is explained in detail in the next section.

D.2 Tables in Detail

D.2.1 INFO

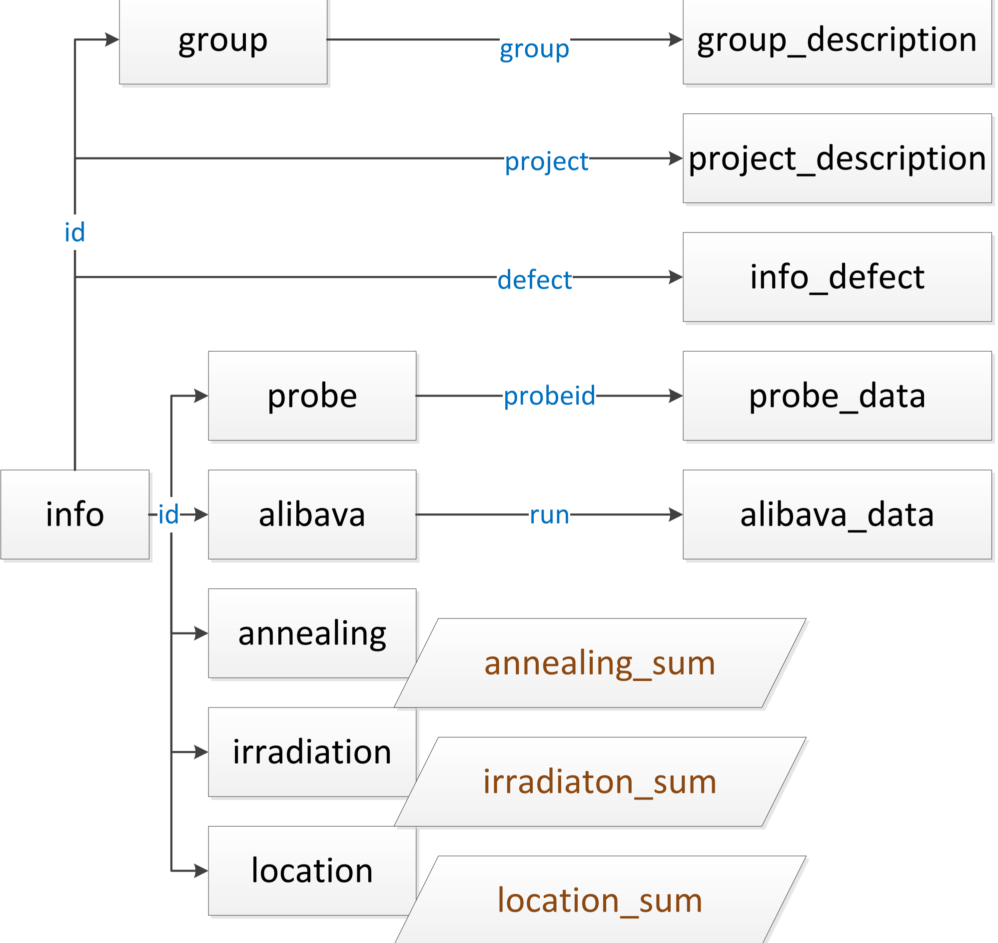

Figure D.1: Database link structure.
The tables (squares) are connected by the identifier (arrow). The summary of the tables is generated on request by dedicated processes (diamonds).

Table D.1: The "info" table in the IEKP database.

Field	Type	Description
id	int	Unique identifier for structures
name	varchar	Name of the structure
project	varchar	Corresponding project of the structure
manufacturer	varchar	Manufacturer of the structure
class	varchar	Type of structure, e.g. Diode, Sensor, Pixel.
sensortype	varchar	bulk type of the structure
thickness	float	Thickness of the structure
width	float	Width of the structure
length	float	Length of the structure
strips	int	Number of strips (if strip sensor)
pitch	float	Pitch of the strips (if strip sensor)
coupling	enum	Coupling of the strips (AC,DC; if strip sensor)
date	date	Date of first entry
contact	text	Responsible person for this structure
institute	text	Institute, the structure belongs to
status	varchar	Status flag of the structure (not used)
backup_name	varchar	Original name, if name has been changed
F_p_aim_n_cm2	double	Aim of proton fluence
F_n_aim_n_cm2	double	Aim of neutron fluence
parent	varchar	Parent project
defect	tinyint	flagged if defect

Table D.2: The "info_defect" table in the IEKP database.

Value	Description
0	working
1	structure destroyed
2	high leakage current
3	high leakage current when guard applied
4	lost

D.2.2 ALIBAVA

The "alibava" table contains a mixture of measurement settings and environment variables, and analysis parameters and results. For each measurement, one new entry line is created. The analysis then adds all data to the same line, when the measurement is analyzed. In this way, the correlation is automatically clear. The whole table is seen in table D.3. Each entry's type is given along with a short description of the values.

Table D.3: The "alibava" table in the IEKP database.

Field	Type	Description
alibava_uid	int	Unique identifier
run	int	Running number of measurements at each station
id	int	Sensor ID
ped_run	int	Pedestal run
date	datetime	Date recorded
source	varchar	Signals generated by radioactive source (RS) or Laser
voltage	float	Applied voltage
current	double	Current measured by the high voltage source
temperature	float	Temperature on the sensor
x_position	double	x-position of the XYZ table
y_position	double	y-position of the XYZ table
z_position	double	z-position of the XYZ table
signal	double	MPV of the landau-gauSS in ADC
sigma_signal	double	Statistical error on the signal
electron_sig	double	Signal in electrons
signal_e_err	double	Statistical error on the electron signal
trigger	int	Number of triggers taken in the run
chi2_signal	double	χ^2 of the landau-gauss fit
chi2_snr	double	χ^2 of the signal to noise distribution
comment	text	Comment
mpv_snr	double	MPV of the signal to noise distribution
sigma_snr	double	Statistical error on the signal to noise distribution
mpv_signal	double	Not used any more! Maintained for contingency
mean_clustersize	double	Mean clustersize of the obtained signal from a gaussian fit to the cluster size
mean_clustersize_cut	double	Mean cluster size taken from all strips in the histogram
mean_clusternoise	double	Noise of the whole cluster
mean_commonmode	double	Average of the commonmode
sigma_commonmode	double	Sigma of the gaussian fit of the commonmode
strip_mosthits	int	Strip with most hits (center of source)
lownoise_limit	double	Limit of the noise, strips will be flagged, if noise is below

Continued on next page.

Field	Type	Description
highnoise_limit	double	Limit of the noise, strips will be flagged, if noise is above
timing_one_ns	int	Start of the search window in ns for the fit of the time profile
timing_two_ns	int	End of the search window in ns for the fit of the time profile
operator	varchar	Operator of the measurement
temperature_daughterboard	double	Temperature measured by the beetle chip
cern_timestamp	bigint	Timestamp of the CERN timeserver
RH	float	Relative humidity during the measurement
median_noise_used_strips	double	Median of the noise of the strips used for the analysis (± 10 of the hit strip)
clusters	int	Number of clusters found
station	tinyint	Number of the measurement station[1]
chip	tinyint	Board (1st digit) and chip (2nd digit) the sensor is bonded to; e.g. 51 for chip 1 on board 5
signal_e_syserror	double	Systematic error of the conversion from ADC to electrons
flag	enum()	good, bad, meas or valid to indicate the quality of the measurement
fakehits	double	Number of hits faked by discharges or noise
SeedSig_MPV	double	MPV of the seed strip
SeedSig_MPV_error	double	Statistical error on the MPV of the seed strip
SeedSig_chi2_ndf	double	$\chi^2/nDoF$ - an error estimation of the seed signal
Signal_chi2_ndf	double	$\chi^2/nDoF$ - an error estimation of the ADC signal

The statistical error of the landau-gauss distribution is calculated by root. (todo).

D.2.3 PROBESTATION

The probestation measurements are saved in two tables, one, "probe", for the parameters of the measurements and the other one, "probe_data" for the curve data. The structure of "probe" is listed in table D.4 and the structure of "probe_data" can be found in table D.5. The tables are again divided into the field name, the type and a short description of the value.

The field probeid is unique in the probe table and links the parameters to the measurements in probe_data, where it is saved with each measurement point. So for each measurement, e.g. IV, there's one entry in probe and as many in probe_data as there are data points.

1 3 for the small station, 4 for the big station

Table D.4: The “probe” table in the IEKP database.

Field	Type	Description
probeid	int	Unique identifier
id	int	Sensor ID
paraX	varchar	Parameter measured for x
paraY	varchar	Description of the parameter measured for y
paraZ	varchar	Description of the parameter measured for z
date	datetime	Date of the measurement
operator	varchar	Operator of the measurement
temperature	float	Average temperature during the measurement
RH	float	Average relative humidity during the measurement
station	tinyint	Identifier number of the probe station
frequency	float	Frequency used by the LCR-meter for the measurement
comment	text	Comment
flag	enum()	good, bad, meas, valid; indicating the quality of the measurement
cern_timestamp	bigint	Timestamp from the CERN timeserver
guardring	binary	Measurement with (1) or without (0) guard ring
amplitude_LCR	float	Amplitude of the low voltage applied by the LCR-meter
mode_LCR	enum()	“parallel” or “serial” mode of the LCR-meter
N_steps	int	Number of steps of this measurement
starttime	datetime	Start of the measurement
endtime	datetime	End of the measurement
bias	double	Not used
Vdep	double	Not used yet, to be built in
fitmode	int	Not used yet, to be built in

Table D.5: The “probe_data” table in the IEKP database.

Field	Type	Description
probe_uid	bigint	Unique identifier
probeid	int	Link to the “probe” table
datax	double	Data recorded for parameter X
datay	double	Data recorded for parameter Y
dataz	double	Data recorded for parameter Z
temperature	float	Temperature at measurement point
RH	float	Relative humidity at measurement point

E

ROOT FRAMEWORK FOR DATABASES

The root framework to read data from different databases, to change results for the ALiBaVa analysis and to write data to the IEKP database is written in C++. Several libraries with dedicated functions are available. The full list of source and header files (.cpp and .h) for the various classes are listed in table E.1.

To handle data from the IEKP database, probedata is the most important class. Other classes can be used if desired, e.g. to create an XML file from local data to upload to CMS Upgrade Database.

The SQL queries, which are needed to process data from the IEKP database or the CMS Upgrade database, are found directly in the source files. The framework makes use of the functions provided by ROOT [Roo]. One has to include the SQL libraries for ROOT when compiling it.

To avoid security leaks, the framework uses its own access to the IEKP database and is found only compiled on the server.

The framework is also used by the IEKP database website viewer to quickly visualize measured data.

Table E.1: List of libraries for the ROOT framework for databases.

Class	Dependency	Function
AlibavaData	probedata	Get alibava data
alibava_plot	AlibavaData	Plot alibava data
probedata	XY	Read and Write probestation data, plot probestation data
eXML	probedata	Create XML file for the CMS Upgrade Database
lyondata	probedata	Read data from the CMS Upgrade Database
plot	XY, probedata	Visualize data
resulttree	probedata	Create root tree for exported data
XY	–	Provide functions to handle and manipulate XY data
XYZ	XY	Provide functions to handle and manipulate XYZ data
tctdata	XYZ	Functions to handle calculate TCT data

BIBLIOGRAPHY

[A+13] Altan, L. et al.: *Investigation of charge multiplication in silicon strip detectors*. 22nd RD50 Workshop. https://indico.cern.ch/getFile.py/access?contribId=6&sessionId=4&resId=0&materialId=slides&confId=209612. Version: Jun 2013 (cited on pages 188, 189 and 191.)

[Adv04] Advanced Laser Diode Systems (Publisher): *Picosecond Injection Laser (PiLas)*. Berlin, Germany: Advanced Laser Diode Systems, 2004. – http://www.alsgmbh.de (cited on page 60.)

[Ali] *Alice – A Large Collider Experiment*. http://aliceinfo.cern.ch (cited on page 5.)

[ATL] *ATLAS – The Atlas Experiment*. http://atlas.web.cern.ch (cited on page 5.)

[B+02] Braibant, S. et al.: Investigation of design parameters for radiation hard silicon microstrip detectors. In: *Nuclear Instruments and Methods in Physics Research Section A: Accelerators, Spectrometers, Detectors and Associated Equipment* 485 (2002), Nr. 3, 343 - 361. http://dx.doi.org/10.1016/S0168-9002(01)02120-9. – DOI 10.1016/S0168–9002(01)02120–9. – ISSN 0168–9002 (cited on page 143.)

[B+13] Betancourt, C. et al.: A charge collection study with dedicated RD50 charge multiplication sensors. In: *Nuclear Instruments and Methods in Physics Research Section A: Accelerators, Spectrometers, Detectors and Associated Equipment* (2013), Nr. 0. http://dx.doi.org/10.1016/j.nima.2013.05.186. – DOI 10.1016/j.nima.2013.05.186. – ISSN 0168–9002 (cited on page 188.)

[BBPS98] Borchi, E. ; Bruzzi, M. ; Pirollo, S. ; Sciortino, S.: Temperature and frequency dependence of the capacitance of heavily irradiated silicon diodes. In: *Solid-State Electronics* 42 (1998), Nr. 11, 2093 - 2096. http://dx.doi.org/10.1016/S0038-1101(98)00186-5. – DOI 10.1016/S0038–1101(98)00186–5. – ISSN 0038–1101 (cited on page 46.)

[Bet30] Bethe, H.: Zur Theorie des Durchgangs schneller Korpuskularstrahlen durch Materie. In: *Annalen der Physik* 397 (1930), P. 325 – 400 (cited on page 15.)

[Blo33] Bloch, F.: Zur Bremsung rasch bewegter Teilchen beim Durchgang durch Materie. In: *Annalen der Physik* 403 (1933), P. 285 – 320 (cited on page 15.)

[Bro97] Browne, E.: Nuclear Data Sheets for A = 90. In: *Nuclear Data Sheets* 82 (1997), Nr. 3, 379 - 546. http://dx.doi.org/10.1006/ndsh.1997.0021. – DOI 10.1006/ndsh.1997.0021. – ISSN 0090–3752 (cited on page 17.)

[BS11] Bernard-Schwarz, M.: *Measurements and Irradiation Analysis of Silicon Structures for the CMS Upgrade*, Vienna University of Technology, Diploma Thesis, 2011. http://www.hephy.at/fileadmin/user_upload/Publikationen/diploma_mbs.pdf (cited on page 107.)

[C+03] Chatterji, S. et al.: Analysis of interstrip capacitance of Si microstrip detector using simulation approach. In: *Solid-State Electronics* 47 (2003), Nr. 9, 1491 - 1499. http://dx.doi.org/10.1016/S0038-1101(03)00102-3. – DOI 10.1016/S0038–1101(03)00102–3. – ISSN 0038–1101 (cited on page 104.)

[C+05] Chiochia, V. et al.: Simulation of Heavily Irradiated Silicon Pixel Sensors and Comparison With Test Beam Measurements. In: *Nuclear Science, IEEE Transactions on* 52 (2005), aug., Nr. 4, P. 1067 – 1075. http://dx.doi.org/10.1109/TNS.2005.852748. – DOI 10.1109/TNS.2005.852748. – ISSN 0018–9499 (cited on pages 110, 174.)

[C+06] Chiochia, V. et al.: A double junction model of irradiated silicon pixel sensors for LHC. In: *Nuclear Instruments and Methods in Physics Research Section A: Accelerators, Spectrometers, Detectors and Associated Equipment* 568 (2006), Nr. 1, 51 - 55. http://dx.doi.org/10.1016/j.nima.2006.05.199. – DOI 10.1016/j.nima.2006.05.199. – ISSN 0168–9002. – New Developments in Radiation Detectors, Proceedings of the 10th European Symposium on Semiconductor Detectors (cited on page 174.)

[C+10] Casse, G. et al.: Enhanced efficiency of segmented silicon detectors of different thicknesses after proton irradiations up to $1 \times 10^{16}\, n_{eq} cm^{-2}$. In: *Nuclear Instruments and Methods in Physics Research Section A: Accelerators, Spectrometers, Detectors and Associated Equipment* 624 (2010), Nr. 2, 401-404. http://dx.doi.org/10.1016/j.nima.2010.02.134. – DOI 10.1016/j.nima.2010.02.134. – ISSN 0168–9002. – New Developments in Radiation Detectors, Proceedings of the 11th European Symposium on Semiconductor Detectors. (cited on page 188.)

[C+13] Casse, G. et al.: Charge multiplication in irradiated segmented silicon detectors with special strip processing. In: *Nuclear Instruments and Methods in Physics Research Section A: Accelerators, Spectrometers, Detectors and Associated Equipment* 699 (2013), Nr. 0, 9 - 13. http://dx.doi.org/10.1016/j.nima.2012.04.033. – DOI 10.1016/j.nima.2012.04.033. – ISSN 0168–9002. – Proceedings of the 8th International Hiroshima Symposium on the Development and Application of Semiconductor Tracking Detectors (cited on page 188.)

[CC74] Chelikowsky, J. R. ; Cohen, M. L.: Electronic structure of silicon. In: *Phys. Rev. B* 10 (1974), Dec, 5095–5107. http://dx.doi.org/10.1103/PhysRevB.10.5095. – DOI 10.1103/PhysRevB.10.5095 (cited on page 21.)

[CCS02] Campbell, D. ; Chilingarov, A. ; Sloan, T.: Frequency and temperature dependence of the depletion voltage from CV measurements for irradiated Si detectors. In: *Nuclear Instruments and Methods in Physics Research Section A: Accelerators, Spectrometers, Detectors and Associated Equipment* 492 (2002), Nr. 3, 402 - 410. http://dx.doi.org/10.1016/S0168-9002(02)01353-0. – DOI 10.1016/S0168–9002(02)01353–0. – ISSN 0168–9002 (cited on page 46.)

[CER] *CERN – The European Organization for Nuclear Research*. http://www.cern.ch (cited on page 6.)

[Chi11] Chilingarov, A.: *Generation current temperature scaling*. http://rd50.web.cern.ch/rd50/doc/Internal/rd50_2011_001-I-T_scaling.pdf. Version: 2011. – RD50 Technical Note RD50-2011-01 (cited on page 28.)

[CMMO75] Canali, C. ; Majni, G. ; Minder, R. ; Ottaviani, G.: Electron and hole drift velocity measurements in silicon and their empirical relation to electric field and temperature. In: *IEEE Transactions on Electron Devices* 22 (1975), Nr. 11, P. 1045–1047. http://dx.doi.org/10.1109/T-ED.1975.18267. – DOI 10.1109/T–ED.1975.18267. – ISSN 0018–9383 (cited on pages 50, 66.)

[CMS] *CMS – The Compact Muon Solenoid Experiment*. http://cms.web.cern.ch (cited on pages 5, 7, 8 and 9.)

[CMS98] CMS Collaboration: The Tracker Project / CERN/LHCC 98-6. 1998. – Technical Design Report. – CMS TDR 5 (cited on page 8.)

[CMS13] CMS Collaboration: FLUKA particle flux maps for CMS Detector. Version: 2013. http://cms.cern.ch/iCMS/jsp/db_notes/notestable1.jsp?CMSNoteID=DP-2013/028. 2013. – CMS Performance Note. – CMS DP-2013/028 (cited on page 10.)

[Cz017] Czochralski, J.: Metalle. In: *Z. Phys. Chem.* 92 (1917), P. 219 (cited on page 31.)

[D+13] Dragicevic, M. et al.: Comparing Spreading Resistance Profiling and C-V characterisation to identify defects in silicon sensors. In: *JINST* 8 (2013). http://dx.doi.org/10.1088/1748-0221/8/02/C02018. – DOI 10.1088/1748–0221/8/02/C02018 (cited on pages 83, 85 and 86.)

[Dan97] Daniel, H.: *Physik 2, Elektrodynamik, Relativistische Physik*. de Gruyter, 1997 (cited on pages 22, 65.)

[Die03] Dierlamm, A.: *Studies on the Radiation Hardness of Silicon Sensors*, Universität Karlsruhe (TH), PhD Thesis, 2003. – IEKP-KA/2003-23 (cited on pages 35, 56.)

[Die09] Dierlamm, A.: CMS Tracker upgrade issues and plans. In: *Nuclear Instruments and Methods in Physics Research A* (2009). http://dx.doi.org/10.1016/j.nima.2009.01.196. – DOI 10.1016/j.nima.2009.01.196 (cited on page 11.)

[E+04] Eremin, V. et al.: Double peak electric field distortion in heavily irradiated silicon strip detectors. In: *Nuclear Instruments and Methods in Physics Research Section A: Accelerators, Spectrometers, Detectors and Associated Equipment* 535 (2004), Nr. 3, 622-631. http://dx.doi.org/10.1016/j.nima.2004.06.143. – DOI 10.1016/j.nima.2004.06.143. – ISSN 0168–9002 (cited on pages 53, 144 and 174.)

[Ebe09] Eber, R.: *Untersuchungen an Magnetic-Czochralski-Dioden nach gemischter Bestrahlung mit Neutronen und Protonen mittels der Transient Current Technique*, Universität Karlsruhe (TH), Diploma Thesis, 2009. http://www-ekp.physik.uni-karlsruhe.de/pub/web/thesis/iekp-ka2009-30.pdf. – IEKP-KA/2009-30 (cited on page 61.)

[Ebe11] Eber, R. on behalf of the CMS Tracker Collaboration: Silicon Sensor Developments for the CMS Tracker Upgrade. In: *Astroparticle, Particle, Space Physics and Detectors for Physics Applications* Vol. 7, World Scientific, 2011 (Proceedings of the 13th ICATPP Conference), 856-860 (cited on page 126.)

[Erf09] Erfle, J.: *Entwicklungen für neue Siliziumstreifensensoren und deren Qualitätskontrolle*, Universität Karlsruhe (TH), Diploma Thesis, 2009. http://www-ekp.physik.uni-karlsruhe.de/pub/web/thesis/iekp-ka2009-27.pdf. – IEKP-KA/2009-27 (cited on page 57.)

[EVL02] Eremin, V. ; Verbitskaya, E. ; Li, Z.: The origin of double peak electric field distribution in heavily irradiated silicon detectors. In: *Nuclear Instruments and Methods in Physics Research Section A: Accelerators, Spectrometers, Detectors and Associated Equipment* 476 (2002), Nr. 3, 556 - 564. http://dx.doi.org/10.1016/S0168-9002(01)01642-4. – DOI 10.1016/S0168–9002(01)01642–4. – ISSN 0168–9002 (cited on page 53.)

[Fre12] Frech, S.: *Einfluss von Strahlenschäden auf Siliziumstreifensensoren aus unterschiedlichen Grundmaterialien*, Karlsruher Institut für Technologie, Diploma Thesis, 2012. http://www-ekp.physik.uni-karlsruhe.de/~thesis/data/iekp-ka2012-21.pdf. – IEKP-KA/2012-21 (cited on pages 10, 36, 40, 58, 184, 185 and 211.)

[Fur06] Furgeri, A.: *Qualitätskontrolle und Bestrahlungsstudien an CMS Siliziumstreifensensoren*, Universität Karlsruhe (TH), PhD Thesis, 2006. – IEKP-KA/2005-1 (cited on page 47.)

[Gar12] García, M.: *First investigation of silicon microstrips for the CMS Tracker upgrade using edge-TCT*. 21st RD50 Workshop, Nov 2012 (cited on pages 110, 112.)

[GM86] Gatti, E. ; Manfredi, P.F.: Processing the signals from solid-state detectors in elementary-particle physics. In: *La Rivista del Nuovo Cimento* 9 (1986), Nr. 1, 1-146. http://dx.doi.org/10.1007/BF02822156. – DOI 10.1007/BF02822156. – ISSN 0393–697X (cited on page 51.)

[Gut] Guthoff, M.: *Radiation Simulation Plotting tool v.1.4, CMS-BRIL Radiation Simulation*. https://cms-project-fluka-flux-map.web.cern.ch/cms-project-fluka-flux-map/index.shtml, Last check: 2013-09-03 (cited on page 8.)

[H+03] Härkönen, J. et al.: Processing of microstrip detectors on Czochralski grown high resistivity silicon substrates. In: *Nuclear Instruments and Methods in Physics Research Section A: Accelerators, Spectrometers, Detectors and Associated Equipment* 514 (2003), Nr. 1-3, 173 - 179. http://dx.doi.org/DOI:10.1016/j.nima.2003.08.102. – DOI DOI: 10.1016/j.nima.2003.08.102. – ISSN 0168–9002. – Proceedings of the 4th International Conference on Radiation Effects on Semiconductor Materials, Detectors and Devices (cited on page 31.)

[H+09] Hall, G. et al.: Design of a trigger module for the CMS Tracker at SLHC. (2009). http://indico.cern.ch/getFile.py/access?contribId=13&sessionId=19&resId=1&materialId=paper&confId=49682 (cited on page 11.)

[Hal08] Hall, G.: The upgrade program of the CMS Tracker at SLHC. In: Brenner, R. (Publisher): *Proceedings of 17th International Workshop on Vertex detectors, Vertex 2008*, 2008 (cited on page 9.)

[Har09] Hartmann, F.: *Evolution of Silicon Sensor Technology in Particle Physics*. Springer, 2009 (cited on pages 16, 20, 24, 25, 26 and 47.)

[Hof11] Hoffmann, K.-H.: Campaign to identify the future CMS tracker baseline. In: *Nuclear Instruments and Methods in Physics Research Section A: Accelerators, Spectrometers, Detectors and Associated Equipment* 658 (2011), Nr. 1, 30 - 35. http://dx.doi.org/10.1016/j.nima.2011.05.028. – DOI 10.1016/j.nima.2011.05.028. – ISSN 0168–9002. – RESMDD 2010 (cited on page 12.)

[Hof13] Hoffmann, K.-H.: *Development of new Sensor Designs and Investigations on Radiation Hard Silicon Strip Sensors for the CMS Tracker Upgrade at the High Luminosity Large Hadron Collider*, Karlsruher Institut für Technologie, PhD Thesis, 2013 (cited on pages 10, 47, 57, 80, 90, 104, 105, 184, 185 and 211.)

[Huh02] Huhtinen, M.: Simulation of non-ionising energy loss and defect formation in silicon. In: *Nuclear Instruments and Methods in Physics Research Section A: Accelerators, Spectrometers, Detectors and Associated Equipment* 491 (2002), Nr. 1-2, 194 - 215. http://dx.doi.org/10.1016/S0168-9002(02)01227-5. – DOI 10.1016/S0168–9002(02)01227–5. – ISSN 0168–9002 (cited on pages 33, 35.)

[IL09] Ibach, H. ; Lüth, H.: *Festkörperphysik*. Springer, 2009 (cited on page 22.)

[Iof] *Ioffe - Semiconductors on NSM*. http://www.ioffe.ru/SVA/NSM/Semicond/, Last check: 2013-04-04 (cited on pages 65, 73.)

[ITE] Instytut Technologii Elektronowej - Warsaw (cited on page 13.)

[ITM] *SIMS laboratory, Physics Institute of the Polish Academy of Science, Warsaw, Poland* (cited on pages 13, 14.)

[JCOQ77] Jacoboni, C. ; Canali, C. ; Ottaviani, G. ; Quaranta, A. A.: A review of some charge transport properties of silicon. In: *Solid-State Electronics* 20 (1977), Nr. 2, 77 - 89. http://dx.doi.org/10.1016/0038-1101(77)90054-5. – DOI 10.1016/0038–1101(77)90054–5. – ISSN 0038–1101 (cited on pages 50, 74 and 75.)

[Jun07] Junkes, A.: *Radiation induced Point and Cluster defects*, Universität Hamburg, Diploma Thesis, 2007 (cited on page 41.)

[Jun11] Junkes, A.: *Influence of Radiation Induced Defect Clusters on Silicon Particle Detectors*, DESY Hamburg, PhD Thesis, 2011 (cited on pages 40, 41, 80, 82, 87 and 88.)

[K+02a] Kramberger, G. et al.: Determination of effective trapping times for electrons and holes in irradiated silicon. In: *Nuclear Instruments and Methods in Physics Research Section A: Accelerators, Spectrometers, Detectors and Associated Equipment* 476 (2002), Nr. 3, 645 - 651. http://dx.doi.org/10.1016/S0168-9002(01)01653-9. – DOI 10.1016/S0168–9002(01)01653–9. – ISSN 0168–9002 (cited on pages 165, 167.)

[K+02b] Kramberger, G. et al.: Effective trapping time of electrons and holes in different silicon materials irradiated with neutrons, protons and pions. In: *Nuclear Instruments and Methods in Physics Research Section A: Accelerators, Spectrometers, Detectors and Associated Equipment* 481 (2002), Nr. 1-3, 297 - 305. http://dx.doi.org/10.1016/S0168-9002(01)01263-3. – DOI 10.1016/S0168–9002(01)01263–3. – ISSN 0168–9002 (cited on page 168.)

[K+06] Krupka, J. et al.: Measurements of Permittivity, Dielectric Loss Tangent, and Resistivity of Float-Zone Silicon at Microwave Frequencies. In: *IEEE Transactions on Microwave Theory and Techniques* 54 (2006), Nr. 11, P. 3995 – 4001. http://dx.doi.org/10.1109/TMTT.2006.883655. – DOI 10.1109/TMTT.2006.883655. – ISSN 0018–9480 (cited on page 65.)

[K+07] Kramberger, G. et al.: Annealing studies of effective trapping times in silicon detectors. In: *Nuclear Instruments and Methods in Physics Research Section A: Accelerators, Spectrometers, Detectors and Associated Equipment* 571 (2007), Nr. 3, 608 - 611. http://dx.doi.org/10.1016/j.nima.2006.10.399. – DOI 10.1016/j.nima.2006.10.399. – ISSN 0168–9002 (cited on page 168.)

[K+10] Kramberger, G. et al.: Investigation of Irradiated Silicon Detectors by Edge-TCT. In: *IEEE Transactions on Nuclear Science* 57 (2010), Nr. 4, P. 2294–2302. http://dx.doi.org/10.1109/TNS.2010.2051957. – DOI 10.1109/TNS.2010.2051957. – ISSN 0018–9499 (cited on page 110.)

[Kla92] Klaassen, D. B. M.: Unified Mobility Model for Device Simulation – I. Model Equations and Concentration Dependence. In: *Solid State Electronics* 53 (1992), Nr. 7, P. 953 – 959 (cited on page 67.)

[KLF93] Kraner, H.W. ; Li, Z. ; Fretwurst, E.: The use of the signal current pulse shape to study the internal electric field profile and trapping effects in neutron damaged silicon detectors. In: *Nuclear Instruments and Methods in Physics Research Section A: Accelerators, Spectrometers, Detectors and Associated Equipment* 326 (1993), 350-356. http://dx.doi.org/10.1016/0168-9002(93)90376-S. – DOI 10.1016/0168–9002(93)90376–S. – ISSN 0168–9002 (cited on pages 52, 165.)

[Kor11] Kornmayer, A.: *Untersuchungen zur Signalkopplung an neuartigen Siliziumstreifensensorgeometrien*, Karlsruhe Institute of Technology, Diploma Thesis, 2011. http://www-ekp.physik.uni-karlsruhe.de/~thesis/data/iekp-ka2011-17.pdf (cited on pages 126, 128 and 129.)

[Kra01] Kramberger, G.: *Signal development in irradiated silicon detectors*, University of Ljubljana, PhD Thesis, 2001. http://www-f9.ijs.si/~gregor/papers/dok_eng.pdf (cited on page 56.)

[L+87] Luera, Theodore F. et al.: Neutron Damage Equivalence for Silicon, Silicon Dioxide, and Gallium Arsenide. In: *Nuclear Science, IEEE Transactions on* 34 (1987), Nr. 6, P. 1557–1563. http://dx.doi.org/10.1109/TNS.1987.4337515. – DOI 10.1109/TNS.1987.4337515. – ISSN 0018–9499 (cited on page 33.)

[L+01] Lindström, G. et al.: Developments for radiation hard silicon detectors by defect engineering–results by the CERN RD48 (ROSE) Collaboration. In: *Nuclear Instruments and Methods in Physics Research Section A: Accelerators, Spectrometers, Detectors and Associated Equipment* 465 (2001), Nr. 1, 60 - 69. http://dx.doi.org/10.1016/S0168-9002(01)00347-3. – DOI 10.1016/S0168–9002(01)00347–3. – ISSN 0168–9002 (cited on page 31.)

[L+10a] Lange, J. et al.: Properties of a radiation-induced charge multiplication region in epitaxial silicon diodes. In: *Nuclear Instruments and Methods in Physics Research Section A: Accelerators, Spectrometers, Detectors and Associated Equipment* 622 (2010), Nr. 1, 49 - 58. http://dx.doi.org/10.1016/j.nima.2010.07.036. – DOI 10.1016/j.nima.2010.07.036. – ISSN 0168–9002 (cited on page 188.)

[L+10b] Li, Z. et al.: Equal-double junctions in 24GeV/c proton-irradiated MCZ n- and p-type Si detectors: A systematic transient current technique investigation. In: *Nuclear Instruments and Methods in Physics Research Section A: Accelerators, Spectrometers, Detectors and Associated Equipment* 612 (2010), Nr. 3, 539 - 548. http://dx.doi.org/10.1016/j.nima.2009.08.082. – DOI 10.1016/j.nima.2009.08.082. – ISSN 0168–9002. – Proceedings of the 7th International Conference on Radiation Effects on Semiconductor materials, Detectors and Devices (RESMDD 2008) (cited on page 53.)

[LHC] *LHC-b – The Large Hadron Collider beauty experiment*. http://lhcb.web.cern.ch (cited on page 5.)

[Lin03] Lindström, G.: Radiation damage in silicon detectors. In: *Nuclear Instruments and Methods in Physics Research Section A: Accelerators, Spectrometers, Detectors and Associated Equipment* 512 (2003), Nr. 1-2, 30 - 43. http://dx.doi.org/10.1016/S0168-9002(03)01874-6. – DOI 10.1016/S0168–9002(03)01874–6. – ISSN 0168–9002. – Proceedings of the 9th European Symposium on Semiconductor Detectors: New Developments on Radiation Detectors (cited on page 34.)

[LMF99] Lindström, G. ; Moll, M. ; Fretwurst, E.: Radiation hardness of silicon detectors – a challenge from high-energy physics. In: *Nuclear Instruments and Methods in Physics Research Section A: Accelerators, Spectrometers, Detectors and Associated Equipment* 426 (1999), Nr. 1, 1 - 15. http://dx.doi.org/10.1016/S0168-9002(98)01462-4. – DOI 10.1016/S0168–9002(98)01462–4. – ISSN 0168–9002 (cited on page 49.)

[LRS96] Levinshtein, M.E. ; Rumyantsev, S.L. ; Shur, M.: *Handbook Series on Semiconductor Parameters*. Vol. 1: *Handbook series on semiconductor parameters. 1. Si, Ge, C (diamond), GaAs, GaP, GaSb, InAs, InP, InSb*. World Scientific Publishing Company, Incorporated, 1996. – ISBN 978-9-810-22934-4 (cited on page 65.)

[M+10] Mandic, I. et al.: Observation of full charge collection efficiency in heavily irradiated n+p strip detectors irradiated up to 3×10^{15} neq/cm^2. In: *Nuclear Instruments and Methods in Physics Research Section A: Accelerators, Spectrometers, Detectors and Associated Equipment* 612 (2010), Nr. 3, 474 - 477. http://dx.doi.org/10.1016/j.

nima.2009.08.004. – DOI 10.1016/j.nima.2009.08.004. – ISSN 0168–9002. – Proceedings of the 7th International Conference on Radiation Effects on Semiconductor materials, Detectors and Devices, RESMDD 2008 (cited on page 188.)

[MH10] Marco-Hernández, R.: A portable readout system for silicon microstrip sensors. In: *Nuclear Instruments and Methods in Physics Research Section A: Accelerators, Spectrometers, Detectors and Associated Equipment* 623 (2010), Nr. 1, 207 - 209. http://dx.doi.org/10.1016/j.nima.2010.02.197. – DOI 10.1016/j.nima.2010.02.197. – ISSN 0168–9002 (cited on pages 57, 211.)

[Mol99] Moll, M.: *Radiation Damage in Silicon Particle Detectors*, Universität Hamburg, Doktorarbeit, 1999 (cited on pages 34, 36, 37, 38, 39, 40, 142, 145 and 174.)

[Mou06] Mouche, P.: *Overall view of the LHC. Vue d'ensemble du LHC*. Sep 2006 (cited on page 6.)

[MSS83] Masetti, G. ; Severi, M. ; Solmi, S.: Modeling of carrier mobility against carrier concentration in arsenic-, phosphorus-, and boron-doped silicon. In: *IEEE Transactions on Electron Devices* 30 (1983), Nr. 7, P. 764 – 769. http://dx.doi.org/10.1109/T-ED.1983.21207. – DOI 10.1109/T–ED.1983.21207. – ISSN 0018–9383 (cited on page 67.)

[NN00] Nishi, Y. ; Nishi, N. ; Doering (Publisher): *Handbook of Semiconductor Manufacturing Technology*. Marcel Dekker Inc, 2000 (cited on page 31.)

[P+05] Petasecca, M. et al.: A comprehensive numerical simulation of heavily irradiated p-type and n-type silicon detectors. In: *Nuclear Science Symposium Conference Record, 2005 IEEE* Vol. 3, 2005. – ISSN 1095–7863, P. 1490 –1493 (cited on page 174.)

[P+06] Petasecca, M. et al.: Numerical simulation of radiation damage effects in p-type silicon detectors. In: *Nuclear Instruments and Methods in Physics Research Section A: Accelerators, Spectrometers, Detectors and Associated Equipment* 563 (2006), Nr. 1, 192 - 195. http://dx.doi.org/10.1016/j.nima.2006.01.093. – DOI 10.1016/j.nima.2006.01.093. – ISSN 0168–9002. – Proceedings of the 7th International Workshop on Radiation Imaging Detectors (IWORID 2005) (cited on page 174.)

[Pfi10] Pfister, T.: *Aufbau einer vollautomatischen Messstation zur Bestimmung der Ladungssammlungseffizienz hochbestrahlter Silizium-Streifensensoren*, Karlsruher Institut für Technologie, Diploma Thesis, 2010. http://www-ekp.physik.uni-karlsruhe.de/~thesis/data/iekp-ka2010-20.pdf. – IEKP-KA/2010-20 (cited on pages 58, 211.)

[PFL08] Pintilie, I. ; Fretwurst, E. ; Lindström, G.: Cluster related hole traps with enhanced-field-emission – the source for long term annealing in hadron irradiated Si diodes. In: *Appl. Phys. Lett.* 92 (2008). http://dx.doi.org/10.1063/1.2832646. – DOI 10.1063/1.2832646 (cited on page 41.)

[PLJF09] Pintilie, I. ; Lindstroem, G. ; Junkes, A. ; Fretwurst, E.: Radiation-induced point- and cluster-related defects with strong impact on damage properties of silicon detectors. In: *Nuclear Instruments and Methods in Physics Research Section A: Accelerators, Spectrometers, Detectors and Associated Equipment* 611 (2009), Nr. 1, 52 - 68. http://dx.doi.org/10.1016/j.nima.2009.09.065. – DOI 10.1016/j.nima.2009.09.065. – ISSN 0168–9002 (cited on page 41.)

[PMP05] Petasecca, M. ; Moscatelli, F. ; Pignatel, G.U.: Analysis and simulation of charge collection efficiency in silicon thin detectors. In: *Nuclear Instruments and*

Methods in Physics Research Section A: Accelerators, Spectrometers, Detectors and Associated Equipment 546 (2005), Nr. 1-2, 291 - 295. http://dx.doi.org/10.1016/j.nima.2005.03.051. – DOI 10.1016/j.nima.2005.03.051. – ISSN 0168–9002. – Proceedings of the 6th International Workshop on Radiation Imaging Detectors - Radiation Imaging Detectors 2004 (cited on page 174.)

[PMPP06] Petasecca, M. ; Moscatelli, F. ; Passeri, D. ; Pignatel, G.U.: Numerical Simulation of Radiation Damage Effects in p-Type and n-Type FZ Silicon Detectors. In: *IEEE Transactions on Nuclear Science* 53 (2006), oct., Nr. 5, P. 2971 –2976. http://dx.doi.org/10.1109/TNS.2006.881910. – DOI 10.1109/TNS.2006.881910. – ISSN 0018–9499 (cited on page 174.)

[Poe13] Poehlsen, Th.: *Charge Losses in Silicon Sensors and Electric-Field Studies at the* $\mathrm{Si}-\mathrm{SiO}_2$ *Interface*, Universität Hamburg, PhD Thesis, 2013 (cited on page 171.)

[PRSZ06] Povh ; Rith ; Scholz ; Zetsche: *Teilchen und Kerne: Eine Einführung in die physikalischen Konzepte*. Springer, 2006. – ISBN 978-3-540-36686-7 (cited on page 15.)

[RD5] *RD 50 – Radiation hard semiconductor devices for very high luminosity colliders*. http://rd50.web.cern.ch (cited on pages 32, 143 and 188.)

[Roo] *Root | A Data Analysis Framework*. http://root.cern.ch (cited on pages 63, 218.)

[S+06] Swartz, M. et al.: Observation, modeling, and temperature dependence of doubly peaked electric fields in irradiated silicon pixel sensors. In: *Nuclear Instruments and Methods in Physics Research Section A: Accelerators, Spectrometers, Detectors and Associated Equipment* 565 (2006), Nr. 1, 212 - 220. http://dx.doi.org/10.1016/j.nima.2006.05.002. – DOI 10.1016/j.nima.2006.05.002. – ISSN 0168–9002. – Proceedings of the International Workshop on Semiconductor Pixel Detectors for Particles and Imaging, PIXEL 2005 (cited on page 174.)

[Sila] *Siliconfareast: Properties of Si, Ge, and GaAs at 300K*. http://ww.siliconfareast.com/sigegaas.htm, Last check: 2013-04-04 (cited on pages 65, 66.)

[Silb] *Silvaco, Inc., Santa Clara, CA 95054, USA*. http://www.silvaco.com. – 2013 (cited on page 72.)

[Sil13] Silvaco, Inc. (Publisher): *Silvaco Atlas User's Manual*. Santa Clara, CA 95054: Silvaco, Inc., 4 2013. http://www.silvaco.com (cited on pages 72, 73.)

[SLH] *SLHC – The Preparatory Phase of the Large Hadron Collider upgrade (SLHC-PP)*. http://info-slhc-pp.web.cern.ch (cited on page 9.)

[SN07] Sze, S. M. ; Ng, Kwok K.: *Physics of Semiconductor Devices*. 3rd edition. John Wiley & Sons, 2007. – ISBN-13: 978-0-471-14323-9 (cited on page 41.)

[Ste13] Steinbrück, G.: *Silicon Material Studies: Summary of Diode Measurements with Focus on Polarity*. CMS internal Sensor Meeting, Aug 2013 (cited on page 14.)

[Str12] Strelzyk, M.: *Design studies of n-in-p silicon strip sensors for the CMS tracker*, Karlsruher Institut für Technologie, Diploma Thesis, 2012. http://www-ekp.physik.uni-karlsruhe.de/pub/web/thesis/iekp-ka2012-22.pdf. – IEKP-KA/2012-22 (cited on pages 10, 108, 113 and 116.)

[Syn] *Synopsys, Inc., 700 East Middlefield Rd., Mountain View, California 94043-4033, U.S.A.* http://www.synopsys.com. – 2013 (cited on page 64.)

[Syn12] Synopsys (Publisher): *Sentaurus Device*. Version G-2012.06. Mountain View, CA, USA: Synopsys, 2012 (cited on pages 50, 65, 66, 67, 68, 69, 73, 76, 87, 204 and 205.)

[Sze85] Sze, Simon M.: *Semiconductor Devices : Physics and Technology*. John Wiley & Sons, 1985. – ISBN 978-0-471-83704-6 (cited on pages 25, 27 and 31.)

[The] The National Institute of Standards and Technology (NIST): *Mean Excitation Energy of Silicon*. http://physics.nist.gov/cgi-bin/Star/compos.pl?matno=014 (cited on page 15.)

[The08] The CMS Collaboration: The CMS Experiment at the CERN LHC. In: *Journal of Instrumentation* 3 (2008), P. S08004. http://dx.doi.org/10.1088/1748-0221/3/08/S08004. – DOI 10.1088/1748–0221/3/08/S08004 (cited on page 6.)

[The12] The CMS Collaboration: Observation of a new boson at a mass of 125 GeV with the CMS experiment at the LHC. In: *Physics Letters B* 716 (2012), Nr. 1, 30 - 61. http://dx.doi.org/10.1016/j.physletb.2012.08.021. – DOI 10.1016/j.physletb.2012.08.021. – ISSN 0370–2693 (cited on page 9.)

[The13] The CMS Collaboration: Observation of a new boson with mass near 125 GeV in pp collisions at $\sqrt{s} = 7$ and 8 TeV. In: *Journal of High Energy Physics* 2013 (2013), Nr. 6, 1-127. http://dx.doi.org/10.1007/JHEP06(2013)081. – DOI 10.1007/JHEP06(2013)081 (cited on page 5.)

[TL] Technology Ltd. e.World: *phpMaker 8*. http://www.hkvstore.com/phpmaker, Last check: 2013-07-18 (cited on page 62.)

[Tre11] Treberspurg, W.: *Manufacturing Process of Silicon Strip Sensors and Analysis of Detector Structures*, Vienny University of Technology, Diploma Thesis, 2011. http://www.hephy.at/fileadmin/user_upload/Publikationen/DA_WT_Version6.pdf (cited on pages 104, 107.)

[Tre12] Treberspurg, W.: *Enhanced Measurement Methods for Sensor Characterization*. CMS Tracker Week, 02 2012 (cited on pages 84, 102.)

[TRI] *TRIGA Mark II Reactor*. www.rcp.ijs.si/ric/description-a.html. – 2013-03-11 (cited on page 56.)

[Tri08] Tricomi, A.: SLHC: The LHC luminosity upgrade. In: *Nuclear Instruments and Methods in Physics Research Section A: Accelerators, Spectrometers, Detectors and Associated Equipment* 596 (2008), Nr. 1, 43 - 47. http://dx.doi.org/10.1016/j.nima.2008.07.118. – DOI 10.1016/j.nima.2008.07.118. – ISSN 0168–9002. – Proceedings of the 8th International Conference on Large Scale Applications and Radiation Hardness of Semiconductor Detectors (cited on page 9.)

[Uni] University of Lyon: *BigBrowser*. https://lyosvn.in2p3.fr/constructiondb/wiki/Download, Last check: 2013-07-18 (cited on page 63.)

[V+07] Verbitskaya, E. et al.: Concept of Double Peak electric field distribution in the development of radiation hard silicon detectors. In: *Nuclear Instruments and Methods in Physics Research Section A: Accelerators, Spectrometers, Detectors and Associated Equipment* 583 (2007), Nr. 1, 77 - 86. http://dx.doi.org/10.1016/j.nima.2007.08.228. – DOI 10.1016/j.nima.2007.08.228. – ISSN 0168–9002. – Proceedings of the 6th International Conference on Radiation Effects on Semiconductor Materials, Detectors and Devices - RESMDD 2006 (cited on pages 53, 174.)

[Vir02] *Virginia Semiconductors: The General Properties of Si, Ge, SiGe, SiO2 and Si3N4*. Version: 06 2002. http://www.virginiasemi.com/pdf/generalpropertiessi62002.pdf, Last check: 2013-04-04 (cited on pages 65, 66.)

[W+96] Wunstorf, R. et al.: Investigations of donor and acceptor removal and long term annealing in silicon with different boron/phosphorus ratios. In: *Nuclear Instruments and Methods in Physics Research Section A: Accelerators, Spectrometers, Detectors and Associated Equipment* 377 (1996), Nr. 2-3, 228 - 233. http://dx.doi.org/10.1016/0168-9002(96)00217-3. – DOI 10.1016/0168–9002(96)00217–3. – ISSN 0168–9002. – Proceedings of the Seventh European Symposium on Semiconductor (cited on pages 37, 147.)

[WB90] Windisch, D. ; Becker, P.: Silicon lattice parameters as an absolute scale of length for high precision measurements of fundamental constants. In: *Phys. Stat. Sol. (a)* 118 (1990), P. 379–388. http://dx.doi.org/10.1002/pssa.2211180205. – DOI 10.1002/pssa.2211180205 (cited on page 20.)

[WC64] Watkins, G. D. ; Corbett, J. W.: Defects in Irradiated Silicon: Electron Paramagnetic Resonance and Electron-Nuclear Double Resonance of the Si-E Center. In: *Phys. Rev.* 134 (1964), Jun, A1359–A1377. http://dx.doi.org/10.1103/PhysRev.134.A1359. – DOI 10.1103/PhysRev.134.A1359 (cited on page 37.)

[Wik05] Wikipedia: *Diamond Cubic-F lattice*. http://en.wikipedia.org/wiki/File:Diamond_Cubic-F_lattice_animation.gif. Version: 10 2005. – last checked: 2013-09-19 (cited on page 23.)

[Wik06] Wikipedia: *Tetrahedal molecular geometry*. http://en.wikipedia.org/wiki/File:Tetrahedal-3D-balls.png. Version: 12 2006. – last checked: 2013-09-19 (cited on page 23.)

[Wür09] Würfel, P.: *Physics of Solar Cells*. WILEY-VCH, 2009. – ISBN 978-3-527-40857-3 (cited on pages 22, 24.)

[Y+06] Yao, W-M et al.: Accelerator Physics of Colliders. In: *J. Phys. G: Nucl. Part. Phys.* 33 1 (2006), P. 252 (cited on page 6.)

[Zha13] Zhang, J.: *X-Ray Radiation Damage Studies and Design of a Silicon Pixel Sensor for Science at the XFEL*, Universität Hamburg, PhD Thesis, 2013 (cited on pages 41, 42.)

[Zon98] Zontar, D.: *Study of radiation damage in silicon detectors for high luminosity experiments at LHC*, University of Ljubljana, PhD Thesis, 1998. http://cds.cern.ch/record/1390822/files/CERN-THESIS-98-023.pdf (cited on pages 35, 56.)

LIST OF FIGURES

Figure 2.1 The LHC and its experiments. 6
Figure 2.2 The CMS detector. 7
Figure 2.3 The CMS all-silicon tracker. 8
Figure 2.4 Cross section of the CMS detector and particle identification scheme. . . . 9
Figure 2.5 Fluences at the HL-LHC at 3000 fb^{-1} 10
Figure 2.6 Comparison of the number of tracks at the LHC and HL-LHC. 11
Figure 2.7 2S-Module and working principle of the track trigger. 11
Figure 2.8 Structures on the HPK wafer 13
Figure 2.9 Oxygen Concentration in HPK material. 14
Figure 3.1 Working principle of a silicon detector 16
Figure 3.2 Mean energy loss of electrons in silicon 16
Figure 3.3 Generated electron-hole-pairs in silicon. 17
Figure 3.4 Cut through diode. 18
Figure 3.5 Cut through a MOS device. 19
Figure 3.6 3d schematic of strip sensor. 20
Figure 3.7 p-stop atoll isolation. 20
Figure 3.8 Reduced Zone Scheme of Silicon 21
Figure 3.9 Classification of solids. 22
Figure 3.10 Tetrahedal structure and diamond lattice of silicon. 23
Figure 3.11 pn-junction at the moment of contact. 24
Figure 3.12 Forming of the space charge region. 26
Figure 3.13 Current-voltage characteristics of an ideal diode. 28
Figure 3.14 Ideal capacitance-voltage characteristics. 29
Figure 3.15 Doping Profile obtained from CV measurement. 30
Figure 3.16 Float zone and Czochralski process. 31
Figure 4.1 Simulation of distribution of vacancies in silicon. 33
Figure 4.2 Crystal defects in silicon: vacancy and interstitial 33
Figure 4.3 Displacement damage functions D(E). 34
Figure 4.4 Impact of defects on sensor properties 35
Figure 4.5 Fluence generated volume current in silicon 36
Figure 4.6 Type inversion in n-bulk silicon. 37
Figure 4.7 Anealing of α. 38
Figure 4.8 Annealing of $|N_{eff}|$ 39
Figure 4.9 Charge collection efficiency loss due to trapping 40
Figure 4.10 Fixed oxide charges as a function of ionising dose. 42
Figure 5.1 IV measurement of an un-irradiated diode. 45
Figure 5.2 CV measurement of an un-irradiated diode. 46
Figure 5.3 CV measurement of an irradiated diode. 47
Figure 5.4 Resistance between pad and guard ring. 48
Figure 5.5 Flatband voltage of a MOS device. 48
Figure 5.6 Sketch of the TCT setup 49
Figure 5.7 Absorption of light in silicon. 50
Figure 5.8 Absorption of red or infrared light in silicon. 51
Figure 5.9 Current density and free carrier density in an irradiated sensor 53
Figure 5.10 Effective space charge and electric field in an irradiated sensor 54
Figure 5.11 Double Peak signal of TCT measurements. 54
Figure 6.1 Probestation at IEKP 58
Figure 6.2 Strip sensor readout system (ALiBaVa) 59

Figure 6.3 Cold chuck and laser mount at the Picolaser Setup. 60
Figure 6.4 Diode Box and cold chuck. 61
Figure 6.5 Picolaser Setup. 62
Figure 7.1 Principle of coupled defect levels. 69
Figure 7.2 Example for device plot and a cut through a device made with svisual. . . 71
Figure 7.3 Saturation velocities for electrons and holes at 300 K in Synopsys and Silvaco. 75
Figure 7.4 Electric field at 300 K in Synopsys and Silvaco. 76
Figure 7.5 Mobility for electrons and holes at 300 K in Synopsys and Silvaco. 77
Figure 7.6 Drift velocity for electrons and holes at 300 K in Synopsys and Silvaco. . . 78
Figure 8.1 Simple Diode Simulation Structure 80
Figure 8.2 Diode Simulation Structure with Periphery 81
Figure 8.3 Simulated and measured CV of FZ320N, FZ320P/Y 82
Figure 8.4 Simulated and measured CV of FZ200N, FZ200P/Y 82
Figure 8.5 Simulated and measured CV of FZ120N, FZ120P/Y 83
Figure 8.6 Simulated and measured CV of MCz200N, MCz200P/Y 83
Figure 8.7 Doping profiles of n-bulk and p-bulk FZ diodes 84
Figure 8.8 Doping profiles of n-bulk and p-bulk MCz and FTH diodes 84
Figure 8.9 Principle of the spreading resistance measurement 85
Figure 8.10 Doping profile of FZ p-bulk wafers measured with the spreading resistance method 86
Figure 8.11 Doping profile from CV compared to the doping profile used in the simulation 86
Figure 8.12 Leakage current of un-irradiated diodes 87
Figure 8.13 Diode naming scheme for diodes on the HPK wafer. 88
Figure 8.14 Current variation of diodes over one wafer. 88
Figure 8.15 Leakage current of un-irradiated diodes 89
Figure 8.16 Simulation with the H220K defect. 89
Figure 8.17 Active area of n-bulk diodes with and without guard ring 91
Figure 8.18 Simulation of a diode with grounded and floating guard ring. 94
Figure 8.19 Comparison of CV curve shapes. 94
Figure 8.20 Intensity of different wavenlengths in silicon. 98
Figure 8.21 Equivalent readout circuit of TCT setups. 99
Figure 8.22 Comparison of measured and simulated TCT pulse. 100
Figure 8.23 Comparison of IR laser and MIP signals. 101
Figure 8.24 Comparison of charge collection of different signals. 101
Figure 8.25 Strip geometry of HPK strip sensors. 102
Figure 8.26 Coupling Capacitance of strip sensors. 104
Figure 8.27 Interstrip Capacitance of strip sensors. 105
Figure 8.28 Bias network of a strip sensor. 106
Figure 8.29 Electric Fields in un-irradiated n-bulk strip sensors. 106
Figure 8.30 Electric field in p-bulk sensors with different isolation. 108
Figure 8.31 Electric Field at the Strips for FZ320P. 108
Figure 8.32 CCE of a un-irradiated n-bulk strip sensor. 109
Figure 8.33 Signals induced in two strips of a un-irradiated FZ320N sensor. 110
Figure 8.34 Edge-TCT simulation device. 111
Figure 8.35 Edge-TCT signals in a FZ320P strip sensor. 112
Figure 8.36 Edge-TCT measurement of a FZ320N sensor. 112
Figure 9.1 Advanced Diode Geometries 114
Figure 9.2 Advanced Diode Design p-stop placing options. 115
Figure 9.3 Advanced diode layouts placed on the production wafer 117
Figure 9.4 Qualification of the ITE diodes 118
Figure 9.5 Current of different diodes on two ITE wafers. 119
Figure 9.6 Capacitance of different diodes on two ITE wafers. 119

Figure 9.7 R_{PG} measurements on diodes on the ITE wafer. 120
Figure 9.8 Layout of the CNM wafer. 121
Figure 9.9 Current of CNM diodes across the wafer. 122
Figure 9.10 Breakdown behaviour of diodes on the CNM wafer. 122
Figure 9.11 Capacitance of diodes on the CNM wafer. 123
Figure 9.12 Optical inspection of CNM diodes. 124
Figure 9.13 Resistance between pad and guard of diodes on the CNM wafer. 124
Figure 10.1 Baby Pitch Adapter 127
Figure 10.2 CAC of FZ320N_01_BPA_1. 128
Figure 10.3 Cint of FZ320N_01_BPA_1. 129
Figure 10.4 Signal and signal to noise ratio of a BPA sensor. 129
Figure 10.5 Cluster noise and cluster size of BPA. 130
Figure 10.6 Sketch of the simulation of a BPA. 131
Figure 10.7 2d Simulation model of the BPA 132
Figure 10.8 Simulation of Signals on the BPA. 133
Figure 10.9 Layout of the DMPA. 134
Figure 10.10 Qualification of the DMPA 135
Figure 10.11 Capacitance AC-DC of the DMPA. 136
Figure 10.12 Measurements of the DMPA. 137
Figure 10.13 Simulated Signals in the DMPA. 138
Figure 11.1 Volume scaled current vs. Fluence measured for diodes. 143
Figure 11.2 Depletion voltage of diodes. 144
Figure 11.3 Concentration dependence of the generated current in the EVL model . . . 145
Figure 11.4 Variation of the cross sections in the EVL model 146
Figure 11.5 Hamburg Model for different irradiations. 147
Figure 11.6 CV curves of proton irradiated FZ320N diodes. 148
Figure 11.7 Simulated depletion voltage of n-bulk diodes. 149
Figure 11.8 Simulated depletion voltage of p-bulk diodes. 149
Figure 11.9 Summary for $F = 10^{15}\,n_{eq}cm^{-2}$ 153
Figure 11.10 Measurement and Simulation of TCT signals at $F = 1.1 \times 10^{14}\,n_{eq}/cm^2$ (p). 154
Figure 11.11 Measurement and Simulation of TCT signals at $F = 2.9 \times 10^{14}\,n_{eq}/cm^2$ (p). 156
Figure 11.12 Comparison of TCT simulation and measurement at $F = 2.9 \times 10^{14}\,n_{eq}/cm^2$ (p). 156
Figure 11.13 TCT Measurement and comparison with simulation at $F = 10^{15}\,n_{eq}/cm^2$ (p). 157
Figure 11.14 Influence of saturation velocity on the TCT pulse. 158
Figure 11.15 Influence of the mobility on the TCT pulse. 158
Figure 11.16 Electric fields in a FZ320N diode simulated with the proton model. 162
Figure 11.17 Electric fields in a FZ320P diode simulated with the proton model. 163
Figure 11.18 Electric fields in a FZ200P diode simulated with the proton model. 164
Figure 11.19 Simulation of the signal evolution in a diode at $F = 10^{14}\,n_{eq}cm^{-2}$. 167
Figure 11.20 Trapping time fit in the simulation at $F = 10^{14}\,n_{eq}cm^{-2}$. 168
Figure 11.21 Trapping time fit in the simulation at $F = 10^{15}\,n_{eq}cm^{-2}$. 168
Figure 11.22 Trapping time corrected simulated TCT pulse and integrated signal at $10^{14}\,n_{eq}cm^{-2}$. 170
Figure 11.23 Trapping time corrected simulated TCT pulse and integrated signal at $10^{15}\,n_{eq}cm^{-2}$. 170
Figure 11.24 CCE of FZ320N at several fluences and $-20\,°C$. 171
Figure 11.25 TCT signals at $0\,°C$ and $-20\,°C$ in comparison. 173
Figure 11.26 Simulated CV and TCT curve at $T = 0\,°C$. 173
Figure 12.1 Electric fields at the strips in a neutron irradiated n-bulk sensor. 178
Figure 12.2 Electric fields at the strips in a proton irradiated n-bulk sensor. 179
Figure 12.3 Electric fields at the strips in a proton irradiated p-bulk sensor. 180

Figure 12.4 Electric field in the bulk for FZ320P and FZ200P strip sensors at different fluences. 181
Figure 12.5 Electric fields at the strips for a FZ200P sensor with different p-stop concentrations. 182
Figure 12.6 Signals in a FZ320N strip sensor after irradiation. 183
Figure 12.7 Comparison of experimental and simulated CCE for FZ320N. 184
Figure 12.8 Comparison of experimental and simulated CCE for FZ320P. 185
Figure 12.9 Simulated CCE vs. fluence for irradiated n-bulk sensors. 186
Figure 12.10 Simulated CCE vs. fluence for irradiated p-bulk sensors. 186
Figure 12.11 Charge loss between strips for irradiated strip sensors. 187
Figure 12.12 Simulated current in a strip sensor at $F = 5 \times 10^{15}\, n_{eq} cm^{-2}$. 188
Figure 12.13 Measured current in an RD50 sensor at $F = 5 \times 10^{15}\, n_{eq} cm^{-2}$. 189
Figure 12.14 Simulated electric field near the strip for $F = 5 \times 10^{15}\, n_{eq} cm^{-2}$ 190
Figure 12.15 Measured charge multiplication on dedicated RD50 samples. 191
Figure 12.16 Electric field at the strips for $F = 5 \times 10^{15}\, n_{eq} cm^{-2}$ dependent on the strip width. 191
Figure 12.17 Impact ionization rate for different strip width and oxide charge concentration at $F = 5 \times 10^{15}\, n_{eq} cm^{-2}$. 192
Figure 12.18 Electron density for different strip width and oxide charge concentration. . 192
Figure D.1 Database link structure. 213

LIST OF TABLES

Table 4.1 Hardness factors of particles used in this work. 35
Table 4.2 Parameters of the Hamburg-Model 40
Table 4.3 Important defects in silicon irradiated by hadrons 41
Table 5.1 Parameters of the drift velocity model. 50
Table 5.2 TCT pulse shape classification 55
Table 7.1 Default parameters used in the simulation 66
Table 7.2 Parameters for the Canali Model 67
Table 7.3 Default and used parameters of the temperature dependent lifetime. . . . 68
Table 7.4 Standard parameters for the bandgap model in Synopsys Sentaurus. . . . 73
Table 7.5 Default Parameters for the Saturation Velocity in Synopsys Sentaurus . . . 74
Table 7.6 Default Parameters for the Saturation Velocity in Silvaco Atlas 74
Table 7.7 Parameters for the charge carrier mobility models. 75
Table 7.8 Parameters for the comparison of simulation packages. 77
Table 8.1 Full depletion voltage and doping profile description of diodes before irradiation 81
Table 8.2 Parameters for the simulation of leakage current 87
Table 8.3 Parameters of the H220K defect 89
Table 8.4 Fit for the active area of diodes. 91
Table 8.5 Percentage of total capacitance. 92
Table 8.6 Dimensions of HPK diodes from the GDS file. 93
Table 8.7 Measured Capacitances with and without floating guard ring and their difference. 95
Table 8.8 Depletion Voltage of un-irradiated diodes with and without grounded guard ring. 96
Table 8.9 Parameters for HPK strips. 103
Table 8.10 Parameters for RD50 strip sensors. 103
Table 9.1 Variation of Parameters for advanced Diode Design. 115
Table 11.1 Simulation: Original EVL model 144
Table 11.2 Simulation:Neutron model 150
Table 11.3 Simulation:Proton model 150
Table 11.4 Electron trapping times of FZ320N. 166
Table 11.5 Trapping time from simulation at different voltages. 169
Table 11.6 Proton Model for $T = 0\,°C$. 172
Table D.1 Database: “info” table 214
Table D.2 Database: “info_defect” table 214
Table D.3 Database: “alibava” table 215
Table D.4 Database: “probe” table 217
Table D.5 Database: table “probe_data” 217
Table E.1 List of libraries for the ROOT framework for databases. 219

»Ich kann dir nur die Tür zeigen, hindurchgehen musst du selbst.«

— *aus Matrix.*

ACKNOWLEDGMENTS – DANKSAGUNG

This work would not have been possible without the support of many people, whom I'd like to thank here! –
Diese Arbeit wäre nicht gelungen ohne die Hilfe und Unterstützung derjenigen, denen ich hier danken möchte!

Mein erster Dank gilt Herrn Prof. Dr. Thomas Müller für die Chance, meine Doktorarbeit am Institut für Experimentelle Kernphysik in einem spannenden Gebiet der Detektorentwicklung durchzuführen.

Prof. Dr. Wim de Boer möchte ich für die hilfreiche Unterstützung bei viele Fragestellungen sowie für die Übernahme des Korreferats danken.

Dr. Alexander Dierlamm danke ich besonders für die gute Hilfestellung, viele gute Vorschläge und sein Engagement.

Weiter möchte ich danken:

- Dr. Hans Jürgen Simonis für die Administration des Netzwerks und der Hardware sowie für viele Diskussionen,
- Frank Hartmann für CERN-seitige Unterstützung,
- Felix Bögelspacher für die vielen Bestrahlungen und das Beisteuern elektronischer Komponenten,
- Tobias Barvich für die kompetente technische Beratung sowie Umsetzung,
- Pia Steck für viele gebondete Dioden und viele weitere kleine Arbeiten,
- Diana Fellner und Brigitte Gering für alle organisatorische und bürokratische Arbeiten,
- meinen Mitstreitern: Andreas Nürnberg, Moritz Guthoff, Karl-Heinz - Kalle - Hoffmann, Martin Printz, Stefan Heindl,
- vielen weiteren Unterstützern und Helfern: Prof. Dr. Ulrich Husemann, Dr. Thomas Weiler, Dr. Martin Frey, Dr. Mike Schmanau, Dr. Alexandra Junkes[1], Sabine Frech, Lokman Altan, Benedikt Freund, Volker Heine, Joachim Erfle[1], Thomas Pöhlsen[1], Thomas Eichhorn[2], Andreas Kornmayer,
- meinen Freunden, besonders Andi, Manu, Timo, Bastian, Nicole, Martin, Philip,
- Eva Herold,
- und zu guter Letzt meinen Eltern Adeltraud und Gerhard für ihre unverzichtbare und anhaltende Unterstützung sowie meiner Schwester Isabelle und meinem Großvater Hans Wolf.

Dem Graduiertenkolleg "Elementarteilchenphysik bei höchster Energie und höchster Präzision" danke ich sehr für die Unterstützung bei der Promotion und für die Organisation der Workshops, die zum regen wissenschaftlichen Austausch geführt haben.

1 Universität Hamburg
2 DESY Hamburg

A big thank you goes out to the CMS Upgrade Simulation Working Group for many many discussions and inspirations to many simulations.

I'd escpecially like to thank the RD50 collaboration for many interesting suggestions and proposals, fruitful discussions and the friendly atmosphere within the group.

Thanks to all people from the ESHEP 2012 summer school for good physics discussions and a great time.

This work is supported by the Initiative and Networking Fund of the Helmholtz Association, contract HA-101 ("Physics at the Terascale").

The research leading to the results of this thesis has received funding from the European Commision under the FP7 Research Infrastructures project AIDA, grant agreement no 262025.

PUBLICATIONS

Robert Eber on behalf of the CMS Tracker Collaboration: Silicon Sensor Developments for the CMS Tracker Upgrade. In: Astroparticle, Particle, Space Physics and Detectors for Physics Applications. Vol. 7, World Scientific, 2011. Proceedings of the 13th ICATPP Conference. 856-860.

Robert Eber: Untersuchungen an Magnetic-Czochralski-Dioden nach gemischter Bestrahlung mit Neutronen und Protonen mittels der Transient-Current-Technique, Universität Karlsruhe (TH), Diploma Thesis, 2009. – IEKP-KA/2009-30.

DECLARATION

Diese Arbeit wurde selbständig angefertig. Quellen wurden gekennzeichnet.

Karlsruhe, November 2013

Robert Eber